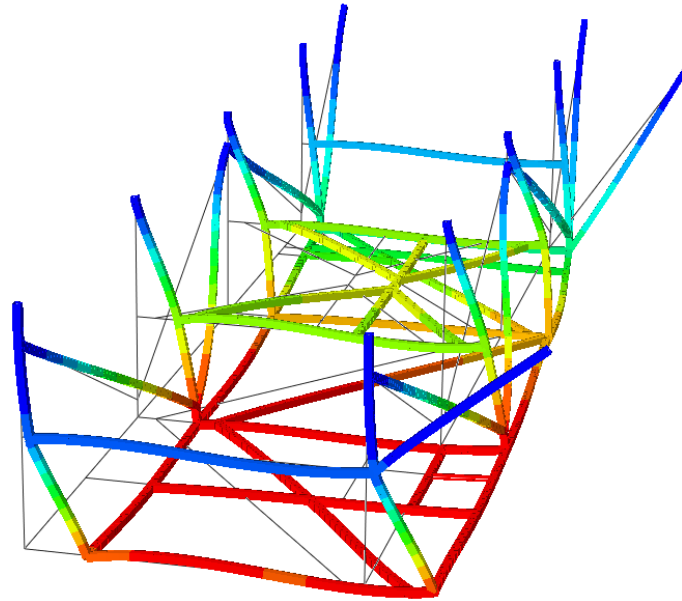




LUND
UNIVERSITY



INELASTIC CAPACITY OF PIPE RACK STRUCTURES

**Study of Dynamic Response to Accidental
Explosion Events in an Offshore Topside
Environment**

ADAM HALVORSEN STÅLMARCK

Structural
Mechanics

Master's Dissertation

DEPARTMENT OF CONSTRUCTION SCIENCES

STRUCTURAL MECHANICS

ISRN LUTVDG/TVSM--15/5205--SE (1-146) | ISSN 0281-6679

MASTER'S DISSERTATION

INELASTIC CAPACITY OF PIPE RACK STRUCTURES

Study of Dynamic Response to Accidental
Explosion Events in an Offshore Topside
Environment

ADAM HALVORSEN STÅLMARCK

Supervisors: Professor **PER-ERIK AUSTRELL**, Div. of Structural Mechanics, LTH, Lund together with **ARSWENDY ARSWENDY**, Senior Structural Engineer, AET, Aker Solutions and **JAN CHRISTOFERSEN**, Department Manager Structural, Aker Solutions.

Examiner: Professor **KENT PERSSON**, Div. of Structural Mechanics, LTH, Lund.

Copyright © 2015 Division of Structural Mechanics,
Faculty of Engineering (LTH), Lund University, Sweden.

Printed by Media-Tryck LU, Lund, Sweden, June 2015 (*Pl*).

For information, address:

Div. of Structural Mechanics, LTH, Lund University, Box 118, SE-221 00 Lund, Sweden.

Homepage: <http://www.byggmek.lth.se>

Abstract

Steel structures in an offshore processing environment must be designed for an accidental explosion event. The current verification procedure implemented at Aker Solutions (AKSO) enforces an elastic single degree of freedom (SDOF) analogy to implicitly account for dynamic effects in linear static FE analyses. The implication of this approach is that structures are designed to remain within their elastic range during an explosion event, generating weight and cost inefficient designs. The objective of this thesis was therefore to determine the inelastic capacity of a typical pipe rack structure subjected to blast. A modified verification procedure was also evaluated to determine if this unutilized capacity may be accounted for via incorporation of an inelastic SDOF-response model.

Research on the blast phenomena showed that the dominant load effects from interaction between a pipe rack structure and a blast pulse were governed by the dynamic blast-pressure, idealized as a symmetric triangular pulse-excitation to characterize the typical deflagration type explosion. This pressure was converted to drag loads and assigned to structural members in the conducted finite element analysis (FEA) study, aiming to reveal the true dynamic structural response to pulse excitations of varying magnitudes.

A specific pipe rack design from a previous AKSO project was chosen for evaluation. The associated piping configuration was accounted for implicitly in the FEA study via simplified calculations of mass contribution and transfer of blast loading to the analyzed rack structure. Failure criteria were also established to prevent rupture of safety critical pipe lines according to the defined post-blast functionality requirements.

Results from full nonlinear FE analyses showed that the original pipe rack design remained completely elastic during simulations of the design blast-pulse scenario. The validity of the current verification procedure was thereby confirmed and the associated elastic SDOF-model was found to prevail with great accuracy. Failure criteria were not exceeded until the original design-pulse had been magnified by a factor of 4.8 to a corresponding peak pressure of approximately 1 barg and pulse duration of 50 milliseconds. The amount of inelastic capacity possessed by the pipe rack at this load level was quantified by the observed ductility ratio of 2.25. The expanded SDOF analogy failed to capture the inelastic dynamic response with a satisfactory level of precision. However, conservative estimates of a pipe rack structures full capacity were obtained when this inelastic SDOF-model was incorporated into the modified verification procedure.

Preface

This thesis has been devoted to the topic of dynamic, inelastic behavior of pipe rack structures subjected to an accidental explosion event in an offshore topside environment. The study was initiated by the structural department at Aker Solutions (Aker Engineering & Technology AS) and the work has been conducted at their headquarters in Oslo, Norway between January and June of 2015. This paper is published as a Master's Dissertation report by the Department of Structural Mechanics at Lund University, Sweden.

First and foremost, I would like to thank and express my gratitude towards Arswendy Arswendy and Jan Christofersen, my mentors and supervisors at Aker Solutions whom have provided much assistance and guidance throughout the entire process. Your time and knowledge has been an invaluable asset in my work with this thesis.

I would also like to thank all other staff at Aker Solutions that have been involved in the process and helped me by sharing their knowledge. Among these people, Richard Curbo deserves to be recognized and thanked for his collaboration and help on piping related matters.

Finally, I would like to thank Assoc. Professor Per-Erik Austrell for supervising my work on behalf of the Department of Structural Mechanics. Your guidance and help has been much appreciated.

Lund, June 2015

Adam Halvorsen Stålmärck

Table of Contents

| | | |
|-------|---|----|
| 1 | Introduction | 1 |
| 1.1 | Background | 1 |
| 1.1.1 | Verification Procedures for Accidental Explosion Events | 1 |
| 1.1.2 | Pipe Rack Structures | 2 |
| 1.2 | Objective | 4 |
| 1.3 | Method | 4 |
| 1.4 | Limitations | 5 |
| 1.5 | Outline | 5 |
| 2 | Characteristics of Explosions | 7 |
| 2.1 | Types of Explosions | 7 |
| 2.2 | Blast Pressure-Pulses | 8 |
| 2.3 | Load Effects on Structures | 12 |
| 2.4 | CFD and Design Load Output | 17 |
| 2.5 | Concluding Remarks | 20 |
| 3 | Structural Mechanics in Blast Scenario | 23 |
| 3.1 | Structural Dynamics | 23 |
| 3.1.1 | Damping in Blast Scenario | 24 |
| 3.1.2 | SDOF System | 24 |
| 3.1.3 | MDOF System | 26 |
| 3.1.4 | Dynamic Properties of Structural Systems | 26 |
| 3.2 | Nonlinear Material Behavior | 29 |

| | | |
|-------|--|----|
| 3.3 | Inelasticity and Failure in Simple System | 32 |
| 4 | Analytical Methods and Verification Procedures | 37 |
| 4.1 | Linear-Elastic Biggs Method | 37 |
| 4.2 | The Conventional Method | 41 |
| 4.3 | Elasto-Plastic Biggs Method | 42 |
| 4.4 | The Proposed Method | 45 |
| 5 | Finite Element Analysis Study | 49 |
| 5.1 | Reference Coordinate System | 50 |
| 5.2 | Piperack01_P30_M50 | 51 |
| 5.3 | FE Models | 52 |
| 5.3.1 | FE Model A | 52 |
| 5.3.2 | FE Model B | 54 |
| 5.4 | Assumptions | 56 |
| 5.5 | Failure Criteria | 56 |
| 5.6 | Material Models | 57 |
| 5.7 | Basic Load Cases | 59 |
| 5.8 | Blast Loads | 59 |
| 5.9 | Scope of Work | 60 |
| 6 | Results and Conclusions | 63 |
| 6.1 | Analysis A.1 | 63 |
| 6.2 | Analysis B.1 | 67 |
| 6.3 | Analysis B.2 | 71 |
| 6.4 | Analysis B.3 | 76 |
| 6.5 | The Conventional Method | 83 |
| 6.6 | The Proposed Method | 86 |
| 6.7 | Analysis B.4 | 88 |
| 6.8 | Analysis B.5 | 90 |
| 6.9 | Analysis B.6 | 94 |

| | | |
|------------|--|-----|
| 7 | Discussion and Recommendations on Further Work | 101 |
| | References | 105 |
| Appendix A | FEA Study Documentation | 107 |
| Appendix B | Shielding Coefficient | 132 |
| Appendix C | Plastic Strain Criterion Study | 136 |
| Appendix D | Matlab Script | 137 |
| Appendix E | Static Pushover Analysis | 140 |

Abbreviations

| | |
|-------|--|
| AISC | American Institute of Steel Construction |
| AKSO | Aker Solutions |
| ALS | Accidental Limit State |
| API | American Petroleum Institute |
| ASCE | American Society of Civil Engineers |
| CFD | Computational Fluid Dynamics |
| DAF | Dynamic Amplification Factor |
| DIF | Dynamic Increase Factor |
| DNV | Det Norske Veritas |
| DOF | Degree of Freedom |
| EOM | Equation of Motion |
| FE | Finite Elements |
| FEA | Finite Element Analysis |
| FLACS | Flame Acceleration Simulator |
| GZ | Ground Zero |
| HD | Hold Down |
| LG | Line Guide |
| LS | Line Stop |
| MDOF | Multi Degree of Freedom |
| OD | Outer Diameter |
| PDMS | Plant Design Manager System |
| PSA | Petroleum Safety Authority |
| RHS | Rectangular Hollow Section |
| RS | Rest Support |
| SDOF | Single Degree of Freedom |
| TNT | Trinitrotoluene |
| VCE | Vapor Cloud Explosion |

Nomenclature

| | |
|--------------------|--|
| c | Damping |
| f_{ds} | Dynamic design stress |
| f_n | Natural cyclic frequency of vibration |
| f_D | Damping force |
| f_I | Inertial force |
| f_S | Internal force |
| k | Stiffness |
| m | Mass |
| m_{ps} | Pipe mass at location of internal pipe support |
| p | External force |
| \mathbf{p} | External force vector |
| p_0 | Peak pulse-force |
| p_1 | Design-pulse peak pressure |
| $p_{1,limit}$ | Limiting peak blast-pressure |
| p_d | Dynamic pressure |
| p_{d0} | Peak dynamic pressure |
| p_s | Overpressure |
| p_{s0} | Peak overpressure |
| q_o | Drag load |
| q_{nL} | Axially distributed blast-load for lower-level rack member |
| q_{nU} | Axially distributed blast-load for upper-level rack member |
| r_i | Inner pipe section radius |
| r_o | Outer pipe section radius |
| t | Time |
| t_1 | Design-pulse phase duration |
| t_d | Positive phase duration |
| t_{dd} | Positive phase duration of dynamic pressure |
| t_{dp} | Positive phase duration of overpressure |
| t_m | Time of maximum dynamic response |
| $t_{max,resp}$ | Time of recorded maximum dynamic response |
| u | Displacement |
| \mathbf{u} | Displacement vector |
| \dot{u} | Velocity |
| $\dot{\mathbf{u}}$ | Velocity vector |

| | |
|---------------------|---|
| \ddot{u} | Acceleration |
| $\ddot{\mathbf{u}}$ | Acceleration vector |
| u_0 | Maximum dynamic response |
| v | Air particle velocity |
| y | Displacement |
| \dot{y} | Velocity |
| \ddot{y} | Acceleration |
| y_{el} | Maximum elastic displacement |
| y_m | Maximum dynamic displacement |
| | |
| A | Area |
| A_{Blast} | Exposed blast area |
| A_P | Blast-exposed pipe area |
| A_{RM} | Blast-exposed rack area |
| \mathbf{C} | Damping matrix |
| C_d | Drag coefficient |
| C_r | Reflection coefficient |
| E | Young's modulus |
| F | External force |
| F_1 | Peak pulse-force |
| \mathbf{F}_{int} | Internal forces |
| FCF | Fluid content factor |
| $H1$ | OD of largest pipe section at lower rack level |
| $H2$ | OD of largest pipe section at upper rack level |
| I_o | Magnitude of impulse |
| I_p | Magnitude of free-field pressure pulse |
| \mathbf{K} | Stiffness matrix |
| L_{eff} | Effective length |
| L_t | Tributary length |
| M | Uniaxial bending moment |
| \mathbf{M} | Mass matrix |
| M_p | Plastic moment-resisting capacity |
| M_{pu} | Ultimate dynamic moment-resisting capacity |
| M_y | Yield moment |
| P_{nL} | Concentrated blast-force transferred to lower-level rack member |
| P_{nU} | Concentrated blast-force transferred to upper-level rack member |
| P_r | Reflected pressure |
| P_{so} | Peak overpressure |
| PL | Concentrated blast-force transferred via pipe support |
| R | Spring resistance |
| R_M | Perfectly-plastic internal resistance |
| RFn | Reaction forces in direction n |

| | |
|--------------|--|
| S | Elastic section modulus |
| T | Natural period of vibration |
| T_n | Natural period of vibration |
| U | Velocity of blast wave |
| Un_{max} | Maximum global displacement in direction n |
| UDL | Uniformly distributed blast-load |
| W | Strain energy |
| W_m | Member width |
| W_{mpipe} | Weight per meter pipe |
| WC_{mpipe} | Content weight per meter pipe |
| W_{RS} | Width of rack section |
| Z | Plastic section modulus |

| | |
|---------------------------|---|
| ε | Strain |
| ε^e | Elastic strain |
| ε^p | Plastic strain |
| $\varepsilon_{failure}$ | Strain at failure |
| $\varepsilon_{failure}^p$ | Plastic strain at failure |
| ε_{max}^p | Maximum recorded plastic strain |
| ρ | Density |
| ρ_{fluid} | Piping fluid content density |
| ρ_{mod} | Modified material density |
| σ | Stress |
| σ_{max} | Overall maximum von Mises stress |
| σ_{ult} | Ultimate stress |
| σ_y | Arbitrary stress level beyond yield |
| σ_{yo} | Initial yield stress |
| $\sigma(\varepsilon_x)$ | Axial stress in beam element |
| ω_n | Natural circular frequency of vibration |
| Φ_n | Natural mode vector |
| μ | Ductility ratio |
| η | Shielding coefficient |
| τ | Pulse duration |

| | |
|------------------|-------------------------------------|
| $(u_{st})_0$ | Amplitude of static equilibrium |
| Δ_{max} | Maximum displacement at failure |
| Δ_{yield} | Displacement at first initial yield |

1 Introduction

1.1 Background

Steel structures on off- and onshore processing facilities shall be designed for an accidental explosion event according to safety regulations applicable to the oil and gas industry. These regulatory documents provide a framework of general safety criteria, defining hazardous subsequent effects associated with an accidental explosion to consider in the design and verification process. In order to limit the consequential damages from an explosion, engineers must make use of analytical tools and theoretical models accurately reflecting the structural response in such an event.

Research conducted in the academic environment on the topic of explosion effects and blast-resistant design is sparse and much work was produced during the 1950s and 1960s. More extensive research within this field tends to happen in the military sector and the U.S. Department of Defense has made several publications on the topic of blast available to the public. In the realm of academics, much more attention has been devoted to seismic effects on structures and the analytical toolbox available for seismic design purposes is therefore more comprehensive.

However, many institutions within the industry and structural engineering community such as DNV, AISC and ASCE offer guidelines and recommended practices on blast-resistant design and verification procedures. A common suggested approach is to adopt approximate analytical methods to predict the overall maximum dynamic response of a structure subjected to blast. These analytical methods are based on a single degree of freedom (SDOF) analogy where the complexity of the problem is reduced by idealizing both the structural system and the load scenario.

1.1.1 Verification Procedures for Accidental Explosion Events

The SDOF analogy is enforced in the verification procedure implemented at Aker Solutions (AKSO) today, where the dynamic structural response in an accidental explosion event is implicitly accounted for via an approximate analytical method developed by Biggs (1964). This specific analytical method is consistently referred to as the *Linear-elastic Biggs method* within this report while the entire verification procedure utilizing this method will be referred to as the *conventional method*.

The implication of the current verification procedure outlined by the *conventional method* is that structural systems are designed to remain within their linear-elastic range during a blast event. Consequently, the accidental explosion event governs the design of a large portion of steel structures on processing facilities, generating very robust structural configurations that increase the total weight and cost budget. This undesirable outcome is the main reason to why AKSO has initiated the study conducted within this thesis, aiming to investigate the unutilized inelastic capacity possessed by

structures designed according to the *conventional method* and wheatear this capacity could be accounted for via implementation of a modified verification procedure recently developed at AKSO.

This modified verification procedure will be referred to as the *proposed method*. It also enforces a SDOF analogy via application of another approximate method developed by Biggs (1964) referred to as the *Elasto-plastic Biggs method*.

Both the *conventional method* and *proposed method* verifies structures for accidental explosion events through linear static FE analyses were the blast pressure is applied as static wind load. This procedure does not comply with the dynamic nature of an accidental explosion event and is unfit to capture the structural response to such a severe and rapid load scenario. Hence, dynamic effects associated with a blast wave interacting with a structure must be incorporated into this static FE formulation somehow. This is achieved through implementation of the two approximate methods as following chapters will describe in detail.

The procedure defined as the *conventional method* account for the dynamic effects by applying a dynamic amplification factor (DAF) to the calculated static blast loads, thus implicitly scaling all field variables derived from the static FE simulation and implicitly accounting for an overall maximum dynamic response. The DAF is obtained from the *Linear-elastic Biggs method*, an analytical approach that determines the normalized dynamic response of an undamped, linear-elastic SDOF system subjected to a triangular pulse excitation. The only input parameter needed to find the applicable DAF through the *Linear-elastic Biggs method* is the ratio of blast pulse duration over the natural period of the structural system.

The strategy of the *proposed method* is to establish an initial design of a structure from a verification process accounting for all limit states and load scenarios except the accidental explosion event. Through implementation of the *Elasto-plastic Biggs method*, the intention is to demonstrate that the full capacity possessed by this initial design exceeds the capacity required to withstand loading imposed by the design blast-pulse. The theory behind the *Elasto-plastic Biggs method* also relates to the response of an undamped SDOF-system to a triangular pulse excitation. However, inelastic capacity is built into the SDOF-model via an idealized resistance function implying that an allowable response is no longer limited to the linear-elastic range within the *proposed method*.

1.1.2 Pipe Rack Structures

Processing facilities comprise of numerous of different load-bearing components, outfitting steel structures and equipment. The scope of this thesis will be limited and focus solely on pipe rack structures designed for an offshore topside environment. A pipe rack system consists of mainly two structural components; (1) a rack structure and (2) the pipe lines containing hydrocarbons or other fluid content which are supported by the rack structure. This structural system is of particular interest since a ruptured pipe would act as a fuel resource, potentially intensifying fires caused by an initial explosion or causing new explosions due to the highly ignitable and explosive nature of the hydrocarbons.

Figure 1-1 show part of an offshore topside processing facility. A typical pipe rack configuration located in an external area is highlighted in yellow. A more detailed view of its structural components is provided by Figure 1-2.

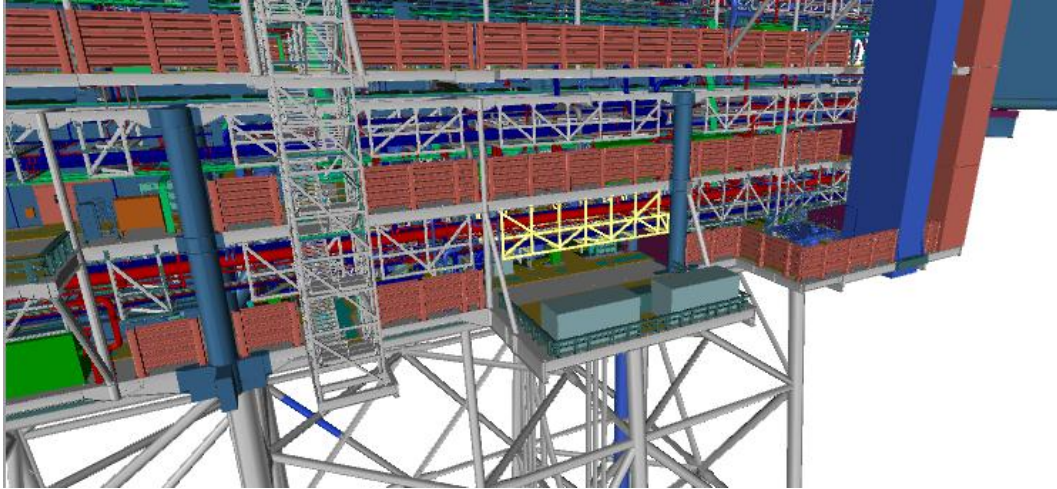


Figure 1-1 Pipe rack structure located in external area of an offshore processing facility.

Figure 1-2 show how the pipe lines are locally supported by the specific rack structure. This rack structure has two main levels where the pipe lines are drawn and attached to horizontal members via pipe supports designed to constrain the pipe section relative the rack structure in specified directions. The typical rack structure is a three-dimensional truss system of RHS profiles (Rectangular Hollow Section) connected to the above deck structure.

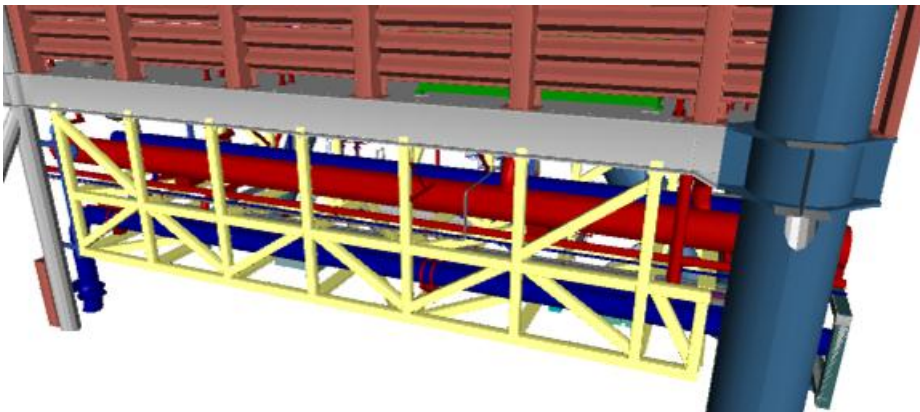


Figure 1-2 Typical pipe rack configuration.

The only purpose of the rack structure is to offer support and protection to the attached pipe lines, which are the critical components in this structural system. Failure of a safety critical pipe line shall therefore govern any procedure aiming to verify an interactive response between a rack structure and an attached pipe line configuration. A complex aspect of this problem to be addressed within the

thesis is how to account for this interactive response within the frame work of a manageable, efficient and reliable verification procedure.

The dynamic response of a pipe rack structure in an accidental explosion event has been studied in pervious theses conducted by Aarønæs and Nilsson (2014) and A. Su (2012). However, these publications primary focus is on evaluation of the *Linear-elastic Biggs method* and its associated linear-elastic SDOF analogy. With this thesis, the study is extended to a dynamic response within the inelastic range and evaluation of a SDOF-model accounting for inelastic capacity.

1.2 Objective

The main objective of this thesis is to determine the extent of the inelastic capacity possessed by a typical pipe rack configuration subjected to an accidental explosion event. To achieve this, it is critical that the interactive response of the entire structural assembly is accounted for in the process.

Furthermore, the thesis aims to evaluate and conclude on the accuracy of the approximate analytical methods incorporated into the two verification procedures referred to as the *conventional method* and the *proposed method*. How well do the analytical methods based on a SDOF analogy account for the complex nature of this problem?

The validity of the two different verification procedures shall also be confirmed within the scope of this thesis. Is a pipe rack design verified in accordance with the *conventional method* going to remain elastic during the design explosion event? Will the *proposed method* be successful in providing a reliable estimate of a pipe rack structures inelastic capacity?

1.3 Method

A comprehensive FEA study was conducted within the scope of this thesis. The commercial FE software Abaqus and its specific analysis product Abaqus/Standard was used to run all simulations within this numerical study. Linear static analyses and Eigen frequency analyses were conducted for evaluation of the *conventional method* and the *proposed method*. Full nonlinear ¹ analyses were performed to reveal the “true” response of the pipe rack structure and to determine its full inelastic capacity.

A literature study on the topic of explosions and structural response to blast was also conducted. Recommended practices and guidelines provided by the industry were consulted along with textbooks and publications from distinguished authors within the academic environment. The basics of fundamental theoretical aspects within the fields of explosion effects, dynamics, material response and inelastic behavior were studied and explained. The knowledge gained from these studies was used to define the physical problem numerically in the FEA study and thus ensure that the FE simulations would generate reliable results.

¹ A full nonlinear FE formulation accounts for dynamics, plastic material behaviour and nonlinear kinematics.

The underlying theory behind the approximate analytical methods developed by Biggs (1964) was explained and a numerical Matlab script was created for calculating DAFs in accordance with the *Linear-elastic Biggs method*.

1.4 Limitations

The numerical study is limited to evaluation of one specific pipe rack configuration, verified according to the *conventional method* in a previous AKSO project.

Among the load effects associated with the blast phenomena, only the generated pressure-pulse was considered. Secondary effects such as impact from flying objects were excluded from the scope.

Structural steel is the material mainly utilized in the design of a pipe rack assembly. Exceptions are found for some pipe lines designed from an anisotropic, non-metallic material. However, the theoretical and numerical study is limited to steel material models.

No other approximate methods than the SDOF analogies defined by the *Linear-elastic Biggs method* and *Elasto-plastic Biggs method* were studied.

1.5 Outline

Chapter 2 contains a theoretical study on characteristics of explosions and load effects on structures at interaction with a blast wave.

Chapter 3 covers fundamental theory within the field of structural mechanics associated with a severe dynamic structural response during an accidental explosion event.

Chapter 4 describes the theory behind the approximate analytical methods evaluated within this thesis. Verification procedures utilizing these analytical methods are also outlined in detail.

Chapter 5 and referenced appendices provides a complete documentation of the FEA study conducted within this thesis.

Chapter 6 contains results and conclusions associated with the FEA study and evaluated verification procedures.

Chapter 7 discusses the results and conclusions presented in the preceding chapter and provides recommendations on further work.

2 Characteristics of Explosions

2.1 Types of Explosions

An explosion is defined by CCPS (1996) as the phenomena of blast-pressure pulse generation through rapid release of energy. The energy that has been stored prior to release can be of various forms such as chemical, nuclear or electrical, but independent of source the energy release may only be defined as “explosive” if it produces a pressure-pulse that can be heard (CCPS, 1996). Except from the audible blast, coupled into the air as airblast and into the ground as ground shock, the general explosion is also characterized by a flash due to energy release through thermal radiation according to Alfawakhiri and Marchand (2004). However, the component of the explosion mainly responsible for structural damage to a building is the generated pressure-pulse, propagating outwards into the surrounding atmosphere as illustrated in Figure 2-1 (ASCE, 2010). This will be made evident when discussing load effects associated with accidental blast scenarios later on.

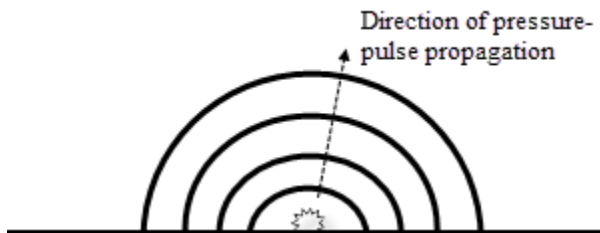


Figure 2-1 Propagation of blast-pressure pulse from explosion occurring at ground surface.

Most of the material on structural blast-resistance is developed considering explosion events such as acts of terrorism, where the explosions originate from the use of TNT or other high-yield explosives in military applications. However, these types of explosions are not necessarily of the same nature as the accidental explosion events that govern the possible blast scenarios in petrochemical facilities (ASCE, 2010). This observation is confirmed by (CCPS, 1996), stating that chemical energy is the most relevant energy source to be considered for such scenarios. However, it is important to understand that the source of energy itself does not necessarily govern the load effects generated by an explosion. The governing factor is whether the explosion can be categorized as a detonation or a deflagration, the former being associated with high-yield explosives such as TNT.

The chemical energy release can be categorized as either a deflagration or a detonation, where the difference between them lies in the mechanism of energy transfer from reacted material to unreacted material. The energy transfer in a deflagration happens through heat and mass transfer and the explosive reaction propagates relatively slowly into the surrounding unreacted material as it is heated

above autoignition temperature. The speed of energy transfer through this process is always less than the speed of sound. On the contrary, the process of energy transfer to unreacted material in a detonation is very rapid, with supersonic propagation speeds. The governing transfer mechanism for detonations is through shock compressive heating (CCPS, 1996).

As a first step in the process of determining blast loads for structural design in a petrochemical environment, the most relevant types of accidental explosions must be identified. ASCE (2010) provides this information categorized into four basic types; (1) Vapor Cloud Explosions (VCE), (2) Pressure Vessel Explosions, (3) Condensed Phase Explosions and (4) Dust Explosions. Among these four types, vapor cloud explosions are considered the primary concern for processing plants. VCEs are gas explosions that generate pressure-pulses through the combustion process of a premixed gas cloud. They are often categorized as deflagrations, but if extremely energetic in nature, they are better defined by the mechanisms of a detonation. Consequently, both detonations and deflagrations are possible accidental events in petrochemical facilities and both phenomena are therefore to be described further.

For detailed descriptions of the four types of explosions mentioned above, reference is made to publications such as (CCPS, 2010). For the purpose of this thesis, focus is shifted towards the different blast pressure-pulses that the various explosion types give rise to. As described in (ASCE, 2010), these pressure-pulses have the characteristics of either a; (1) Shock wave, associated with detonations, or (2) Pressure wave, characteristics of a deflagration.

2.2 Blast Pressure-Pulses

As a result from the distinct differences between the two energy release processes, the characteristics of the blast-pressure pulse generated by a deflagration (shock wave) or a detonation (pressure wave) will evidently be different in nature (CCPS, 1996). As summarized by (ASCE, 2010), the shock wave is characterized by an instantaneous rise in overpressure² while the pressure rise for a pressure wave happens gradually. Overpressure is also referred to as incident pressure or static pressure, as it defines an isotropic state of pressure. This is made clear as the features of both pressure waves are studied more thoroughly. It should be noted that the features described within this section capture the initial blast wave characteristics, prior to any interaction with obstacles or other disturbances. At this state, the term free-field blast wave is adopted.

The characteristics of a nuclear-blast (shock wave), originating from an explosion at or near the ground surface, is explained by Biggs (1964) as a circular chock front propagating from the epicenter of the surface burst. The shock wave created from the blast has the same distribution of overpressure p_s at any instant in time, traveling with a velocity U along a radial line in all directions from the epicenter or ground zero (GZ). Its pressure-pulse profile is given by Figure 2-2, where the peak pressure p_{s0} is found at the chock front.

² Overpressure is defined relative ambient atmospheric pressure

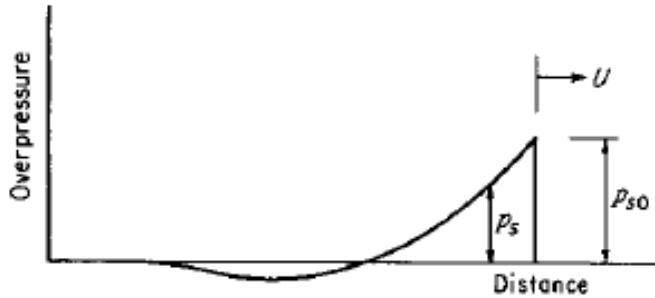


Figure 2-2 Shock wave propagating from GZ of a nuclear surface burst. Biggs (1964, p.277)

As the shock front strikes an object, Biggs (1964) breaks down the total loading effect into three components; (1) initial diffraction effect, (2) effects from general overpressure p_s and (3) drag effects. Although a separate section has been devoted to discuss these effects, the drag effects are briefly expanded upon at this stage in order to continue the discussion on blast wave characteristics. As explained in (AISC, 2013), a dynamic pressure will develop behind the shock front as a result of air particle movement and impose drag loads on the structure similar to those caused by a wind gust. This dynamic pressure is denoted p_d by Biggs (1964), who illustrates the variation of overpressure and dynamic pressure over time in Figure 2-3. The durations of the positive phases of overpressure t_{dp} and dynamic pressure t_{dd} are shown for purposes that will be explained later on.

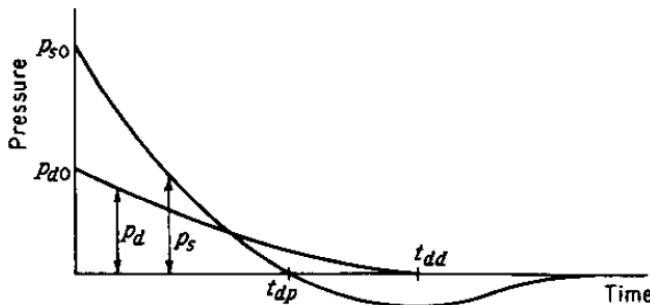


Figure 2-3 Pressure-time curves for shock wave overpressure and dynamic pressure at a fixed point on ground. Biggs (1964, p.277)

Biggs (1964) also show the important relation of how the peak values and durations of the pressure components, i.e. p_{s0} , p_{d0} , t_{dp} and t_{dd} , vary with the distance from GZ. Figure 2-4 shown below account for the effects imposed specifically by a weapon size of 1 megaton (1-MT), and the pulse durations shown for the nuclear blast are many orders of magnitude greater than those applicable to blast-resistant designs in a petrochemical environment. Still, it serves the purpose of illustrating general trends. It is seen that as the distance from point of burst increases, the peak overpressure decays and the pulse duration lengthens. These relations apply in general to any type of explosion, for both shock and pressure waves, according to (ASCE, 2010) and (AISC, 2013).

In addition, the velocity of the blast-pulses will decrease as the distance from GZ increases. According to (Bjerketvedt, et al., 1993), a shock wave typically propagates at an initial velocity of

1500-2000 meters per second whereas for a pressure wave the range is much wider and from the order of 1-1000 meters per second.

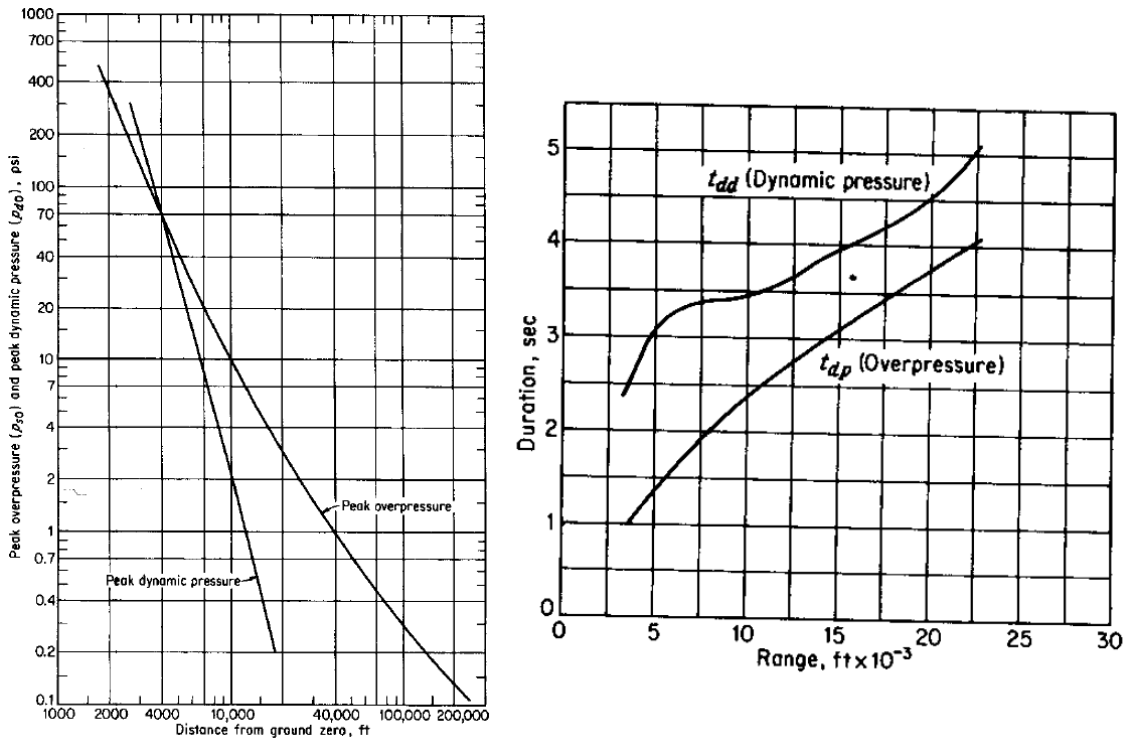


Figure 2-4 Variation of shock wave parameters with distance from ground zero. Biggs (1964, pp. 278-279)

The distribution of overpressure characterizing a pressure wave, to be compared to the shock wave in Figure 2-3, is illustrated in Figure 2-5. Note that only the positive phase duration t_d is shown, but that a negative phase exists similar to what was shown for the shock wave profile.

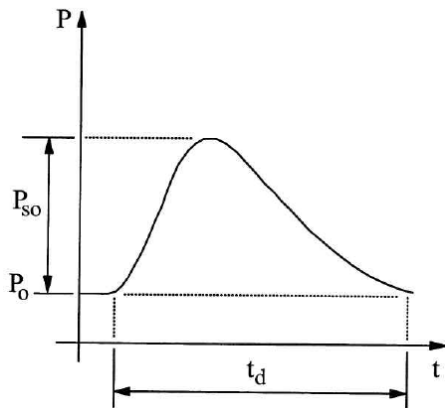


Figure 2-5 Pressure-time curve for a pressure wave. ASCE (2010, p.15)

The pressure wave has a finite rise time to peak overpressure P_{so} . Compared to a shock wave, its peak overpressure is smaller in magnitude and the wave duration is longer (CCPS, 1996). It should be

noted that a pressure wave eventually will develop a shock front and acquire the characteristics of a shock wave. The theory behind this phenomenon is described in (CCPS, 1996) and illustrated in Figure 2-6. As the higher-pressure intervals of the wave contains higher temperature material and thus travels with a greater speed, the arbitrary wave configuration shown in Figure 2-6 (a) will gradually transform into the wave configuration shown in Figure 2-6 (c).

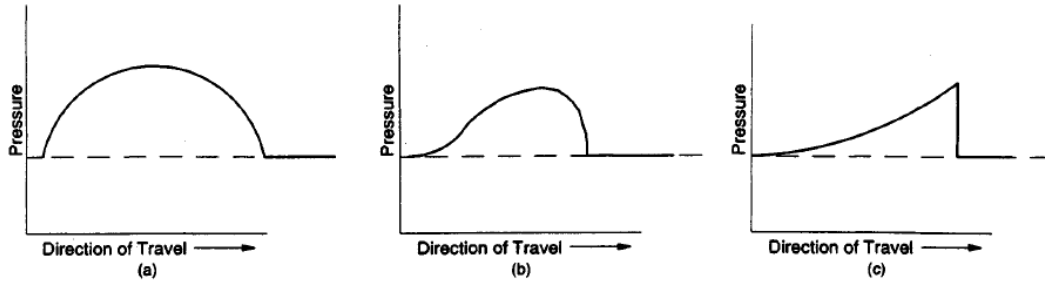


Figure 2-6 Development of shock front in arbitrary pressure wave. CCPS (1996, p.133)

Since the process of energy transfer for a deflagration is slow in nature, the shock front might not be fully developed until the wave is at a significant distance from GZ, which for a weak deflagration could imply that the magnitude of the blast wave at this point in time has decayed to that of a sound wave (CCPS, 1996).

Considering that the siting conditions on an offshore facility is characterized by a very limited amount of space, one can conclude that no mitigating effects due to large distances from GZ and the structure to be analyzed can be accounted for. The initial characteristics of a pressure wave shown in Figure 2-5 must therefore be assumed to define the governing blast-pulses that structures offshore might experience.

The severity of structural damage caused by an explosion is mainly governed by the peak pressure and positive phase duration, which define the idealized blast-pulse illustrated in Figure 2-7 (CCPS, 1996).

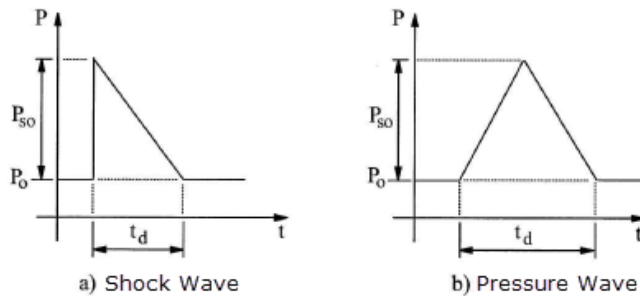


Figure 2-7 Idealized triangular blast-pulses for (a) shock waves and (b) pressure waves. ASCE (2010, p. 19)

The idealized blast pulses are useful tools in blast-resistant design procedures, as they may be converted into impulses to load structural components in analyses. Through linearization of the

overpressure profiles shown in Figure 2-3 and Figure 2-5, triangular blast pulses are defined according to Equation (2.1) by the area under the pressure-time curves in SI units Pascal-seconds. These represent the free-field blast-pulses prior to interaction with a structural component, and are denoted I_P within this thesis.

$$I_P = \int_0^{t_d} P_s(t) dt = 0.5 \cdot P_{so} \cdot t_d \quad (2.1)$$

where $P_s(t)$ define the function of overpressure over time; P_{so} is the peak overpressure; and t_d is the positive phase duration.

The impulse I_o , which quantifies the total loading that a structural component will feel, has SI units Newton-seconds. The impulse must be specified in relation to the component being subjected to the pulse excitation, and is obtained by multiplying the pressure-time integral in Equation (2.1) by the area A of the structural component facing the blast wave according to Equation (2.2).

$$I_o = A \int_0^{t_d} P_s(t) dt = A \cdot 0.5 \cdot P_{so} \cdot t_d \quad (2.2)$$

Blast data is naturally provided on the format prior to interaction with the structure to be analyzed, specified as pulses. As shown later on, many simplified methods of defining blast pulses for analyses involve manipulating Equation (2.1) to obtain an expression for the phase durations, given by Equation (2.3):

$$t_d = 2I_P/P_{so} \quad (2.3)$$

As seen in Figure 2-7, the negative phases of overpressure have been excluded when idealizing the blast waves. Most of the literature agrees on the validity of this approach since it is assumed to reduce the structures peak response in the general case. As stated by Biggs (1964, p.278), the negative phase give rise to less significant suction effects that “may normally be ignored for structural design purposes”. However, there is an exception to the rule as explained in (AISC, 2013). If the structure subjected to the impact has a short fundamental period relative the pulse duration, the time span where suction forces are present might concur with the structure’s rebound phase, thereby causing a new extreme response scenario. Both (AISC, 2013) and (DOD, 2014) states that open-frame structures, such as pipe racks, are especially vulnerable to these effects. However, this thesis will not cover any simplified methods available to account for the negative phase and reference is made to (DOD, 2014) for further reading on the topic.

2.3 Load Effects on Structures

An implication of the research having focused on explosions from use of TNT or other high-yield explosives is that most available data and empirical methods used for simplified blast load calculation

relate to shock waves. Numerous of design charts and simplified equations are provided by (DOD, 2014) to help estimate free-field shock wave parameters that govern the blast design loads. Although this thesis primary focus is not directed towards evaluating or documenting these empirical methods, some of the material covered by the literature is reproduce as it would help broaden the general understanding of blast load effects.

Figure 2-8 illustrate the principle of “equivalent shock loading” that can be applied to a pressure wave in order to make use of some of the empirical relations related to shock waves.

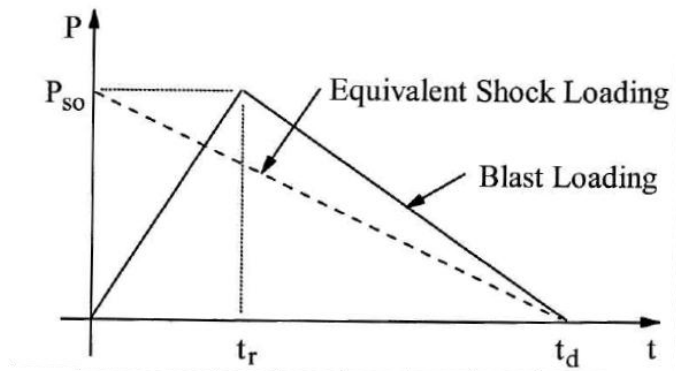


Figure 2-8 Illustration of “equivalent shock loading”. ASCE (2010, p.20)

The equivalent shock-pulse is assigned the same peak overpressure P_{so} as the pressure wave. A fictitious duration, denoted t_d in Figure 2-8, is then calculated from the constraint that both pulses must be of the same magnitude according to Equation (2.3).

The remaining part of this section will be devoted to the load effects imposed on a structure as it interacts with the blast wave. It should be mentioned that other damaging effects are associated with explosions, such as fragments from a bursting vessel or ground shock loads. However, the most destructive component of an explosion will usually be the blast wave (DOD, 2014) and no other components will be considered further.

It is found that one specific type of structure is widely used within the literature when discussing and illustrating load effects on structures. The structure referred to is an above-ground rectangular building without openings, with one side facing the shock wave which is assumed to act perpendicular to the front wall of the building. Furthermore, GZ of the explosion is assumed to be at or near the ground surface, a conservative assumption compared to an airblast according to (DOD, 2014) as peak overpressures will see amplification effects due to ground reflection.

When the blast wave interacts with an object, a sequence of events that constitute the total load effects follows as illustrated in Figure 2-9. The main three components defined by Biggs (1964) in previous sections are further explained by Rogers (1959). As the shock front reaches the building, Figure 2-9 (b), the blast wave is reflected on its front face, subjecting it to a reflected pressure in addition to the peak overpressure found at the shock front. Next, the blast wave is diffracted around

the sides of the building, Figure 2-9 (c), meaning that the amplified pressure initially acting on the front face due to reflection effects, rapidly drops off to the initial peak overpressure value, which is the load that the sides and the roof of the building will see. At this stage, the rear face of the building has not yet been subjected to any pressure loads. Consequently, a pressure differential between front and rear faces exist which give rise to net translational forces in the direction of the wave travel. This pressure differential is referred to as the diffraction effect. In addition, the previously discussed dynamic pressure will generate drag forces on all structural components that lie in the path of the blast wave.

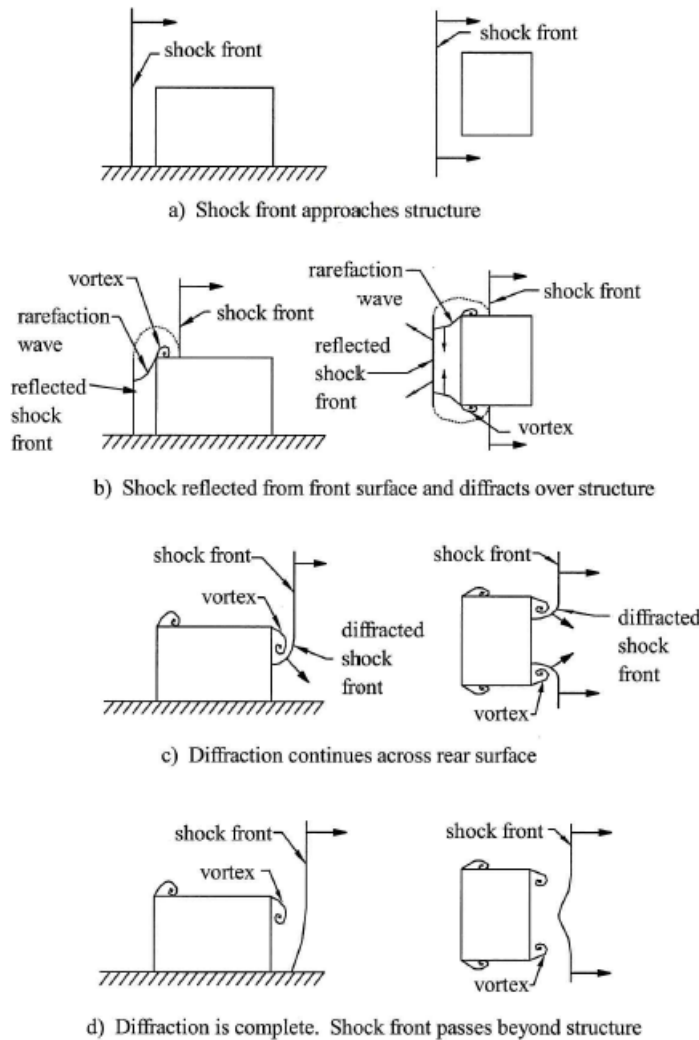


Figure 2-9 Blast wave interaction with rectangular building. ASCE (2010, p.23)

The significant difference between a typical pipe rack structure and a solid rectangular building must be addressed. Focus is therefore shifted towards clarifying what load effects are dominant and applicable to open frame structures such as a pipe rack.

Important conclusions are found in the literature on blast, stating that the drag loads from the dynamic pressure will emerge as the dominant load effect for open-frame structures (ASCE, 2010). Loads arising from diffraction effects will not be as critical since all structural components will experience a rapid equalizing of overpressure (Rogers, 1959). Specific recommendations are provided by OMEA (2003, p. 5), stating that diffraction and reflection effects can be neglected for obstacles with dimensions smaller than 0.3 meters. Concluding that the dynamic pressure will indeed be a governing factor in the process of determining blast loads on pipe racks, it is given more attention when defining simplified tools and equations that can be used to estimate the different loading components.

From fluid mechanics it is known that the dynamic pressure simply depends on the air density and particle velocity. Enforcing the wind analogy, a shape factor is used to convert the dynamic pressure to a drag load q_o , acting on a structural component as suggested by Biggs (1964) in Equation (2.4). Drag loads are directional, i.e. they are mathematically defined by a vector in space that may strike the surface of an object from an infinite number of angles depending on location of GZ and the direction of wave travel.

$$q_o = p_d \cdot C_d \quad (2.4)$$

where $p_d = \frac{1}{2} \rho v^2$ is the dynamic pressure; ρ is the density of the air particles; v is the particle velocity; and C_d is the drag coefficient associated with the structural component.

Simplified methods that relate dynamic pressure to overpressure are often provided in the blast-literature. A dynamic design pressure may be taken as 1/3 of the peak overpressure according to (OMEA, 2003), with a duration calculated according to Equation (2.3) using the overpressure-pulse as input. An alternative approach is given by (DOD, 2014) in Figure 2-10, illustrating the empirical relationship between peak dynamic pressure and peak shock-wave overpressure.

A typical pipe rack configuration is a structural system that consists of individual components (frame members and piping) typically smaller than 0.3 meters, indicating that drag pressures according to Equation (2.4) should be assigned to each individual member. However, the configuration itself is very congested, as an extensive amount of piping is usually fitted within the frame structure. Hence, mitigating shielding effects might prevail when considering the entire pipe rack as one structural unit. Conclusions on this topic, relating specifically to pipe rack structures, are drawn by FABIG (2005). It is stated that conventional design codes for wind load may be consulted to calculate dynamic blast-pressure loads and shielding effects, as the two load cases may be considered equivalent.

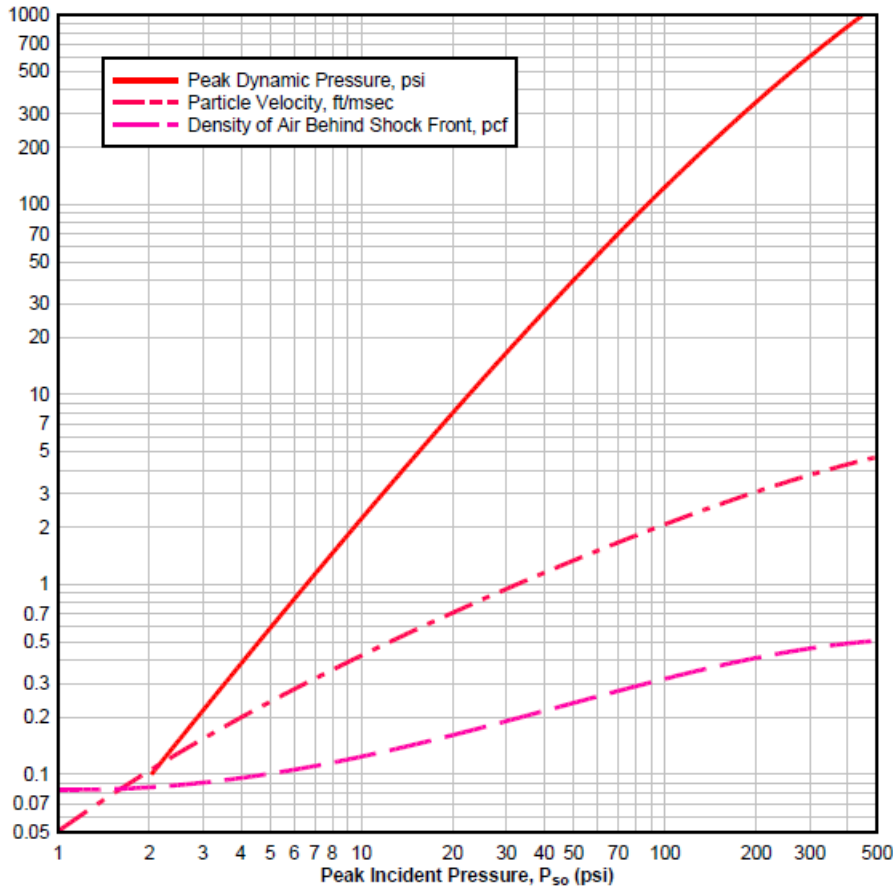


Figure 2-10 Peak shock wave overpressure versus peak dynamic pressure, density of air and particle velocity. DOD (2014, Figure 2-3)

The phenomenon of reflected pressure is further explained in (Bjerketvedt, et al., 1993). When the blast wave hits the surface of an obstacle, the dynamic pressure following the wave has to come to an immediate stop. At this point, the dynamic pressure is transformed into a static pressure which in principle constitutes the total reflection effect. The peak reflected pressure P_r can be determined empirically by factoring the peak overpressure P_{so} with a reflection coefficient C_r according to Equation (2.5). The coefficient depends on the magnitude of the peak overpressure, angle of incident of the wave front relative to the reflecting surface and the type of blast wave. C_r will always be greater than 2 if the wave front strikes perpendicular to the surface and may be determined from design charts provided by ASCE (2010, p. 18).

$$P_r = P_{so} \cdot C_r \quad (2.5)$$

The reflected pressure will impose an additional impulse loading on small objects subjected to free-field shock waves as described by (Bjerketvedt, et al., 1993). Figure 2-11 illustrates this contribution to an idealized, free-field drag-pulse where the dynamic pressure has been converted to drag pressure through Equation (2.4). The trace of the modified pressure-pulse in Figure 2-11 is really the shape of

the impulse loading that the object will feel. The duration of the reflective pulse is roughly obtained by calculating the time it takes for the blast wave to pass the object, i.e. dividing the dimension of the object in direction of wave travel with the wave's propagation speed. Hence, the impact of this additional impulse loading will be less significant if the dimension of the object, in this case the pipe diameter, is small.

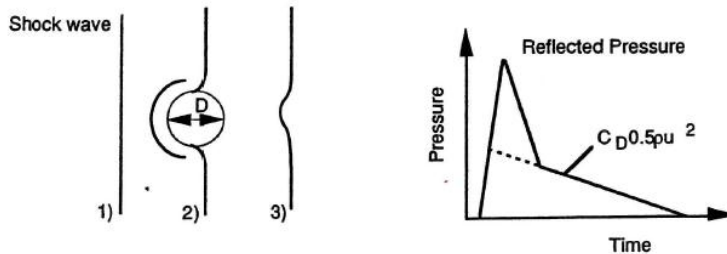


Figure 2-11 Modification to idealized blast-pulse due to reflection effects at interaction with small object. Bjerketvedt, et al. (1993, p.111)

2.4 CFD and Design Load Output

The design loads used for structural verification in an accidental explosion event at AKSO are provided by safety consultants and have been derived through computational fluid dynamics (CFD) software. This approach is common within the offshore industry as facility layouts are very confined and complex in nature (ASCE, 2010). It is of great importance for engineers to be able to interpret the provided design loads for application to specific structural analyses, as the load output itself is currently delivered to AKSO's structural department in a very general format, with little information on the process behind the load derivation. Hence, a descriptive summary of the process of safety assessment and CFD analysis that generate the design load output utilized by the *conventional* and the *proposed method* will be covered next.

CFD will allow for simulations of blast wave propagation in a dense environment full of obstacles, typical features of the governing siting conditions at an offshore installation (ASCE, 2010). The design blast loads provided to AKSO are based on CFD simulations of cloud explosions, i.e. VCE, by the use of FLACS code. The formation and dispersion of the gas cloud is analyzed, where the FLACS code account for the complex interaction between the gas flow and obstacles in its path. The FLACS analysis can provide many output parameters characterizing the blast-pulses, the most important being the pressure-time curves of incident and dynamic pressure (Bjerketvedt, et al., 1993).

The information provided below is obtained from two typical types of project documents that are established by safety consultants for each AKSO project. The document referred to as *load specification* is utilized by structural engineers for analyses and contain design-pulse parameters in tabular form. The extensive process of safety assessment and blast simulation from where the design loads are established is documented in the report referred to as the *total safety assessment*.

More than a hundred simulations are usually performed within each module of the platform, taking into account different gas cloud sizes, location of leakage points and ignition points, degree of confinement, venting and congestion in the area, and several other factors that determine the nature of the explosion. The size of the modelled gas clouds typically vary from 2%-50% of the total volume of the module being analyzed. As a result of the many input parameters, a great number of blast-pressure pulses are obtained, varying in magnitude, duration and location of origin.

It is also important to emphasize that the process of blast-load determination is probabilistic in nature, governed by international standards such as (NORSOK Z-013, 2010). As an example taken from a *total safety assessment* report, the ignition events with explosive potential were determined to occur every 676 years on average. Such probability data will be considered when calculating pressure exceedence curves, which are used to determine the design loads referred to as *dimensioning accidental load* when illustrated in Figure 2-12. In addition, a safety margin will be added to obtain the final design loads to be implemented in the structural analyses. Note that this safety margin is only applicable to the magnitude of design pressures, not the pulse durations. This approach is a requirement from the Petroleum Safety Authority (PSA) and shall account for analytical uncertainties, future modifications and design changes.

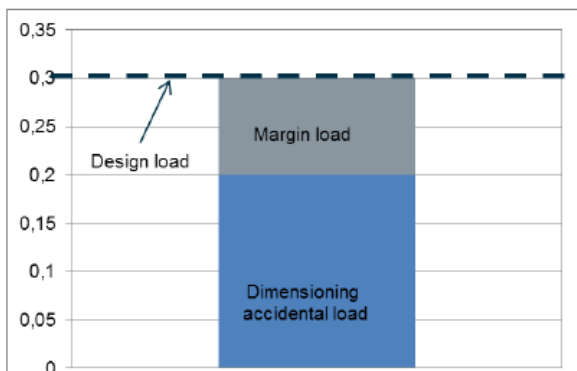


Figure 2-12 Safety margin in blast design loads.

The idealized blast-pulse shown in Figure 2-13 illustrates the assumed characteristics of the pressure-time curves (both incident and dynamic pressure), derived from a safety assessment process in an offshore topside environment. The graphical illustration is provided in the *load specification* along with design blast-pressures and phase durations relating to a specific topside module. In general, only the positive phase parameters, p_1 and t_1 , are specified by the safety consultant. For each of the defined modules in the topside analysis model, the following is usually included in a load specification:

- i. Local overpressure
- ii. Global overpressure
- iii. Dynamic pressure
- iv. Positive phase durations

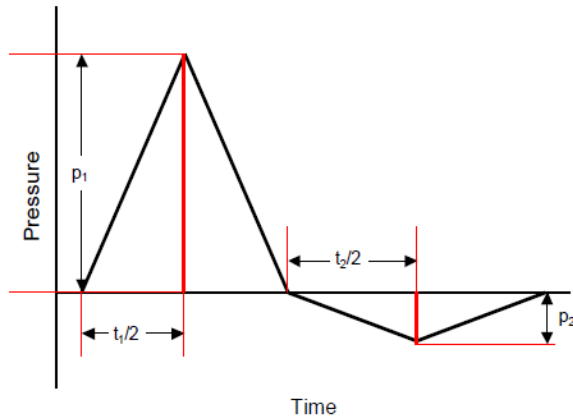


Figure 2-13 Idealized design blast-pulse from load specification report.

The blast wave components listed above are calculated for each explosion simulation in FLACS, at specific target areas given by either pressure panels or monitor points. Local overpressures are calculated at different 3x3 meter areas, such as a region of a blast wall. For global overpressure calculations, the panels have the size of an entire deck or wall. The overpressure data account for all the load effects discussed in previous sections, both reflective pressures and pressure differentials. The dynamic pressure is calculated at a large number of monitor points. The magnitude of the dynamic design-pressures, prior to adding the margin load, is obtained by first excluding local peak values at the most severe monitor points, before calculating the maximum average value in all of the 5x5x5 meter volume blocks that define the total module volume. An interesting note is that the highest dynamic pressures on offshore topside modules are often registered near vent openings.

The dynamic pressure is calculated in FLACS according to the formula of p_d given in association with Equation (2.4). Naturally, these calculations do not account for reflective or diffraction load effects arising from interaction with the specific structure to be analyzed, e.g. a pipe rack. For circumstances where only the dynamic pressure-component may be considered for structural analyses, the studied safety assessment documents provide the same recommendations as (OMEA, 2003), limiting the allowable object dimension to less than 0.3 meters.

FLACS code is not capable of calculating pressure-time curves that capture the load effects from wave interaction with small objects (<0.3 meters), as the mesh size of the analysis model is too coarse. However, it is possible to capture these effects for pipe rack structures, where many small objects are grouped close together. The “true” pressure-variance across a specific pipe rack section could therefore be calculated by locating monitor points inside and immediately outside the rack section. If this approach is adapted, the FLACS load output would account for all interactive effects, including shielding effects and the effects of flow acceleration through the dense rack environment. The latter effect of flow acceleration is associated with an increase in turbulence as the fluid passes through a dense environment of obstacles, resulting in an increase of pressure across the length of the rack in direction of the wave travel. Hence, the shielding and flow acceleration effects counteract each other (FABIG, 2005).

It has been discovered that no distinction between phase durations of incident and dynamic pressure-time curves was made in certain *load specification* documents. In general, the range of 50 to 200 milliseconds was attached to all design-pulses. These blast wave durations are calculated according to Equation (2.3) for each panel or point where the non-idealized, true pressure-pulse has been recorded in the FLACS analysis. The magnitudes of the dynamic pressure-pulses are obviously used as input in Equation (2.3) when calculating drag-pulse durations. Figure 2-14 show pulse duration plots where data from all simulations in a specific module have been included.

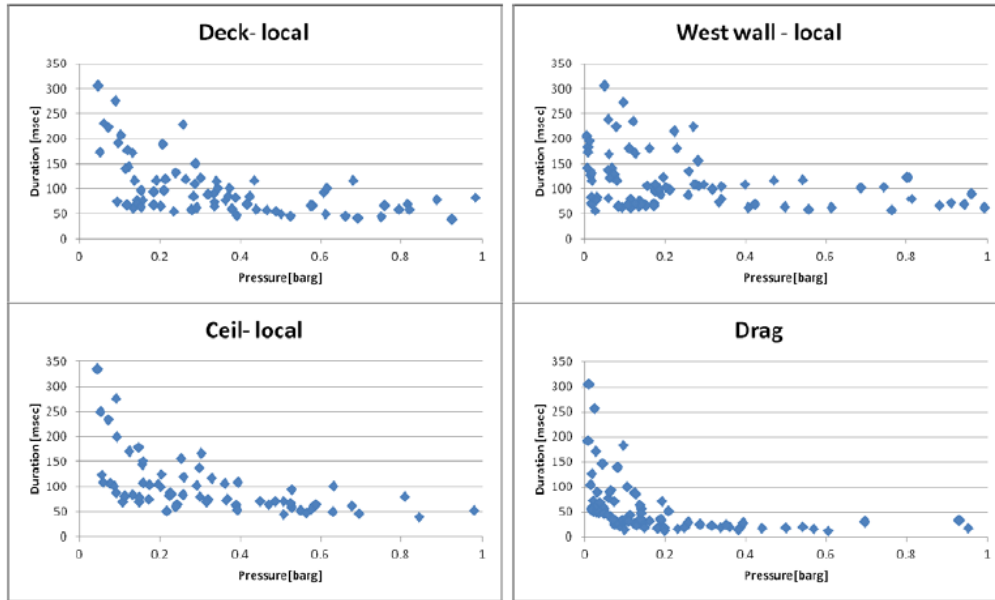


Figure 2-14 Pressure-duration plots calculated from FLACS analysis.

It is clear that the dynamic pressure-pulses (plot labeled “Drag”) tend to have shorter durations than those derived from the general overpressure (calculated as local pressures acting on ceiling, deck and wall for the data shown in Figure 2-14). This trend has been observed for all of the analyzed modules and must therefore be considered to hold in general for topside-environments offshore. Note that the unit of pressure is given in barg or bar(g), where 1 barg equals 100 kPa.

2.5 Concluding Remarks

The first conclusions to be drawn relate to the characteristics of the blast-pulses applicable for analyses of pipe rack structures in an offshore environment. It is concluded that pressure waves generated by deflagration type explosions, such as cloud explosions, are the most relevant. The free-field, idealized blast pulse that best captures the “true” nature of this blast scenario is given by Figure 2-7 (b). An identical idealization is associated with the pulse parameter data provided in the *load specifications* in order to define the design blast-pulse to be implemented in the structural analyses and verification process.

As made evident in previous sections, the shape and magnitude of the impulse that will load a specific component in a structural system depend on what load effects have been accounted for. For a pipe rack structure, it is concluded that the dynamic pressure will be the dominant load component and that reflected and differential pressures are less significant when defining the impulse to be assigned individual members. Hence, a design-pulse specified from dynamic pressure-curve data may be directly considered in analyses of a pipe rack without accounting for other load effects.

An important conclusion is that dynamic blast-pressures and ordinary wind gusts may be treated as equivalent load scenarios. This implies that the methods developed for wind load application to structural systems, found in all international design codes, may be used to calculate drag loads on structural members. These codes may also be used along with sound engineering judgment to account for shielding effects in the structural assembly.

Conclusions should also be drawn in relation to the study of the *total safety assessment* and *load specification* documents, as well as the method of CFD analysis. First, the phase durations of the dynamic pressure-pulses documented in safety assessment reports have been found to be shorter compared to those provided in the corresponding load specification. This observation should be discussed further with the people responsible for providing the load specification in an attempt to increase the accuracy of the load output associated with drag-critical structures.

The accuracy of the load specification could be further improved considering pipe rack structures, as FLACS code has the ability to calculate the pressure variance through a specific rack section located within a module, thus accounting for all effects from interaction with the structure. However, the level of detail in the current FLACS analysis approach would have to be increased in order to obtain such specific load output. Naturally, any change in the volume of the safety assessment scope will induce increased costs. To establish if such cost would exceed possible benefits, further studies on the topic is suggested, aiming to compare the design-loads implemented in structural analyses with the results from a detailed FLACS analysis of a specific pipe rack.

An important general note to be made in relation to blast loads is that any process of determining design-pulses is full of uncertainties. Even though the most sophisticated methods available is used to determine the design loads in AKSO projects, the safety assessment process and blast simulation through CFD have their flaws. These are defined primarily by the sensitivity to how well the analysis model corresponds to actual siting conditions and the probabilistic nature of the load derivation process. If an actual explosion event occurs, chances are that the generated blast-pulse that will impose loading on a pipe rack will be different from the design-pulse accounted for in the analysis and verification process. Again, it is stressed that this fact persists although the best available methods have been employed and that the conducted safety assessment is in accordance with international standards that govern such processes. However, this inescapable level of uncertainty that is associated with determining blast loads is often referenced within the blast literature to justify implementation of approximate analytical methods such as the *Linear-elastic Biggs method* and *Elasto-plastic Biggs method*.

3 Structural Mechanics in Blast Scenario

3.1 Structural Dynamics

Many of the available blast-resistant design guides, such as (ASCE, 2010) and (AISC, 2013) refer to the publication by Biggs (1964) when discussing the dynamic aspect of the blast phenomena. Biggs himself states in that same publication that there is no distinction to be made between explosions and other dynamic loading scenarios in terms of the governing fundamental theory of structural dynamics. For simplicity, and due to the fact that the theory on structural dynamics is well established, the work of Chopra (2011) is implicitly used as the main reference for this introductory subsection on structural dynamics unless mentioned otherwise.

The most fundamental aspect of structural analysis in general is that displacements, stresses or other field variables of interest must be obtained during a state of system equilibrium. Using an example that many structural engineers are familiar with, field quantities in a simply supported two-dimensional beam, such as shear or moment distribution, may be obtained by simply solving the equations of static equilibrium of forces.

For dynamic problems, equilibrium is governed by the equation of motion (EOM) which is derived from Newton's second law of motion, shown in Equation (3.1) for a linear-elastic SDOF system. The EOM applies to both single degree of freedom systems (SDOF) and multi degree of freedom systems (MDOF) as shown in the following subsections.

$$m\ddot{u}(t) + c\dot{u}(t) + ku(t) = p(t) \quad (3.1)$$

where \ddot{u} , \dot{u} and u are the time-dependent accelerations, velocities and displacements of each DOF; m is the mass associated with the DOF; c is the damping associated with the DOF; k is the stiffness associated with the DOF; and $p(t)$ is the time-dependent (i.e. dynamic or transient) external force.

Since this thesis focus is on inelastic structural response, the governing format of the EOM as shown in Equation (3.1) will have to be slightly modified to account for the subsequent effect that the stiffness of the structural system will be displacement-dependent. For inelastic dynamic systems, Equation (3.2) prevails.

$$m\ddot{u}(t) + c\dot{u}(t) + k(u)u(t) = p(t) \quad (3.2)$$

The EOM is central in the development of a dynamic numerical FE formulation implemented in analysis software such as Abaqus. How to construct such a FE formulation will not be explain within this thesis. For general information on the topic, reference is made to Krenk (2009) where nonlinear

FE formulations are developed for different numerical elements such as beams and continuum using the theory of minimum potential energy to define the weak form formulation of the EOM. For information on the implicit, dynamic FE formulation governing simulations conducted in Abaqus/Standard within this thesis, reference is made to (Abaqus, 2015b).

3.1.1 Damping in Blast Scenario

When considering a dynamic structural response to pulse excitation, important conclusions with respect to the damping of the system, denoted c in Equation (3.2), should be drawn already at this stage. The damping coefficient/matrix (SDOF/MDOF) serves the purpose of quantifying the combined effects of a system's energy-dissipating mechanisms. Consequently, damping is the phenomena accounting for the gradual decay of dynamic motion in a system that has been subjected to external loading over a finite period of time. If a structural system would not see any damping effects, it would simply enter a steady-state of free-vibration, oscillating back and forth about its initial equilibrium position in eternity. The sources of energy-dissipation in a structural system are many, such as friction between components in a steel connection design, thermal radiation due to repeated elastic straining or air resistance.

Damping effects are usually ignored in dynamic analyses of explosion events. Since the peak response of a structure subjected to blast loading will occur almost instantly and within the first cycle of motion, damping effects will have little impact on the peak displacements and are small relative to the effects of inelastic deformation (ASCE, 2010). As explained by Chopra (2011), damping effects are critical when evaluating a structure subjected to a harmonic excitation frequency close to its own natural frequency. For this scenario, the amount of damping will control both the amplitude of the system's steady-state response and the rate at which it is obtained. However, for structures subjected to pulse-type excitations such as blast waves, Chopra (2011) concludes that the level of conservatism in neglecting damping is small and that the accuracy in the computed response is not very compromised by doing so.

Damping will therefore be ignored in any analyses carried out within the scope of this thesis, and the governing EOM is reduced to the format given by Equation (3.3):

$$m\ddot{u}(t) + k(u)u(t) = p(t) \quad (3.3)$$

3.1.2 SDOF System

The SDOF system naturally consists of one DOF, defining the one-dimensional motion of a single mass component m subjected to an external load component. The mass component is assumed to be supported by a massless structure, providing stiffness k in the direction of motion. Damping properties are also idealized and incorporated into the one-dimensional EOM through the damping coefficient, c . No structural system is this simple in nature, as the mass, stiffness and damping properties in reality will depend on the combined contribution from all structural elements. However, the SDOF analogy is frequently used for simplified dynamic analyses and most of the approximate analytical methods developed for explosions events are based on this idealization.

Chopra (2011) demonstrates how the SDOF analogy can be applied to a two-dimensional frame shown in Figure 3-1 to determine its lateral displacement time-history response.

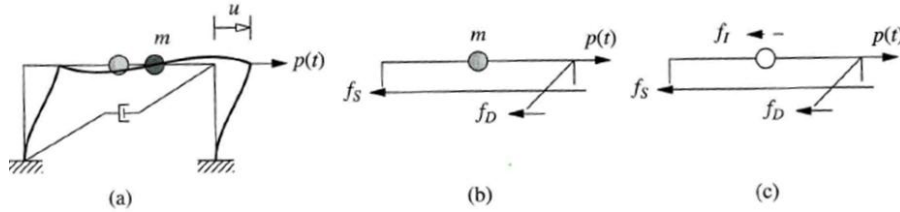


Figure 3-1 Illustration of a two-dimensional frame as a SDOF-system governed by the EOM. Chopra (2011, p. 14)

Figure 3-1 illustrate the components of the EOM as given by Equation (3.1) in terms of forces, where the externally applied force $p(t)$ must be equal to the sum of inertia forces $f_I = m\ddot{u}$, internal forces $f_S = ku$, and damping forces $f_D = c\dot{u}$ for equilibrium to hold. Reference is made to Chopra (2011) for guidance on simplified methods to use when establishing the scalar values of mass, stiffness and damping properties of the frame shown in Figure 3-1 that allows for a SDOF analogy response to be evaluated.

The SDOF-system is often visualized by the mass-spring-damper model shown in Figure 3-2. Closed form solutions of a SDOF-response are available in textbooks such as Chopra (2011) for different types of standardized external excitations. The derivations consist of solving the second order differential equation defined by the governing EOM along with applicable initial conditions. The linear-elastic SDOF response to pulse-excitation will be discussed in detail within Chapter 4, as the *Linear-elastic Biggs method* is based on this idealized response-model. A modified SDOF-model accounting for inelastic capacity is also included in Chapter 4 as the theory behind the *Elasto-plastic Biggs method* is explained. However, the mathematical process of solving differential equations governed by initial value problems is excluded from the scope, and closed-form solutions will simply be reproduced in their final format. Reference is made to Chopra (2011) for description of the full derivation process.

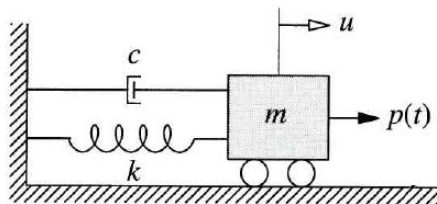


Figure 3-2 Mass-spring-damper model illustrating the components of a SDOF-system. Chopra (2011, p.20)

3.1.3 MDOF System

In order to expand the dynamic analysis and thus obtain more information on the overall response of a structural system, the analytical model must be discretized using multiple DOFs. When more DOFs are added to the analytical model, i.e. when the mesh is refined, the level of detail in the analysis increase and more data can be extracted. However, a fine mesh will increase the computational cost and is not always required to achieve the purpose of the individual analysis task.

For the MDOF-system, the EOM is formulated in terms of matrices and vectors, as the response of multiple DOFs is being considered simultaneously. The general format given by Equation (3.1) for an elastic system is written according to Equation (3.4), where upper case bold letters denotes a matrix and lower case bold letters denotes a vector.

$$\mathbf{M}\ddot{\mathbf{u}}(t) + \mathbf{C}\dot{\mathbf{u}}(t) + \mathbf{K}\mathbf{u}(t) = \mathbf{p}(t) \quad (3.4)$$

where $\ddot{\mathbf{u}}$, $\dot{\mathbf{u}}$ and \mathbf{u} contain accelerations, velocities and displacements related to each DOF; \mathbf{M} is the mass-matrix; \mathbf{C} is the damping-matrix; \mathbf{K} is the stiffness-matrix; and $\mathbf{p}(t)$ contains the external force components acting at each DOF.

The field variables to be solved for will usually be coupled through the off-diagonal terms in the mass-, damping-, and stiffness-matrices, implying that analytical closed-form solutions for SDOF-responses cannot be directly applied to individual DOFs. The method of modal analysis can be used to uncouple the system of equations by identifying its natural modes of vibration. For each separate mode of vibration, the EOM will be uncoupled and the response may be computed at each DOF according to the closed-form solutions applicable to SDOF-systems. The modal responses will then be combined to obtain the total response.

The concept of natural modes of vibrations is explained in the section on dynamic properties of structural systems below, but the method of solving for MDOF-response through modal analysis will not be discussed further as a full nonlinear FE formulation will be utilized within this thesis. Modal analysis is only applicable to linear-elastic systems where it can be preferred over direct integration methods in numerical solution software due to savings in computational cost (Abaqus, 2015a).

3.1.4 Dynamic Properties of Structural Systems

The dynamic response of a structural system will depend on the nature of the external loading, but also on the dynamic properties of the structure itself. The *natural period of vibration* of a structural system, denoted T_n and commonly referred to as *natural period* only, define the time required for an undamped system to complete one cycle of vibration. As discussed previously, an undamped system subjected to a finite dynamic excitation will eventually enter a steady-state of free-vibration as the force is removed, as illustrated in Figure 3-3.

In order to calculate the natural period of a system, its *natural circular frequency of vibration* has to be determined according to Equation (3.5).

$$\omega_n = \sqrt{\frac{k}{m}} \quad [\text{rad/s}] \quad (3.5)$$

where ω_n is the natural circular frequency; k is the stiffness of the structural system; and m is the mass.

The *natural period* T_n may now be defined according to Equation (3.6) in units of seconds.

$$T_n = \frac{2\pi}{\omega_n} \quad (3.6)$$

For completeness, the dynamic property defining the number of cycles per second is provided in Equation (3.7). This property is referred to as a systems *natural cyclic frequency of vibration* f_n , in units of cycles per second or hertz.

$$f_n = \frac{\omega_n}{2\pi} = \frac{1}{T_n} \quad (3.7)$$

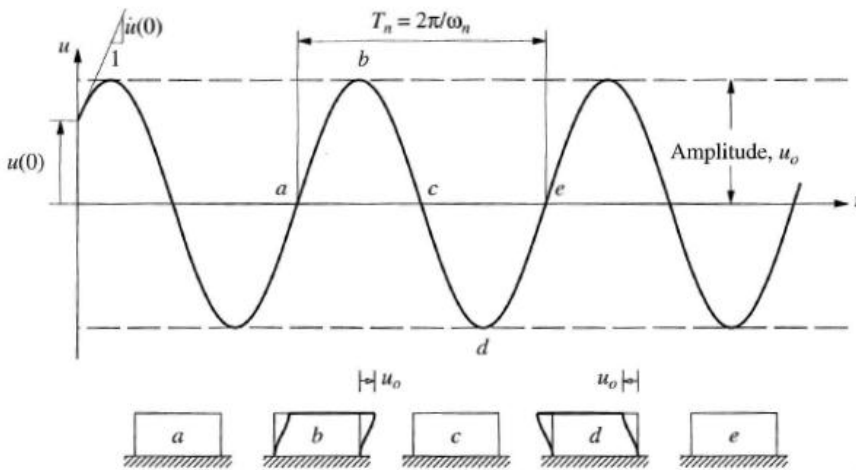


Figure 3-3 Free vibration of undamped, linear-elastic SDOF system. Chopra (2011, p.40)

When defining dynamic properties of damped systems undergoing free vibration, the terms *critical damping coefficient* and *damping ratio* are employed. These properties are important for certain load scenarios, but may be ignored in analysis of response to pulse-excitations for reasons provided in Section 3.1.1.

The dynamic properties covered by Equations (3.5) to (3.7) relate to the free vibration phase of a linear-elastic, undamped structural system, and depend on its stiffness and mass. For SDOF-systems, the application of these equations is straight forward. For MDOF-systems however, the dynamic properties cannot be entirely defined by a single set of scalar function values. When discussing dynamic properties of MDOF-systems, the term *natural modes of vibration* must be introduced. The

concept of natural modes of vibration also relate to the free vibration response of an undamped, elastic system.

Contrary to the free vibration of an SDOF-system shown in Figure 3-3, the corresponding response of an MDOF-system cannot be defined by a single harmonic motion. Instead, the dynamic motion of the entire system must be defined from the harmonic response of each individual DOF within the system, which will be different in nature depending on the governing natural mode of vibration.

A MDOF-system's natural modes of vibration may be defined as follows. If the system's DOFs are given initial displacement conditions prior to release that define a specific deflected shape maintained during the following vibration phase in a simple harmonic motion, then this deflected shape and associated motion constitute a natural mode of vibration. The fact that the deflected shape, also referred to as the *mode shape*, is maintained also implies that the simple harmonic motions of all individual DOFs vibrate in the same phase. Hence, explicit values of the natural cyclic frequency ω_n and the natural period T_n may be associated with each natural mode of vibration.

The definitions of the natural period and natural cyclic frequency given in relation to Equations (3.5) and (3.6) apply to each individual natural mode of vibration in the MDOF-system. Determining the dynamic properties of a MDOF-system is a matter of solving the eigenvalue problem, where the mode shapes are given by the eigenvectors and the natural cyclic frequencies by the associated eigenvalues. The algebraic equation which defines the *matrix eigenvalue problem* is given by Equation (3.8).

$$[\mathbf{K} - \omega_n^2 \mathbf{M}] \boldsymbol{\phi}_n = \mathbf{0} \quad (3.8)$$

where \mathbf{K} and \mathbf{M} are the stiffness and mass matrices; $\boldsymbol{\phi}_n$ is the natural mode vector of the n^{th} mode; and ω_n is the n^{th} scalar valued natural cyclic frequency.

Equation (3.8) represents a set of N algebraic equations corresponding to the analyzed N-DOF system. The non-trivial solutions to Equation (3.8) are obtained from the *characteristic equation* defined by Equation (3.9).

$$\det[\mathbf{K} - \omega_n^2 \mathbf{M}] = 0 \quad (3.9)$$

A polynomial of order N in ω_n^2 is obtained when Equation (3.9) is expanded from where the N real and positive roots of ω_n^2 can be solved for due to the symmetrical and positive definite properties of the mass and stiffness matrices. When the N number of eigenvalues ω_n ($n=1,2,\dots,N$) are known, Equation (3.8) is used to solve for the corresponding N number of natural modes of vibration $\boldsymbol{\phi}_n$. The natural modes may only be determined and expressed in terms of relative response quantities, e.g. displacements, and not absolute values.

The natural frequencies are conventionally labeled in ascending order, starting with the lowest frequency ω_1 . The corresponding mode shape, i.e. ϕ_1 , is referred to as the *fundamental mode* whereas higher order modes relate to the higher values of natural frequencies. According to Austrell (2015), the modes that are triggered by the external loading in a MDOF-system, and thus characterizing its dynamic response, depend both on the loads spatial distribution and its variation with time.

3.2 Nonlinear Material Behavior

As stated in (ASCE, 2010), the most important feature of a blast-resistant structure is the ability to absorb a large amount of blast energy without complete failure of structural integrity. Such structures are said to possess a high level of *ductility*, a term that is explained further in following sections. Structural steel is the material used in design of pipe rack members and the only material to be evaluated in this thesis. The material used for design of piping will vary depending on its content, and the characteristics of certain common pipe line materials will deviate from the structural steel behavior discussed herein. This issue will be addressed as the material models implemented in the FE analyses are discussed later on.

Steel is a very ductile material due to its significant strength and inelastic capacity, allowing it to undergo large plastic deformations prior to brittle failure modes such as fracture. It is defined as an elasto-plastic material characterized by the behavior illustrated in the stress-strain diagram in Figure 3-4.

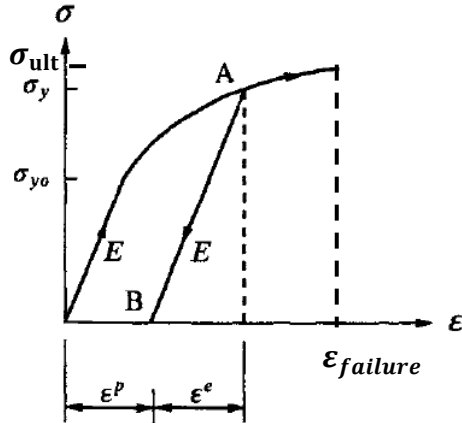


Figure 3-4 Elasto-plastic material behavior. Ottosen and Ristinmaa (2005, p. 203)

As described by Ottosen and Ristinmaa (2005), the behavior of steel is linear-elastic until the initial yield stress σ_{y0} is reached. The stiffness of the material associated with the linear part of the response curve is equal to the Young's modulus E , and the elastic strains developed in this region are fully reversible after unloading, i.e. no permanent deformations occur. The constitutive relation in the linear-elastic range is simply given by Hook's Law in Equation (3.10).

$$\sigma = E \cdot \varepsilon \quad (3.10)$$

When an elasto-plastic material is loaded beyond initial yield to an arbitrary stress level σ_y at point A, the response becomes nonlinear and plastic strains develop. Plastic strains are irreversible and cause permanent deformation which is illustrated in Figure 3-4 as unloading occurs at point A. The path of unloading in the plastic region will always occur elastically with stiffness E , graphically revealing the amount of irreversible plastic strains ε^p reached at point A as the path intersects the strain-axis at point B. If the material is once again loaded, the response will follow the elastic unloading-path from B to A until it reaches the highest previously recorded stress σ_y . At this point, the behavior will continue to follow the nonlinear response curve as additional plastic strains develop until failure occurs at the point defined by $\varepsilon_{failure} = \varepsilon^e + \varepsilon_{failure}^p$. The stress level associated with failure is commonly referred to as the *ultimate stress*, denoted σ_{ult} .

Figure 3-4 illustrates how the yield stress σ_{y0} in a material fiber increases as plastic strains develop. This phenomenon is referred to as *strain hardening*. It is important that the material model implemented in a nonlinear analysis account for the material's true constitutive relation and strain hardening behavior. This is made evident as Ottosen and Ristinmaa (2005) define the *strain energy* W of the material as the area under the stress-strain curve shown in Figure 3-5.

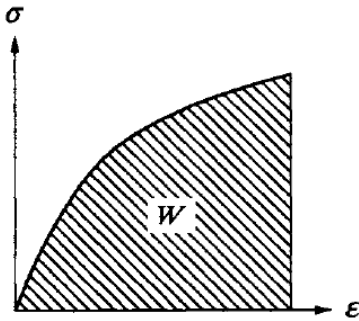


Figure 3-5 Material strain energy for uniaxial loading. Ottosen and Ristinmaa (2005, p. 69)

As Figure 3-5 show, the strain energy may be quantified according to Equation (3.11). It defines the internal energy developed in the material as it deforms, which will be utilized to absorb the external energy component in the system's EOM originating from the blast wave. The inelastic or plastic capacity of the material is therefore defined by the amount of allowable plastic strain prior to failure and the strength of the material defined by the stress developed under the elastic range as well as the plastic, strain hardening range.

$$W = \int_0^{\varepsilon} \sigma(\varepsilon) d\varepsilon \quad (3.11)$$

The true material behavior illustrated in Figure 3-4 is often idealized in simplified analytical methods. The *elastic-ideal plastic* material model shown in Figure 3-6 is a common idealization of structural steel characteristics. This idealization fails to account for *strain hardening*, assuming that the stress remains constant at initial yield σ_{y0} as the plastic strains develop. Compared to the elasto-plastic

behavior, the elastic-ideal plastic model underestimates the inelastic capacity of the material as the developed strain energy defined by Equation (3.11) will be lower for all values of strain in the inelastic range, suggesting that the idealization is on the conservative side.

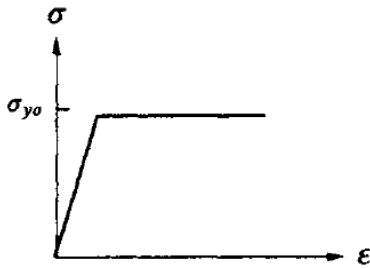


Figure 3-6 Idealized elastic-ideal plastic material behavior. Ottosen and Ristinmaa (2005, p. 204)

However, the conservatism in ignoring the strain hardening effects is not definite when considering verification of a structural system as a whole. As discussed further in Section 3.3 below, the internal forces developed at plastic hinges will be underestimated if such an approach is chosen, implying that the forces induced on other members or connections in the structural system will not be representative to the true internal force distribution. As the full nonlinear analyses to be conducted within this thesis aim to be as representative to the actual conditions as possible, numerical implementation of the idealization given by Figure 3-6 is not sufficient.

Bi- or tri-linear idealizations of the elasto-plastic material model will account for strain hardening effects and may be used as an alternative to a precise stress-strain function derived from laboratory test data. Such idealizations are shown in Figure 3-7.

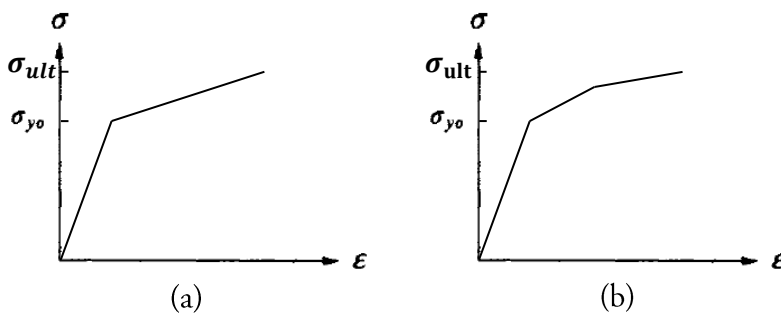


Figure 3-7 Bilinear (a) and trilinear (b) idealization of elasto-plastic material behavior.

Material specifications provided by suppliers or design codes will usually include values of yield stress, ultimate stress, Young's modulus, plastic strain data etc. to define the elasto-plastic material behavior according to one of the material models shown above. However, these values are in general associated with a nonlinear material response to conventional static loading.

Rapid dynamic loading will affect the mechanical properties of steel material due to the phenomenon of *strain rate sensitivity*. As explained in (ASCE, 2010), the nature of the blast loading will cause the

material to deform rapidly, at a rate which is still however slower than that of the applied loading. This will increase the inelastic material strength and cause the stress-strain curve to shift upwards as shown in Figure 3-8. The dynamic strength values associated with the initial yield state and the ultimate state are therefore larger than the corresponding static strength values. Consequently, the blast-resistance of the structure will increase as the material's strain energy capacity will increase, given that the strain levels associated with yield and failure remain unaffected.

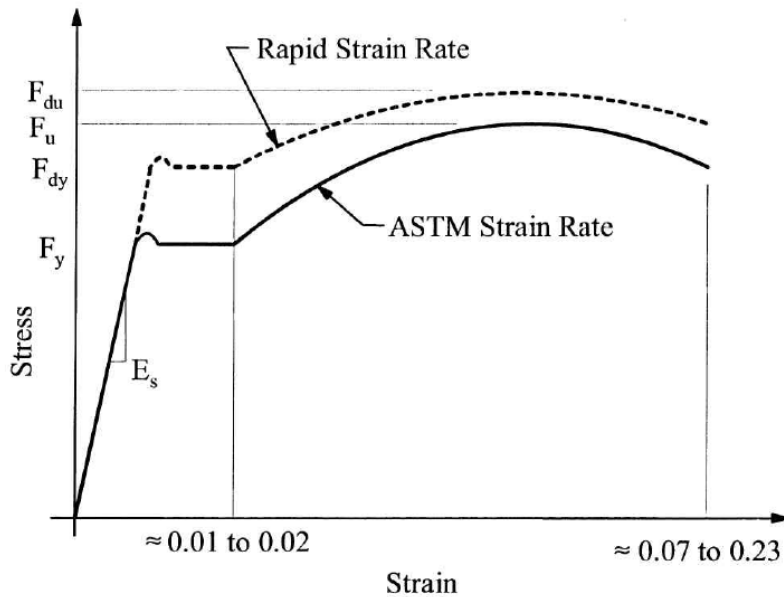


Figure 3-8 Effect of strain rate on mechanical properties of structural steel. ASCE (2010, p. 57)

According to (ASCE, 2010), the increase in strength is positively correlated with the rapidity of the strain rate, i.e. how fast the material deforms. It is negatively correlated with increased static yield strength of the material, i.e. steel grade. The excess dynamic strength can be on the order of 10-30% and is more significant for the initial yield state than the ultimate stress state. Ignoring it will have the same implications as ignoring the strain hardening phenomena as discussed previously. A *Dynamic Increase Factor* (DIF) is commonly used in blast-resistant design to scale static strength values and thus account for the strain rate effects. Reference is made to (ASCE, 2010) or (DOD, 2014) for further information on implementation of DIFs in a blast-resistant design procedure.

The blast-resistant design literature agrees on the above documented effects of rapid strain rates. In addition, there is a general consensus that the Young's modulus is unaffected by the rapid loading as seen in Figure 3-8. However, the effects on steel material strain levels associated with failure were found to be formulated differently in studied publications. While (ASCE, 2010) states that strain levels are relatively unaffected by a rapid material response, Dusenberry (2010) argues that the level of elongation associated with rupture is reduced as a consequence of this phenomenon.

3.3 Inelasticity and Failure in Simple System

The previous section explained how the inelastic capacity of the material was defined by the amount of strain energy developed prior to failure. This section aims to identify additional components

governing the inelastic capacity of an entire structural system. As explained in (ASCE, 2010), this capacity is defined by the total strain energy available in the system which is a function of material properties, member section properties, properties of the global structural system and the amount of allowable plastic deformations.

The capacity at material level has already been covered. The next step is therefore to define a measure of inelastic capacity at member level. Structural members in a pipe rack configuration comprise of slender beam elements, where the rack structure is commonly designed using RHS-members with rectangular hollow cross-sections. Assuming that a uniformly applied blast-pressure will trigger a predominantly flexural structural response, the inelastic capacity of an individual member may be defined by the plastic moment-resisting capacity of its cross-section, M_p .

In conventional design codes, M_p for uniaxial bending of a symmetric section is defined by the idealized stress distribution shown in Figure 3-9 (c). Figure 3-9 (a) show the general stress distribution in a symmetric cross-section for bending within the elastic range. When the outer fibers reach initial yield, the maximum elastic bending capacity defined by M_y is exceeded. The maximum stress level is assumed to remain at initial yield for increased loading and progress inward towards the neutral axis, as shown in Figure 3-9 (b), until the rectangular stress distribution characterizing a fully plastified section is reached in Figure 3-9 (c). In reality, the stress in the outer fibers will continue to increase due to strain hardening effects but this additional resistance is usually not considered in design codes defining moment-resisting capacity of beams in the inelastic range (DOD, 2014).

According to fundamental beam theory described by Gustafsson (2014), the moment at any point along a beam axis is obtained by integrating the axial stress distribution over the cross-sectional area. Hence, beam section moments defined above may be determined according to Equation (3.12).

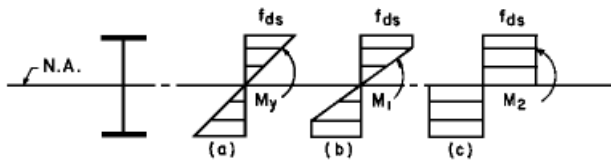


Figure 3-9 Stress distribution in gradually plastified beam cross-section. DOD (2014, p. 5-26)

$$M = \int_A \sigma(\varepsilon_x) dA \quad (3.12a)$$

$$M_y = S \cdot \sigma_{y0} \quad (3.12b)$$

$$M_p = Z \cdot \sigma_{y0} \quad (3.12c)$$

where M is the uniaxial bending moment for an arbitrary distribution of axial bending stress $\sigma(\epsilon_x)$; M_y is the yield moment calculated from the elastic section modulus S ; M_p is the plastic moment-resisting capacity calculated from the plastic section modulus Z ; and σ_{y0} is the initial yield stress.

Note that (DOD, 2014) uses the notation f_{ds} contrary to σ_{y0} in Figure 3-9. The notation f_{ds} is used to define the ultimate dynamic moment-resisting capacity M_{pu} where the static initial strength value defined by σ_{y0} has been scaled with a DIF to account for strain rate effects as discussed in previous section. Additional manipulation is required to derive the dynamic design stress f_{ds} and reference is made to (DOD, 2014) for a complete definition. For the purpose of this thesis, it is sufficient to inform that minor adjustments are made to Equation (3.12c) in simplified blast-resistant design procedures in order to estimate an idealized moment-capacity of a beam cross-section undergoing a severe dynamic flexural response.

The final step is to define inelastic capacity at the system level. In order to so, a simple system that comprise of a beam with fixed ends illustrated in Figure 3-10 is considered. The inelastic capacity of this simple system is determined in Appendix E through the method of *static pushover analysis* as explained by Kanvinde (2014).

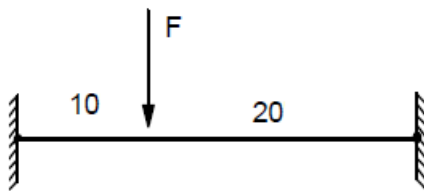


Figure 3-10 Two dimensional beam with fixed ends subjected to an eccentric point load.

The static pushover analysis defined by the stepwise analytical process outlined in Appendix E may be summarized by the associated *pushover curve* shown in Figure 3-11. The pushover curve defines an important concept in blast-resistant design and is generally referred to as a *resistance curve*. Figure 3-11 shows the downward deflection u at the point of load application versus the externally applied point load, F .

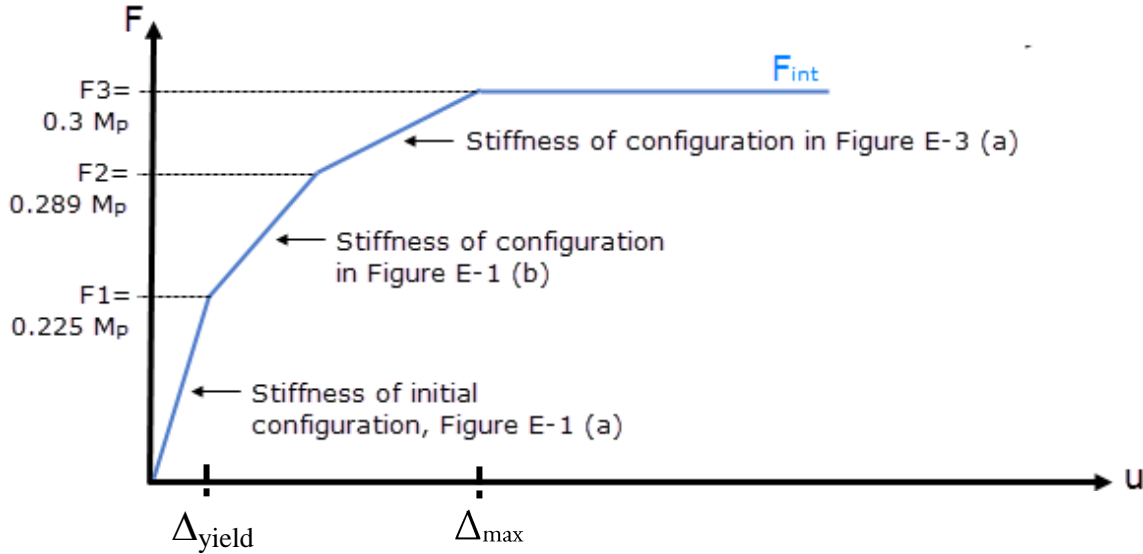


Figure 3-11 Pushover curve illustrating inelastic capacity of simple system.

The *resistance curve* shows the internal forces F_{int} developed within the simple system, defining its total inelastic capacity. The analysis conducted in Appendix E has successfully tied the material-, member- and system levels together to show how the characteristics of the resistance curve depend on the global properties of the structural configuration as well as the material and section properties of the beam element. The internal work developed within the system is given by the area under the resistance-deflection curve. Since both the stress and the deflection of the member is a function of strain, so are the internal forces F_{int} . Hence, the total amount of available resistance up to a certain level of displacement (indirectly strain) is defined by the amount of internal work, i.e. amount of total strain energy, developed within the system.

Figure 3-11 is again referenced as the ductility ratio of a structural system is defined. The ductility ratio μ is calculated according to Equation (3.13) and provides an alternative measure of a structure's inelastic capacity. If failure of the simple system associated with Figure 3-11 is defined by the deflection Δ_{max} reached at the external load level $F3$, the ductility is calculated as the ratio of this maximum allowable deflection over the deflection attained at first yield, i.e. at load level $F1$.

$$\mu = \frac{\Delta_{max}}{\Delta_{yield}} \quad (3.13)$$

where μ is the ductility ratio; Δ_{max} is the maximum allowable displacement associated with failure; and Δ_{yield} is the displacement associated with first initial yield in any structural member.

It was briefly stated in Section 3.2 that the internal force distribution in a system will be underestimated if effects from *strain hardening* and rapid *strain rates* are ignored, and that such an approach is not always on the conservative side. This is made evident from Figure 3-11 and associated theory outlined above. In the analytical model of the simple system, the fixed supports will experience internal forces that depend on the magnitude of M_p . Such support loads or connection

forces will naturally be underestimated if an increased material strength is not accounted for. This should be considered in procedures aiming to verify support configurations based on the internal force-capacity of adjoining members.

The inelastic capacity defined from the static pushover analysis in Figure 3-11 is not necessarily representative to a dynamic response scenario and was merely included to define and describe the concept of inelastic behavior. Deformation patterns in the dynamic scenario will be governed by the triggered mode shapes and the transient nature of the external loading as explained in Section 3.1. FEA software may be utilized to perform more sophisticated pushover analyses that account for both geometric and material nonlinearity effects associated with an inelastic response to blast. However, the load is still applied slowly to the structure implying that dynamic effects are not accounted for.

When defining the full capacity of the simple system in Figure 3-11, it was assumed that the highly stressed locations were able to develop their full resistance. However, the full inelastic capacity of a structural system is only ensured if premature failure modes are successfully avoided. These premature failure modes are also referred to as secondary modes of failure and consist of two main categories according to (DOD, 2014):

1. Instability modes of failure
2. Brittle modes of failure

Instability modes of failure occur at both system level and member level. At system level, instability is associated with *bifurcation*. Bifurcation in a structural system is caused by a sudden change in the structural configuration, generating large displacements that eventually lead to failure through excessive deformations or collapse. Instability at member level consists of lateral torsional buckling or local buckling. Brittle failure is associated with the complex fracture phenomena, and is strongly related to detailing of connections (DOD, 2014).

4 Analytical Methods and Verification Procedures

4.1 Linear-Elastic Biggs Method

The *Linear-elastic Biggs method* is based on the response of a linear-elastic, undamped SDOF-system subjected to a symmetrical triangular pulse. In Chapter 2, it was concluded that such an idealized triangular pulse should be used to define the blast-loading imposed on the pipe rack members within this study. The symmetry in the pulse is defined by the peak force (or peak pressure) occurring at time $t = t_d/2$. Since damping is excluded, the governing format of the EOM and the associated analytical model is given by Equation (4.1) and Figure 4-1.

$$m\ddot{u}(t) + ku(t) = p(t) \tag{4.1}$$

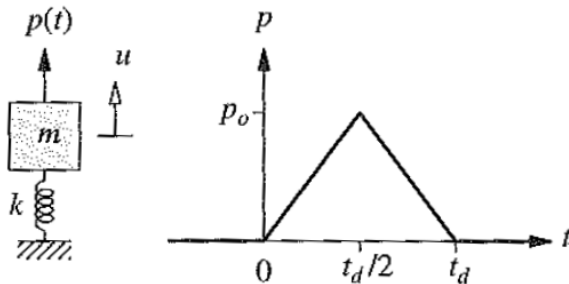


Figure 4-1 Analytical SDOF model for Linear-elastic Biggs method. Chopra (2011, p.148)

The closed-form solution to the response associated with the *Linear-elastic Biggs method* is given by Equation (D.1) in Appendix D, and it is recommended that this appendix is studied in conjunction to this section. The response governed by Equation (D.1) is provided by Chopra (2011) on the form of normalized dynamic displacement, i.e. the dynamic response at time t divided by the amplitude of the static equilibrium position of the dynamic oscillation. The amplitude of the static equilibrium is calculated according to Equation (D.2) of Appendix D and is defined by the displacement resulting from static application of the peak pulse-force p_0 shown in Figure 4-1. The term *Dynamic Amplification Factor* (DAF) is therefore adopted in substitute to the term normalized dynamic response, as it reveals the overall maximum amplification of the static response when dynamic effects are accounted for.

A Matlab script was developed and attached to Appendix D, calculating and visualizing the full time-history response governed by Equation (D.1) for user specified input values of t_d/T_n . The response is

divided into the three main phases of the pulse loading, i.e. the period of pressure rise governed by Equation (D.1a), the period of pressure decay associated with Equation (D.1b) and the period of free-vibration response calculated according to Equation (D.1c).

Before drawing important conclusions on key parameters and their effect on the response governed by Equation (D.1), the concept of *pure impulse excitation* as defined by Biggs (1964) will be discussed. If a pulse is considered “pure”, calculations of the SDOF-response may be simplified further. As explained by Biggs (1964), a *pure impulse* is characterized by having a duration that is much smaller than the natural period of the structural system to be analyzed. The ratios of t_d/T_n that define a *pure impulse* will be covered after providing the fundamental theory behind the concept.

Chopra (2011) uses Newton’s second law of motion to quantify the rate of change in momentum for a body being subjected to a force $p(t)$, given by Equation (4.2).

$$\frac{d}{dt}(m\dot{u}) = p(t) \quad (4.2)$$

where m is the mass of the body; \dot{u} denotes the velocity; and $p(t)$ is the external force.

If the mass is constant, Equation (4.3) prevails where \ddot{u} denotes the acceleration of the mass.

$$m\ddot{u} = p(t) \quad (4.3)$$

Integrating both sides yields:

$$\int_{t_1}^{t_2} p(t) dt = m(\dot{u}_2 - \dot{u}_1) = m\Delta\dot{u} \quad (4.4)$$

The term on the left hand side in Equation (4.4) is the magnitude of the impulse as shown previously, equal to the change in momentum. The same relation is obtained if the stiffness and damping terms in the EOM given by Equation (3.1) are neglected prior to integrating both sides. Considering a scenario where the pulse duration is very small, Biggs (1964) explains that very little spring resistance ($f_S = ku$) and damping resistance ($f_D = c\dot{u}$) will develop during the short time-period of loading, and that the relation provided by Equation (4.4) alone may be assumed to govern equilibrium in the system during this time. Hence, when the pulse is characterized by an infinitesimal duration, the relation given by Equation (4.4) may be idealized according to Equation (4.5).

$$I_o = m\Delta\dot{u} = m\dot{u}(0) \rightarrow \dot{u}(0) = \frac{I_o}{m} \quad (4.5)$$

It is seen that a *pure impulse excitation* may accurately be treated as an initial value problem, where a mass at rest ($u(0) = 0$) is given an initial velocity $\dot{u}(0)$ calculated according to Equation (4.5) that

will govern the following free-vibration response of the SDOF-system. The overall maximum response u_0 under this free-vibration phase is calculated according to Equation (4.6).

$$u_0 = \frac{I_0}{m\omega_n} = I_0 \frac{2\pi}{kT_n} \quad (4.6)$$

Using Equation (2.2) and Equation (D.2) to rewrite the expression, the DAF for triangular *pure impulse excitation* is given by Equation (4.7).

$$DAF = \frac{u_0}{(u_{st})_0} = \pi \frac{t_d}{T_n} \quad (4.7)$$

As made evident in the paragraphs above, the ratio between pulse-duration and the systems natural period will govern the SDOF-response. This ratios impact on the dynamic response is graphically illustrated in a shock spectrum shown in Figure 4-2.

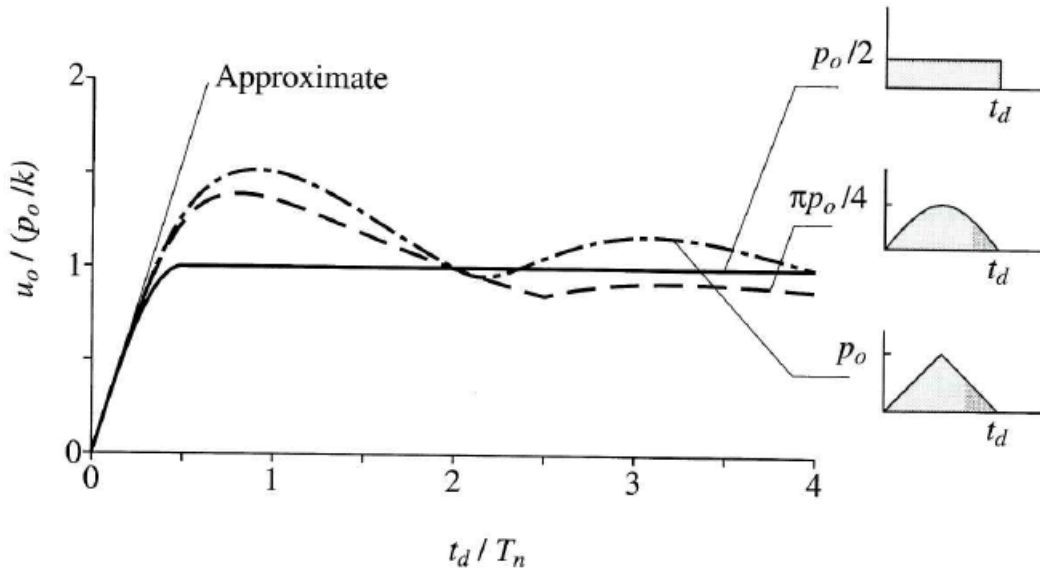


Figure 4-2 Shock spectrum for three different pulse-shapes of equal magnitude. Chopra (2011, p.153)

Figure 4-2 show the overall maximum response of a linear-elastic, undamped SDOF-system subjected to three different pulses of equal area. The vertical axis is scaled to the DAF of the triangular pulse. The graph related to the symmetric triangular pulse is obtained by extracting the maximum DAF calculated according to Equation (D.1) for different ratios. The linear part of the graph that prevails for small ratios t_d/T_n is defined by Equation (4.7).

The first conclusion to be drawn in relation to Figure 4-2 is that the shape of the pulse has no impact on the dynamic response if the duration is short relative to the natural period, i.e. if the structure is being subjected to a *pure impulse excitation*. Chopra (2011) provides the limiting range of $t_d/T_n < 1/4$ to define this specific load scenario where Equation (4.7) provides an accurate solution of the DAF.

The overall maximum response illustrated in the shock spectrum is either found during the forced vibration phase, Equation (D.1a)/ (D.1b), or the free-vibration phase, Equation (D.1c). For the triangular pulse, the maximum overall response will develop under the forced vibration phase if $t_d/T_n > 1/2$, implying that the pulse shape will have a great impact on the response. For the larger values in this region, the response is much influenced by the rapidity of the pulse excitation. If instead $t_d/T_n < 1/2$, the peak response is obtained during the free-vibration phase and controlled by the time integral of the pulse.

In Figure 4-3, SCI (1992) explains which features of an idealized blast-pulse that has a significant impact on the dynamic response depending on the governing ratio of t_d/T_n . In Figure 4-3, the pulse duration is denoted τ and natural period denoted T . Three main loading regimes are established, where the definition *impulsive* correspond to that of a *pure impulse* above. It is noted that Figure 4-3 is not associated with SDOF-response specifically, and that ranges of ratios used for classification are slightly different than those provided by Chopra (2011) above. However, comments on which features of a blast-pulse that are critical to preserve in the idealized representation in order for an analytical response to prevail with accuracy coincide in general.

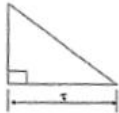
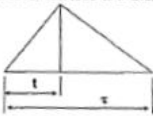
| | Impulsive Short $\tau / T < 0.4$ | Dynamic Intermediate $0.4 < \tau / T < 2.0$ | Quasi-static Long $\tau / T > 2.0$ |
|---------------------------------|---|---|--|
| Peak Value | Preserving the exact peak value is not critical. | Preserve peak value - increase or decrease in this quantity will result in a similar increase or decrease in response except if the peak is associated with a very short duration spike. | |
| Duration | Preserving the exact load duration is not critical. | Preserve load duration since in this range it is close to the natural period of the structure. Even slight changes may affect response. | Load duration is not too important if response is purely elastic, but it becomes significant when response is plastic. |
| Impulse | Accurate representation of the impulse is important, with negative impulse included in some cases. | Accurate representation of the impulse is important. Additionally, the impulse in the top one-third pressure range should be similar under both actual and idealised curve. | Accurate representation of the impulse is not important. |
| Rise Time | Preserving rise time is not important. | Preserving rise time is very important; ignoring it can significantly affect response. | |
| Idealised Pressure/Time History | General shape of idealised load is a right-angle triangle:  | General shape of idealised load is a triangle:  A tri- or tetra-linear form can be used to represent the rise and decay of the load more accurately, thus predicting slightly better response. | |

Figure 4-3 Guidance on idealization of blast-pulse characteristics. SCI (1992, p. 3.9)

It has been concluded that the relationship between the blast-pulse duration and the natural period of the structural system does not only determine the dynamic response of a linear-elastic, undamped SDOF-system, but also reveals its sensitivity to pulse-shape idealization.

As made evident by paragraphs above, the *Linear-elastic Biggs method* may be utilized to calculate the DAF associated with the response of a linear-elastic, undamped SDOF-system subjected to a

symmetrical triangular pulse. The DAF depends on the ratio of t_d/T_n as shown by the shock spectra in Figure 4-2. An additional shock spectrum is provided in Figure 4-4 for a more detailed representation of the DAF related specifically to the symmetrical triangular pulse. Figure 4-4 is incorporated into the verification procedure referred to as the *conventional method* as described in the following section.

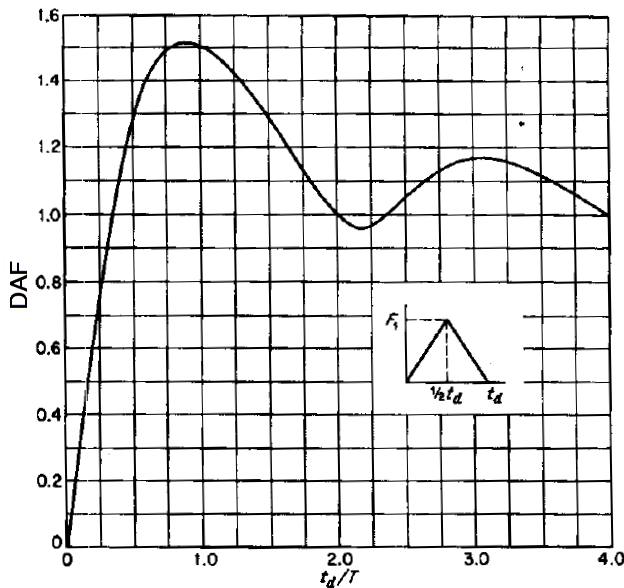


Figure 4-4 Shock spectrum for linear-elastic SDOF system subjected to a symmetric triangular pulse. Biggs (1964, p. 47)

4.2 The Conventional Method

The verification procedure currently implemented at AKSO with respect to the accidental explosion event is outline below. This procedure is referred to as the conventional method. Recall from the introduction that structures are verified through linear static FE analyses limiting the analytical preciseness to linear-elastic theory and static structural response.

The conventional method is defined by the following steps:

STEP 1: The peak pressure characterizing the design blast-pulse is converted to static drag-loads in accordance with conclusions from Chapter 2. This calculation process is fully explained in Chapter 5 and associated appendices.

Outcome: Static blast-loads calculated for individual members in the FE model.

STEP 2: An Eigen frequency analysis is conducted to determine the dynamic properties of the structural configuration. T_n associated with the first natural mode of vibration characterized by global displacement in the direction of the assigned blast load shall be chosen for implementation into the *Linear-elastic Biggs method*. In accordance with

conventional labeling of natural vibration modes discussed in Chapter 3, the first modes are related to the lower values of natural frequencies.

Outcome: Natural period T_n for implementation into the *Linear-elastic Biggs method*.

STEP 3: The maximum DAF is determined in accordance with the *Linear-elastic Biggs method* and Figure 4-4 based on the range of durations t_d characterizing the design blast-pulse and the natural period of the structure T_n obtained in Step 2.

Outcome: Maximum DAF.

STEP 4: Static blast-loads calculated in Step 1 are amplified by applying the DAF obtained in Step 3 and assigned to structural members in the FE model. Static FE simulations are conducted for all applicable blast directions.

Outcome: Analysis results from static FE simulations.

STEP 5: Structural members are finally code checked according to international standards such as (NORSOK N-004, 2013).

Outcome: Verified blast-resistant structural design.

4.3 Elasto-Plastic Biggs Method

The *Elasto-plastic Biggs method* also relates to an analytical response of an undamped SDOF-system subjected to a triangular pulse excitation. However, the model is expanded through incorporation of a bilinear resistance function to account for inelastic behavior during the dynamic response.

The *Elasto-plastic Biggs method* is summarized by a single response chart, just as the *Linear-elastic Biggs method* was summarized by the shock spectrum in Figure 4-4. Before describing underlying theory, this response chart is presented in Figure 4-5. Biggs (1964) uses a different notation than what has been employed in previous sections of this thesis in accordance with Chopra (2011). These differences are outlined below along with definitions of new notation introduced by Biggs (1964) in Figure 4-5.

Displacements, velocities and accelerations are denoted y , \dot{y} and \ddot{y} in contrary to u , \dot{u} and \ddot{u} . Hence, y_{el} denotes the amount of displacement reached at the end of the elastic response range and y_m denotes the maximum displacement attained prior to elastic rebound. Combined, they define the ductility ratio μ of the idealized inelastic system as explained in Chapter 3. The triangular pulse excitation and its peak force-component are referred to as $F(t)$ and F_1 in contrary to $p(t)$ and p_o .

The bilinear function is characterized by the perfectly-plastic internal resistance R_M , developed at y_{el} and maintained constant throughout the inelastic response until y_m is attained. This resistance

function governs the internal spring forces developed within the SDOF system and is a function of displacement as explained below.

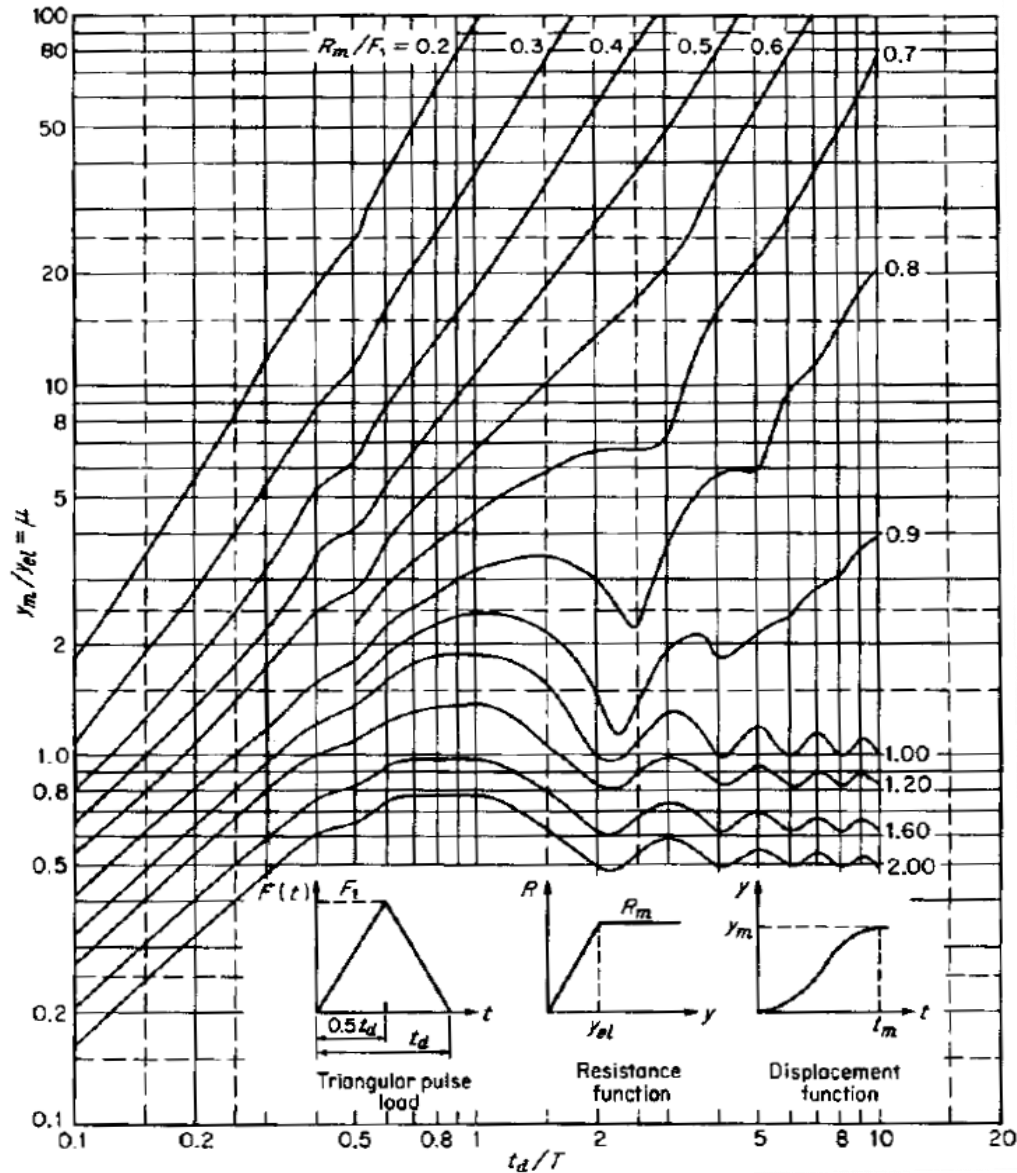


Figure 4-5 Response chart for inelastic SDOF-system subjected to a symmetric triangular pulse. Biggs (1964, p. 78)

The intended use of the response chart as explained by Biggs (1964) is to derive the overall maximum dynamic displacement y_m of the inelastic SDOF-system. The external force-function $F(t)$ and its components F_1 and t_d are assumed to be known. When the analytical SDOF model has been established with idealized mass m , elastic stiffness k and resistance R_M , the natural period T_n and elastic displacement y_{el} are easily obtained. At this stage, ratios t_d/T_n and R_M/F_1 are known and the associated ductility ratio μ can be read of the chart in Figure 4-5. The maximum displacement is finally calculated from the relation $y_m = \mu \cdot y_{el}$.

It will be shown in the following section that the proposed method utilizes the response chart to determine a peak pulse-force F_1 rather than following the intended procedure of calculating a maximum dynamic displacement. It should also be noted that the bottom curve of Figure 4-5, corresponding to a ratio of $R_M/F_1 = 2$, define a SDOF-response completely within the elastic range. Hence, if $R_M/F_1 > 2$ the response may be determined according to the *Linear-elastic Biggs method* and Figure 4-4.

In addition to Figure 4-5, Biggs (1964) provides a similar response chart developed to reveal the time after load application at which the maximum displacement y_m is attained, i.e. t_m . This response chart is not utilized by the proposed method and thus not included herein. Reference is made to the publication of Biggs (1964) where this chart is presented.

It is possible to derive the closed-form analytical solution of the time-history response associated with the inelastic SDOF-system defined by Figure 4-6 and Equation (4.8) below. However, this process is tedious and will not be explained in great detail herein. Reference is made to Biggs (1964) where this closed-form solution is derived for a suddenly applied, constant load. The corresponding solution with respect to a triangular pulse is not derived explicitly but the general procedure is explained. In shortness, the analytical response has to be calculated in stages considering discontinuities in both the response (elastic, plastic and rebound) as well as the force application (pressure rise, pressure decay and free vibration). At each stage, a differential equation defined by the governing EOM must be solved for from initial conditions given by the final displacement and velocity from the preceding stage.

An alternative to the rigorous approach outlined above is to establish nondimensional EOMs for the elastic respectively inelastic range and solve for the maximum overall response of the SDOF-system by use of numerical procedures. This was the approach adopted by Biggs (1964) when constructing the chart in Figure 4-5 and reference is made to this publication for a detailed description of this procedure.

The fundamental difference between the two SDOF-systems associated with the *Linear-elastic Biggs method* and the *Elasto-plastic Biggs method*, is that the spring stiffness for the inelastic system is no longer a linear function with slope k throughout the time-history response, but instead a unique function of displacement. The general format of the EOM, associated with the analytical SDOF model shown in Figure 4-6, is therefore written according to Equation (4.8) where the spring force is denoted $R(y)$ to emphasize its dependency on displacements.

$$m\ddot{y}(t) + R(y) = F(t) \tag{4.8}$$

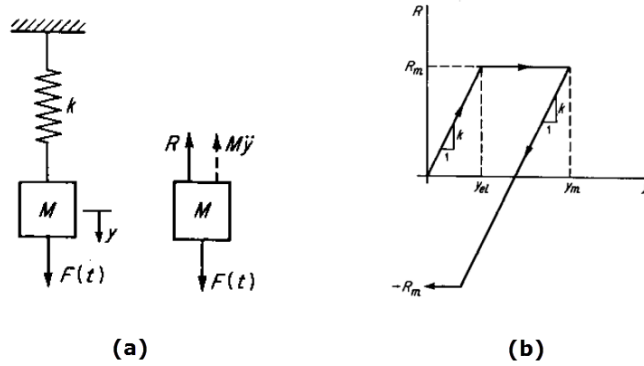


Figure 4-6 Analytical SDOF model (a) and associated resistance function (b) for Elasto-plastic Biggs method. Biggs (1964, p. 22)

When solving for the response numerically, the format of the general spring resistance $R(y)$ must be continuously updated and enforced via the EOM depending on if the response at the next time increment is within the; (1) initial elastic range, (2) inelastic range or (3) the elastic rebound range. These three main response phases are illustrated in Figure 4-6 (b). The governing format of the spring resistance $R(y)$ for each separate phase is given by Equation (4.9). Along with Equation (4.8), it defines the EOM to be enforced within each response range in the numerical solution routine.

$$R(y) = \begin{cases} ky & \text{if } 0 < y < y_{el} \\ R_m & \text{if } y_{el} < y < y_m \\ R_m - k(y_m - y) & \text{if } (y_m - 2y_{el}) < y < y_m \end{cases} \quad (4.9)$$

Equations (4.8) and (4.9) do not cover an extended response into a negative inelastic range as this is unlikely to occur. Additional formats of the general spring resistance $R(y)$ could however be established to cover this scenario.

4.4 The Proposed Method

The verification procedure recently developed at AKSO with respect to the accidental explosion event is outline below. This procedure is referred to as the proposed method. Analyses are limited to a linear static FE formulation as described in Chapter 1.

Recall that an initial structural design verified for all limit states and load scenarios except the accidental explosion event has been established prior to application of the proposed method. The procedure defined by the steps outlined below is therefore intended to verify this initial design for a blast scenario defined by the design blast-pulse.

The proposed method is defined by the following steps:

- STEP 1/ These steps are identical to the first two steps of the conventional method. Hence,
STEP 2 reference is made to Section 4.2.

Outcome: Static blast-loads calculated for individual members in the FE model. Natural period T_n for implementation into the *Elasto-Plastic Biggs method*.

STEP 3: Static blast-loads calculated in Step 1 are assigned to structural members in the FE model. Static pushover-analyses are conducted for all applicable blast directions and the loading is increased proportionally until first initial yield in any structural member within the assembly is registered. In the post-processing, the following two field variables associated with the structural response at first initial yield are documented:

1. overall maximum global displacement in direction of applied blast loading, denoted $U1_{max}$ in Chapter 6 and
2. the sum of reaction forces at supports in direction of the applied blast loading, denoted $\Sigma RF1$ in Chapter 6.

Enforcing the SDOF analogy on the analyzed MDOF-system, $U1_{max}$ is assumed to represent y_{el} as defined by the *Elasto-Plastic Biggs method* and $\Sigma RF1$ will represent the perfectly-plastic internal resistance R_M .

Outcome: Parameters y_{el} and R_M for implementation into the *Elasto-Plastic Biggs method*.

STEP 4: The ductility ratio μ is calculated from y_{el} derived in Step 3 and a predefined value of y_m governed by the established failure criteria. Hence, y_m is not derived explicitly within the procedure but instead based on previous experience and studies.

Outcome: Ductility ratio μ for implementation into the *Elasto-Plastic Biggs method*.

STEP 5: A span of ratios t_d/T_n may now be established based on the range of durations t_d characterizing the design blast-pulse and the natural period of the structure T_n determined in Step 2. This span of ratios t_d/T_n and the ductility ratio μ calculated in Step 4 will define a horizontal line in Figure 4-5. Any point along this horizontal line is said to have two specific response curves associated with it, one immediately above the point and one immediately beneath it. For example, if $\mu = 5$ and $0.5 < t_d/T_n < 2$, the point along this line defined by ratio $t_d/T_n = 1$ is said to be associated with response curve $R_M/F_1 = 0.6$ above it and curve $R_M/F_1 = 0.7$ beneath it. In Step 5, the overall highest value of R_M/F_1 associated with any of the points along the horizontal line is chosen for further calculations.

Outcome: Ratio of R_M/F_1 associated with failure of the idealized SDOF-system.

STEP 6: The peak pulse-force F_1 is solved for from the internal resistance R_M determined in Step 3 and the ratio (R_M/F_1) obtained from Step 5 according to the relation $\frac{R_M}{F_1} = (R_M/F_1) \rightarrow F_1 = \frac{R_M}{(R_M/F_1)}$. It is now evident that the overall highest ratio chosen from points on the horizontal line in Step 5 will generate the overall lowest value of F_1 , which is assumed to be a conservative estimate of the maximum peak pulse-force that the SDOF-system can withstand prior to failure at a level of displacement defined by μ .

Outcome: Magnitude of peak pulse-force F_1 associated with failure of the idealized SDOF-system.

STEP 7: This step involves converting the peak pulse-force F_1 calculated in Step 6 to a limiting peak blast-pressure $p_{1,limit}$. In order to do so, an exposed blast area A_{Blast} associated with the analyzed structure must be calculated.

A_{Blast} is calculated by summing up the area of all member sections that were considered exposed to the dynamic blast-pressure in a specific direction and thus assigned static loading in the FE model. This area has already been identified when calculating static blast-loads in Step 1.

The limiting peak blast-pressure $p_{1,limit}$, assumed to define the full capacity of the initial structural design, may now be calculated from $p_{1,limit} = F_1/A_{Blast}$.

Outcome: Limiting peak blast-pressure $p_{1,limit}$ assumed to define the full capacity of the initial structural design.

STEP 8: The limiting peak blast-pressure $p_{1,limit}$ calculated in Step 7 is compared to the peak blast-pressure of the design-pulse, p_1 .

If $p_{1,limit} > p_1$, the structure will not exceed established failure criteria and the initial design is considered verified for the accidental explosion event.

If $p_{1,limit} < p_1$, the structure does not have sufficient capacity to withstand the design blast-pulse. The initial design must therefore be modified and reanalyzed via the procedure outlined by Step 1 to Step 8 above until the criteria $p_{1,limit} > p_1$ is met.

Outcome: Verified blast-resistant structural design.

5 Finite Element Analysis Study

This chapter provides an overview of the FEA study conducted within this thesis. The specific physical problem being analyzed, i.e. the response of a pipe rack structure subjected to an accidental explosion event, is fully described herein in terms of governing conditions such as characteristics of the design blast-pulse and properties of the evaluated structural configuration. This chapter gives full insight into how the different aspects of the physical problem have been accounted for in the FEA study. Assumptions made in the process of defining the problem numerically are also included. The full extent of the study is not documented within the main body of this report which provides more of a general, yet comprehensive, overview. Detailed documentation on implemented pre-processing data such as blast-load calculations as well as specific Abaqus modeling commands utilized in the FE simulations can be found in appendices which are frequently referenced in subsections below.

The FEA scope is outlined in Table 5-1 and the objectives of each of the conducted analyses are summarized at the end of this chapter in Section 5.9. As made evident by this chapter, a stepwise analysis strategy was adopted. The work flow defining the full analysis procedure follows a strict sequential order, where the analyses as listed in Table 5-1 were conducted in a descending order, starting with Analysis A.1. This sequential order was implemented to allow for stepwise conclusions to be drawn that could validate utilized methods and procedures, such as blast-load calculations, as well as reduce the extent of the scope for subsequent analyses. Hence, certain analyses within the scope were dependent on preceding FEA results as outlined in Table 5-1.

| Analysis Label | FE Model | Analysis Type | Dependency on preceding FEA |
|-----------------------|-----------------|----------------------|------------------------------------|
| A.1 | A | Static | None |
| B.1 | B | Static | A.1 |
| B.2 | B | Static pushover | A.1, B.1 |
| B.3 | B | Eigen frequency | A.1 |
| B.4 | B | Full nonlinear | A.1, B.1, B.2 |
| B.5 | B | Full nonlinear | A.1, B.1, B.2 |
| B.6 | B | Full nonlinear | A.1, B.1, B.2 |

Table 5-1 Analysis matrix outlining FEA scope.

Two different FE models were established, defining the structural configurations that were considered in each of the analyses listed in Table 5-1. Both FE models are fully described in Section 5.3, where FE model A is seen to contain only an idealized pipe line configuration whereas FE model B contain only a rack structure. The geometries in both models are governed by a specific pipe rack design, verified for an accidental explosion event in accordance with the conventional method during

a previous AKSO project. This specific pipe rack configuration is labeled *Piperack01_P30_M50* and described further in Section 5.2.

The main structural components in a pipe rack system, i.e. the piping configuration and the rack structure, are currently being verified separately by engineering teams from two different AKSO departments. However, this multi-disciplinary problem requires that the interactive response of the entire structural system is being considered in the verification process. For AKSO structural department to achieve this and still maintain a manageable and efficient verification process, the preferred approach consists in accounting for the piping configurations impact on the structural response implicitly in a FE simulation of a model containing only a rack structure. This implies that the piping configuration's contribution in mass, stiffness and blast-loading must be accounted for in analyses of the rack structure to obtain a reliable solution. System failure modes must also be established considering possible failure modes of the pipe lines. The preferred approach outline above was adopted within this FEA study as described by the following sections and referenced appendices of this report.

A total number of 7 main FE analyses were performed in this study as shown in Table 5-1. The analyses are categorized into four types; (1) Static, (2) Static pushover, (3) Eigen frequency and (4) Full nonlinear. For a complete characterization of each analysis type, reference is made to Appendix A where the pre-processing procedures governing all FE simulations are documented.

5.1 Reference Coordinate System

Three main directions are frequently referenced in relation to the right-handed, rectangular Cartesian coordinate system defining the orientation of the FE models in Abaqus as illustrated by Figure 5-1.

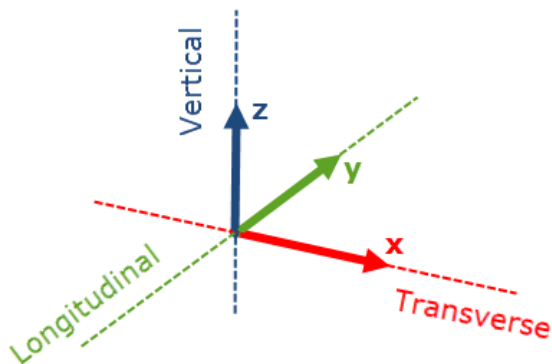


Figure 5-1 Reference Coordinate System.

The following naming convention is adopted in documentation of the FEA study:

- Transverse direction defined parallel to global X-axis or 1-axis.
- Longitudinal direction defined parallel to global Y-axis or 2-axis.
- Vertical direction defined parallel to global Z-axis or 3-axis.

5.2 Piperack01_P30_M50

A specific pipe rack design from a previous AKSO project, and the associated siting and loading conditions governing this design, was evaluated within this FEA study. The chosen pipe rack design labeled *Piperack01_P30_M50* is illustrated in Figure 5-2 along with a plan view showing the layout of the process module from where the governing design blast-pulse was derived according to the procedures outlined in Chapter 2.

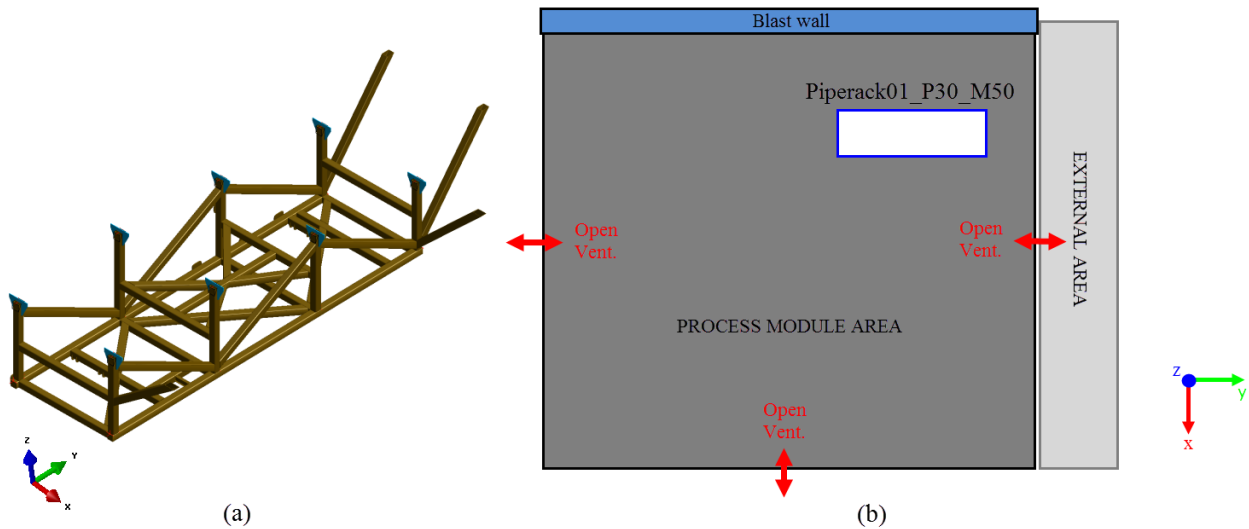


Figure 5-2 ISO view of *Piperack01_P30_M50* (a) and plan view of process module layout (b).

Figure 5-2 (b) show the true proportions of *Piperack01_P30_M50* relative the size of the process module. The process module has a height of 7 meters and an area of 25x27.5 meters while the external boundaries of the pipe rack, excluding braces, enclose a volume of 2.3x8.5x2 meters. Hence, the pipe rack structure occupies approximately 0.8 % of the total process module volume. The process module is enclosed by a blast wall in $-X$ direction and steel plated deck structures in both vertical directions, whereas all other directions allow for open ventilation.

An extensive amount of piping is fitted within the process module as illustrated by Figure 5-3. The configuration to the left show only the module framing and *Piperack01_P30_M50* highlighted in yellow. The configuration to the right includes in addition all piping located within the module volume.

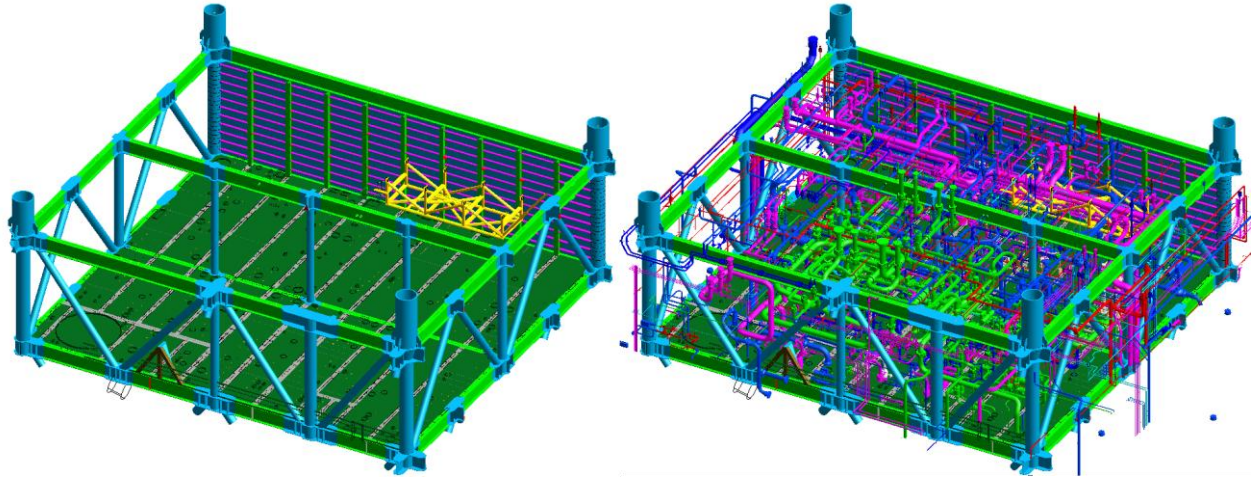


Figure 5-3 PDMS model of process module illustrating piping layout.

Piperack01_P30_M50 provides support to part of the complex pipe line layout shown in Figure 5-3. The piping layout on an offshore topside facility is not standardized and the configuration at the location of a specific pipe rack is more or less unique. For analysis purposes, the piping configuration was idealized in order to maintain a manageable FE model. The idealized configuration that was incorporated in this study is described in Section 5.3. For comparison to the idealized FE model, Figure 5-4 has been included below to illustrate the actual piping layout in the vicinity of *Piperack01_P30_M50*.

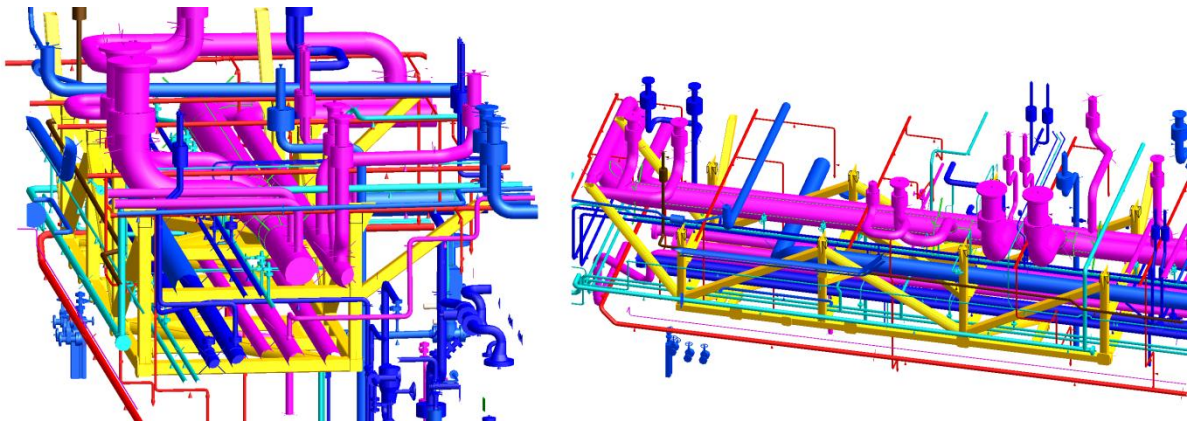


Figure 5-4 Actual piping layout in vicinity of *Piperack01_P30_M50*.

5.3 FE Models

5.3.1 FE Model A

The FE model labeled A contain only an idealized representation of the pipe line configuration illustrated in Figure 5-4 as well as associated pipe supports accounted for implicitly through modelling of boundary conditions. Figure 5-5 and Table 5-2 define geometrical and material properties of the piping configuration as well as the fluid content associated with each pipe line. Pipe

lines are labeled with its associated ISO stress number according to AKSO project documents. The orientation of the pipe lines relative the rack structure is illustrated in Figure 5-6.

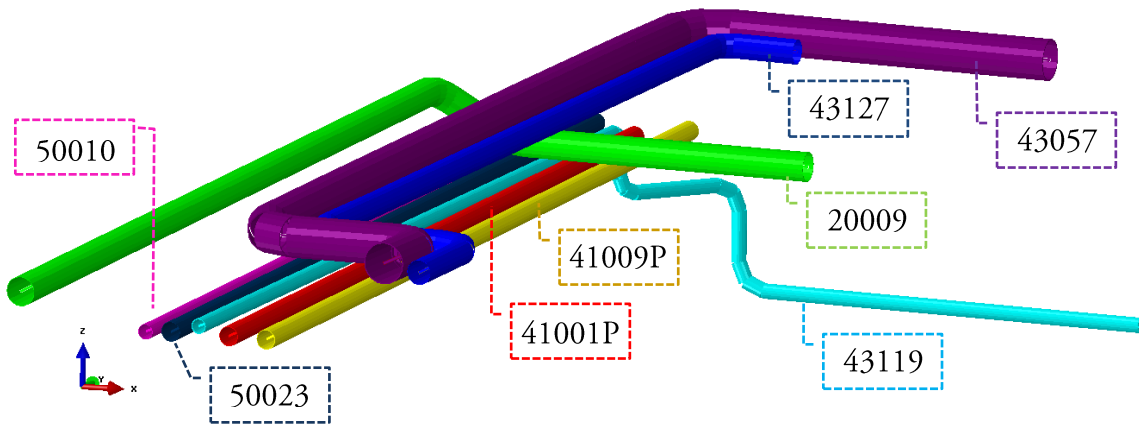


Figure 5-5 Idealized pipe line configuration in FE Model A.

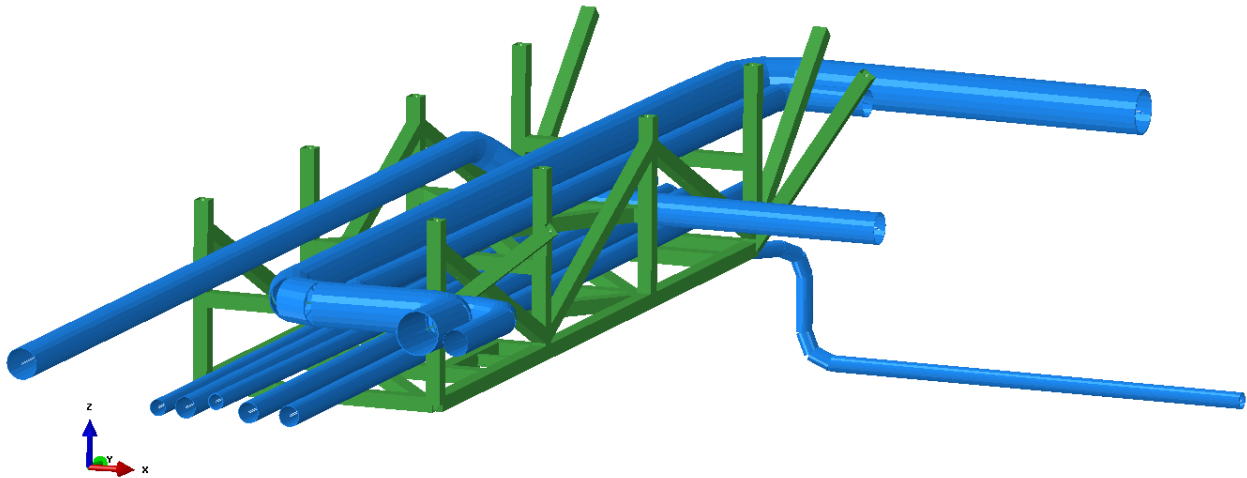


Figure 5-6 Orientation of pipe line configuration relative Piperack01_P30_M50.

The piping configuration in FE model A has been idealized to only include the larger pipe lines assumed to add significant mass contribution to the structural system as a whole and transfer significant loads to the rack structure via the supports. The pipe line geometries are modeled according to structural drawings and plant design manager system (PDMS) model coordinates defining the exact location of attached pipe supports.

In order to simplify the FE model, the segments of each pipe line reaching beyond the first set of external supports have been excluded. External supports, contrary to internal supports, are those attached to structural members that are not part of the rack structure. This idealization implies that the true contribution in mass and blast loading from the pipe lines might be somewhat compromised in the FEA study.

| Pipe Line | Pipe Section Properties | | Fluid Content/ Density (ρ_{fluid}) [kg/m ³] | Material Code |
|-------------------|-------------------------|---------------------|--|---------------|
| | Diameter (OD) [mm] | Wall Thickness [mm] | | |
| 43057 | 457 | 12.7 | Gas, Flare / 13.24 | A312 S31254 |
| 43127 | 273.1 | 4.19 | Gas, Flare / 2 | A790 S31803 |
| 20009 | 323.9 | 6.35 | Hydrocarbons vapor / 19 | A790 S31803 |
| 41009P/ 41001P | 219.1 | 8.18 | Fresh Water / 900 | A333 6 |
| 43119 | 168.3 | 11 | Gas, Flare / 13.24 | A312 S31254 |
| 50023 | 219.1 | 4.9 | Sea water / 1018 | GRE |
| 50010 | 168.3 | 3.9 | Sea water / 1027 | GRE |

Table 5-2 Properties of piping configuration in FE Model A.

Pipe supports are designed to allow for small rotations of piping and attached support configuration, thus not transferring any moment to pipe rack members. Although small rotations of the support configuration will not transfer overturning moments to the rack members, large rotations possibly will. Torsional rotation of the pipe line will also be hindered to some extent due to frictional forces between piping and support configuration. Constraining of rotational DOFs is not considered in the FE implementation of this study or in the simplified calculation procedures documented in Appendix A, implying that only transfer of forces to the rack structure is accounted for.

Each pipe support is designed with one or several of the following support functions with the purpose to constrain specific translational DOFs; rest support (RS), hold down (HD), line guide (LG) and line stop (LS). The true support functions of all internal supports are accounted for while the external supports are consistently idealized with full fixity, constraining all translational and rotational DOFs. Reference is made to Section A.2 of Appendix A which provides a detailed documentation on the support functions and location of all pipe supports attached to *Piperack01_P30_M50*. The documentation provided in Appendix A also explains how the support functions were enforced through modeling of boundary conditions in FE model A and how they govern simplified calculations of load and mass contribution in analyses of FE model B.

5.3.2 FE Model B

The FE model labeled B contains an accurate representation of the rack configuration design illustrated in Figure 5-2 (a). Figure 5-7, Figure 5-8 and Table 5-3 show the geometrical properties of FE model B and thus the design of *Piperack01_P30_M50*. The structural members in FE model B are defined numerically in Abaqus by use of three dimensional beam elements. Utilizing a beam element model to simulate a structural response has implications on the numerical preciseness of generated field output variables. Such implications are addressed and discussed further in Section 5.5.

Another implication of this beam element model is that it does not reflect the actual design of the joints. Rack structure joints are commonly designed by welding adjoining members together with eccentricities. No offsets were modeled at the joints in FE model B to account for such eccentricities,

implying that there is an overlap of material at these locations adding local stiffness and capacity to the numerical representation.

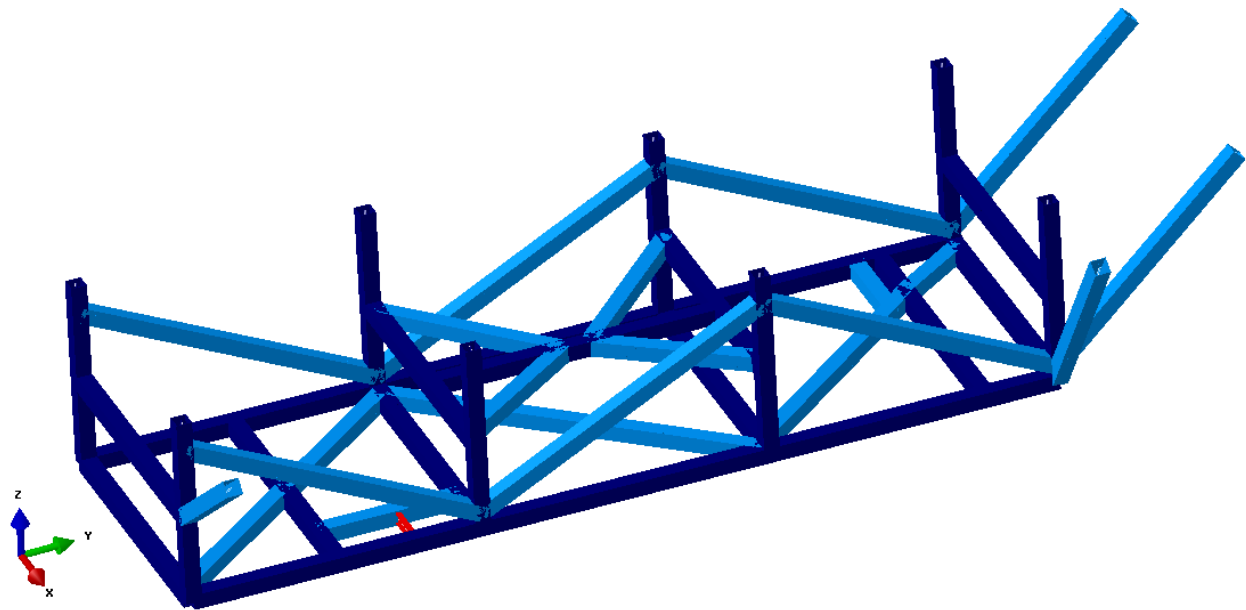


Figure 5-7 Numerical representation of Piperack01_P30_M50 in FE Model B.

| Section Profile | Number of Structural Elements | Color Code Figure 5-7 | Section Properties [m] |
|-----------------|-------------------------------|-----------------------|------------------------|
| SHS150x8.0 | 25 | Dark blue | See Figure 5-8 (a) |
| SHS150x6.0 | 20 | Light blue | See Figure 5-8 (b) |
| IPE120 | 1 | Red | See Figure 5-8 (c) |

Table 5-3 Geometry of FE Model B.

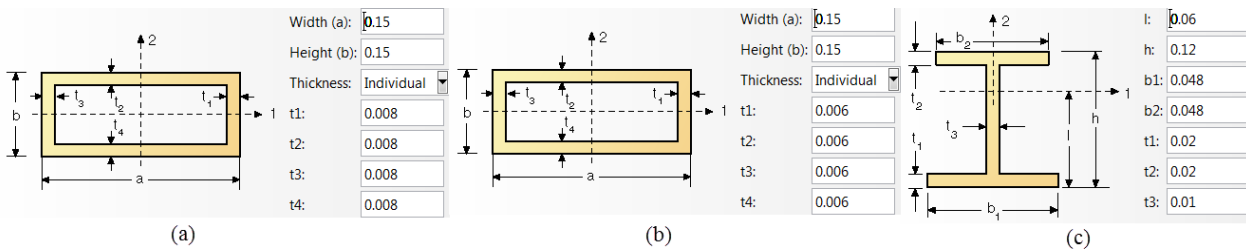


Figure 5-8 Section properties of pipe rack beam members in FE model B.

The design and modelling of connections that fix the rack configuration to the above deck structure is shown and described in Section A.3 of Appendix A. The eight vertical beam elements shown in Figure 5-7 are attached to deck girders by gusset plates that are assumed to constrain motion in all DOFs except rotation about global X-axis. The four brace elements are welded directly to deck girders and this connection is assumed to provide full fixity, constraining motion in all DOFs.

5.4 Assumptions

The blast loads will be assigned globally to the entire structural configuration at once. Hence, a structural response due to a localized blast event affecting the immediate vicinity of a pipe rack member is not covered within the scope. According to Section 5.2 and Section 2.4, the volume enclosed by the pipe rack structure is less than 1 % of the module volume and the cloud sizes from where the design blast-loads are derived typically vary from 2%-50%. A global, uniformly distributed load application associated with the blast wave engulfing the entire rack at once is therefore considered to capture the nature of the most relevant accidental explosion event.

The pipe supports are designed according to the same philosophy employed in the conventional method, where DAFs are applied to static design blast-loads in order for the supports to remain elastic under the blast event. Pipe support designs were not modeled explicitly in the analyses of this study, implying that their true capacity could not be evaluated. For this study, it is therefore assumed that the pipe support designs will not be a critical component governing the inelastic capacity of the system.

5.5 Failure Criteria

The failure criteria established herein are governed by the following post-blast functionality requirements of the structural system:

1. Safety critical pipe lines should not rupture.
2. Rack structure should not collapse or deform in such way that safety critical pipe lines rupture.

Two explicit failure criteria have been established to meet the post-blast functionality requirements in the FEA study of *Piperack01_P30_M50*. One relates to allowable global deflections and the other defines a limiting plastic strain on the rack members as explained below.

The deformation criteria defining system failure with respect to the piping configuration is provided by the AKSO piping department. A maximum global deflection in direction of the blast wave of ± 100 mm is set as the limiting value. This deflection limit is assumed to govern rupture of safety critical pipe lines.

Relative displacements between pipe supports could serve the purpose of a more specific failure criterion. Due to the complex nature and uniqueness of a pipe rack configuration, such a criterion would depend strongly on the specific geometry and properties of each separate pipe line. This type of detailed failure criterion is not practical in the sense of maintaining an efficient verification process and has not been established for this study. However, relative displacements between internal supports were registered and documented in association with some of the analyses in order to provide data for further investigations by the piping department.

The second failure criterion is given by a maximum allowable plastic strain of 15.3 percent assumed to prevent local fracture in rack members. Along with the global deflection criteria, it is assumed to ensure that the rack structure fulfills functionality requirement number 2 above. The 15.3 percent strain criteria has been provided by the AKSO structural department, based on research and development of a bilinear material model for the structural steel used in design of the rack members. The material models implemented in the study are illustrated and discussed in Section 5.6.

The structural members in FE model B are defined numerically by beam elements. The beam element is a one dimensional approximation of a three dimensional continuum, where the solution variables are a function of position along the beam axis only. The strain calculated at an integration point along the axis will therefore be defined by a single scalar value assumed to represent the straining of all material points in the entire cross-section at this location (Abaqus, 2015b). Hence, a strain-based failure criteria of 15.3% aiming to capture a local failure mode such as fracture should not be directly applied if a beam element model is utilized. This is shown by the internal AKSO-study attached to Appendix C comparing strain levels registered in a beam element model versus a more detailed shell element model. It concludes that a plastic straining of 3% should be used conservatively for beam element models. Hence, failure due to fracture within this FEA study is defined by a numerical value of plastic straining corresponding to 3%.

Table 5-4 summarizes the failure criteria governing the FE analyses performed in Abaqus within this study. For evaluation of the *proposed method*, it was assumed that failure would be governed by the global deflection criteria and a value of 100 millimeters was therefore assigned to the input parameter y_m in the process of estimating a limiting peak blast-pressure $p_{1,limit}$ as described in Section 4.4.

| Failure Criterion | Response Quantity |
|---|-------------------|
| Max. allowable global deflection | ± 100 mm |
| Max. allowable plastic strain, $\epsilon_{failure}^p$ | 3.0% / (15.3%) |
| Numerical value / (Theoretical value) | |

Table 5-4 Failure criteria established for FEA study.

The full nonlinear FE formulation used to simulate the dynamic response of *Piperack01_P30_M50* enforces equilibrium in the deformed configuration at each time step and accounts for geometric and material nonlinear effects. Hence, the instability modes of failure identified in Chapter 3 are accounted for in general. What has not been considered in this numerical study is premature failure from bifurcation specifically associated with geometrical imperfections. Brittle failure through fracture is accounted for by the strain criteria.

5.6 Material Models

The bilinear material model specified by Figure 5-9 and Table 5-5 was implemented and assigned to rack members in analyses containing FE model B. This idealized model of the structural steel used in

design of the rack members have been developed based on studies conducted by the AKSO structural department.

As discussed in Chapter 3, this bilinear representation of the material behavior will account for *strain hardening* effects. It should be noted however that the material data in Table 5-5 correspond to a nonlinear material response to conventional static loading, implying that *strain rate* effects discussed in Chapter 3 were not enforced via implemented material data. Since no Abaqus commands were utilized to automatically account for such effects in the numerical simulations, the *strain rate* phenomenon has been excluded from the scope of this FEA study.

In Chapter 3, it was found that the *strain rate* phenomenon will increase the strength of the material while static strain levels associated with failure are unaffected or possibly reduced depending on referenced source. For this thesis, strain rate effects are assumed to have a negligible impact on strain levels in accordance with (ASCE, 2010), implying that the overall inelastic material capacity has been underestimated by neglecting these effects.

Excluding *strain rate* effects is therefore a conservative approach considering that more plastic deformation will be generated and that the failure criteria established to define the pipe rack's inelastic capacity within this numerical study are based on allowable plastic strain levels and allowable deflections.

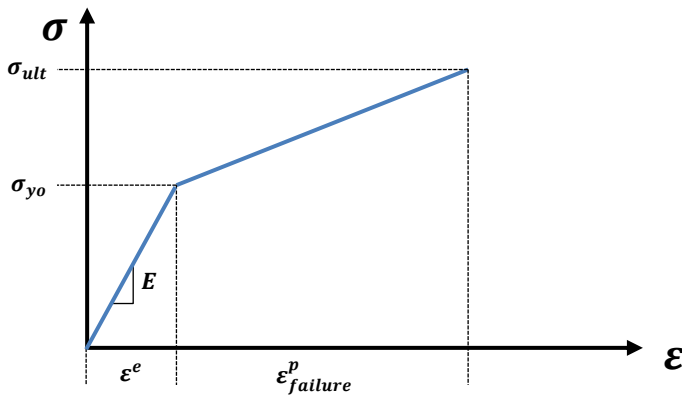


Figure 5-9 Bilinear material model assigned to rack members in FEA study.

| Density [kg/m ³] | Young's Modulus, E [MPa] | Poisson's Ratio | Yield Stress, σ_{y0} [MPa] | Ultimate Stress, σ_{ult} [MPa] | Max. allowable plastic strain, $\epsilon_{failure}^p$ [%] |
|---------------------------------|-------------------------------|-----------------|--------------------------------------|--|--|
| 7833.334 | 205.0E+3 | 0.3 | 355 | 510 | 15.3 |

Table 5-5 Specification of material model and material properties associated with rack members.

Reference is made to Section A.4 of Appendix A for description of the material properties assigned to pipe lines based on their associated material codes provided in Table 5-2.

5.7 Basic Load Cases

The basic load cases considered in this study of an accidental explosion event is documented in Section A.5 of Appendix A. Load cases are defined by gravity loads and blast from different directions. Gravity type loads accounted for are defined by self-weight of the rack members, pipe members and weight of pipe content.

As explained in Chapter 2, the number of possible angles and directions defining how a blast pulse might interact with a structure are infinite. Hence, idealizations were made and six basic load cases relating to different directions of blast-loading were included in the study. These six cases cover positive and negative loading in direction of the three main global axes defined in Section 5.1.

5.8 Blast Loads

The design blast-pulse considered in the original design and verification process of *Piperack01_P30_M50* is defined by Figure 5-10 and Table 5-6. It provides the basis for blast-load calculations performed in this study. In this case, the design peak-pressure p_1 correspond to a dynamic pressure to be converted into drag loads imposed on structural members in accordance with the conclusions drawn in Chapter 2.

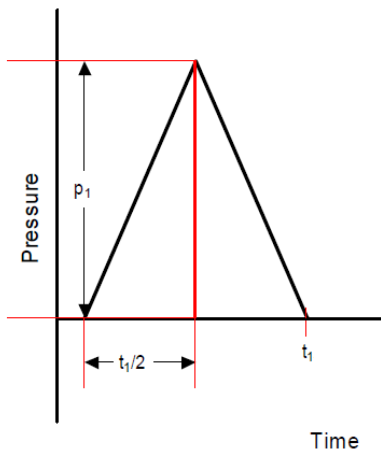


Figure 5-10 Design blast-pulse.

| Peak Design Pressure, p_1 [kPa] | Pulse Duration, t_1 [ms] |
|-----------------------------------|----------------------------|
| 20 | 50-200 |

Table 5-6 Design blast-pulse specification.

Three different load procedures were utilized within the study. The procedures are labeled *Load Procedure 1, 2 and 3* respectively and the differences between them are explained below. Reference is made to Section A.8 of Appendix A for detailed documentation of the different load procedures with respect to associated blast-loads calculations and load application procedures. The specific load procedure implemented for each analysis is summarized in Section A.10 of Appendix A.

All load procedures defined below are consistent in defining the segments of individual members that are exposed to blast in different directions and thus shall be assigned loading. The common approach adopted within the study is that all members which axial direction is not aligned with the direction of the blast shall be assigned loading.

Load Procedure 1

Uniformly distributed drag loads were calculated for the rack members and pipe lines utilizing conventional methods for wind loads in accordance with the conclusions drawn in Chapter 2. However, shielding effects were not considered in this procedure. To account for the drag loads acting on the piping configuration in analyses of FE model B, a simplified but yet rigorous approach was adopted where point loads transferred to rack members via the exact location of the attached pipe support were calculated. The main objective of Analysis A.1 is to confirm the validity of this simplified calculation approach.

Load Procedure 2

Blast loads were calculated according to *Load Procedure 1* with the single exception that the uniformly distributed loads derived for each specific rack member or pipe line account for shielding effects if applicable. This procedure is considered to reflect the true blast load scenario with a high level of accuracy. All full nonlinear analyses are based on this procedure and are therefore assumed to provide the true response of the pipe rack structure subjected to blast.

Load Procedure 3

Blast loads imposed on rack members were calculated according to *Load Procedure 2*. However, blast loads transferred from the piping configuration were calculated according to a more simplified procedure that would make the blast verification procedure less rigorous and more efficient. Instead of transferring point loads at the exact location of a pipe support, this approach involves calculating a distributed load in the axial direction of horizontal rack members supporting an idealized piping layout.

5.9 Scope of Work

Analysis A.1

Analysis A.1 aims to determine how the pipe line masses and blast-loads acting on the pipe line configuration is distributed among the pipe supports attached to the rack configuration. The objective is to evaluate the accuracy of the preferred, simplified calculation procedures documented in Appendix A by comparison of the calculated values and the generated FE results. The conclusions drawn in association with Analysis A.1 will govern how to implicitly account for the pipe lines in the following analyses of the rack structure in FE model B with respect to contribution in mass and blast loading.

Analysis B.1

The purpose of Analysis B.1 is to evaluate the static response of the rack structure considering blast loading in all applicable directions as defined by the basic load cases. Based on the observed stress

response, conclusions on a set of governing directions of blast load will be drawn. Four out of the six global load directions initially considered according to Section 5.7 shall be excluded from following analyses, reducing the load case scope to only one of the three main blast-directions, i.e. transverse, longitudinal or vertical.

Analysis B.2

The main objective of Analysis B.2 is to derive the input parameters y_{el} and R_M for calculations of a limiting blast pressure according to the proposed method. Both *Load Procedure 2* and *Load Procedure 3* will be implemented and compared based on the limiting pressure they ultimately generate via the proposed method. In addition, a desirable outcome is to conclude on a single most critical direction of blast-load and thus further reduce the load case scope in the following full nonlinear analyses.

Analysis B.3

The objective of Analysis B.3 is simply to derive the input parameter T_n for implementation into the conventional method and the proposed method.

Analysis B.4

Analysis B.4 aims to achieve one of the main objectives of this thesis, i.e. conclude on the accuracy of the conventional method and its application of the *Linear-elastic Biggs method* through evaluation of the dynamic response of *Piperack01_P30_M50* when subjected to the design blast-pulse.

Analysis B.5

The purpose of Analysis B.5 is to reveal the accuracy of the proposed method and its application of the *Elasto-plastic Biggs method* with respect to its ability to estimate the inelastic capacity of the pipe rack. The dynamic response of *Piperack01_P30_M50* subjected to a blast-pulse characterized by the limiting blast pressure derived according to the proposed method is studied in this analysis.

Analysis B.6

Analysis B.6 aims to answer the most central question asked within this thesis, i.e. what is the full inelastic capacity of a pipe rack configuration exposed to an accidental explosion event. The answer is derived by determining the peak blast-pressure and thus the magnitude of the pulse excitation which generates a response where failure criteria defined in Section 5.5 are exceeded. Results from Analysis B.6 will therefore reveal how much unutilized capacity a pipe rack configuration designed according to the conventional method possess.

6 Results and Conclusions

This chapter contains results obtained from the FEA study and the verification procedures evaluated within this thesis. Conclusions drawn in association with the presented results are also documented herein. Due to the internal dependencies between analyses outlined by Table 5-1, conclusions are presented within the same subsection as the associated result and in accordance with the sequential order defined in Chapter 5. A complete documentation of the pre-processing data governing results presented in this chapter is provided by Chapter 5 and referenced appendices.

6.1 Analysis A.1

Table 6-1 shows the distribution of pipe configuration mass over each of the internal supports attached to the pipe rack. Results from the preferred simplified approach are compared to results obtained from FEA. Masses from Analysis A.1 were calculated based on the reaction forces obtained in post-processing of a FE simulation containing gravity loading only. Vertical reactions forces at all internal supports were converted to mass by use of a gravity constant of 9.81 m/s^2 . Reference is made to Appendix A for complete documentation of pre-processing data governing analysis A.1 and the simplified procedure of calculating mass contribution. Both procedures account for the mass of the pipe line section itself and the fluid content within.

| Pipe Line | Pipe Support | Simplified Calculations m_{ps} [kt] | Analysis A.1 Results m_{ps} [kt] |
|-------------------|--------------|--|--|
| 43057 | 5016 | 6.12E-04 | 7.04E-04 |
| | 5015 | 5.85E-04 | 4.62E-04 |
| | 5013 | 7.54E-04 | 8.08E-04 |
| 43127 | 5016 | 6.95E-05 | 7.11E-05 |
| | 5015 | 7.81E-05 | 8.31E-05 |
| | 5014 | 7.81E-05 | 6.11E-05 |
| | 5013 | 1.11E-04 | 1.18E-04 |
| 20009 | 5015 | 2.65E-04 | 2.69E-04 |
| | 5013 | 2.80E-04 | 2.88E-04 |
| 41009P/ 41001P | 5008 | 1.70E-04 | 1.73E-04 (41009P) / 1.25E-04 (41001P) |
| | 5007 | 1.97E-04 | 1.56E-04 (41009P) / 1.71E-04 (41001P) |
| | 5006 | 2.95E-04 | 3.19E-04 (41009P) / 3.15E-04 (41001P) |
| 43119 | 5008 | 2.14E-04 | 3.69E-04 |
| | 5007 | 1.20E-04 | 1.97E-06 |

| | | | |
|---|------|-----------------|-----------------|
| | 5006 | 1.20E-04 | 1.51E-04 |
| | 5005 | 1.20E-04 | 1.11E-04 |
| 50023 | 5008 | 9.87E-05 | 9.67E-05 |
| | 5007 | 1.13E-04 | 1.16E-04 |
| | 5006 | 1.13E-04 | 1.12E-04 |
| | 5005 | 1.13E-04 | 1.13E-04 |
| 50010 | 5008 | 4.61E-05 | 4.03E-05 |
| | 5007 | 6.76E-05 | 7.45E-05 |
| | 5006 | 6.76E-05 | 6.55E-05 |
| | 5005 | 6.76E-05 | 6.79E-05 |
| Sum of masses = $\sum m_{ps}$ | | 5.41E-03 | 5.44E-03 |

Table 6-1 Distribution of pipe configuration mass over internal pipe supports.

Table 6-2 shows the distribution of forces imposed on rack members attached to internal pipe supports due to blast-loading acting on the pipe line configuration. The forces documented in Table 6-2 relate to blast-load application in global +X direction. FEA output shown below comprise of reaction forces registered in all global directions from a FE simulation containing blast-loading only, i.e. no gravity loading. Reaction forces in global X or 1-direction, *RF1*, represent the true force contribution in the direction of applied loading, to be compared to the forces calculated by the simplified procedures denoted *PL*. Reference is made to Section A.8 in Appendix A for documentation on these simplified loads calculated according to *Load Procedure 1*.

| Pipe Line | Pipe Support | Simplified Calculations | Analysis A.1 Results | | |
|-------------------|--------------|-------------------------|-----------------------------------|---------------------------|---|
| | | PL [kN] | RF1 [kN] | RF2 [kN] | RF3 [kN] |
| 43057 | 5016 | 0 | 0 | 0 | -0.2 |
| | 5015 | 45.9 | -50.5 | 0 | -2.0E-03 |
| | 5013 | 40.5 | -43.7 | 0 | 0.1 |
| 43127 | 5016 | 0 | 0 | 0 | -0.1 |
| | 5015 | 26.0 | -28.5 | 0 | 1.4E-02 |
| | 5014 | 0 | 0 | 0 | 2.8E-02 |
| | 5013 | 24.2 | -28.3 | 6.8 | -0.1 |
| 20009 | 5015 | 22.6 | -31.7 | 0 | 1.7 |
| | 5013 | 35.6 | -37.0 | 0 | -0.4 |
| 41009P/ 41001P | 5008 | 10.4 | -10.6 (41009P)/ -7.7 (41001P) | 0 (41009P)/ 0 (41001P) | 1.2E-17 (41009P)/ 7.7E-18 (41001P) |
| | 5007 | 12.1 | -9.6 (41009P)/ -10.5 (41001P) | 0 (41009P)/ 0 (41001P) | -3.0E-17 (41009P)/ -2.0E-17 (41001P) |
| | 5006 | 18.1 | -19.5 (41009P)/ -19.3 (41001P) | 0 (41009P)/ 0 (41001P) | 2.0E-17 (41009P)/ 1.3E-17 (41001P) |
| 43119 | 5008 | 11.9 | -12.4 | 0.000 | -1.4 |
| | 5007 | 9.3 | -8.1 | 0 | 0.7 |
| | 5006 | 9.3 | -9.6 | 0.07 | -0.2 |
| | 5005 | 9.3 | -9.2 | 0 | 0.1 |

| | | | | | |
|-----------------------------|------|--------------|---------------|---|----------|
| 50023 | 5008 | 16.5 | -14.5 | 0 | -2.9E-15 |
| | 5007 | 0 | 0 | 0 | 8.4E-15 |
| | 5006 | 24.1 | -26.8 | 0 | -1.0E-14 |
| | 5005 | 0 | 0 | 0 | 8.1E-15 |
| 50010 | 5008 | 6.3 | -5.5 | 0 | -3.3E-18 |
| | 5007 | 9.3 | -10.2 | 0 | 8.2E-18 |
| | 5006 | 9.3 | -9.0 | 0 | -7.4E-18 |
| | 5005 | 9.3 | -9.3 | 0 | 3.7E-18 |
| ∑ Forces in global X | | 390.6 | -411.5 | | |

Table 6-2 Distribution of forces over internal pipe supports due to transverse blast load acting on piping configuration.

Figure 6-1 shows the overall von Mises stress distribution and deformed piping configuration for a FE simulation containing blast load in global +X direction and gravity loading combined. The most critical region is found in vicinity of support 5006 attached to pipe line 50023 with a corresponding peak stress level of approximately 70 MPa.

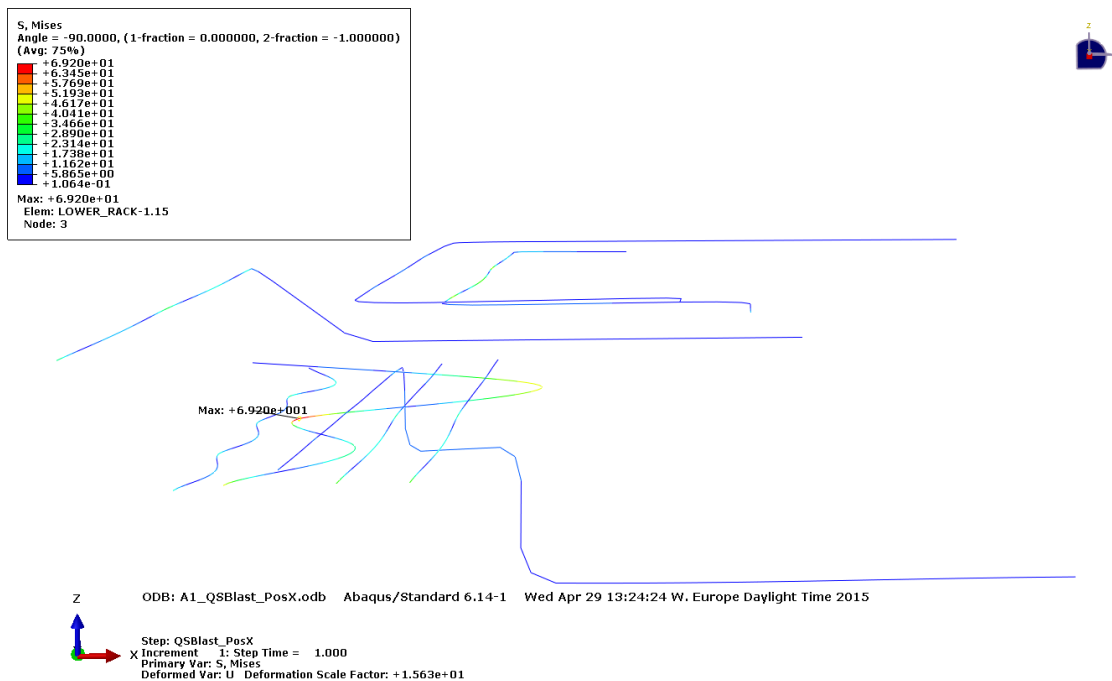


Figure 6-1 Von Mises stress plot of pipe line configuration subjected to gravity loading and blast in global +X direction.

Table 6-1 shows that the simplified mass calculations correspond well to the results generated from FEA. 63 % of the simplified calculations are within a range of $\pm 10\%$ of the FEA result, which accounts for a very precise layout in terms of angles of inclination and bending of the pipe lines. Only two simplified calculations deviate more than 30% from FEA results, where support 5007 of

pipe line 43119 is the most extreme by far. This error in approximation has to do with the complex geometry of 43119 in vicinity of support 5007, where overturning moments will cause uplift not accounted for by the simplified calculations which are conservative in this case. The total mass accounted for by the simplified calculations is only a magnitude of approximately 30 kg less, corresponding to a total deviation of 0.5% from the FEA generated mass.

Table 6-2 shows that the simplified blast load calculations *PL* slightly underestimate the total load impact in general. Deviations from FEA results given by *RF1* are small however, and the least conservative value is found at support 5015 of pipe line 20009 where the simplified calculation accounts for 71 % of the FEA reaction force. This specific support is located in the vicinity of the curved and more geometrically complex segment of 20009. Only two supports account for less than 90% of the load generated through FEA.

It is seen that reaction forces in global Y and Z direction (*RF2* and *RF3*) generated from FEA are small in general. Simplified calculations assume these loads to be zero. Based on the values documented in Table 6-2, this assumption is considered valid. The only significant force not accounted for by the simplified approach is the reaction in global Y direction found at support 5013 of pipe line 43127. Its magnitude is approximately 24% of the reaction at the same support in global +X direction generated by FEA.

The total amount of force in global +X direction accounted for by the simplified calculations is only a magnitude of approximately 21 kN less, corresponding to a total deviation of 5% from the FEA generated forces. It is therefore concluded that the simplified approach is sufficiently accurate. However, conservatism could be added by modifying the tributary length calculations documented in Section A.6 of Appendix A so that the end of a curved pipe segment is used to define exposed pipe length contrary to the center point. This modification is shown in Figure 6-2.

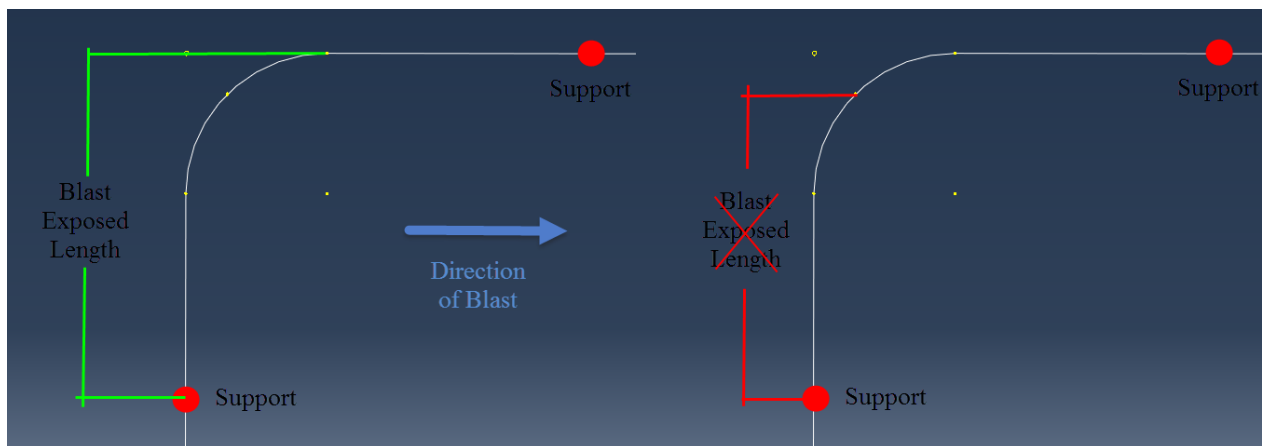


Figure 6-2 More conservative practice (left) and less conservative practice (right) for calculating pipe length exposed to blast.

Overall, the preferred simplified approach of accounting for the pipe line configuration through calculations of mass and blast-load distribution was shown to prevail with good accuracy. It is

concluded that the utilized methods documented in Appendix A are well suited for application to pipe rack structures and that masses and forces documented in Appendix A will be applied in further analyses.

The stress plot shown in Figure 6-1 does not, and is not intended to, verify the structural integrity of the pipe line configuration. Its purpose is to demonstrate the behavior of GRE material pipe lines under static blast loading less severe than dimensioning blast loads for piping. The low elastic stiffness of GRE pipe lines is illustrated in Figure 6-1 by the large displacements associated with pipe line 50023 generating a peak stress level close to the idealized GRE yield stress of 85 MPa.

AKSO piping department does not verify GRE pipe lines for blast and assume that they will fail in a brittle mode. This assumed behavior is confirmed by Figure 6-1 considering the significant flexural response obtained for this anisotropic material pipe line. However, brittle failure during blast should be avoided to prevent hazardous effects from flying objects such as pipe fragments. A bursting pipe would also impose forces on other structural elements in its vicinity and possibly cause severe local damage. It is therefore recommended that the design philosophy with respect to GRE pipe lines is evaluated further by the AKSO piping department and safety consultants.

6.2 Analysis B.1

Figures 6-3 to 6-8 show the overall von Mises stress distribution in the rack structure obtained from the static analysis labeled B.1. Gravity loading and blast in all applicable directions were considered in the six FE simulations documented below. Applied blast loads were derived according to *Load Procedure 1*. Reference is made to Appendix A for complete documentation of pre-processing data governing analysis B.1.

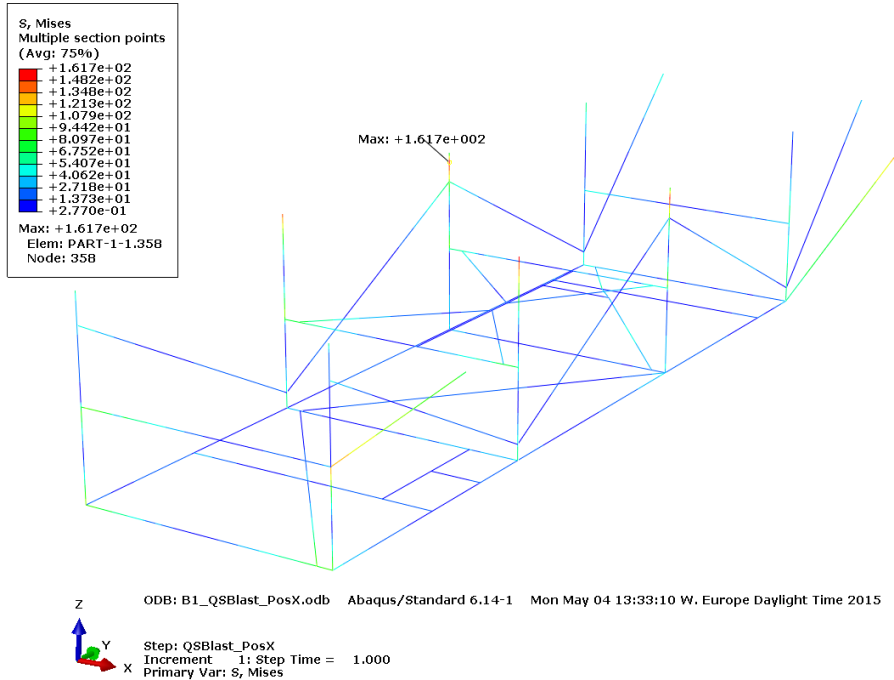


Figure 6-3 Von Mises stress plot of rack structure subjected to gravity loading and blast in global +X direction.

Figure 6-3 show that a peak stress of approximately 162 MPa is registered and that the most critical stress regions are found in vicinity of connections of vertical beam elements and the deck structure.

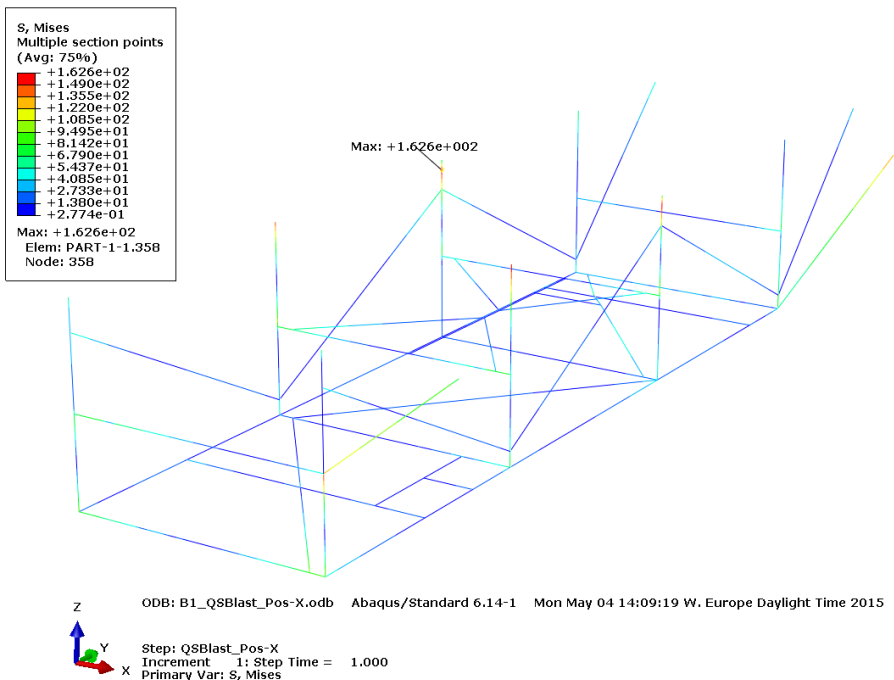


Figure 6-4 Von Mises stress plot of rack structure subjected to gravity loading and blast in global -X direction.

Figure 6-4 show that a peak stress of approximately 163 MPa is registered and that the most critical stress regions are found in vicinity of connections of vertical beam elements and the deck structure.

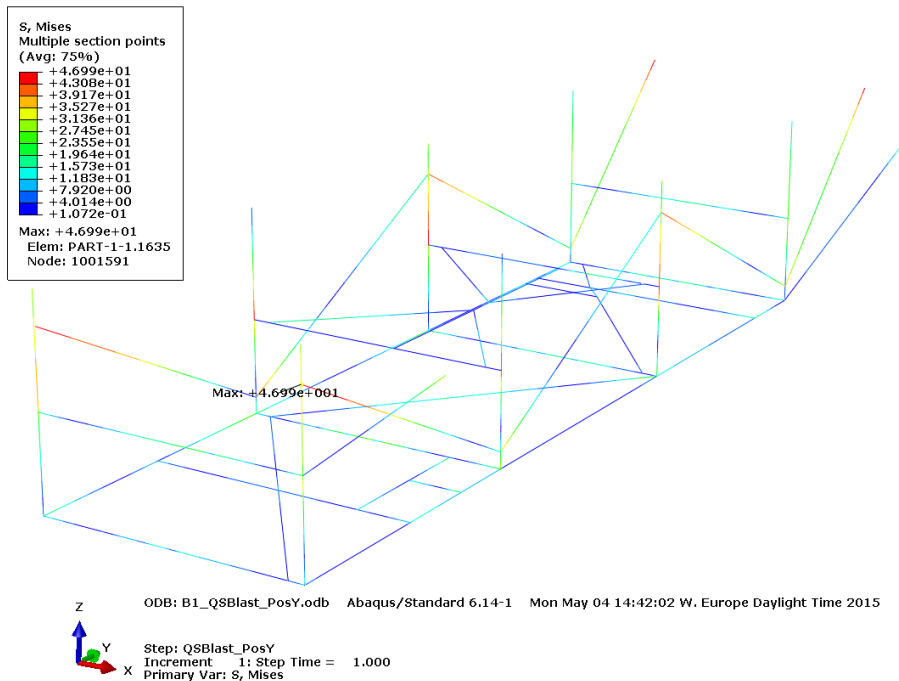


Figure 6-5 Von Mises stress plot of rack structure subjected to gravity loading and blast in global +Y direction.

Figure 6-5 show that a peak stress of approximately 47 MPa is registered and that the most critical stress regions are found at the ends of braces and at joints connecting vertical and horizontal beams.

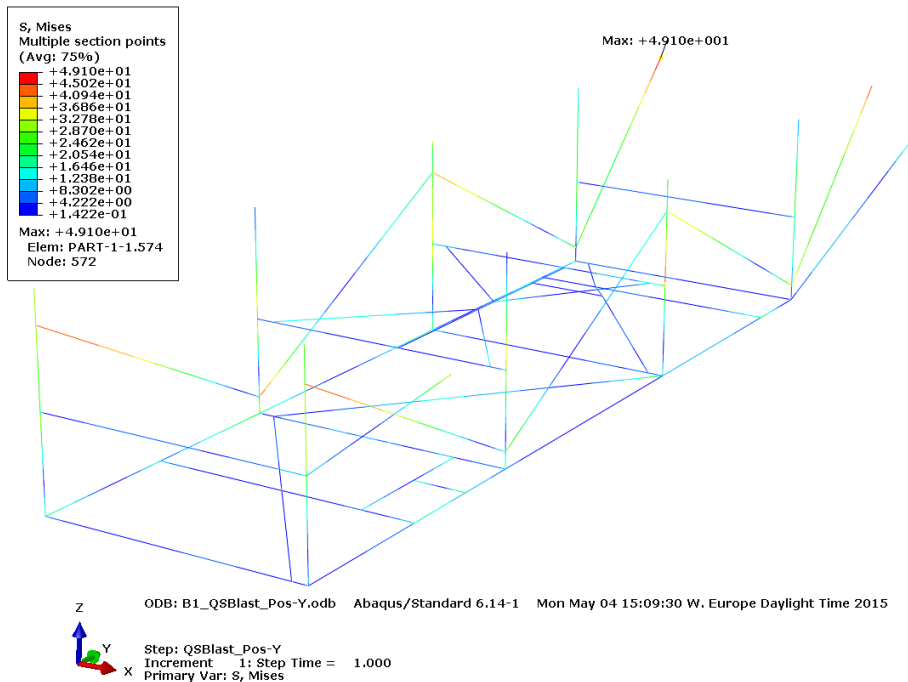


Figure 6-6 Von Mises stress plot of rack structure subjected to gravity loading and blast in global -Y direction.

Figure 6-6 show that a peak stress of approximately 49 MPa is registered and that the most critical stress regions are found at the ends of braces and at joints connecting vertical and horizontal beams.

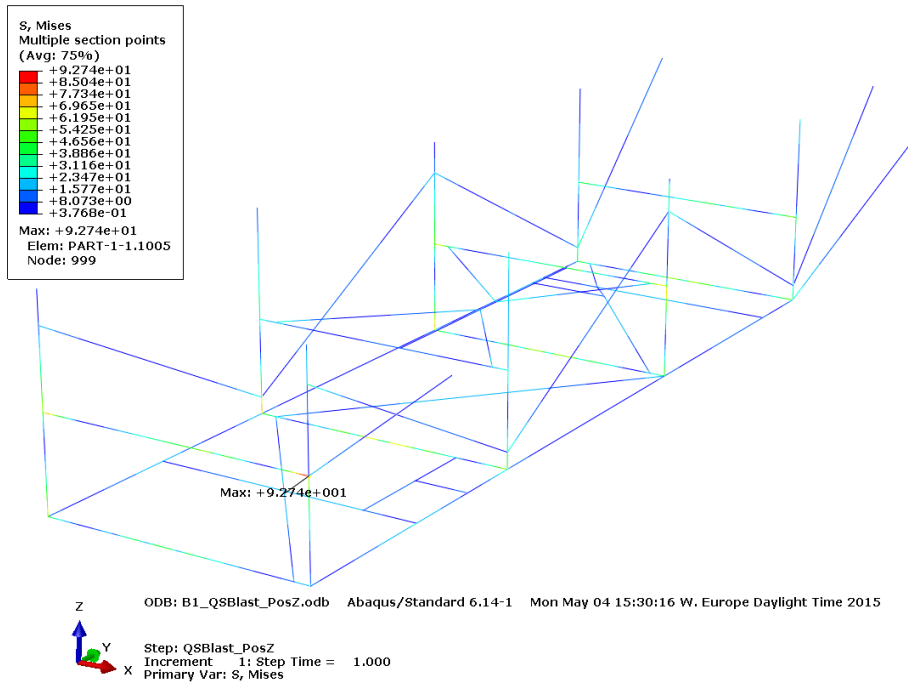


Figure 6-7 Von Mises stress plot of rack structure subjected to gravity loading and blast in global +Z direction.

Figure 6-7 show that a peak stress of approximately 93 MPa is registered and that the most critical stress regions are found in vicinity of rack member joints.

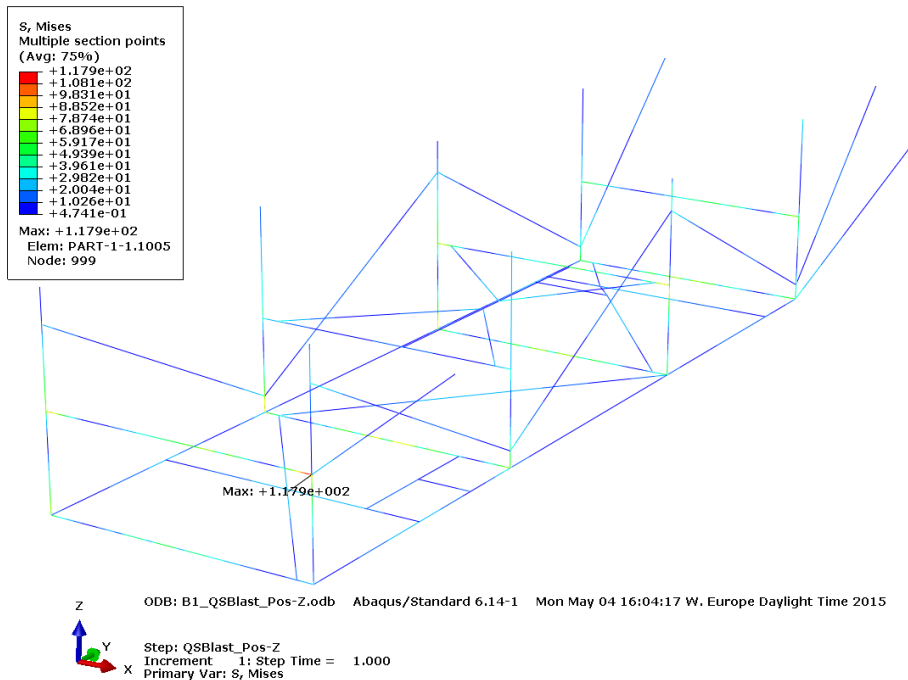


Figure 6-8 Von Mises stress plot of rack structure subjected to gravity loading and blast in global -Z direction.

Figure 6-8 show that a peak stress of approximately 118 MPa is registered and that the most critical stress regions are found in vicinity of rack member joints.

Figures 6-3 to 6-8 show that blast loading in transverse direction, i.e. global $\pm X$ direction, generate the highest overall stress levels in the rack structure. In general, the response is seen to be relatively symmetric as the peak stress values and critical regions correspond well between positive and negative loading along the same global axis. Vertical blast loading is the exception as body forces due to gravity load will magnify the total load effect in global $-Z$ direction while counteract the blast load in global $+Z$ direction.

Based on the observed stress distributions from analysis B.1, it is concluded that transverse blast loading is most likely to generate the most severe response. Compared to loading in longitudinal direction, generated peak stresses are more than three times higher. Loading in $-Z$ direction however was found to generate peak stresses up to approximately 73% of the peak values obtained for blast in transverse direction. It could be argued wheatear loading in $-Z$ direction is realistic for this specific case, considering that the distance between *Piperack01_P30_M50* and the above deck structure is small and that this thesis examines global blast effects generated by a flow of dynamic pressure engulfing the entire pipe rack at once. Based on these arguments, blast in $-Z$ direction was excluded from the set of governing directions to be evaluated further in the study, comprising of global $\pm X$ directions only.

6.3 Analysis B.2

A total of four static pushover analyses were conducted within the scope of Analysis B.2, considering two different blast-load application procedures and two directions of blast load under otherwise identical premises as described Appendix A. Table 6-3 below illustrate these differences and provide a labeling system that is referenced by the tables and figures below presenting the results from each individual analysis.

| Analysis Label | Governing Load Procedure | Direction of Blast Load |
|----------------|--------------------------|-------------------------|
| B.2_1 | <i>Load Procedure 2</i> | Global +X direction |
| B.2_2 | <i>Load Procedure 2</i> | Global -X direction |
| B.2_3 | <i>Load Procedure 3</i> | Global +X direction |
| B.2_4 | <i>Load Procedure 3</i> | Global -X direction |

Table 6-3 Analysis B.2 | Scope and labeling system.

Table 6-4 illustrates the difference between the two evaluated load procedures with respect to how blast loading acting on the pipe line configuration was calculated and assigned to applicable rack members. Both procedures are described in detail in Section A.8 of Appendix A where the naming convention used in Table 6-4 is explained.

| Frame Section | Lower Rack Level | | Upper Rack Level | |
|---------------|------------------|------------------|------------------|------------------|
| | Load Procedure 2 | Load Procedure 3 | Load Procedure 2 | Load Procedure 3 |
| | $\sum PL$ [MN] | P_{nL} [MN] | $\sum PL$ [MN] | P_{nU} [MN] |
| 1 | 0.0309 | 0.0060 | 0 | 0 |
| 2 | 0.0261 | 0.0121 | 0.0586 | 0.0251 |

| | | | | |
|-----------------------------------|--------------|---------------|---------------|---------------|
| 3 | 0.0441 | 0.0121 | 0.0000 | 0 |
| 4 | 0.0140 | 0.0046 | 0.0680 | 0.0126 |
| Σ Forces | 0.115 | 0.0348 | 0.1265 | 0.0377 |

Table 6-4 Comparison of blast-loads transferred via piping configuration according to Load Procedure 2 and Load Procedure 3.

The columns relating to *Load Procedure 2* in Table 6-4 contain the sum of all point loads applied for blast in global +X direction to the specific horizontal rack member defined by referenced frame section and rack level. Hence, the two procedures may be compared based on the total amount of force applied to that member given by either ΣPL or P_{nL}/P_{nU} . The total amount of force applied to the system is summarized by the values in the last row in Table 6-4.

For each of the analyses listed in Table 6-3, field variables defined below were documented for load increments prior to and immediately after appearance of initial yield, σ_{yo} . Values of interest, i.e. magnitudes of the field variables at the exact time of first yield, were obtained through linear interpolation. Post-processing data referenced herein are described below:

1. Overall maximum von Mises stress, σ_{max} .
2. Overall maximum global displacement in direction of blast load, $U1_{max}$. This output variable defines the input parameter y_{el} to be implemented in the *Elasto-plastic Biggs method*.
3. Total sum of reaction forces in direction of blast load, $\Sigma RF1$. This output variable defines the input parameter R_M to be implemented in the *Elasto-plastic Biggs method*.
4. Load amplitude at each documented time increment, governed by the linear amplitude curve implemented in Abaqus as described in Section A.10 of Appendix A.

| Analysis B.2_1 Results | | | | | | Interpolated Values at Initial Yield, σ_{yo} | | |
|----------------------------------|-----------------|-------------------|----------------------------------|-----------------|-------------------|---|-----------------|-------------------|
| Increment no. 13 < σ_{yo} | | | Increment no. 14 > σ_{yo} | | | | | |
| σ_{max} [MPa] | $U1_{max}$ [mm] | $\Sigma RF1$ [kN] | σ_{max} [MPa] | $U1_{max}$ [mm] | $\Sigma RF1$ [kN] | σ_{yo} [MPa] | $U1_{max}$ [mm] | $\Sigma RF1$ [kN] |
| 340.5 | 11.29 | -1652.10 | 366.7 | 12.16 | -1779.19 | 355.0 | 11.78 | -1722.44 |
| Load amplitude = | | 3.25 | Load amplitude = | | 3.5 | Load amplitude = | | 3.39 |

Table 6-5 FEA result from Analysis B.2_1 and interpolated values at initial yield.

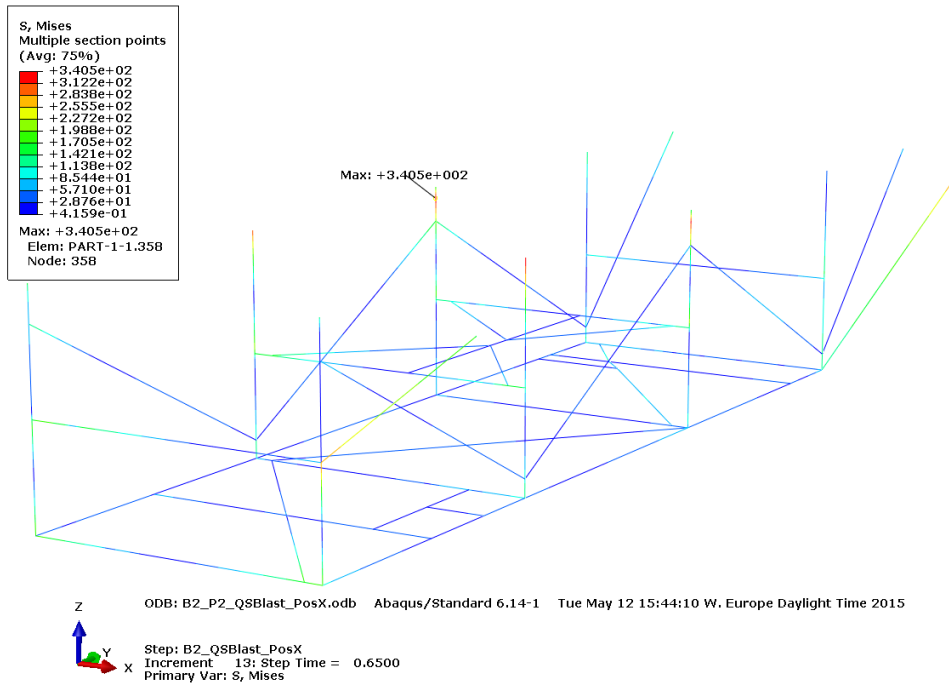


Figure 6-9 Von Mises stress plot from Analysis B.2_1 at increment prior to initial yield.

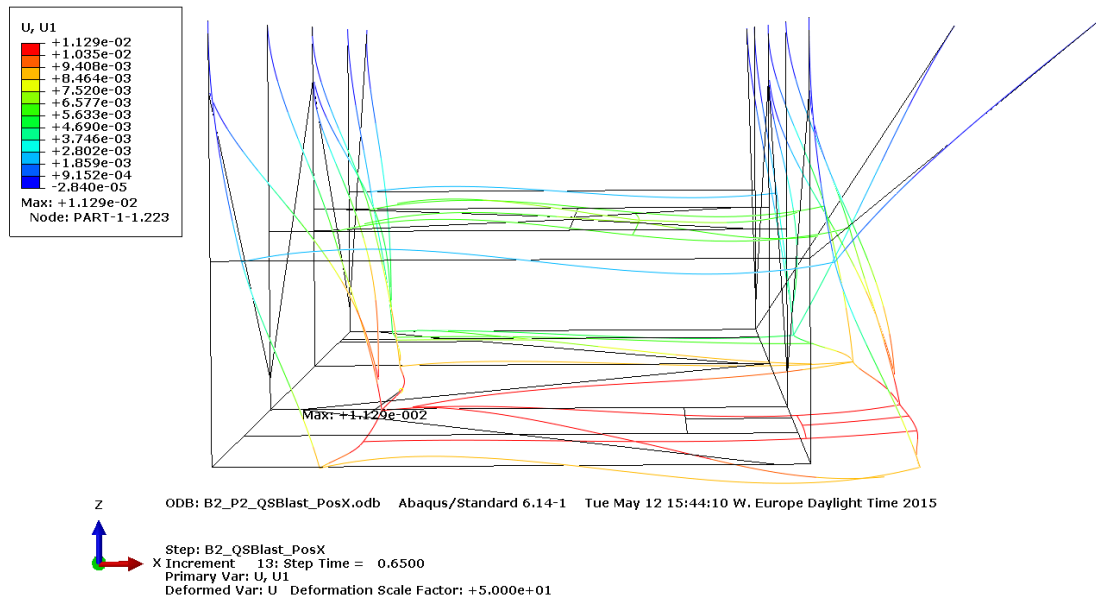


Figure 6-10 Global displacement plot from Analysis B.2_1 at increment prior to initial yield.

| Analysis B.2_2 Results | | | | | | Interpolated Values at Initial Yield, σ_{yo} | | |
|----------------------------------|--------------------|--------------------|----------------------------------|--------------------|--------------------|---|--------------------|--------------------|
| Increment no. 13 < σ_{yo} | | | Increment no. 14 > σ_{yo} | | | | | |
| σ_{max} [MPa] | $U1_{max}$ [mm] | $\sum RF1$ [kN] | σ_{max} [MPa] | $U1_{max}$ [mm] | $\sum RF1$ [kN] | σ_{yo} [MPa] | $U1_{max}$ [mm] | $\sum RF1$ [kN] |
| 339.5 | -11.30 | 1675.14 | 365.6 | -12.17 | 1804.00 | 355.0 | -11.82 | 1751.67 |
| Load amplitude = | | 3.25 | Load amplitude = | | 3.5 | Load amplitude = | | 3.40 |

Table 6-6 FEA result from Analysis B.2_2 and interpolated values at initial yield.

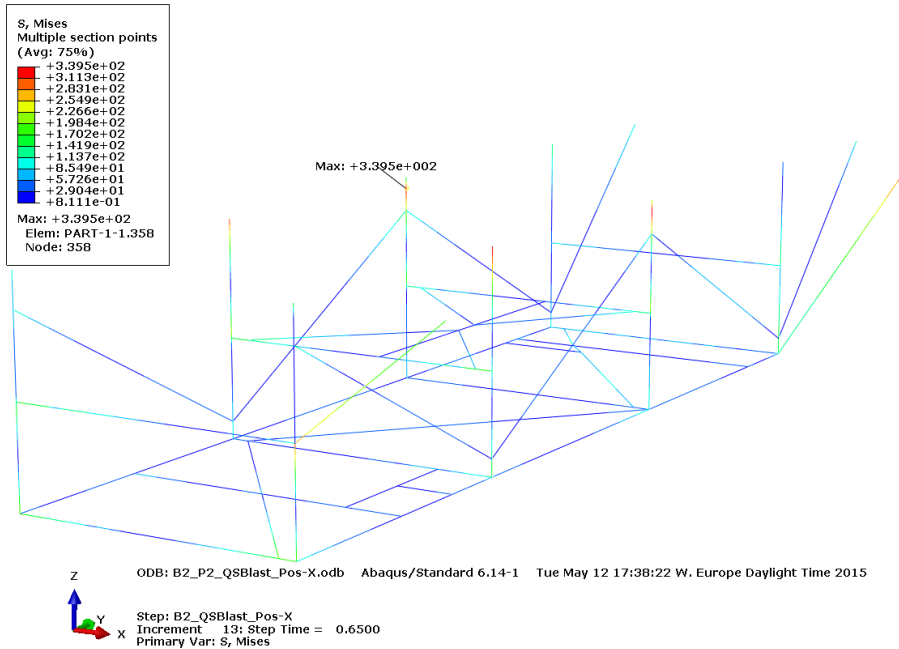


Figure 6-11 Von Mises stress plot from Analysis B.2_2 at increment prior to initial yield.

| Analysis B.2_3 Results | | | | | | Interpolated Values at Initial Yield, σ_{yo} | | |
|----------------------------------|-----------------|-----------------|----------------------------------|-----------------|-----------------|---|-----------------|-----------------|
| Increment no. 16 $< \sigma_{yo}$ | | | Increment no. 17 $> \sigma_{yo}$ | | | | | |
| σ_{max} [MPa] | $U1_{max}$ [mm] | $\sum RF1$ [kN] | σ_{max} [MPa] | $U1_{max}$ [mm] | $\sum RF1$ [kN] | σ_{yo} [MPa] | $U1_{max}$ [mm] | $\sum RF1$ [kN] |
| 335.3 | 9.95 | -1357.36 | 356.2 | 10.57 | -1442.19 | 355.0 | 10.53 | -1437.32 |
| Load amplitude = | | 4.0 | Load amplitude = | | 4.25 | Load amplitude = 4.24 | | |

Table 6-7 FEA result from Analysis B.2_3 and interpolated values at initial yield.

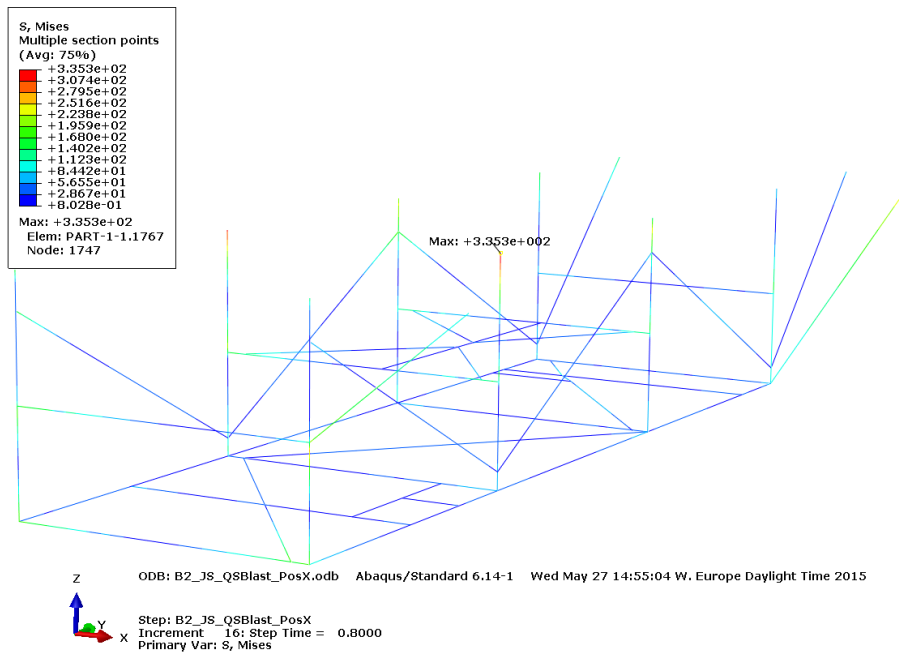


Figure 6-12 Von Mises stress plot from Analysis B.2_3 at increment prior to initial yield.

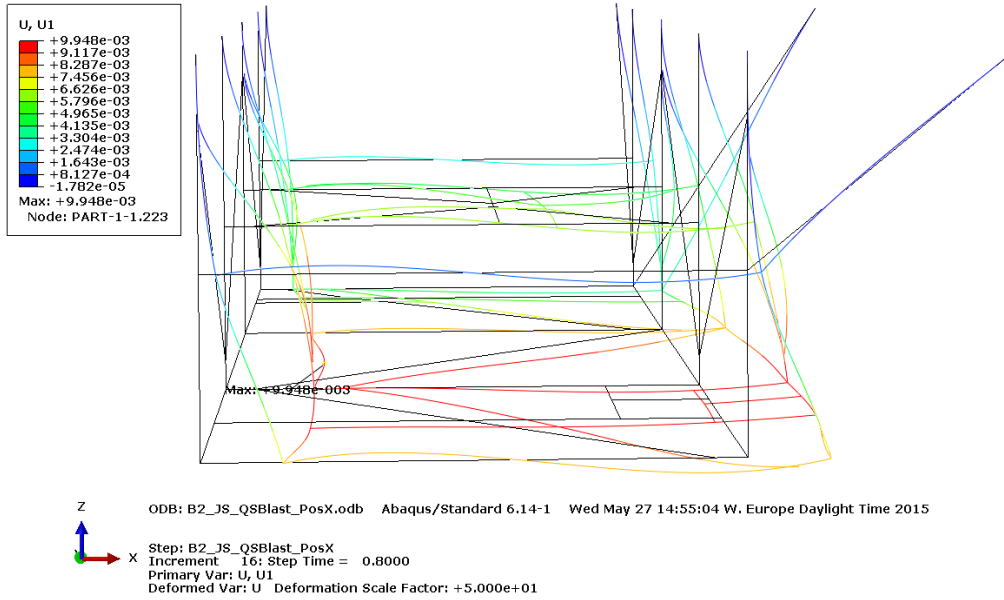


Figure 6-13 Global U1 displacement plot from Analysis B.2_3 at increment prior to initial yield.

| Analysis B.2_4 Results | | | | | | Interpolated Values at Initial Yield, σ_{yo} | | |
|----------------------------------|-----------------|-----------------|----------------------------------|-----------------|-----------------|---|-----------------|-----------------|
| Increment no. 16 $< \sigma_{yo}$ | | | Increment no. 17 $> \sigma_{yo}$ | | | | | |
| σ_{max} [MPa] | $U1_{max}$ [mm] | $\sum RF1$ [kN] | σ_{max} [MPa] | $U1_{max}$ [mm] | $\sum RF1$ [kN] | σ_{yo} [MPa] | $U1_{max}$ [mm] | $\sum RF1$ [kN] |
| 341.0 | -9.87 | 1388.92 | 362.3 | -10.48 | 1475.72 | 355.0 | -10.27 | 1445.97 |
| Load amplitude = | | 4.0 | Load amplitude = | | 4.25 | Load amplitude = | | 4.16 |

Table 6-8 FEA result from Analysis B.2_4 and interpolated values at initial yield.

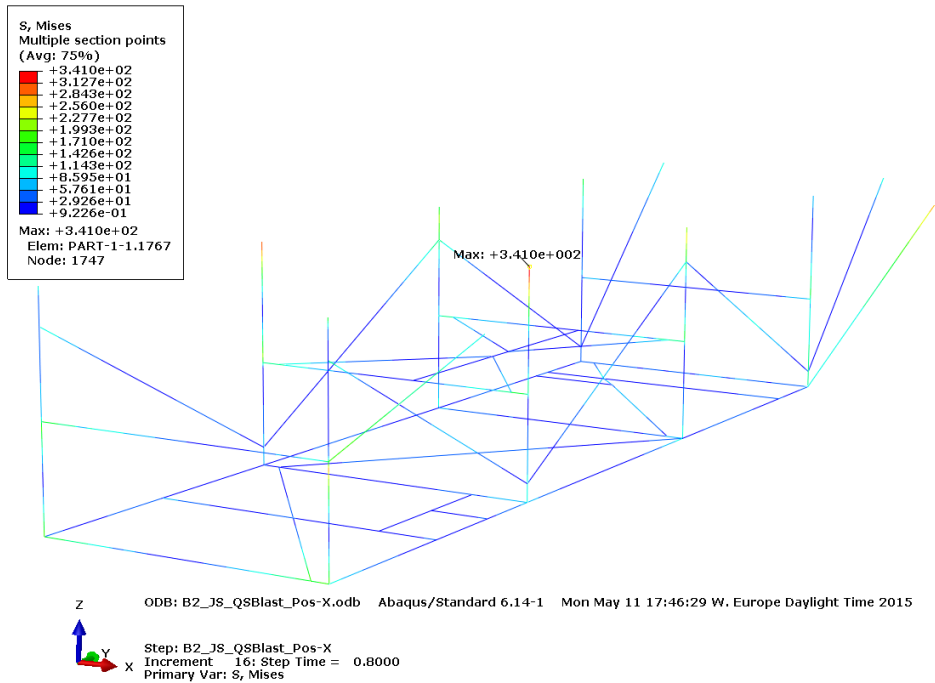


Figure 6-14 Von Mises stress plot from Analysis B.2_4 at increment prior to initial yield.

Field variables associated with a load amplitude of 1 are documented for Analysis B.2_1 in Table 6-9 below. This response is of interest for evaluation of the *Linear-elastic Biggs method* where it would be scaled with the applicable DAF to predict the overall maximum dynamic response. The result presented in Table 6-9 was calculated by scaling the values associated with time increment 13 in Table 6-5 by a factor of 1 over the load amplitude, i.e. $1/3.25$.

| Analysis B.2_1 Results | | | Interpolated Values at Load Amplitude of 1 | | |
|----------------------------------|-----------------|-----------------|--|-----------------|-----------------|
| Increment no. 13 < σ_{yo} | | | | | |
| σ_{max} [MPa] | $U1_{max}$ [mm] | $\sum RF1$ [kN] | σ_{max} [MPa] | $U1_{max}$ [mm] | $\sum RF1$ [kN] |
| 340.5 | 11.29 | -1652.10 | 104.8 | 3.47 | -529.98 |
| Load amplitude = | | 3.25 | Load amplitude = | | 1.0 |

Table 6-9 Results from Analysis B.2_1 and interpolated values at load amplitude of 1.

It is evident from Table 6-4 that *Load Procedure 3* generates transferred blast-loads significantly lower than those obtained through *Load Procedure 2*. For both upper and lower rack level members, *Load Procedure 3* account for approximately 30% of the total forces implemented via *Load Procedure 2*. Since *Load Procedure 2* is considered to reflect the true distribution of blast loads, it is concluded that the simplified procedure defined as *Load Procedure 3* is not suitable for application in a full nonlinear analysis aiming to capture the true response of the structural system. Hence, loads derived from *Load Procedure 2* were utilized in the following full nonlinear analyses within the study.

It is difficult to draw any conclusions regarding a most critical direction of transverse blast-load based on the results obtained from Analysis B.2. Response quantities are very similar when comparing $\pm X$ directions of blast loading applied according to the same governing load procedure. It could be argued that the positive X direction will be more critical for a more severe load scenario as the brace elements would be in compression under the first half-cycle of motion. If the braces were to buckle during the time of the applied loading, the transverse stiffness of the structural system would be reduced which could lead to larger overall peak deformations. Although it cannot be concluded that global +X direction is the most critical, it was chosen as the single direction to be considered further in the study in order to reduce the extent of the scope.

6.4 Analysis B.3

Table 6-10 and referenced figures document the 30 first natural modes of vibration and associated natural cyclic frequencies obtained from the Eigen frequency analysis labeled B.3. The natural periods are calculated according to Equation (3.6). Reference is made to Appendix A for complete documentation of pre-processing data governing Analysis B.3.

| Natural Mode of Vibration / Figure Reference | Characteristics of Mode Shape | Natural Cyclic Frequency f_n [hertz] | Natural Period T_n [ms] |
|--|--|--|---------------------------|
| 1 st Mode / Figure 6-16 (a) | Local displacements in longitudinal direction. | 21.666 | 46.155 |

| | | | |
|---|---|--------|--------|
| 2 nd Mode / Figure 6-15 | Global displacements in transverse direction. | 23.680 | 42.230 |
| 3 rd Mode / Figure 6-16 (b) | Local displacements in longitudinal direction. | 24.844 | 40.251 |
| 4 th Mode / Figure 6-17 (a) | Global displacements in longitudinal direction. | 33.160 | 30.157 |
| 5 th Mode / Figure 6-17 (b) | Local displacements in vertical direction. | 34.194 | 29.245 |
| 6 th Mode / Figure 6-18 (a) | Local displacements in vertical direction. | 35.021 | 28.554 |
| 7 th Mode / Figure 6-18 (b) | Global displacements in multiple directions. | 36.420 | 27.457 |
| 8 th Mode / Figure 6-19 (a) | Local displacements in vertical direction. | 36.750 | 27.211 |
| 9 th Mode / Figure 6-19 (b) | Local displacements in vertical direction. | 37.284 | 26.821 |
| 10 th Mode / Figure 6-20 (a) | Local displacements in multiple directions. | 38.219 | 26.165 |
| 11 th Mode / Figure 6-20 (b) | Local displacements in vertical direction. | 38.818 | 25.761 |
| 12 th Mode / Figure 6-21 (a) | Local displacements in multiple directions. | 39.336 | 25.422 |
| 13 th Mode / Figure 6-21 (b) | Global displacements in longitudinal direction. | 41.605 | 24.036 |
| 14 th Mode / Figure 6-22 (a) | Local displacements in longitudinal directions. | 45.605 | 21.927 |
| 15 th Mode / Figure 6-22 (b) | Local displacements in vertical directions. | 46.667 | 21.428 |
| 16 th Mode / Figure 6-23 (a) | Local displacements in longitudinal directions. | 48.400 | 20.661 |
| 17 th Mode / Figure 6-23 (b) | Global displacements in transverse direction. | 50.688 | 19.729 |
| 18 th Mode / Figure 6-24 (a) | Local displacements in multiple directions. | 56.827 | 17.597 |
| 19 th Mode / Figure 6-24 (b) | Local displacements in vertical directions. | 60.711 | 16.471 |
| 20 th Mode / Figure 6-25 (a) | Global displacements in multiple directions. | 62.181 | 16.082 |
| 21 st Mode / Figure 6-25 (b) | Global displacements in longitudinal direction. | 64.939 | 15.399 |
| 22 nd Mode / Figure 6-26 (a) | Global displacements in vertical direction. | 66.081 | 15.133 |
| 23 rd Mode / Figure 6-26 (b) | Local displacements in vertical directions. | 68.744 | 14.547 |
| 24 th Mode / Figure 6-27 (a) | Local displacements in multiple directions. | 70.184 | 14.248 |

| | | | |
|---|---|--------|--------|
| 25 th Mode / Figure 6-27 (b) | Global displacements in vertical direction. | 72.486 | 13.796 |
| 26 th Mode / Figure 6-28 (a) | Local displacements in vertical directions. | 73.693 | 13.570 |
| 27 th Mode / Figure 6-28 (b) | Global displacements in vertical direction. | 75.637 | 13.221 |
| 28 th Mode / Figure 6-29 (a) | Global displacements in transverse direction. | 78.405 | 12.754 |
| 29 th Mode / Figure 6-29 (b) | Global displacements in vertical direction. | 80.613 | 12.405 |
| 30 th Mode / Figure 6-30 | Global displacements in transverse direction. | 82.560 | 12.112 |

Table 6-10 Specification of the 30 first natural modes of vibration.

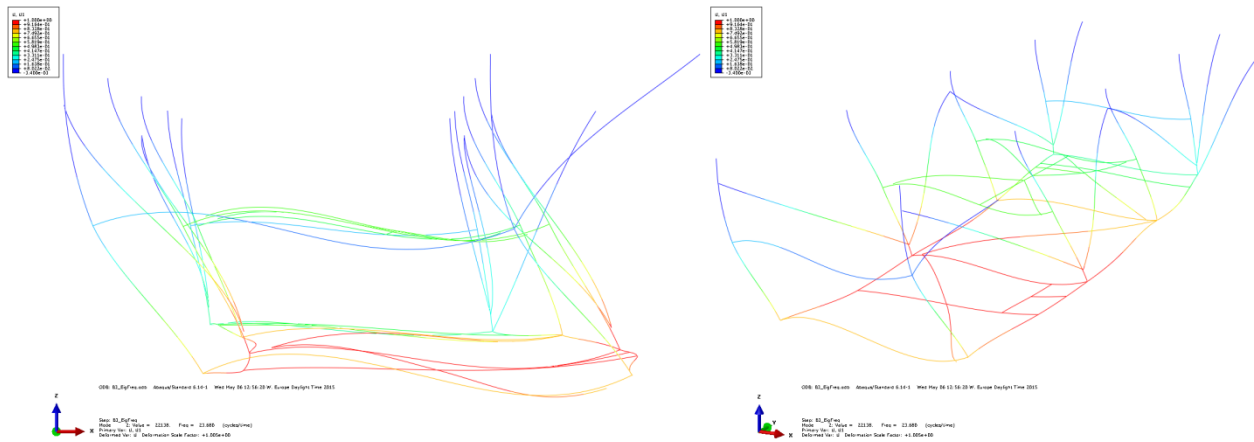


Figure 6-15 2nd natural mode of vibration.

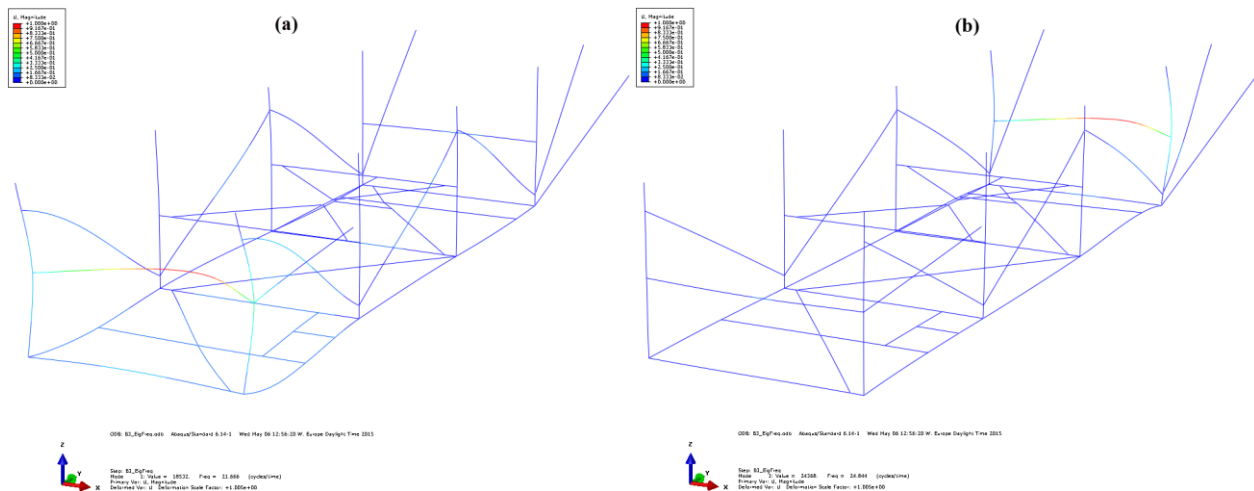


Figure 6-16 1st (a) and 3rd (b) natural mode of vibration.

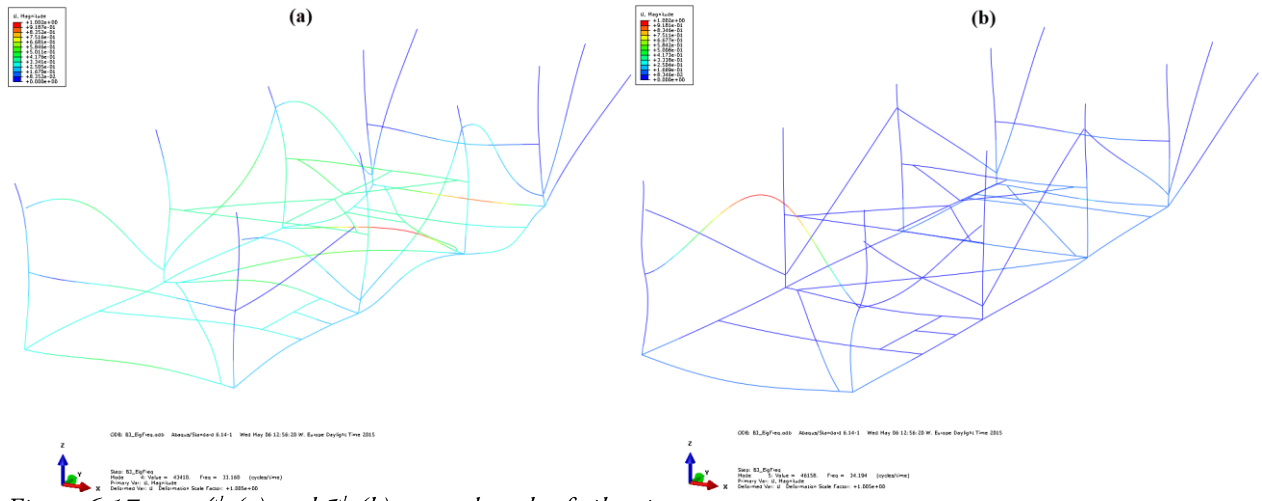


Figure 6-17 4th (a) and 5th (b) natural mode of vibration.

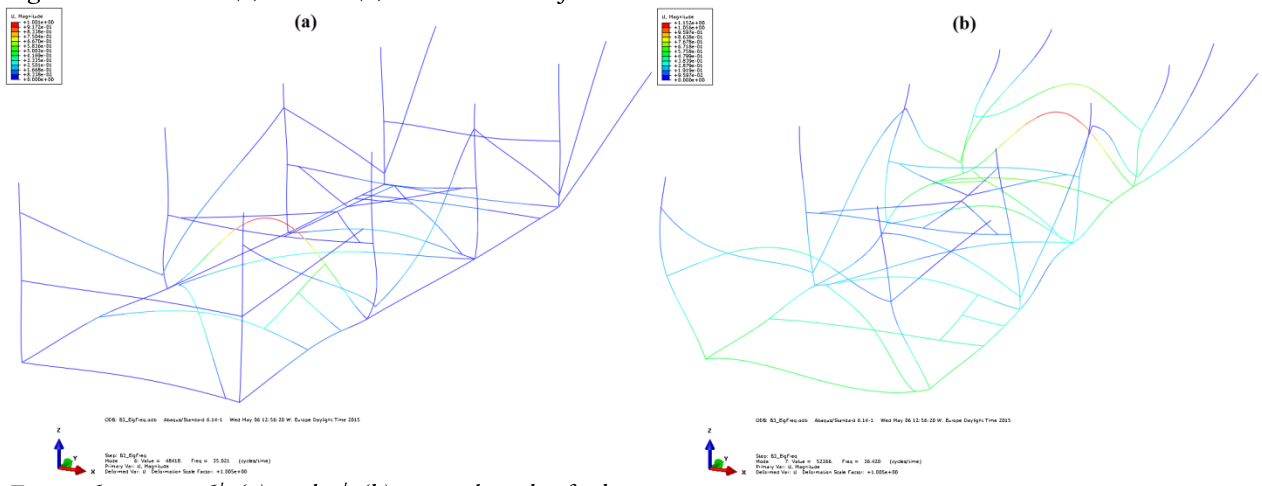


Figure 6-18 6th (a) and 7th (b) natural mode of vibration.

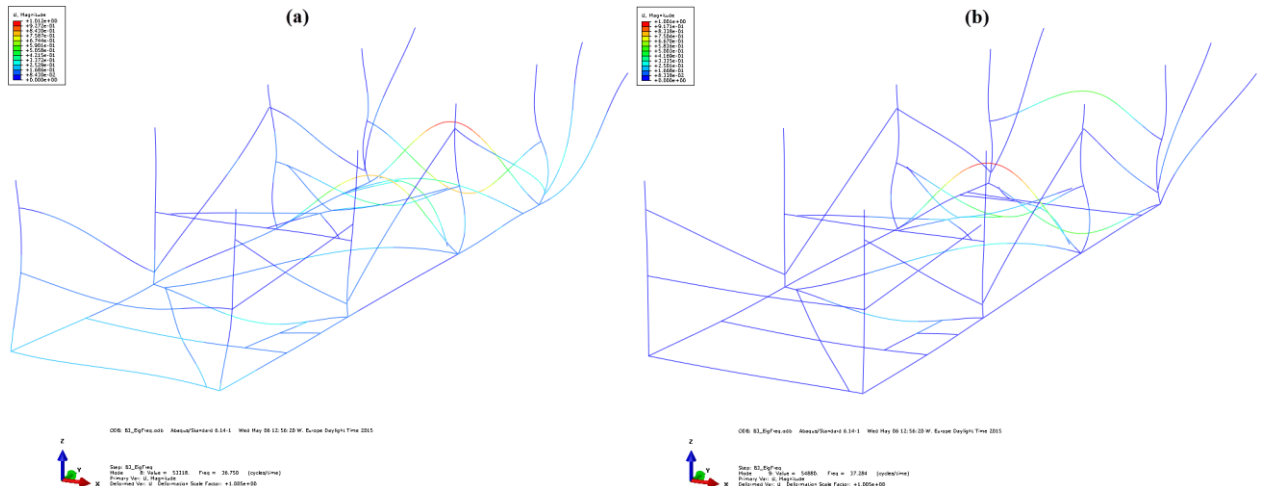


Figure 6-19 8th (a) and 9th (b) natural mode of vibration.

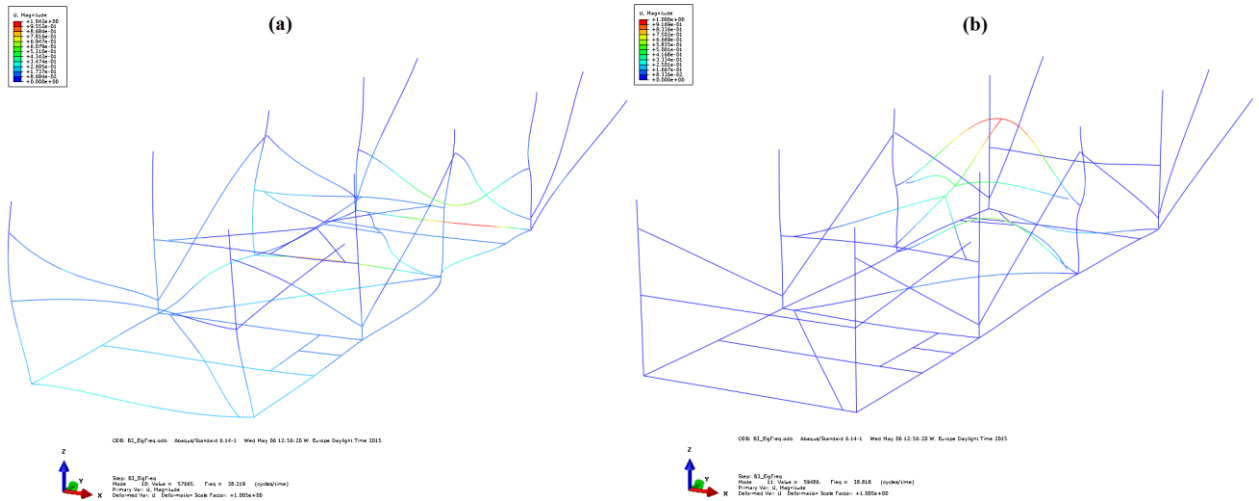


Figure 6-20 10th (a) and 11th (b) natural mode of vibration.

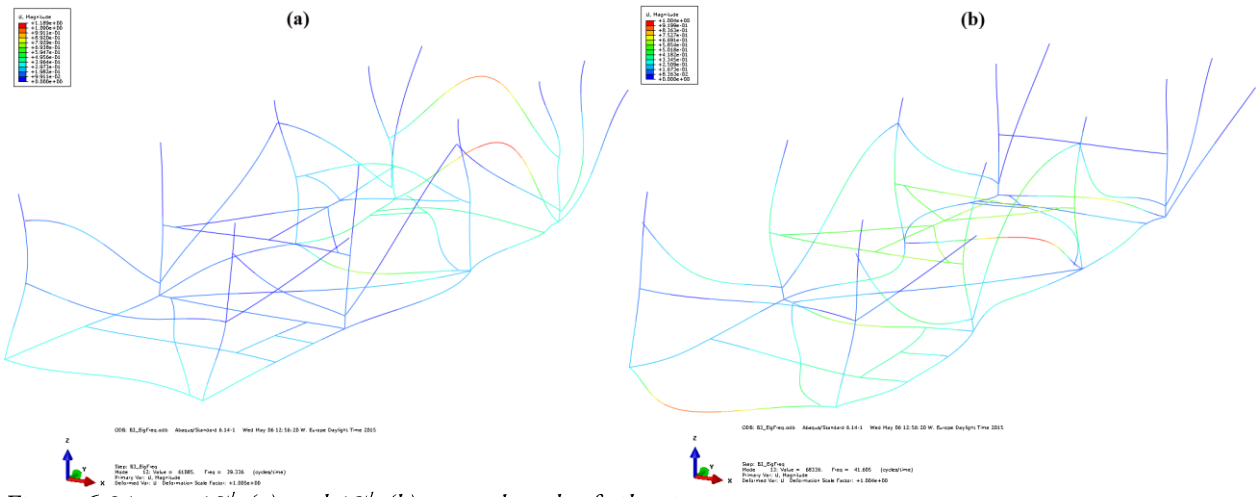


Figure 6-21 12th (a) and 13th (b) natural mode of vibration.

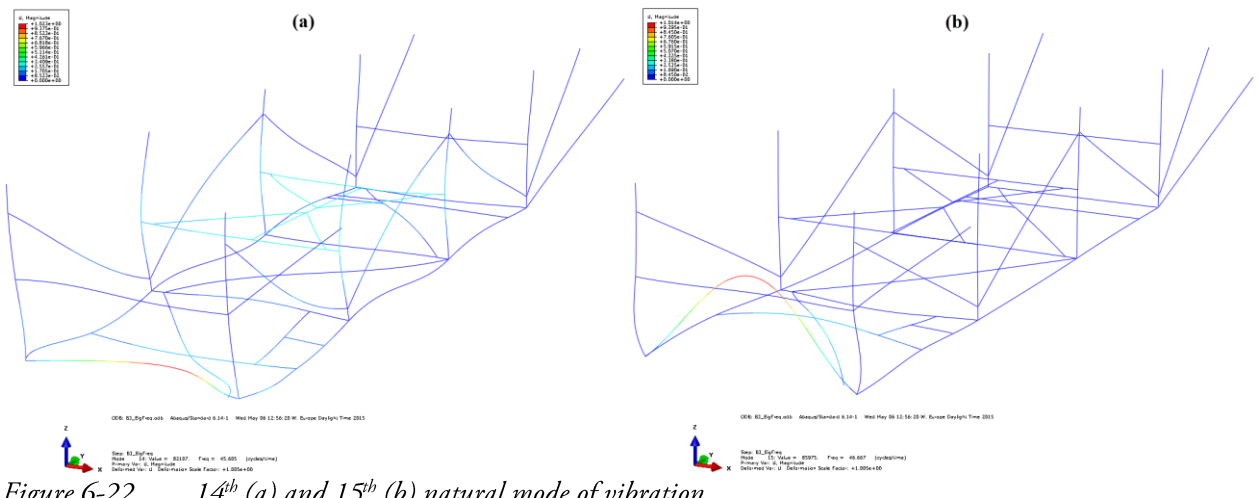


Figure 6-22 14th (a) and 15th (b) natural mode of vibration.

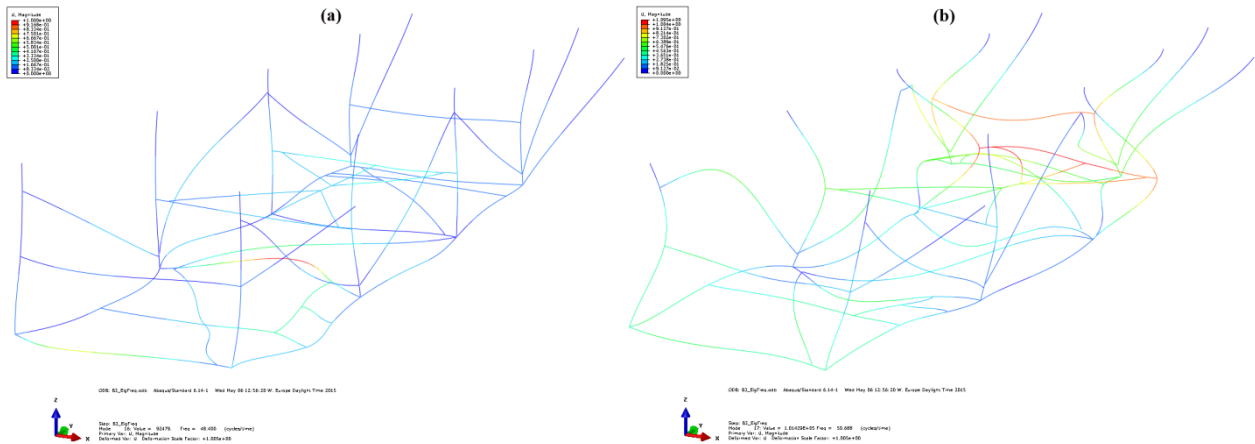


Figure 6-23 16th (a) and 17th (b) natural mode of vibration.

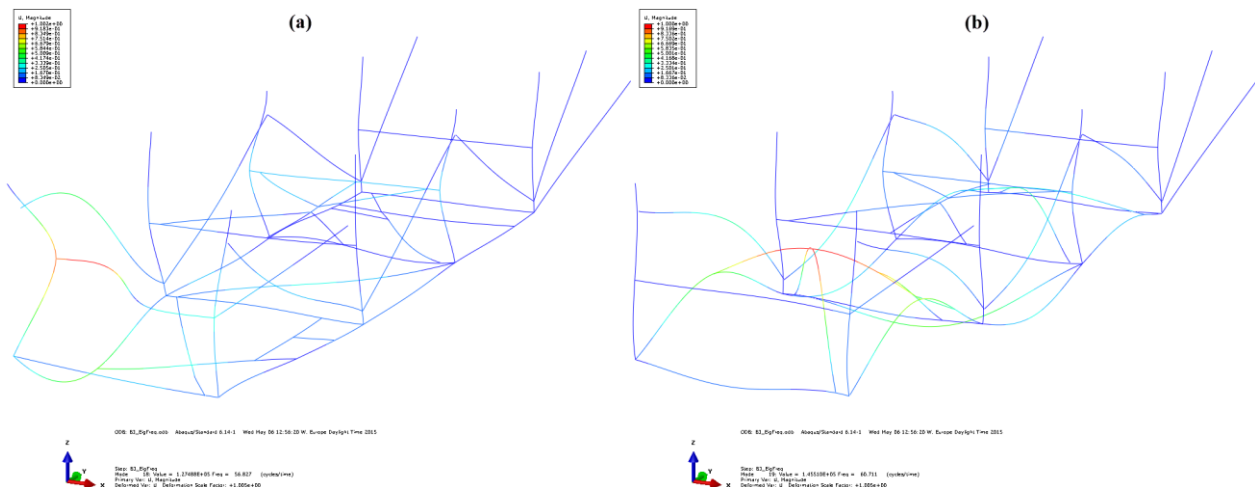


Figure 6-24 18th (a) and 19th (b) natural mode of vibration.

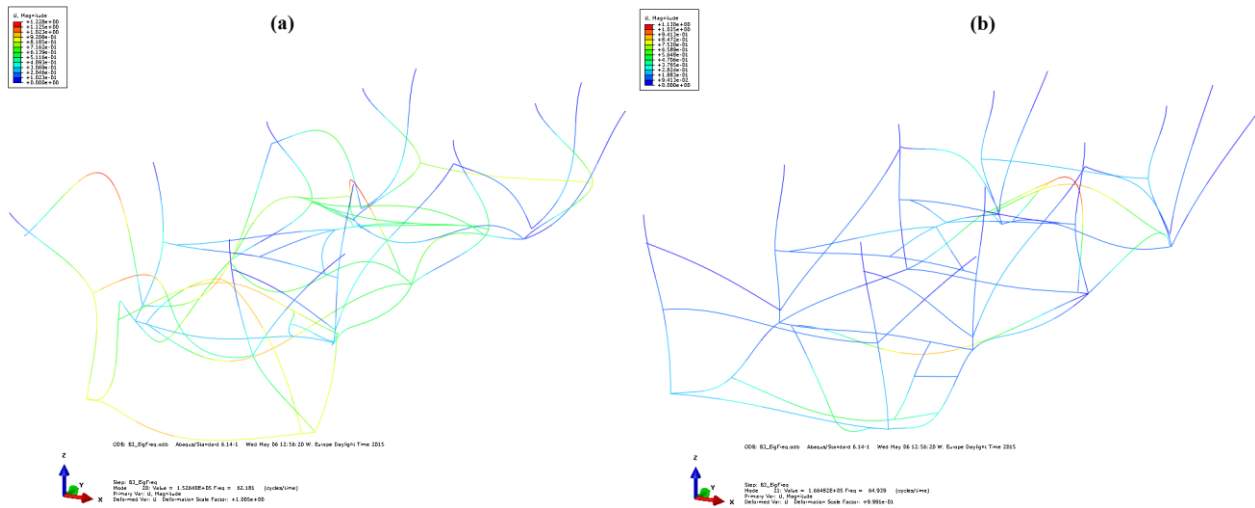


Figure 6-25 20th (a) and 21st (b) natural mode of vibration.

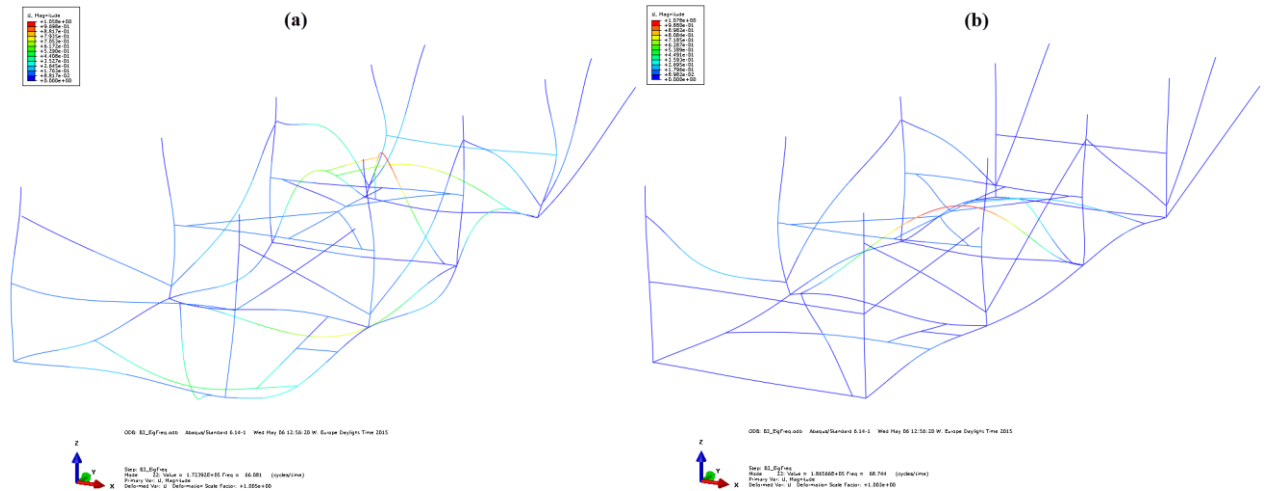


Figure 6-26 22nd (a) and 23rd (b) natural mode of vibration.

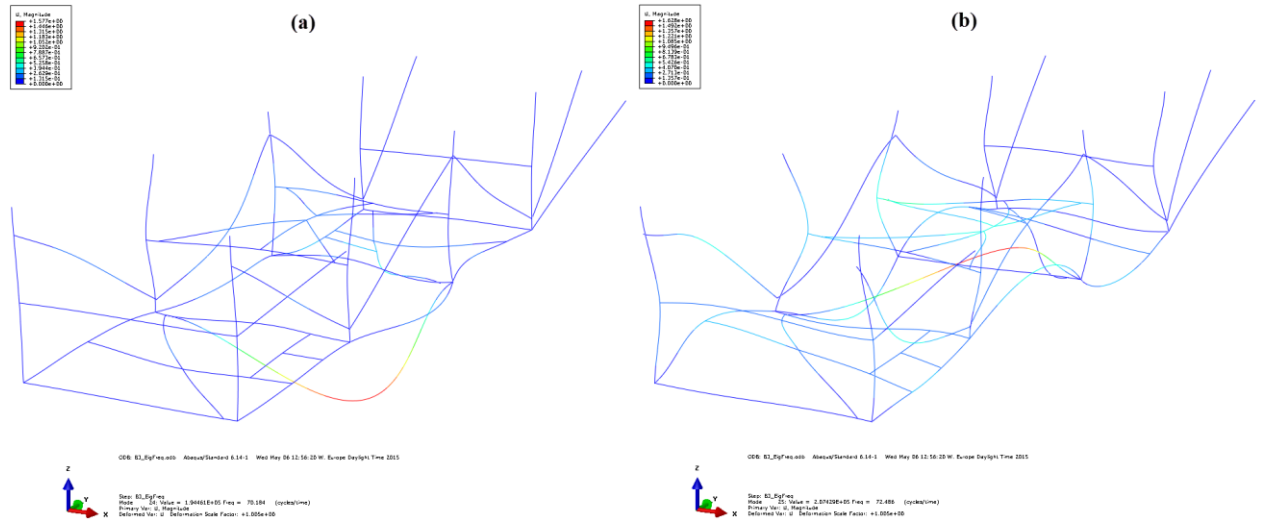


Figure 6-27 24th (a) and 25th (b) natural mode of vibration.

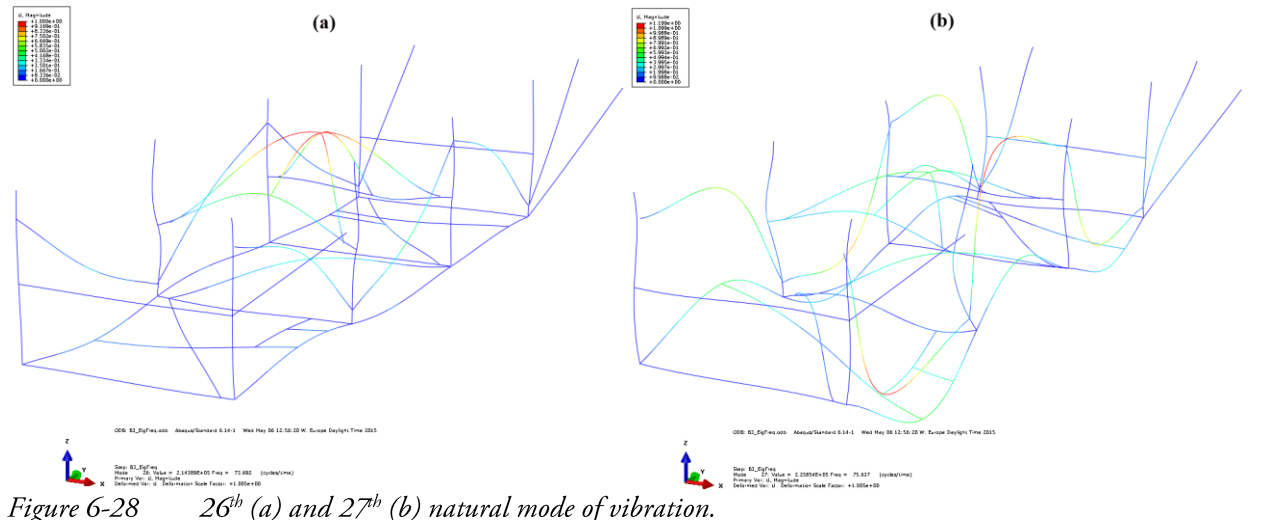


Figure 6-28 26th (a) and 27th (b) natural mode of vibration.

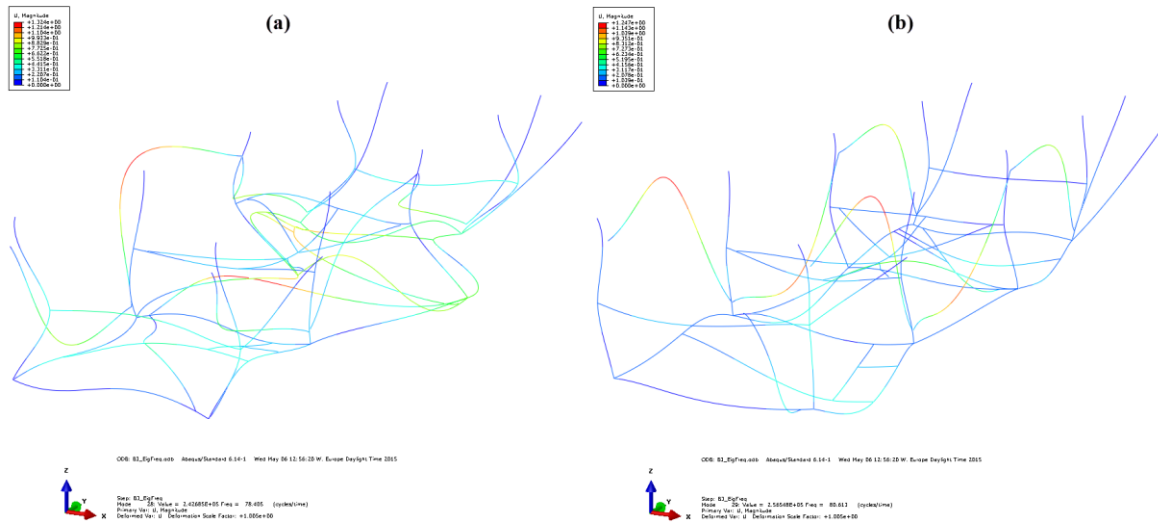


Figure 6-29 28th(a) and 29th(b) natural mode of vibration.

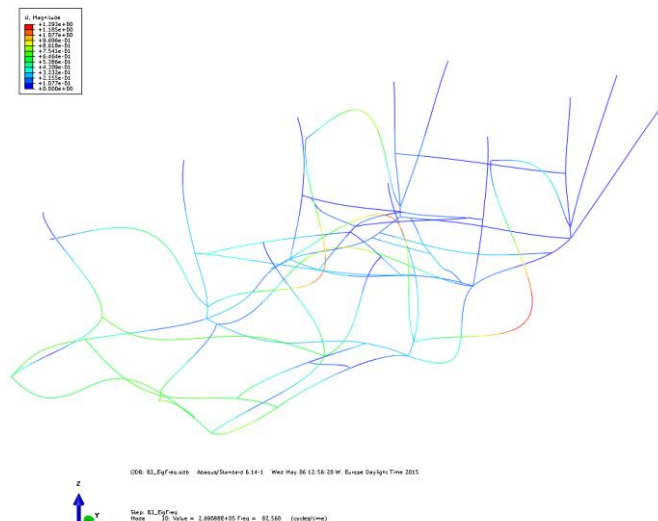


Figure 6-30 30th natural mode of vibration.

According to the procedures outlined by both the conventional and proposed method, the natural period associated with the first natural mode of vibration that is characterized by global displacement in the direction of governing blast load shall be used. This mode is defined for transverse blast loading in Table 6-10 as the 2nd Mode, with a mode shape illustrated in Figure 6-15 and a natural period of 42.230 milliseconds. A natural period of $T_n = 42.23 \text{ ms} \approx 42 \text{ ms}$ was therefore used as input to the analytical methods evaluated in sections below.

6.5 The Conventional Method

Ratios of t_d/T_n to be considered when estimating the dynamic response of *Piperack01_P30_M50* according to the conventional method are governed by a natural period of $T_n = 42 \text{ ms}$ and the pulse duration range of 50-200 milliseconds defined by the design blast-pulse.

According to the *Linear-elastic Biggs method*, the applicable DAF may be obtained from Figure 4-4 as explained in Chapter 4. The full time-history response for specific ratios t_d/T_n however may be visualized by the developed Matlab script attached to Appendix D. This script was utilized to calculate the SDOF-response and associated DAF shown in Figures 6-31 to 6-33 for three different pulse durations as specified below. The calculated DAFs are seen to correspond to the values given by the shock spectrum in Figure 4-4.

Evaluated pulse excitations:

1. $t_d = 50 \text{ ms}, T_n = 42 \text{ ms} \rightarrow t_d/T_n \approx 1.19$
2. $t_d = 96 \text{ ms}, T_n = 42 \text{ ms} \rightarrow t_d/T_n \approx 2.29$
3. $t_d = 126 \text{ ms}, T_n = 42 \text{ ms} \rightarrow t_d/T_n = 3.00$

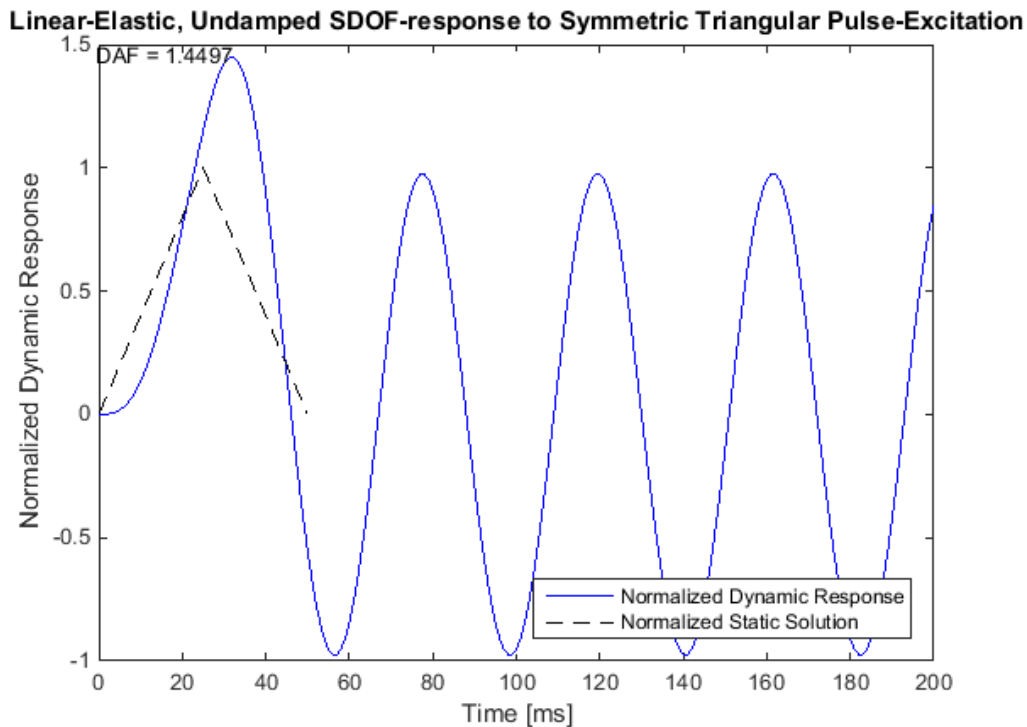


Figure 6-31 Linear-Elastic SDOF-response and DAF for ratio of t_d/T_n equal to 1.19.

Linear-Elastic, Undamped SDOF-response to Symmetric Triangular Pulse-Excitation

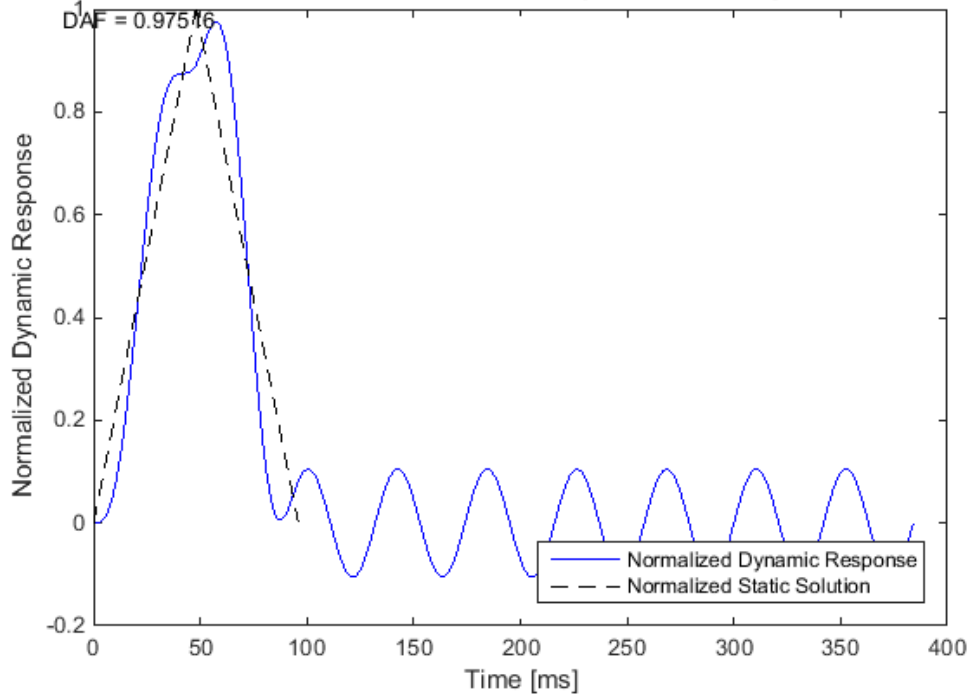


Figure 6-32 Linear-Elastic SDOF-response and DAF for ratio of t_d/T_n equal to 2.29.

Linear-Elastic, Undamped SDOF-response to Symmetric Triangular Pulse-Excitation

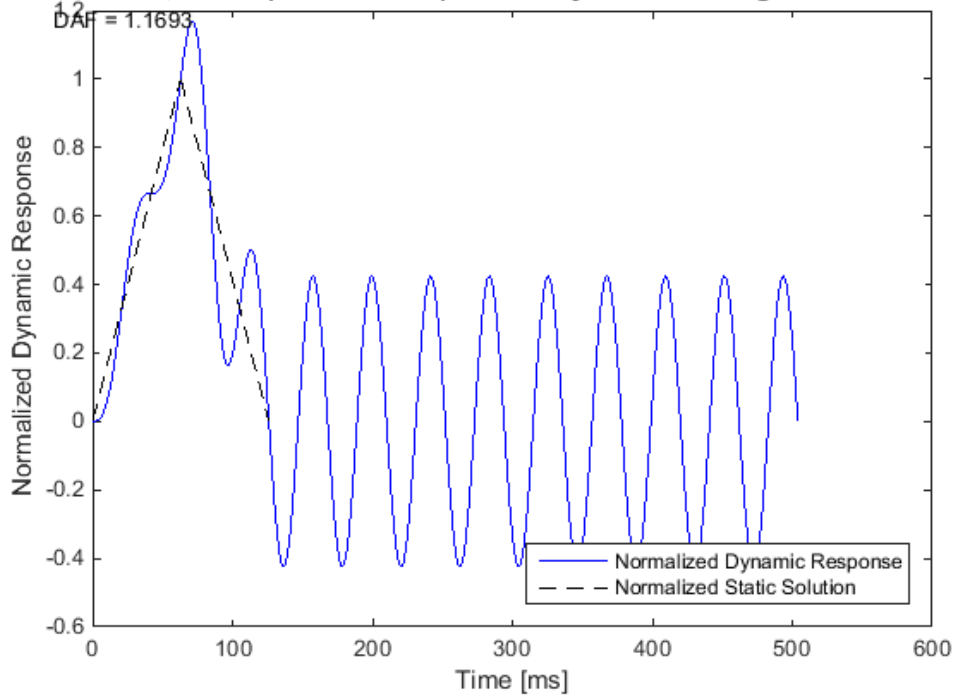


Figure 6-33 Linear-Elastic SDOF-response and DAF for ratio of t_d/T_n equal to 3.0.

Table 6-11 below show the estimated maximum dynamic response of the pipe rack, calculated for the three different pulse durations defined above in accordance with the conventional method. The DAFs shown in Figures 6-31 to 6-33 were used to scale the field quantities σ_{max} and $U1_{max}$ in Table 6-9 associated with a non-amplified load application in global +X direction of blast loads that were calculated based on *Load Procedure 2*.

| Pulse Duration, t_d [ms] | DAF | σ_{max} [MPa] | $U1_{max}$ [mm] |
|----------------------------|------|----------------------|-----------------|
| 50 | 1.45 | 152.0 | 5.03 |
| 96 | 0.98 | 102.7 | 3.40 |
| 126 | 1.17 | 122.6 | 4.06 |

Table 6-11 Maximum dynamic response for various pulse durations according to the conventional method.

6.6 The Proposed Method

Limiting peak blast-pressures $p_{1,limit}$ are documented below, calculated in accordance with the proposed method by enforcing the SDOF analogy explained by the *Elasto-plastic Biggs method*. Table 6-12 show the input parameters that were established in accordance with the procedure outlined in Section 4.4, obtained from analyses B.2 and B.3 as well as the exposed blast-area calculations documented in Section A.9 of Appendix A. Recall from Section 5.5 that y_m was assumed to be governed by the deflection failure criteria of ± 100 mm.

| Input Parameter | Governing B.2 Analysis | | | |
|-------------------------------|------------------------|---------|---------|---------|
| | B.2_1 | B.2_2 | B.2_3 | B.2_4 |
| y_{el} [mm] | 11.78 | 11.82 | 10.53 | 10.27 |
| y_m [mm] | 100 | 100 | 100 | 100 |
| R_M [kN] | 1722.44 | 1751.67 | 1437.32 | 1445.97 |
| T_n [ms] | 42 | 42 | 42 | 42 |
| t_d [ms] | 50-200 | 50-200 | 50-200 | 50-200 |
| A_{Blast} [m ²] | 31.54 | 31.54 | 31.54 | 31.54 |

Table 6-12 Input parameters for calculations of limiting peak blast-pressures according to the proposed method.

For the *Elasto-plastic Biggs method*, the applicable ratio R_M/F_1 may be obtained from Figure 4-5 as explained in Chapter 4. Figure 6-34 show the region from where this governing value was chosen, enclosed by the range of ratios y_m/y_{el} and t_d/T_n defined by the input data in Table 6-12. As shown in Figure 6-34, plotted lines defining the boundaries of the enclosed region are chosen on the conservative side to ensure that the higher bound ratio R_M/F_1 generating the more conservative limiting peak-pressure is captured by the graphical solution method.

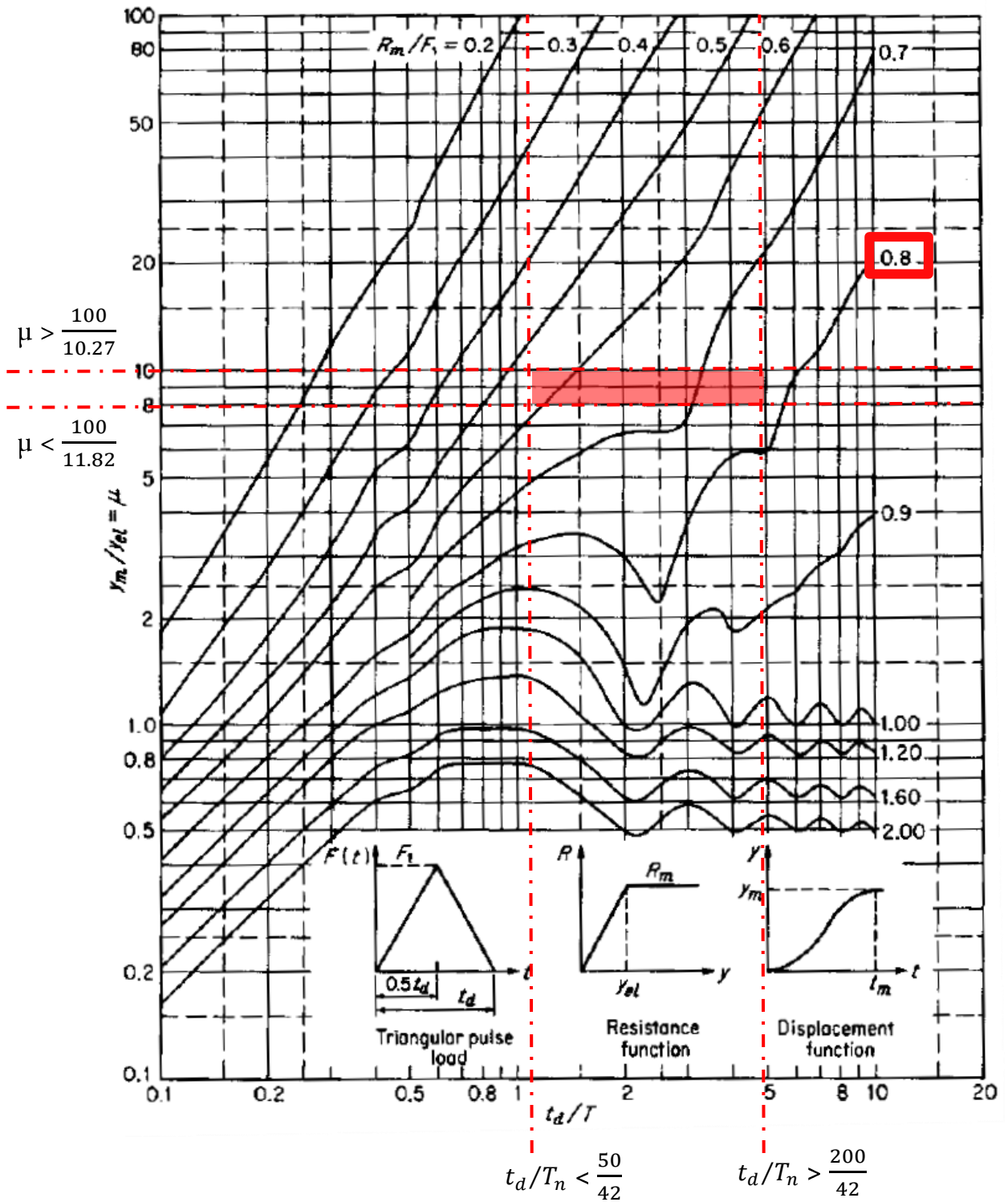


Figure 6-34 Graphical solution of ratio R_M/F_1 governing the limiting peak-pressure according to the proposed method.

Figure 6-34 show that the higher bound ratio of $R_M/F_1 = 0.8$ prevails as the governing output variable for all four different values of y_m/y_{el} provided in Table 6-12. The larger values of ratios t_d/T_n within the established range are seen to govern the inelastic capacity as defined by the *Elasto-plastic Biggs method* in this case.

Based on the governing ratio of R_M/F_1 obtained from Figure 6-34 and input parameters provided in Table 6-12, the limiting pulse-force F_1 and corresponding pulse-pressure $p_{1,limit}$ was calculated in accordance with the procedure outlined by the proposed method. Results are summarized in Table 6-13 below.

| Output Parameter | Governing B.2 Analysis | | | |
|----------------------|------------------------|---------|---------|---------|
| | B.2_1 | B.2_2 | B.2_3 | B.2_4 |
| Max. ratio R_M/F_1 | 0.8 | 0.8 | 0.8 | 0.8 |
| F_1 [kN] | 2153.05 | 2189.59 | 1796.65 | 1807.46 |
| $p_{1,limit}$ [kPa] | 68.3 | 69.4 | 57.0 | 57.3 |

Table 6-13 Limiting peak blast-pressure calculated according to the proposed method.

It is seen that the analyses where *Load Procedure 3* govern the load implementation, i.e. analyses B.2_3 and B.2_4, generate the most conservative result with respect to defining a limiting blast-pressure. Although previously drawn conclusion stated that *Load Procedure 3* should not be utilized in a full nonlinear FE analysis, where *Load Procedure 2* is considered to better account for the true load effects from an accidental blast, the results presented in Table 6-13 suggests that it could however be used in the proposed method where it was found to generate more conservative values of limiting pressures.

6.7 Analysis B.4

Figure 6-35 and Table 6-14 summarize the dynamic response of *Piperack01_P30_M50* when subjected to gravity loading and exposed to blast in global +X direction. Full nonlinear FE simulations were carried out for every 15 millisecond increment within the pulse duration range defined by the design blast-pulse, i.e. 50 to 200 milliseconds. Blast loads applied in analysis B.4 are governed by the peak blast-pressure defined by the design blast-pulse and calculated according to *Load Procedure 2*. The static blast-loads were scaled by an amplitude curve to simulate the pulse excitation as explained in Section A.10 of Appendix A.

For each of the analyzed blast-pulse durations, the following variables are documented:

1. Overall maximum von Mises stress, σ_{max} .
2. Overall maximum global displacement in direction of blast load, $U1_{max}$.
3. The time after application of blast pulse at which maximum response quantities 1 and 2 above were reached, $t_{max,resp}$.

4. The location where the maximum response quantities 1 and 2 above were registered, as shown by Figure 6-35 and referenced in Table 6-14.
5. The maximum value of plastic strain developed, ϵ_{max}^p .

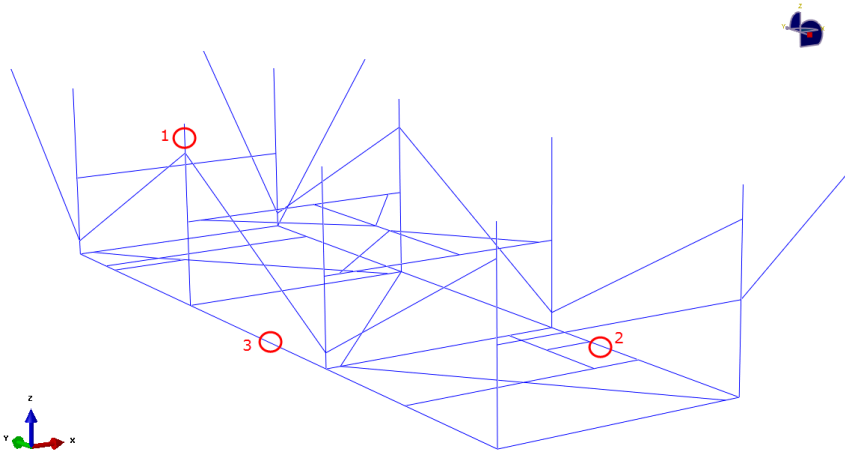


Figure 6-35 Locations where maximum response quantities were obtained in Analysis B.4.

| Pulse Duration, t_d [ms] | Dynamic Stress Response | | | Dynamic Displacements and Plastic Straining | | | |
|-------------------------------|-------------------------|------------------------|----------|---|------------------------|----------|---------------------------|
| | σ_{max} [MPa] | $t_{max,resp}$ [ms] | Location | $U1_{max}$ [mm] | $t_{max,resp}$ [ms] | Location | ϵ_{max}^p [%] |
| 50 | 143.1 | 31.1 | 1 | 5.05 | 32.6 | 2 | 0 |
| 65 | 127.6 | 36.5 | 1 | 4.39 | 36.5 | 3 | 0 |
| 80 | 109.5 | 43.0 | 1 | 3.70 | 40.6 | 3 | 0 |
| 95 | 100.1 | 52.8 | 1 | 3.33 | 55.7 | 3 | 0 |
| 110 | 108.0 | 65.2 | 1 | 3.73 | 65.2 | 3 | 0 |
| 125 | 115.9 | 71.1 | 1 | 3.98 | 71.1 | 3 | 0 |
| 140 | 116.6 | 77.2 | 1 | 3.99 | 77.2 | 3 | 0 |
| 155 | 112.8 | 80.4 | 1 | 3.81 | 80.4 | 3 | 0 |
| 170 | 105.9 | 87.4 | 1 | 3.54 | 87.4 | 3 | 0 |
| 185 | 100.9 | 99.7 | 1 | 3.37 | 99.7 | 3 | 0 |
| 200 | 105.2 | 107.5 | 1 | 3.54 | 113.5 | 3 | 0 |

Table 6-14 Maximum response quantities obtained in Analysis B.4.

The result documented in Table 6-14 show that the dynamic structural response of the pipe rack is well within the elastic range for the governing accidental explosion event defined by the design blast-pulse in Section 5.8. One of the main objectives of this thesis is thereby achieved as the validity of the original design of *Piperack01_P30_M50* and the verification process outlined by the conventional method are confirmed.

The accuracy of the conventional method, determined by the accuracy of the *Linear-elastic Biggs method*, may be evaluated further by comparing the true dynamic response documented in Table 6-14 to the SDOF analogy response estimated by the DAF and documented in Table 6-11. By comparison of the results, it is seen that the *Linear-elastic Biggs method* captures the overall maximum

dynamic response of *Piperack01_P30_M50* with good precision. The approximate method is in general slightly conservative when predicting maximum stresses and displacements, overestimating the peak response with a factor of 1.06 at the most. The response estimated by the *Linear-elastic Biggs method* differ less than 3% from the results obtained in Analysis B.4 for 4 out of the 6 field quantities subjected to comparison.

The SDOF analogy and associated theory on linear-elastic, undamped dynamic response is also found to be accurate considering the time at which the maximum response is predicted to occur. For the specific pipe rack structure and blast conditions analyzed, ratios of t_d/T_n range from approximately 1.2 to 4.8. According to the theory provided in Chapter 4 and Figure 4-3, this correspond to a pulse excitation of type *Dynamic* or *Quasi-static* for which the overall maximum response shall occur during the forced vibration phase. This is confirmed by the data in Table 6-14 showing that $t_{max,resp}$ is consistently found within the time span of the applied blast-pulse duration and within the first half-cycle of motion prior to rebound.

Based on the findings presented above, it is concluded that the SDOF analogy enforced via application of the *Linear-elastic Biggs method* provide a very good estimation of the true dynamic response of a pipe rack structure given that the response is within the linear-elastic range. Hence, the verification process outlined by the conventional method is likely to be very effective in general with respect to generating pipe rack designs that remain within the linear-elastic range during an explosion event.

6.8 Analysis B.5

Figure 6-36 and Table 6-15 summarize the dynamic response of *Piperack01_P30_M50* when subjected to gravity loading and exposed to blast in global +X direction. Full nonlinear FE simulations were carried out for every 15 millisecond increment within the pulse duration range defined by the design blast-pulse, i.e. 50 to 200 milliseconds. Blast loads applied in analysis B.5 are governed by the maximum value of limiting peak blast-pressures (69.4 kPa) calculated according to the proposed method and documented in Table 6-13. Static blast-loads were calculated and applied in accordance with *Load Procedure 2*, and scaled by an amplitude curve to simulate a pulse excitation as explained in Section A.10 of Appendix A.

For each of the analyzed blast-pulse durations, the following variables are documented:

1. Overall maximum von Mises stress, σ_{max} .
2. Overall maximum global displacement in direction of blast load, $U1_{max}$.
3. The maximum value of plastic strain developed, ϵ_{max}^p .
4. The time after application of blast pulse at which maximum response quantities 1, 2 and 3 above were reached, $t_{max,resp}$.
5. The location where the maximum response quantities 1, 2 and 3 above were registered, as shown by Figure 6-36 and referenced in Table 6-15.

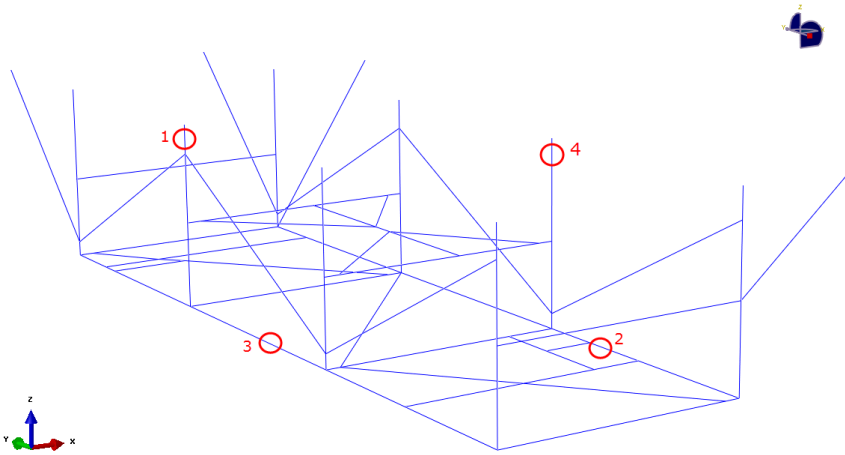


Figure 6-36 Locations where maximum response quantities were obtained in Analysis B.5.

| Pulse Duration, t_d [ms] | Dynamic Stress Response | | | Dynamic Displacements and Plastic Straining | | | | | |
|----------------------------|-------------------------|---------------------|----------|---|---------------------|----------|------------------------|---------------------|----------|
| | σ_{max} [MPa] | $t_{max,resp}$ [ms] | Location | $U1_{max}$ [mm] | $t_{max,resp}$ [ms] | Location | ϵ_{max}^p [%] | $t_{max,resp}$ [ms] | Location |
| 50 | 362.1 | 142.8 | 1 | 17.59 | 32.2 | 2 | 0.7 | 142.8 | 1 |
| 65 | 357.1 | 37.8 | 4 | 15.24 | 35.9 | 3 | 0.3 | 37.8 | 1 |
| 80 | 355.3 | 40.9 | 4 | 12.83 | 40.9 | 3 | 0.1 | 43.3 | 1 |
| 95 | 339.4 | 52.0 | 1 | 11.47 | 57.7 | 3 | 0.03 | 52.0 | 1 |
| 110 | 355.2 | 64.6 | 4 | 12.86 | 64.6 | 3 | 0.09 | 64.6 | 1 |
| 125 | 355.8 | 71.7 | 1 | 13.82 | 71.7 | 3 | 0.16 | 71.7 | 1 |
| 140 | 355.9 | 74.6 | 1 | 13.81 | 74.6 | 3 | 0.18 | 78.8 | 1 |
| 155 | 355.8 | 81.8 | 1 | 13.32 | 81.8 | 3 | 0.15 | 81.1 | 1 |
| 170 | 355.1 | 88.8 | 4 | 12.35 | 83.7 | 3 | 0.09 | 88.8 | 1 |
| 185 | 340.8 | 96.4 | 1 | 11.69 | 101.9 | 3 | 0.04 | 96.4 | 1 |
| 200 | 355.0 | 111.2 | 4 | 12.36 | 111.2 | 3 | 0.08 | 111.2 | 1 |

Table 6-15 Maximum response quantities obtained in Analysis B.5.

Table 6-15 shows that the most severe dynamic response is governed by the shortest pulse duration of 50 milliseconds. In general, the maximum response quantities are registered within the forced vibration phase at the time when the rack structure experience its peak global horizontal displacement, which consistently occurs within the first half-cycle of motion prior to rebound. The only exception to this general behavior is the response obtained from the pulse excitation characterized by a duration of 50 milliseconds, where peak stresses and plastic strains are registered during the free vibration phase. However, it could be argued that the damping phenomenon not considered in this study would cause the free vibration to decay rapidly, implying that the actual peak response is well accounted for within the time period of the forced vibration phase.

Considering only the forced vibration phase of the rack structure associated with excitation by the most critical blast-pulse duration of 50 milliseconds, Figure 6-37 show the location of the elements undergoing the highest level of plastic straining at the time increment of the highest recorded global

displacement $U1_{max}$. It is seen that the largest plastic strain developed at this stage is equal to approximately 0.54 %.

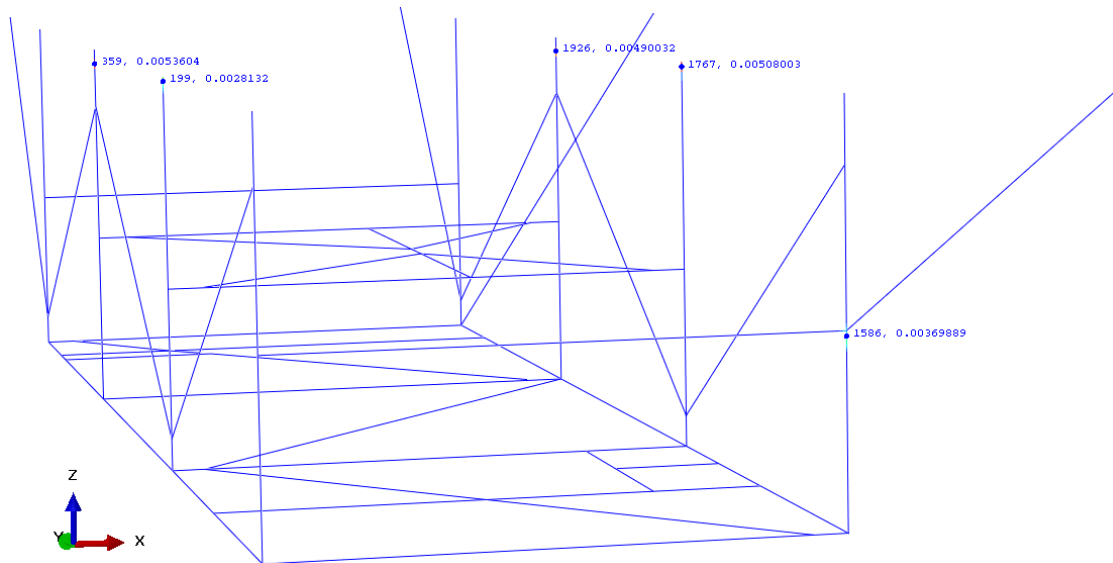


Figure 6-37 Elements undergoing highest recorded level of plastic straining at time increment of $U1_{max}$ for blast-pulse with duration of $t_d=50$ milliseconds.

To further visualize the dynamic response of the pipe rack, the deformed configuration associated with the plastic strain state illustrated by Figure 6-37 is shown in Figure 6-38. The complete time-history response of global horizontal displacements for internal pipe supports is also provided for the most critical pulse duration. The response of internal supports attached to pipe line 43057 and 41009P is shown in Figure 6-39 and Figure 6-40.

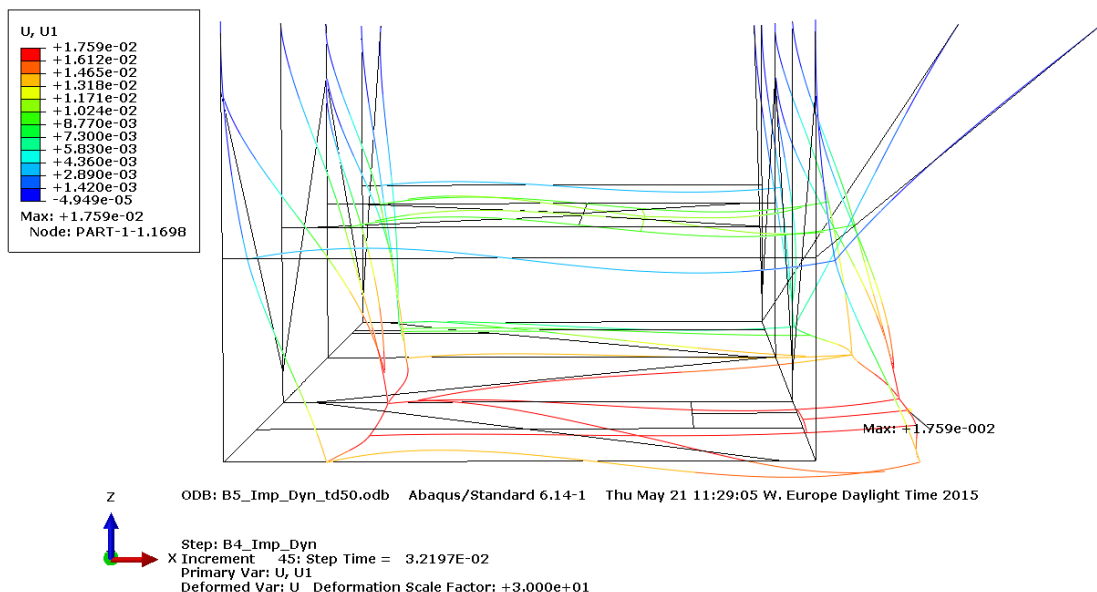


Figure 6-38 Deformed configuration at time increment of $U1_{max}$ for blast-pulse with duration of $t_d=50$ milliseconds.

Pipe Line NO43057 | Internal Pipe Support Displacements

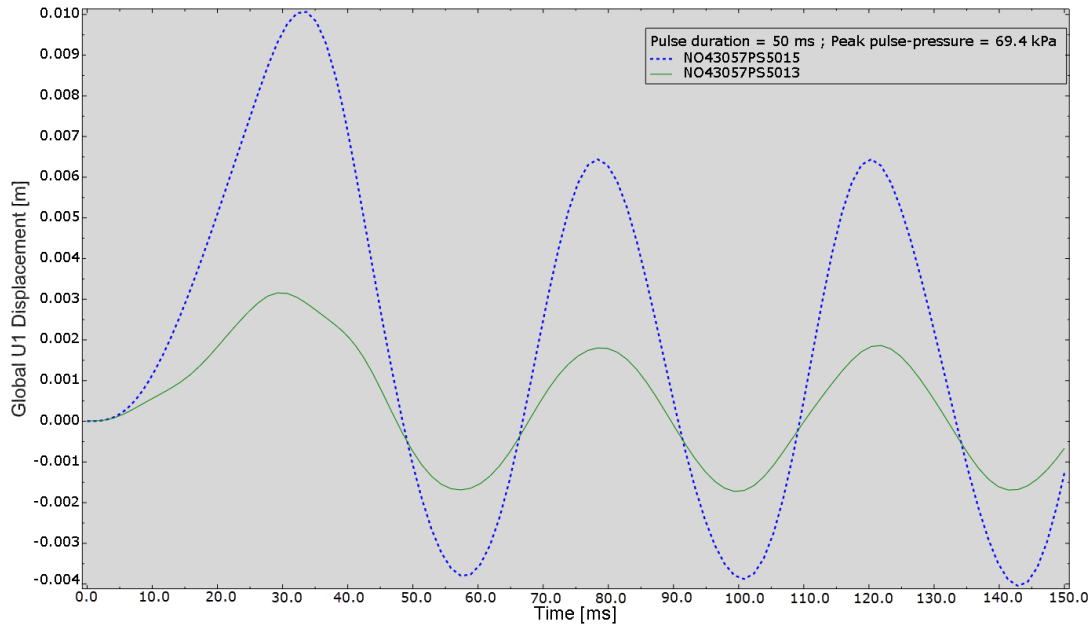


Figure 6-39 Time-history plot showing global U1 displacements of internal pipe supports attached to pipe line 43057 for blast-pulse with duration of $t_d=50$ milliseconds.

Pipe Line NO41009P | Internal Pipe Support Displacements

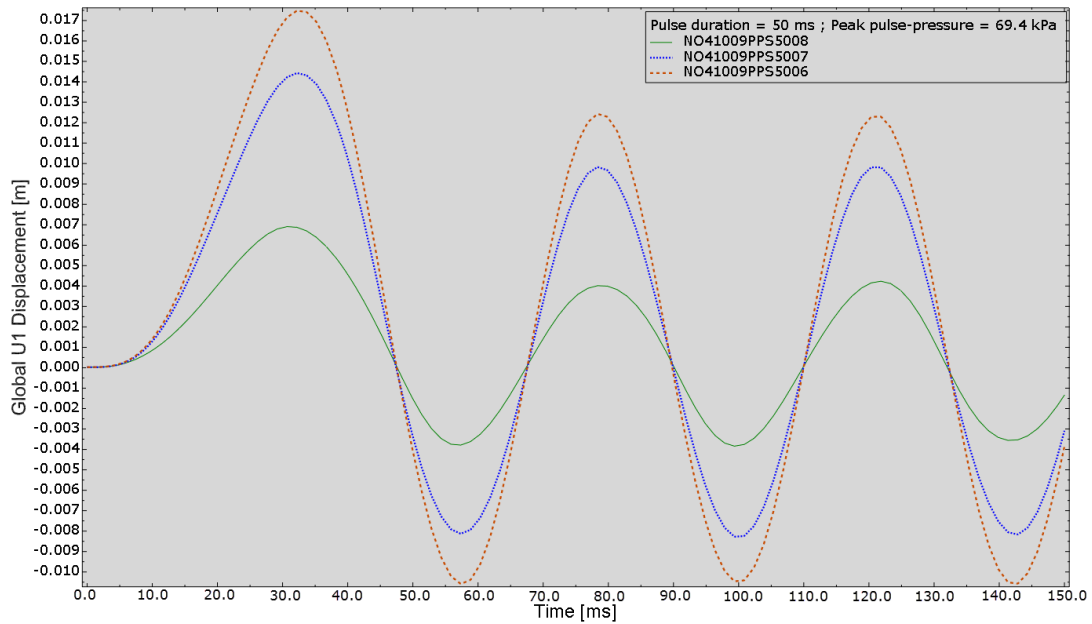


Figure 6-40 Time-history plot showing global U1 displacements of internal pipe supports attached to pipe line 41009P for blast-pulse with duration of $t_d=50$ milliseconds.

The results presented above confirm that the inelastic capacity of *Piperack01_P30_M50* exceeds the capacity estimated by the proposed method. The response to a blast-pulse characterized by a limiting peak-pressure derived from the proposed method was found to be within the inelastic range, but far from exceeding the failure criteria as defined in Section 5.5. Hence, it is concluded that the proposed method was successful in providing a conservative estimate of the inelastic capacity of *Piperack01_P30_M50* and its validity under conditions evaluated in this study is thereby confirmed.

6.9 Analysis B.6

Figure 6-41 and Table 6-16 summarize the dynamic response of *Piperack01_P30_M50* when subjected to gravity loading and exposed to blast in global +X direction. Full nonlinear FE simulations were carried out for every 15 millisecond increment within the pulse duration range defined by the design blast-pulse, i.e. 50 to 200 milliseconds. Blast loads applied in analysis B.6 are governed by a peak blast-pressure generating failure in the structural system as defined in Section 5.8. The magnitude of this blast-pressure was found to be equal to 96 kPa or approximately 1 barg. Static blast-loads were calculated and applied in accordance with *Load Procedure 2*, and scaled by an amplitude curve to simulate a pulse excitation as explained in Section A.10 of Appendix A.

For each of the analyzed blast-pulse durations, the following variables are documented:

1. Overall maximum global displacement in direction of blast load, $U1_{max}$.
2. The maximum value of plastic strain developed, ϵ_{max}^p .
3. The time after application of blast pulse at which maximum response quantities 1 and 2 above were reached, $t_{max,resp}$.
4. The location where the maximum response quantities 1 and 2 above were registered, as shown by Figure 6-41 and referenced in Table 6-16.

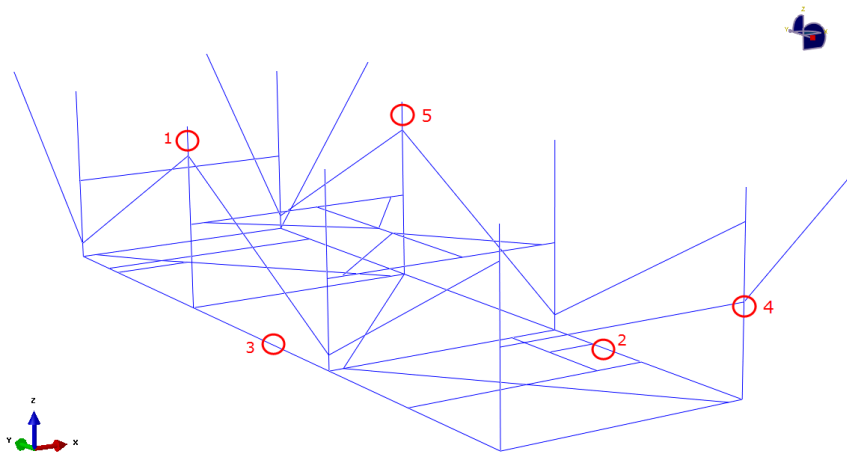


Figure 6-41 Locations where maximum response quantities were obtained in Analysis B.6.

| Pulse Duration, t_d [ms] | Dynamic Displacements and Plastic Straining | | | | | |
|-------------------------------|---|------------------------|----------|---------------------------|------------------------|----------|
| | $U1_{max}$ [mm] | $t_{max,resp}$ [ms] | Location | ϵ_{max}^p [%] | $t_{max,resp}$ [ms] | Location |
| 50 | 26.55 | 35.2 | 2 | 3.06 | 145.4 | 4 |
| 65 | 22.63 | 39.9 | 2 | 1.64 | 153.8 | 1 |
| 80 | 18.99 | 45.0 | 3 | 0.96 | 45.0 | 5 |
| 95 | 17.22 | 58.2 | 3 | 0.60 | 55.3 | 5 |
| 110 | 18.91 | 67.2 | 3 | 0.80 | 67.2 | 1 |
| 125 | 20.73 | 74.0 | 3 | 1.10 | 140.1 | 1 |
| 140 | 21.05 | 79.8 | 3 | 1.17 | 148.6 | 1 |
| 155 | 20.16 | 84.3 | 3 | 1.06 | 84.3 | 5 |
| 170 | 18.79 | 91.3 | 3 | 0.84 | 91.3 | 5 |
| 185 | 17.79 | 99.3 | 3 | 0.67 | 99.3 | 5 |
| 200 | 18.12 | 114.4 | 3 | 0.74 | 114.4 | 1 |

Table 6-16 Maximum response quantities obtained in Analysis B.6

The dynamic response obtained from analysis B.6 follow the same trends observed in analysis B.5. The shortest pulse duration within the design range generate the most severe dynamic response, which in this case correspond to failure as the maximum allowable plastic strain criteria of 3% is exceeded. Peak global displacements consistently occur during the forced vibration phase within the first half-cycle of motion prior to rebound. Peak strain values however are registered during the free response phase in four out of the eleven load scenarios considered.

If the previously presented arguments regarding mitigating effects from damping are taken into consideration, it is of interest to illustrate the most critical response obtained during the forced vibration phase at the time of maximum horizontal displacement. Figure 6-42 therefore show the location of the elements undergoing the highest level of plastic straining at the time increment of the highest recorded global displacement according to Table 6-16 , i.e. $U1_{max} = 26.55 \text{ mm}$. It is seen that the largest plastic strain developed at this stage is equal to approximately 1.93 %.

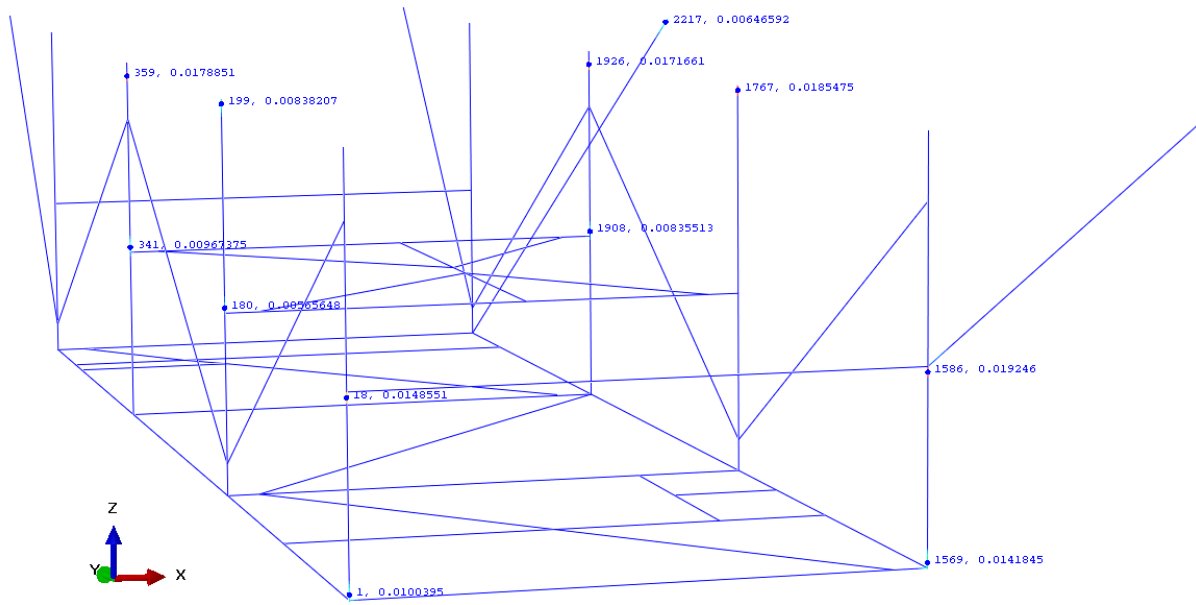


Figure 6-42 Elements undergoing highest recorded level of plastic straining at time increment of $U1_{max}$ for blast-pulse with duration of $t_d=50$ milliseconds.

To further visualize the dynamic response of the pipe rack, the deformed configuration associated with the plastic strain state illustrated by Figure 6-42 is shown in Figure 6-43. The complete time-history response of global horizontal displacements for internal pipe supports is also provided for the blast-pulse with duration equal to 50 milliseconds. The response of internal supports attached to pipe line 43057 and 41009P is shown in Figure 6-44 and Figure 6-45.

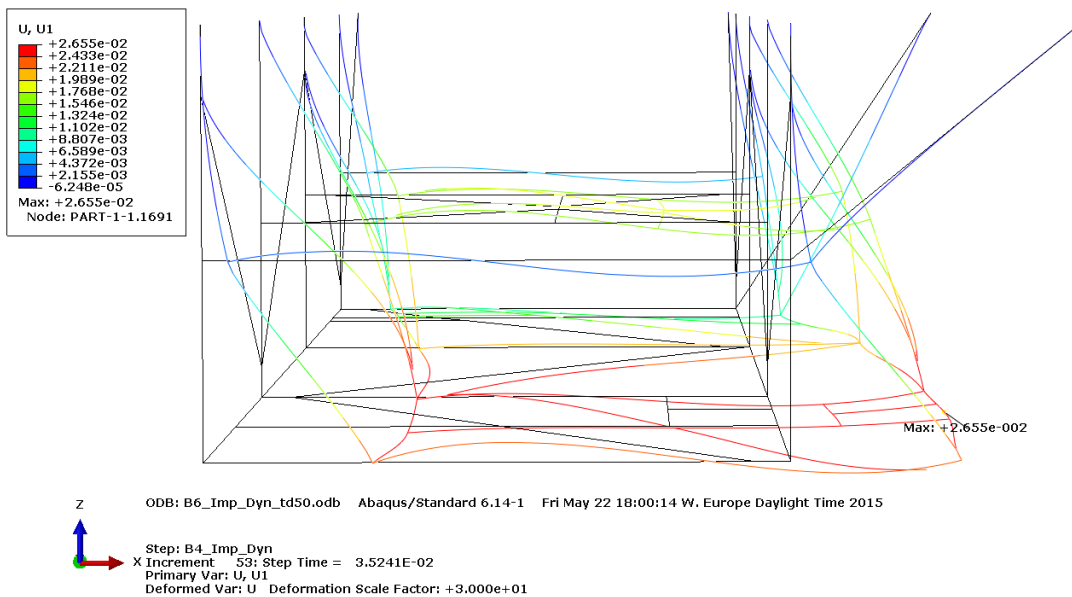


Figure 6-43 Deformed configuration at time increment of $U1_{max}$ for blast-pulse with duration of $t_d=50$ milliseconds.

Pipe Line NO43057 | Internal Pipe Support Displacements

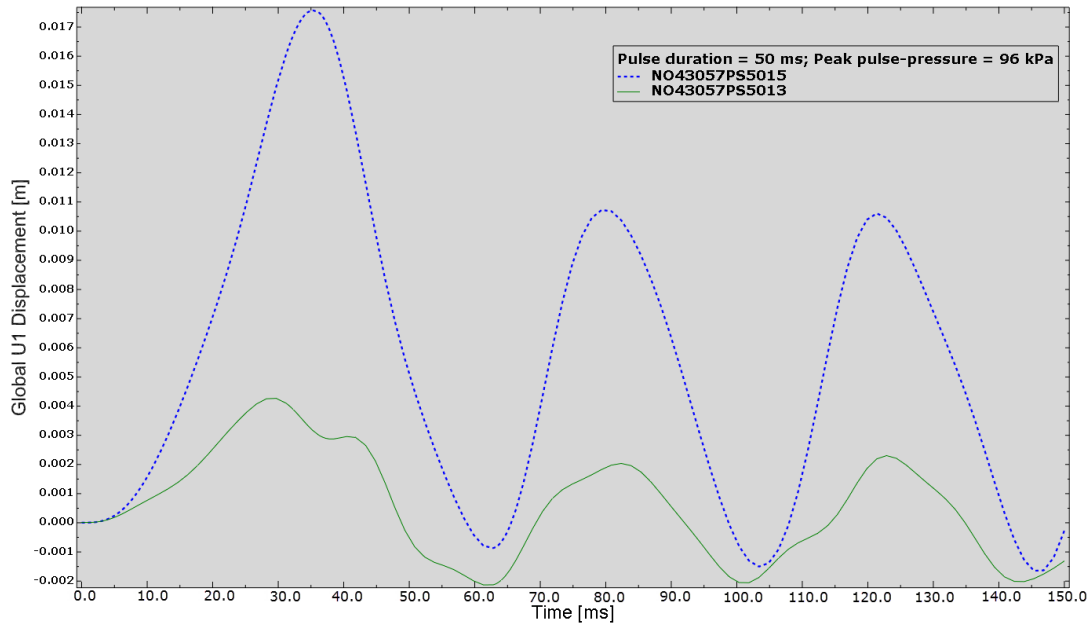


Figure 6-44 Time-history plot showing global U1 displacements of internal pipe supports attached to pipe line 43057 for blast-pulse with duration of $t_d=50$ milliseconds.

Pipe Line NO41009P | Internal Pipe Support Displacements

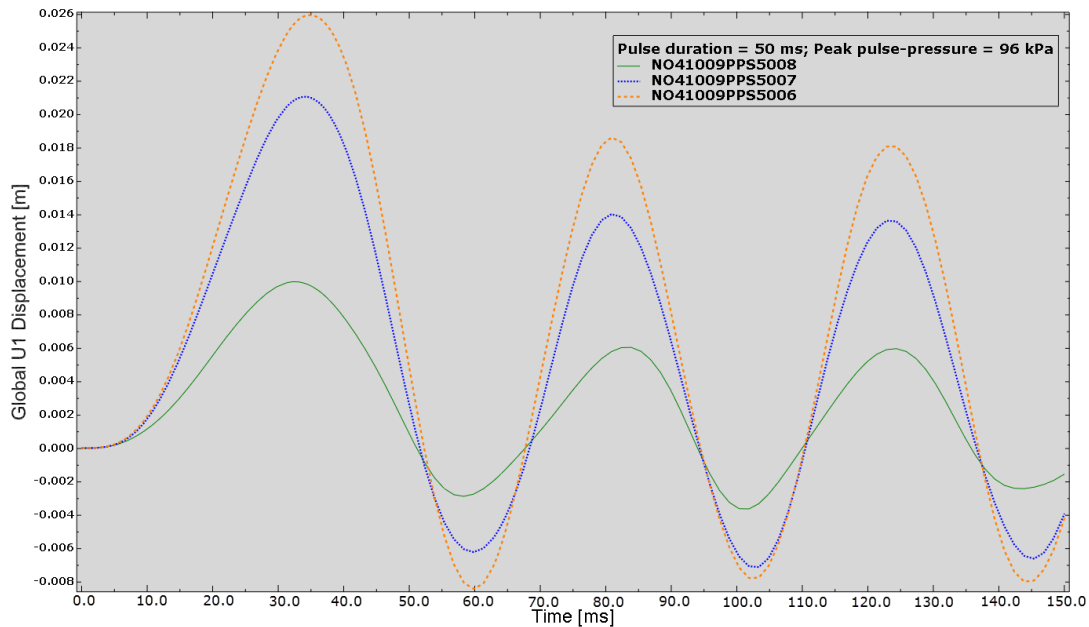


Figure 6-45 Time-history plot showing global U1 displacements of internal pipe supports attached to pipe line 41009P for blast-pulse with duration of $t_d=50$ milliseconds.

The main objective and fundamental purpose of this thesis is achieved through analysis B.6, as the generated results presented above reveal the full inelastic capacity of *Piperack01_P30_M50*. Measured in terms of ductility, the inelastic capacity is determined from the value of y_{el} in Table 6-12 derived from analysis B.2_1 and the maximum global displacement at failure defined by the largest value of $U1_{max}$ documented in Table 6-16. The inelastic capacity is thereby defined by a ductility ratio of; $\mu = 26.55/11.78 \approx 2.25$.

An additional relevant measure to present is one defining the unutilized capacity of a pipe rack structure designed to remain within the elastic range during the design accidental explosion event in accordance with the conventional method. *Piperack01_P30_M50* was designed for a blast-pulse characterized by a peak-pressure of 20 kPa and durations ranging from 50 to 200 milliseconds. Considering that the peak-pressure corresponding to failure for that same range of durations was found to be 96 kPa, the unutilized capacity may be quantified by the factor of 4.8 representing how many times the design-pulse can be magnified when accounting for the full inelastic capacity of the structural system. According to such a definition of unutilized capacity, the original design of *Piperack01_P30_M50* may be considered to possess a spare capacity of; $1 - 1/4.8 \approx 79\%$. In other words, only 21% of the full capacity of *Piperack01_P30_M50* was utilized by the conventional method when verifying its structural integrity for an accidental blast event.

Results from analysis B.5 confirmed that the proposed method's estimation of the inelastic capacity was on the conservative side. Based on the results from analysis B.6 it can now be concluded that the overall maximum value of estimated limiting peak-pressures could be further increased by a factor of $96/69.4 \approx 1.38$ before failure is reached. This implies that if *Piperack01_P30_M50* would have been verified for an accidental explosion event according to the proposed method, approximately 72% of the full capacity would have been accounted for.

Although shown to be on the conservative side, fundamental assumptions governing the output derived from the proposed method in this thesis were shown to be inaccurate. It was assumed that the failure criterion that would govern the inelastic capacity of *Piperack01_P30_M50* was an overall global displacement of ± 100 mm with respect to allowable deflections of the pipe line configuration. Results from analysis B.6 show that the plastic strain criteria of 3% was in fact governing and that maximum global displacement at failure was no more than 26.55 mm.

To evaluate the accuracy of the *Elasto-plastic Biggs method* that governs the output generated from the proposed method, the actual inelastic capacity of the structural system as defined by the results presented herein are considered.

The ratio of R_M/F_1 may be obtained from Figure 6-34 based on the ductility ratio of $\mu = 2.25$ and value of $t_d/T_n = 1.19$ that define the actual inelastic capacity and associated load scenario. Using these input parameters, an even more inaccurate and conservative estimate of a limiting peak-pressure is obtained as the corresponding ratio of R_M/F_1 is found to be slightly bigger than 0.9. If instead the ratio of R_M/F_1 is calculated based on the peak-pressure of 96 kPa, the exposed blast area

documented in Appendix A and the internal resistance derived from Analysis B.2_1 in Table 6-12, a value of $R_M/F_1 \approx 0.57$ is obtained. Combined with a ratio of $t_d/T_n = 1.19$, the *Elasto-plastic Biggs method* estimates a corresponding ductility ratio of around 10 equivalent to a maximum dynamic displacement of approximately 118 mm.

Based on the evaluation of the *Elasto-plastic Biggs method* above, it must be concluded that the SDOF analogy, found to prevail with great accuracy considering a dynamic response of a pipe rack structure within the linear-elastic range, fails to predict the inelastic response of the same structural configuration with a satisfying level of precision.

7 Discussion and Recommendations on Further Work

Much effort was devoted to study the nature of the blast phenomenon and to evaluate the procedures generating the design blast-pulse specifications used in AKSO projects. Key aspects of the accidental explosion event were identified in the theoretical study, including load effects specifically associated with interaction between a blast-pulse and a pipe rack configuration. The loads derived and implemented in the full nonlinear FE simulations are considered to capture the true nature of these interactive blast effects, and it is therefore argued that the load aspect of the problem has been well accounted for in this thesis.

Early conclusions with respect to governing directions of blast loading were drawn within the FEA study based on a static response derived from a static load application. The validity of such an approach is dependent on the static deflected shape corresponding well to the dominant mode shape triggered by the pulse excitation. This correspondence appears to be satisfactory by comparison of the static deflected shape in Figure 6-10 and the deformed configurations associated with a dynamic response illustrated by Figure 6-38 and Figure 6-43. Also, critical regions identified by the static analyses based on peak stresses in Figure 6-9 seem to correspond to critical regions observed in full nonlinear analyses based on high levels of plastic straining as shown in Figure 6-37 and Figure 6-42. These observations suggest that a nonlinear pushover analysis, where a slowly applied load is increased to the point of failure, might capture the inelastic capacity of the system in terms of ductility with a satisfactory precision. The FE formulation should account for both geometric and material nonlinearity in order to capture the true distribution of forces and inelastic behavior. If such an alternative approach is preferred over a full nonlinear dynamic analysis with respect to maintaining an efficient verification process, it is recommended that its accuracy is evaluated further based on the results obtained from this thesis.

It was concluded that the SDOF analogy employed in both verification procedures evaluated within this study prevailed with great accuracy considering a dynamic response of the pipe rack structure completely within the elastic range. However, the analytical SDOF model defined by the *Elasto-plastic Biggs method* was not successfully in capturing the inelastic response of the pipe rack when utilized to its full capacity. Based on the theory covered in chapters 3 and 4, the idealized perfectly-plastic resistance R_M of the inelastic SDOF-system is considered to be the main source of inaccuracy.

This idealized resistance was defined by the amount of internal forces developed in the rack structure at the point of first yield. Such a bilinear resistance function underestimates the true capacity of the system as shown by the pushover curve in Figure 3-11. Additional resistance from material strain

hardening and progressive hinge formation will help absorb the blast energy and thus reduce the peak response. Many publications on blast-resistant design suggest that the stress level used to define a perfectly-plastic resistance R_M should be increased beyond first yield at σ_{y0} in order to increase the accuracy of the inelastic SDOF analogy. It is recommended that such an approach is studied further in order to improve the *Elasto-plastic Biggs method*. As an example, (ASCE, 2010) states that an accurate SDOF modelling of an inelastic response may be obtained by defining the structural resistance equivalent to R_M from the average stress level reached during an estimated response range.

Although concluded to be inaccurate, application of the *Elasto-plastic Biggs method* via the proposed method was found to provide a conservative estimate of the pipe rack structures inelastic capacity. This conservatism is likely to prevail in general considering the discussion above regarding how the true capacity is underestimated by the SDOF analogy. However, it is recommended that the proposed method is evaluated further and applied to pipe rack configurations different from *Piperack01_P30_M50* to verify the conclusions drawn by this study.

The strategy employed in the numerical study implied that the piping configuration had to be accounted for implicitly, considering that only the rack configuration was modeled in analyses aiming to determine the inelastic capacity of the entire structural system. Simplified methods that estimated contribution in inertial masses and transfer of blast-loads acting on the pipe lines were developed and verified within the study. Although idealizations were made in the process of calculating these contributions, key aspects such as the true support functions of all internal pipe supports were taken into consideration. Mass and force contribution is therefore considered to have been successfully incorporated in the numerical solution procedure.

However, contribution in stiffness has not been accounted for in this study. Attempts to run analyses of a FE model containing both an idealized piping configuration and the rack structure, i.e. the configuration shown in Figure 5-6, were made. These attempts were unsuccessful as the pipe supports and associated support functions could not be modeled numerically in a satisfactory way without generating singularities in the numerical FE routines. It may be argued that any contribution in stiffness would have mitigating effects on the peak response found to govern the inelastic capacity in this thesis. Still, it is recommended that the piping configuration's contribution in stiffness is evaluated further to determine any significant effects on the dynamic properties of the entire structural system and thus the peak response governing its inelastic capacity.

The fact that the piping configuration was not explicitly verified through FEA of an interactive response between modeled piping geometry and the rack structure must be considered a weakness of this study. It was stated in the introduction that the pipe lines are critical in verification of the entire structural system and that rupture of safety critical pipes must be prohibited. The latter was accounted for via the deflection failure criteria of 100 mm global displacement, which has not been studied or verified within the scope of this thesis. Hence, further studies are recommended to ensure that the piping configuration will in fact sustain the high blast-pressures associated with utilization of the full structural capacity as defined herein.

The critical regions referred to previously were found in vicinity of gusset plate connections and rack structure joints. Two important notes should be made in relation to these observations as both regions are associated with weaknesses of the numerical study.

First, the beam element model analyzed in the study does not include a detailed representation of a gusset plate connection to an above, stiffened deck girder. This implies that the inelastic capacity of the pipe rack system derived and documented within this thesis is valid only if the gusset plate connection is able to withstand the loading imposed on it by the internal forces developed within the adjoining rack member. According to the governing material model, the load impact from such internal forces will be characterized by a rapid development of a highly plasticized cross-section with peak stresses up to 510 MPa. In addition, the theoretical study in Chapter 3 revealed that strain rate effects should be accounted for in verification of a support configuration not included within the analytical model. If not, the internal forces will be underestimated. It is therefore recommended that the increase in material strength associated with the strain rate phenomenon is studied further to determine if it should be accounted for when verifying the gusset plate connections. Verification of the connections is considered as required further work in order to dismiss premature failure at these locations.

The validity of the results obtained in the study are also dependent on the modeled boundary conditions and how well they reflect the true support conditions offered by a gusset plate connection. In this study, the gusset plate connection is assumed to provide full moment fixity about the global Y-axis which is why the response in this area is found to be high for blast-loading in transverse direction. Since the transverse blast direction and the strain-based failure criteria both were found to govern the inelastic capacity in this study, it is possible that a design modification to the gusset plate connection could further increase the capacity of the structural system. If the gusset plate is rotated 90 degrees and designed with a fold line so that a rotation about global Y-axis is no longer prohibited, then the moment distribution would change and the response at the location of the connection would not be as severe. However, the overall maximum global displacements in transverse direction would probably increase significantly due to this change in design. Still, it is recommended that the consequences of the suggested design modification are evaluated further to determine wheatear the full capacity could be increased beyond the level documented herein.

The second important note to be made with respect to the observed critical response regions is that the beam element model does not provide an accurate representation of the true joint capacity. The fact that no eccentricities were modeled to represent the actual design implies that the local capacity at a joint probably was overestimated in the numerical study. Based on the discussion on critical response regions, it is recommended that further studies are conducted in order to confirm that the inelastic capacity documented within this study is not compromised by premature failure of joints or connections. This could be achieved by connecting local shell element models of a gusset plate connection or joint design to the global FE model of the rack structure, or by analyzing local models

of connections and joints separately based on an idealized load scenario that reflects the internal force-response in adjoining members.

The FE analyses in this study were simulated in Abaqus/Standard, implying that implicit solution methods were utilized to enforce dynamic equilibrium at every time increment. Features and modeling techniques used to pre-process and simulate the dynamic response are backed up by theory described in Abaqus manuals as well as internal knowledge and experience at AKSO. The numerical procedures which generated the results documented in this thesis are therefore considered reliable and without any fundamental errors. However, it is recommended that a convergence study is performed to further instill confidence in the obtained results. Such a study could involve changing the global mesh size or type of beam element.

The main objective of this thesis was to determine the inelastic capacity of a typical pipe rack configuration, designed to remain within its elastic range during an accidental explosion event. This main objective was only partially achieved through this study, as further work recommended above is required in order to present an answer with full coverage.

Accounting for all aspects of this complex physical problem was not feasible within the time frame of this study, considering in addition that no previous studies had been conducted on this specific topic and that the full scope established for the thesis reached beyond this specific task. Although further work is required, many important and valuable conclusions have been drawn herein and it has been shown that a typical pipe rack design is likely to possess a significant spare capacity beyond its elastic range. In addition, secondary objectives were reached as the accuracy of the approximate analytical methods and associated verification procedures were revealed.

Overall, this study has been successful in identifying key aspects of the physical problem. Procedures established herein will also allow for the problem to be interpreted numerically via a reliable full nonlinear FE simulation. The work conducted within this study should therefore be able to contribute to future research on inelastic capacity of pipe rack structures exposed to an accidental explosion event.

References

Aarønæs A. and Nilsson H., 2014. *Dynamic response of pipe rack steel structures to explosion loads*. Department of Civil and Environmental Engineering, Chalmers University of Technology, Gothenburg, Sweden.

Abaqus, 2015a. *Abaqus Analysis User's Guide*. Abaqus 6.14 Documentation, Dassault Systemes Simulia Corp.

Abaqus, 2015b. *Abaqus Theory Guide*. Abaqus 6.14 Documentation, Dassault Systemes Simulia Corp.

AISC, 2013. *Design Guide 26: Design of Blast Resistant Structures*. American Institute of Steel Construction, Chicago, IL.

Alfawakhiri F. and Marchand K.A., 2004. *Facts for Steel Buildings: Blast and Progressive Collapse*. American Institute of Steel Construction.

ASCE, 2010. *Design of Blast-Resistant Buildings in Petrochemical Facilities*. 2 Edition. American Society of Civil Engineers.

Austrell P.E., 2015. Course material in: *VSMN10 – Structural Dynamic Computing*. Division of Structural Mechanics, Faculty of Engineering at Lund University, Sweden.

Biggs J.M., 1964. *Introduction to Structural Dynamics*. McGraw-Hill Companies, New York, NY.

Bjerketvedt D., Bakke J.R. and Wingerden K.V., 1993. *Gas Explosion Handbook Version 1.2*. Gexcon.

CCPS, 1996. *Guidelines for Evaluating Process Plant Buildings for External Explosions and Fires*. American Institute of Chemical Engineers, Center for Chemical Process Safety, New York, NY.

CCPS, 2010. *Guidelines for Vapor Cloud Explosion, Pressure Vessel Burst, BLEVE and Flash Fire Hazards*. 2 Edition. American Institute of Chemical Engineers, Center for Chemical Process Safety, New York, NY.

Chopra A.K., 2011. *Dynamics of Structures*. 4 Edition. Prentice Hall.

DNV-RP-C205, 2010. *Environmental Conditions and Environmental Loads*. Det Norske Veritas.

DOD, 2014. *UFC 3-340-02: Structures to Resist the Effects of Accidental Explosions-Change 2*. U.S. Department of Defense, Washington, DC.

Dusenberry D.O., 2010. *Handbook for Blast-Resistant Design of Buildings*. John Wiley & Sons. Hoboken, NJ.

FABIG, 2005. *Technical Note 8: Protection of Piping Systems subjected to Fires and Explosions*. The Steel Construction Institute, Fire and Blast Information Group.

Gustafsson P.J., 2014. Course material in: *VSMN35 – Beam Theory*. Division of Structural Mechanics, Faculty of Engineering at Lund University, Sweden.

Kanvinde A.M., 2014. Course material in: *ECI 233 - Advanced Design of Steel Structures*. Department of Civil and Environmental Engineering, University of California Davis, Davis, CA.

Krenk S., 2009. *Non-linear Modeling and Analysis of Solids and Structures*. Cambridge University Press.

NORSOK N-001, 2012. *Integrity of offshore structures*. Norwegian Standard.

NORSOK N-003, 2007. *Actions and action effects*. Norwegian Standard.

NORSOK N-004, 2013. *Design of steel structures*. Norwegian Standard.

NORSOK Z-013, 2010. *Risk and emergency preparedness assessment*. Norwegian Standard.

OMAE, 2003. *New Guidance on Fire and Explosion Engineering*. 22nd International Conference on Offshore Mechanics and Arctic Engineering.

Ottosen N.S and Ristinmaa M., 2005. *The Mechanics of Constitutive Modeling*. Elsevier Science.

Rogers G.L., 1959. *Dynamics of Framed Structures*. John Wiley & Sons. New York, NY.

SCI, 1992. *Interim Guidance Notes for the Design and Protection of Topside Structures against Explosion and Fire*. The Steel Construction Institute.

Su A., 2012. *Analysis of Explosion Load Effects in Pipe-racks*. Department of Marine Technology, Norwegian University of Science and Technology, Trondheim, Norway.

Appendix A FEA Study Documentation

Appendix A contains a complete documentation on the methods and procedures used to derive pre-processing data implemented in the FE analyses within this study. The specific features and commands within the Abaqus toolbox utilized in the FE simulations are also presented herein.

A.1 System of Units

The SI system of units as specified by Table A- 1 was used for implementation in Abaqus.

| | SI Unit | Description |
|-------------------|---|----------------------------|
| Length | m | meters |
| Force | MN | MegaNewton |
| Moment | MNm | MegaNewtonmeter |
| Stress | MN/m ² (MPa) | MegaPascal |
| Acceleration | m/s ² (g=9.81 m/s ²) | Meter pr. square second |
| Mass | kt | kilotonnes |
| Density | kt/m ³ | Kilotonnes pr. cubic meter |
| Moment of inertia | m ⁴ | Meter in fourth |
| Sectional Modulus | m ³ | Meter in cubic |

Table A- 1 System of units in Abaqus.

A.2 Modeling of Pipe Support Designs

Table A- 2 below show the DOFs constrained by the different support functions discussed in Section 5.3, given that the supported pipe line section is oriented parallel the global Y-axis of the reference coordinate system which is the case for all internal pipe supports located within *Piperack01_P30_M50*.

| Support Function | DOF1 / Global UX | DOF2 / Global UY | DOF3 / Global UZ | DOF4 / Global URX | DOF5 / Global URY | DOF6 / Global URZ |
|------------------|------------------|------------------|------------------|-------------------|-------------------|-------------------|
| RS | | | x | | | |
| HD | | | x | | | |
| LG | x | | | | | |
| LS | | x | | | | |

Table A- 2 Pipe support functions and constrained DOFs.

The typical pipe support configuration shown in Figure A- 1 is oriented in the global coordinate system and designed with support functions; RS, HD, LG and LS. For this type of pipe support design, the attached pipe line would be considered constrained in DOFs UX, UY and UZ within this study.

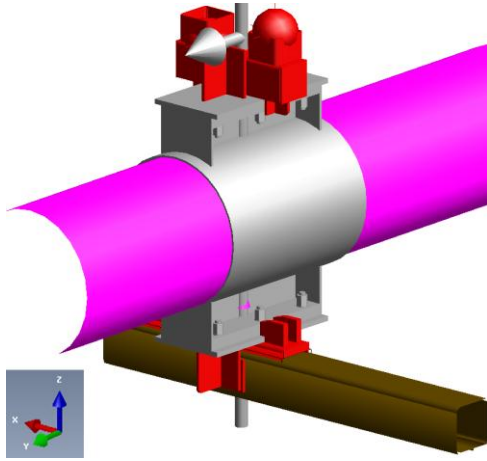


Figure A-1 Typical pipe support configuration.

Figures and tables below show the locations and support functions associated with all pipe supports attached to *Piperack01_P30_M50*. Along with the information provided in Table A-2, they define the properties of all boundary conditions created in order to constrain FE model A. A simplified approach was adopted where all external supports were considered fully fixed, constraining all translational and rotational DOFs.

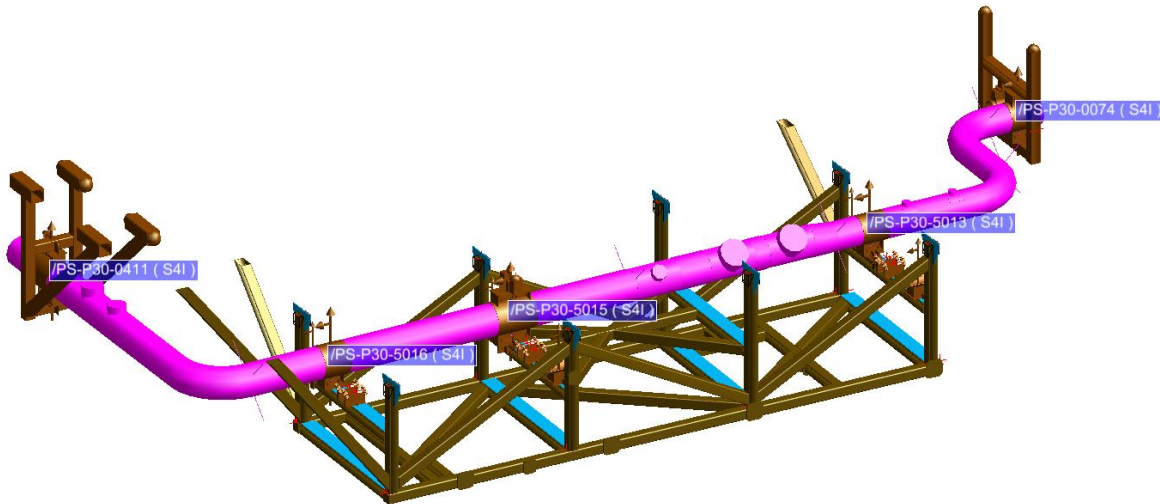


Figure A-2 Pipe supports associated with pipe line 43057.

| Support Label | Support Type | Support Functions | Global Coordinates [m] | | |
|---------------|--------------|-------------------|------------------------|---------|-------|
| | | | X | Y | Z |
| 0411 | External | Fully Fixed | 383.911 | 162.95 | 535.5 |
| 5016 | Internal | RS | 379.69 | 161 | 535.5 |
| 5015 | Internal | RS,LG,HD,LS | 379.69 | 158.25 | 535.5 |
| 5013 | Internal | RS,LG,HD | 379.69 | 152.75 | 535.5 |
| 0074 | External | Fully Fixed | 381.69 | 149.384 | 535.5 |

Table A-3 Pipe supports associated with pipe line 43057.

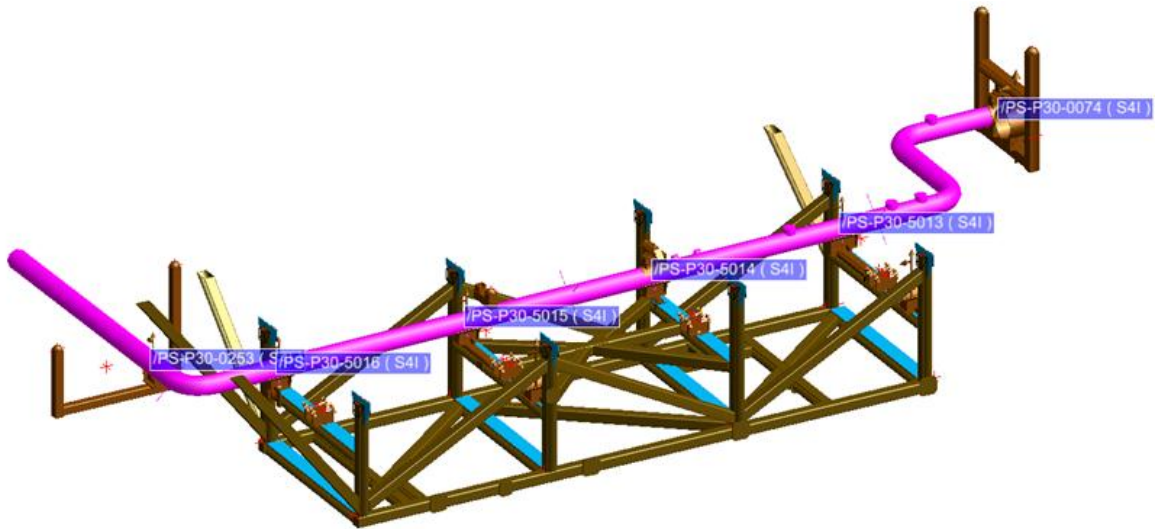


Figure A-3 Pipe supports associated with pipe line 43127.

| Support Label | Support Type | Support Functions | Global Coordinates [m] | | |
|---------------|--------------|-------------------|------------------------|---------|-------|
| | | | X | Y | Z |
| 0253 | External | Fully Fixed | 381.125 | 162.5 | 535.5 |
| 5016 | Internal | RS, HD | 380.2 | 161 | 535.5 |
| 5015 | Internal | RS, LG, HD | 380.2 | 158.25 | 535.5 |
| 5014 | Internal | RS, HD | 380.2 | 155.5 | 535.5 |
| 5013 | Internal | RS, LG, HD, LS | 380.2 | 152.75 | 535.5 |
| 0074 | External | Fully Fixed | 382.1 | 149.384 | 535.5 |

Table A-4 Pipe supports associated with pipe line 43127.

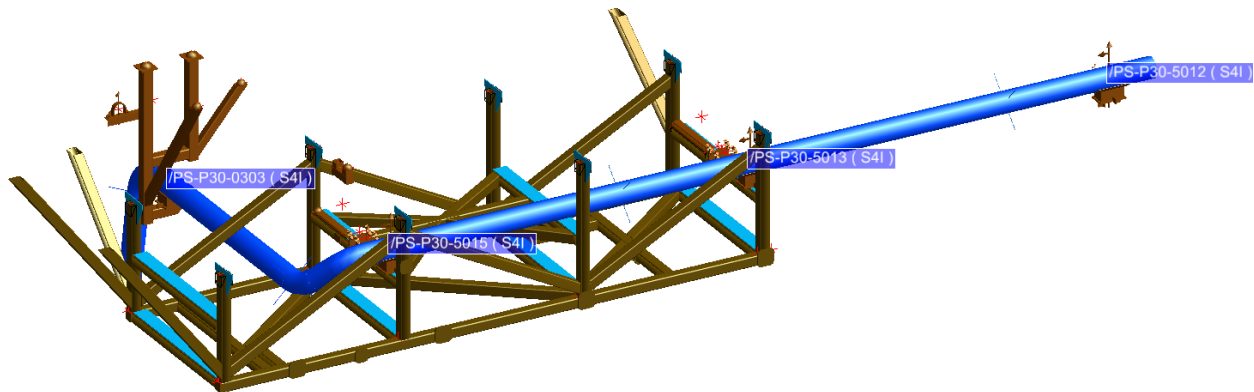


Figure A-4 Pipe supports associated with pipe line 20009.

| Support Label | Support Type | Support Functions | Global Coordinates [m] | | |
|---------------|--------------|-------------------|------------------------|---------|--------|
| | | | X | Y | Z |
| 0303 | External | Fully Fixed | 382.55 | 159.343 | 535.32 |
| 5015 | Internal | RS, LG, HD | 378.35 | 158.25 | 535.5 |
| 5013 | Internal | RS, LG, HD | 378.35 | 152.75 | 535.5 |
| 5012 | External | Fully Fixed | 378.35 | 147.25 | 535.5 |

Table A-5 Pipe supports associated with pipe line 20009.

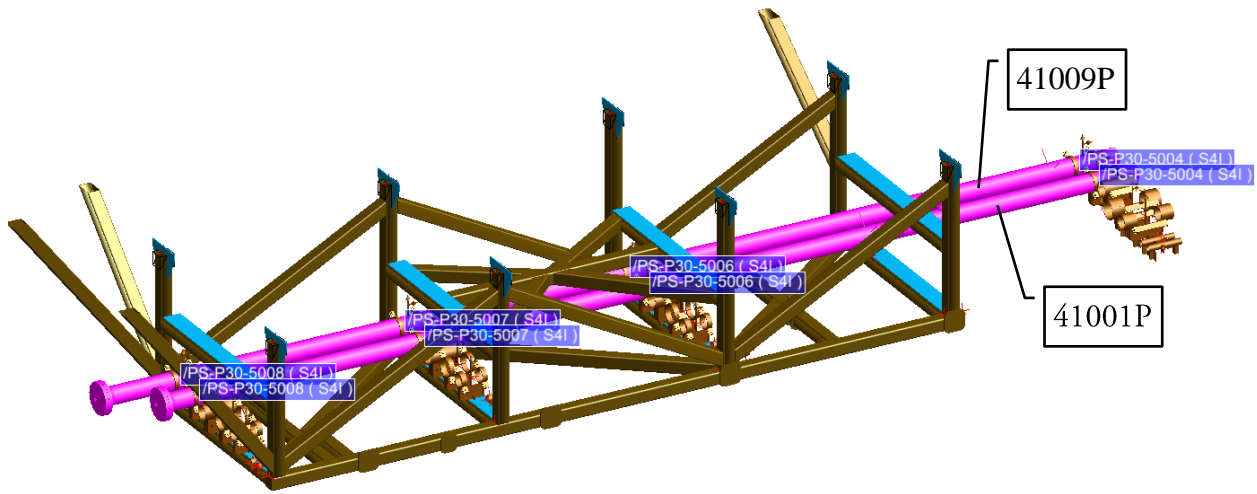


Figure A- 5 Pipe supports associated with pipe lines 41009P and 41001P.

| Support Label | Support Type | Support Functions | Global Coordinates [m] | | |
|---------------|--------------|-------------------|------------------------|--------|------------|
| | | | 41009P/41001P | | |
| | | | X | Y | Z |
| 5008 | Internal | RS, LG, HD | 380.7/379.635 | 161 | 534.640015 |
| 5007 | Internal | RS,LG, HD | 380.7/379.635 | 158.25 | 534.640015 |
| 5006 | Internal | RS,LG, HD | 380.7/379.635 | 155.5 | 534.640015 |
| 5004 | External | Fully Fixed | 380.7/379.635 | 150 | 534.640015 |

Table A- 6 Pipe supports associated with pipe lines 41009P and 41001P.

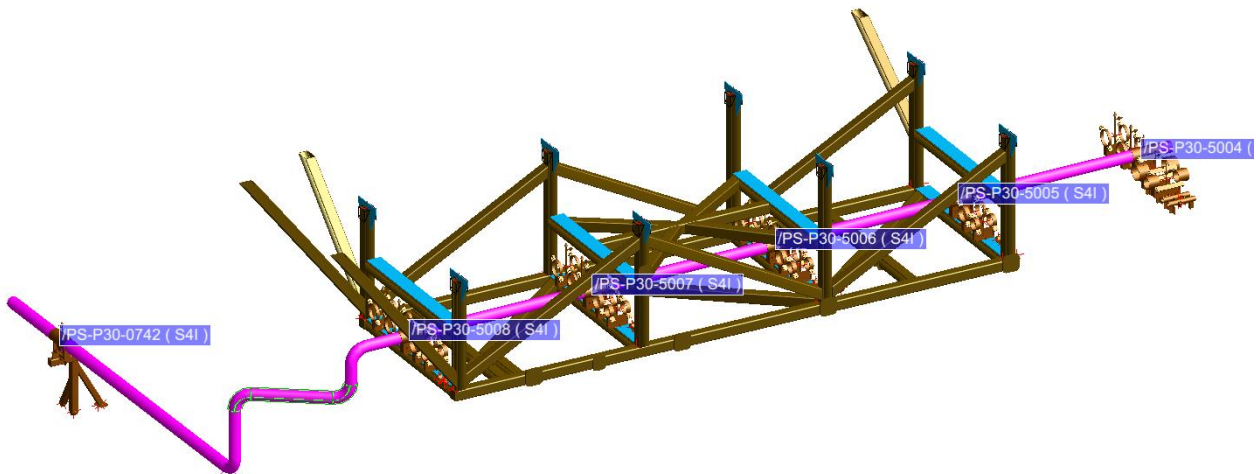


Figure A- 6 Pipe supports associated with pipe line 43119.

| Support Label | Support Type | Support Functions | Global Coordinates [m] | | |
|---------------|--------------|-------------------|------------------------|---------|------------|
| | | | X | Y | Z |
| 0742 | External | Fully Fixed | 384.912 | 163.164 | 533.038 |
| 5008 | Internal | RS, LG, HD | 379.285 | 161 | 534.640015 |
| 5007 | Internal | RS, LG, HD | 379.285 | 158.25 | 534.640015 |
| 5006 | Internal | RS, LG, HD, LS | 379.285 | 155.5 | 534.640015 |
| 5005 | Internal | RS, LG, HD | 379.285 | 152.75 | 534.640015 |
| 5004 | External | Fully Fixed | 379.285 | 150 | 534.640015 |

Table A- 7 Pipe supports associated with pipe line 43119.

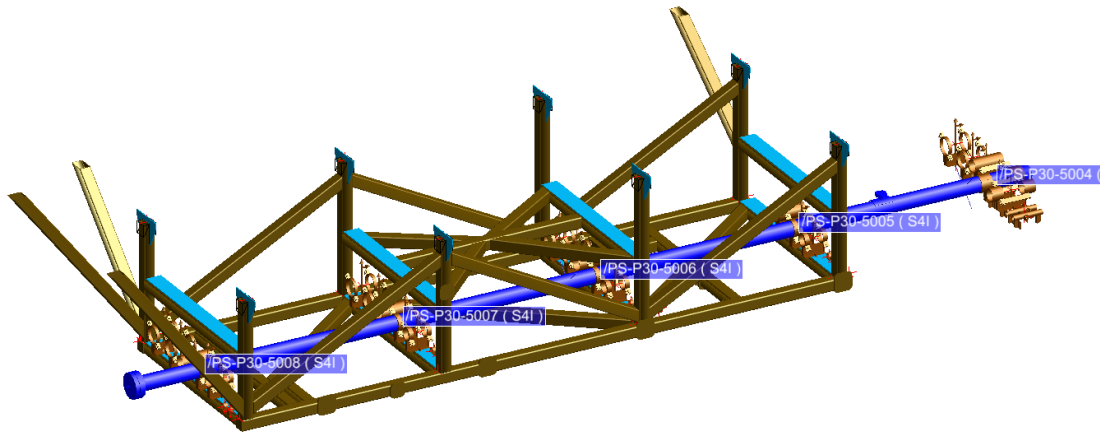


Figure A- 7 Pipe supports associated with pipe line 50023.

| Support Label | Support Type | Support Functions | Global Coordinates [m] | | |
|---------------|--------------|-------------------|------------------------|--------|------------|
| | | | X | Y | Z |
| 5008 | Internal | RS, LG, HD | 378.96 | 161 | 534.640015 |
| 5007 | Internal | RS, HD | 378.96 | 158.25 | 534.640015 |
| 5006 | Internal | RS, LG, HD | 378.96 | 155.5 | 534.640015 |
| 5005 | Internal | RS, HD | 378.96 | 152.75 | 534.640015 |
| 5004 | External | Fully Fixed | 378.96 | 150 | 534.640015 |

Table A- 8 Pipe supports associated with pipe line 50023.

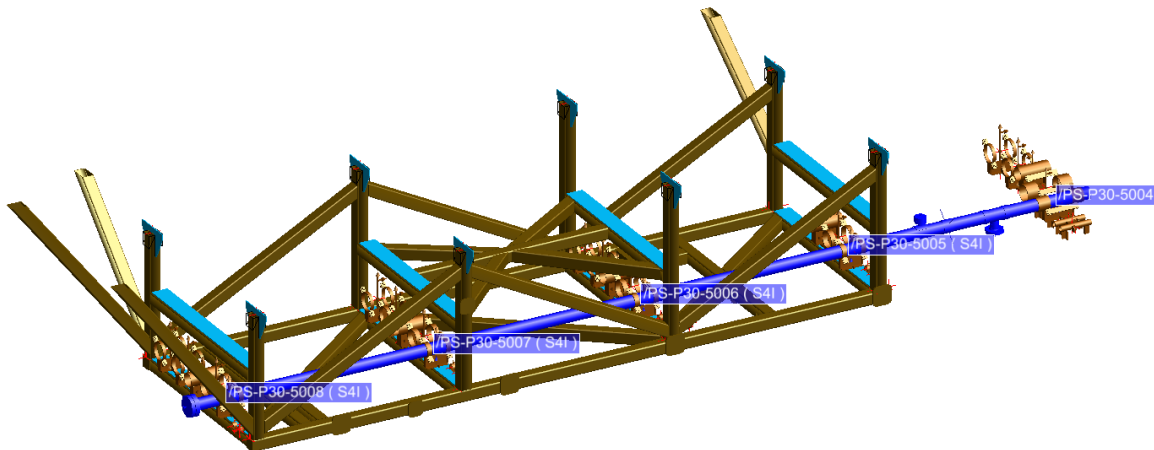


Figure A- 8 Pipe supports associated with pipe line 50010.

| Support Label | Support Type | Support Functions | Global Coordinates [m] | | |
|---------------|--------------|-------------------|------------------------|--------|------------|
| | | | X | Y | Z |
| 5008 | Internal | RS, LG, HD | 378.665 | 161 | 534.640015 |
| 5007 | Internal | RS, LG, HD | 378.665 | 158.25 | 534.640015 |
| 5006 | Internal | RS, LG, HD | 378.665 | 155.5 | 534.640015 |
| 5005 | Internal | RS, LG, HD | 378.665 | 152.75 | 534.640015 |
| 5004 | External | Fully Fixed | 378.665 | 150 | 534.640015 |

Table A-9 Pipe supports associated with pipe line 50010.

A.3 Modeling of Rack Structure Connection Designs

The design of the eight gusset plate connections fixing vertical beam elements to deck girders is shown in Figure A-9. Gusset plates are assumed to be designed with a fold line that allows for rotation about the global X-axis under severe loading while constraining motion in all other DOFs. This assumed behavior was consistently enforced in all analyses of FE model B via boundary conditions constraining DOFs according to Table A-10. The four braces are welded directly to a relatively rigid deck structure as shown in Figure A-9 and are therefore assumed to act as fully fixed supports. This behavior is also enforced in FE simulations according to Table A-10.

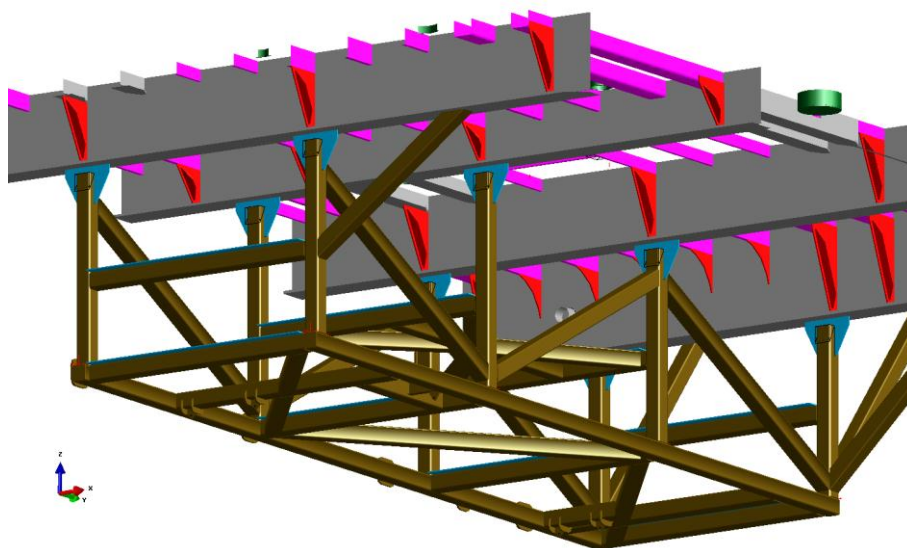


Figure A-9 Illustration of rack structure connection design.

| Support Type | Constrained DOFs | | | | | |
|-------------------------|------------------------|------------------------|------------------------|-------------------------|-------------------------|-------------------------|
| | DOF1 / Global UX | DOF2 / Global UY | DOF3 / Global UZ | DOF4 / Global URX | DOF5 / Global URY | DOF6 / Global URZ |
| Gusset Plate Connection | x | x | x | | x | x |
| Direct Weld | x | x | x | x | x | x |

Table A-10 Constrained DOFs in modelling of rack structure connections.

A.4 Material Properties of Pipe Lines

The linear-elastic mechanical properties and density of the materials associated with each pipe line are provided in Table A- 11 below, specified at a temperature of 20 degrees Celsius. The data is provided by the AKSO piping department responsible for design and verification of all pipe lines.

| Material Code | Density [kg/m ³] | Young's Modulus [MPa] | Yield Stress [MPa] | Poisson's Ratio | Material Description |
|---------------|------------------------------|-----------------------|--------------------|-----------------|--|
| A312 S31254 | 8000.0 | 200.0E+3 | 303 | 0.292 | Stainless steel, isotropic. |
| A790 S31803 | 8027.2 | 195.1285E+3 | 448.159 | 0.292 | Duplex stainless steel, isotropic. |
| A333 6 | 7833.440 | 203.4025E+3 | 241.325 | 0.292 | Carbon steel, isotropic. |
| GRE | 1849 | 12.0E+3 | 85.0 | 0.35 | Glass fiber reinforced epoxy, anisotropic. Mechanical properties provided herein correspond to axial bending mode. |

Table A- 11 Material properties of pipe line configuration.

In order to account for the mass contribution from the piping content, the pipe material density data given by Table A- 11 was scaled with a fluid content factor to obtain a modified density, ρ_{mod} . This factor was calculated based on fluid density data and pipe geometry data in Table 5-2 and results are presented in Table A- 12.

The weight per meter length of each pipe line was calculated according to Equation (A.1).

$$W_{mpipe} = \pi \cdot (r_o^2 - r_i^2) \cdot \rho \quad (A.1)$$

where W_{mpipe} is the weight per meter pipe; r_o is the outer pipe section radius; r_i is the inner pipe section radius; and ρ is the pipe material density.

The weight of pipe content per meter length was calculated according to Equation (A.2).

$$WC_{mpipe} = \pi \cdot r_i^2 \cdot \rho_{fluid} \quad (A.2)$$

where WC_{mpipe} is the content weight per meter pipe; and ρ_{fluid} is the density of the fluid content.

Finally, the fluid content factor (FCF) was obtained through Equation (A.3).

$$FCF = 1 + \frac{WC_{mpipe}}{W_{mpipe}} \quad (A.3)$$

| Pipe Line | Fluid Content Factor (FCF) | Modified Material Density (ρ_{mod}) [kg/m ³] |
|-------------------|----------------------------|---|
| 43057 | 1.014 \approx 1.0 | N/A. Refer to Table 5-2 & Table A-11. |
| 43127 | 1.004 \approx 1.0 | N/A. Refer to Table 5-2 & Table A-11. |
| 20009 | 1.028 \approx 1.0 | N/A. Refer to Table 5-2 & Table A-11. |
| 41009P/ 41001P | 1.684 | 13191.513 |
| 43119 | 1.005 \approx 1.0 | N/A. Refer to Table 5-2 & Table A-11. |
| 50023 | 6.745 | 12471.505 |
| 50010 | 6.597 | 12164.571 |

Table A- 12 Modified pipe material density data.

The mass contribution from piping content is seen to be very small for most pipe lines and has been ignored when considered negligible as illustrated by Table A- 12.

A.5 Load Cases and Combinations

The combination of load factors and load actions considered in this study comply with regulations of an Accidental Limit State (ALS) condition according to (NORSOK N-001, 2012) and (NORSOK N-003, 2007). The governing combination of load actions for ALS is given by Equation (A.4):

$$ALS = 1.0G + 1.0Q + 1.0D + 1.0A \quad (A.4)$$

where G denotes permanent load actions; Q denotes variable load actions; D denotes deformation load actions; and A denotes accidental load actions.

The basic load cases that were considered in analyses of *Piperack01_P30_M50* are summarized in Table A- 13. Self-weight of rack members, pipe members and weight of pipe content constitute the total dead weight in the pipe rack system and the only permanent load actions considered. Accidental loads are defined by the propagation of a blast-pulse in six main directions. No variable or deformation load actions were considered relevant for this study.

| Load Case | Load Action | Description |
|-----------|-------------|------------------------------------|
| 1 | G | Dead-weight in Global -Z Direction |
| 2 | A | Blast Load in Global +X Direction |
| 3 | A | Blast Load in Global -X Direction |
| 4 | A | Blast Load in Global +Y Direction |
| 5 | A | Blast Load in Global -Y Direction |
| 6 | A | Blast Load in Global +Z Direction |
| 7 | A | Blast Load in Global -Z Direction |

Table A- 13 Basic Load Cases.

A.6 Tributary Length Calculations

The analyses of FE model B simulating an accidental explosion event require simplified but precise procedures for calculating the contribution in mass and transfer in blast-loads associated with the piping configuration. The approach adopted in this study includes defining a tributary length for each internal pipe support. The tributary length is denoted L_t and depends on the support function of the pipe support and the direction of the loading.

Each specific support can have a maximum of three different values of tributary length associated with it. The value associated with blast load in vertical direction and gravity loading will naturally be identical. For blast loading in transverse and longitudinal direction however, the tributary length depends on the support functions of other pipe supports attached to the specific pipe line.

The procedure of calculating tributary lengths is presented below.

- STEP 1: Specify load direction and pipe support for calculation of associated tributary length. The support that is considered for calculation is referred to as the *primary support*.
- STEP 2: Determine if the support functions of the *primary support* constrain translational motion in the direction of the load. If the answer is:
NO, then the tributary length is zero.
YES, then continue to Step 3.
- STEP 3: Calculate the length of pipe section between the *primary support* and *secondary supports* exposed to loading in the specific direction. *Secondary supports* are defined as the two supports closest to the *primary support* (one on each side) that also constrains translational motion in the direction of the load. This length is referred to the *exposed length*.
- STEP 4: Assume that the load imposed on the pipe section is shared equally between the *primary support* and *secondary supports*. Hence, the tributary length associated with the *primary support* is calculated as half of the *exposed length*.

The implementation of steps 1 to 4 is demonstrated for the configuration and geometry of pipe line 43057 as specified by Figure A- 2 and Table A- 3. Consider support 5015 as the primary support, constrained in all translational DOFs and therefore associated with three values of tributary length. The following tributary lengths are calculated for loading in the different directions:

Transverse (Global X)

Refer to Figure A- 10 (a). Constrained motion is given by support function LG, thus secondary supports are defined as 0411 and 5013. The exposed length is given by the sum of LX1 and LX2, and the tributary length L_t by $(LX1 + LX2)/2$. Length LX1 is calculated from the center of the curved pipe segment.

Longitudinal (Global Y):

Refer to Figure A- 10 (b). Constrained motion is given by support function LS, thus secondary supports are defined as 0411 and 0074. The exposed length is given by the sum of LY1 and LY2, and the tributary length L_t by $(LY1 + LY2)/2$. Lengths LY1 and LY2 are calculated from the center of the curved pipe segments.

Vertical (Global Z):

Refer to Figure A- 10 (c). Constrained motion is given by support function HD or RS, thus secondary supports are defined as 5016 and 5013. The exposed length is given by the sum of LZ1 and LZ2, and the tributary length L_t by $(LZ1 + LZ2)/2$.

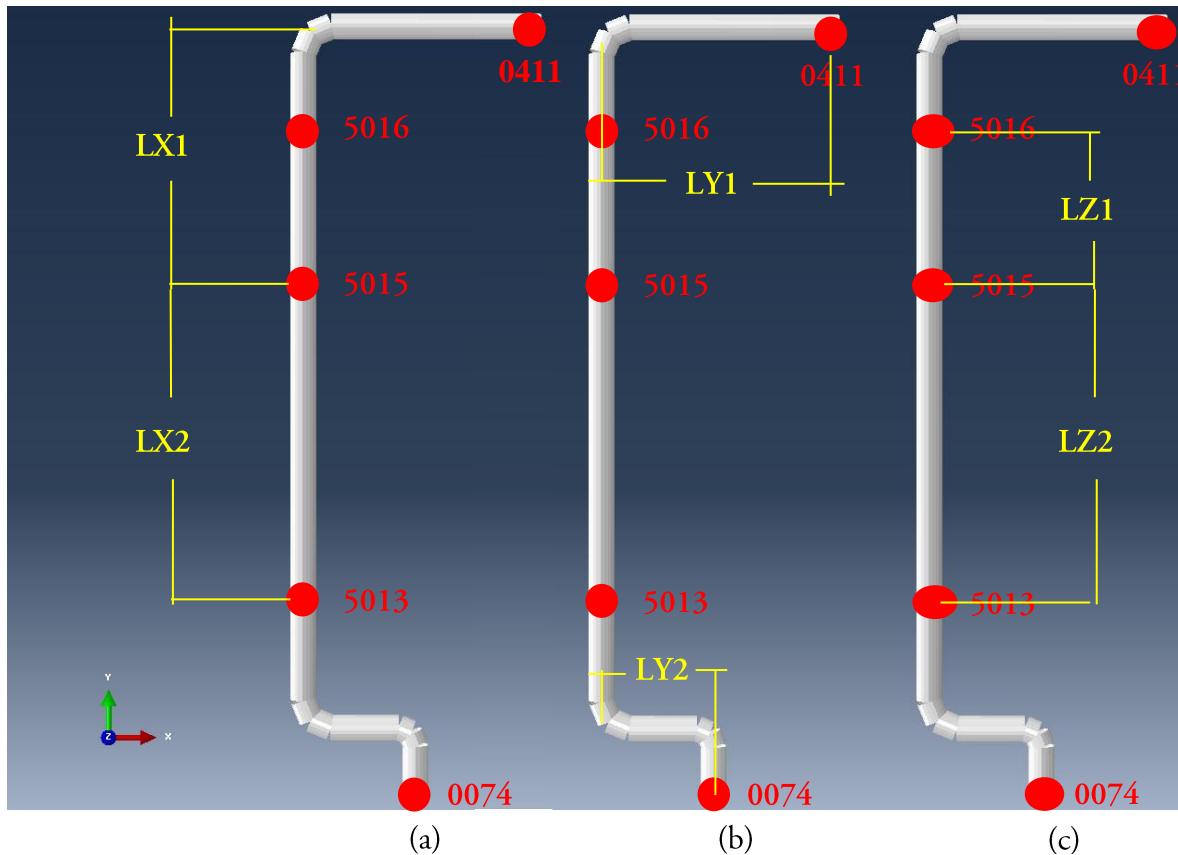


Figure A- 10 Illustration of tributary length calculations.

Table A- 14 shows the calculated tributary lengths for all internal pipe supports and all directions of loading. Values account for the true support functions of each pipe support as documented in Section A.2.

| Pipe Line | Pipe Support | Direction of Loading | | |
|-------------------|--------------|----------------------|--------------------|--------------------|
| | | Transverse | Longitudinal | Vertical |
| | | L _t [m] | L _t [m] | L _t [m] |
| 43057 | 5016 | 0 | 0 | 4.314 |
| | 5015 | 5.027 | 1.947 | 4.125 |
| | 5013 | 4.433 | 0 | 5.316 |
| 43127 | 5016 | 0 | 0 | 2.446 |
| | 5015 | 4.763 | 0 | 2.750 |
| | 5014 | 0 | 0 | 2.750 |
| | 5013 | 4.433 | 0.422 | 3.891 |
| 20009 | 5015 | 3.491 | 0 | 5.214 |
| | 5013 | 5.5 | 0 | 5.5 |
| 41009P/ 41001P | 5008 | 2.375 | 0 | 2.375 |
| | 5007 | 2.75 | 0 | 2.75 |
| | 5006 | 4.125 | 0 | 4.125 |
| 43119 | 5008 | 3.539 | 0 | 4.923 |
| | 5007 | 2.75 | 0 | 2.75 |
| | 5006 | 2.75 | 2.683 | 2.75 |
| | 5005 | 2.75 | 0 | 2.75 |
| 50023 | 5008 | 3.774 | 0 | 2.399 |
| | 5007 | 0 | 0 | 2.75 |
| | 5006 | 5.5 | 0 | 2.75 |
| | 5005 | 0 | 0 | 2.75 |
| 50010 | 5008 | 1.875 | 0 | 1.875 |
| | 5007 | 2.75 | 0 | 2.75 |
| | 5006 | 2.75 | 0 | 2.75 |
| | 5005 | 2.75 | 0 | 2.75 |

Table A- 14 Tributary lengths of internal pipe supports.

A.7 Mass Calculations

The mass contribution from the pipe lines and their content must be considered in order to account for the true inertial properties of the dynamic system. Masses associated with each internal pipe support were calculated based on the tributary lengths in vertical direction given by Table A- 14, the fluid content factor according to Table A- 12 and the pipe weight per meter length given by Equation (A.1).

The masses associated with each pipe support shown in Table A- 15 were calculated according to above referenced data and methods, summarized in Equation (A.5).

$$m_{ps} = L_t \cdot W_{mpipe} \cdot FCF \quad (A.5)$$

| Pipe Line | Pipe Support | L _t [m] | W _{mpipe} [kg/m] | FCF | m _{ps} [kt] |
|-------------------|--------------|--------------------|---------------------------|-------|----------------------|
| 43057 | 5016 | 4.314 | 141.814 | 1 | 6.12E-04 |
| | 5015 | 4.125 | | | 5.85E-04 |
| | 5013 | 5.316 | | | 7.54E-04 |
| 43127 | 5016 | 2.446 | 28.414 | 1 | 6.95E-05 |
| | 5015 | 2.750 | | | 7.81E-05 |
| | 5014 | 2.750 | | | 7.81E-05 |
| | 5013 | 3.891 | | | 1.11E-04 |
| 20009 | 5015 | 5.214 | 50.851 | 1 | 2.65E-04 |
| | 5013 | 5.5 | | | 2.80E-04 |
| 41009P/ 41001P | 5008 | 2.375 | 42.457 | 1.684 | 1.70E-04 |
| | 5007 | 2.75 | | | 1.97E-04 |
| | 5006 | 4.125 | | | 2.95E-04 |
| 43119 | 5008 | 4.923 | 43.487 | 1 | 2.14E-04 |
| | 5007 | 2.75 | | | 1.20E-04 |
| | 5006 | 2.75 | | | 1.20E-04 |
| | 5005 | 2.75 | | | 1.20E-04 |
| 50023 | 5008 | 2.399 | 6.097 | 6.745 | 9.87E-05 |
| | 5007 | 2.75 | | | 1.13E-04 |
| | 5006 | 2.75 | | | 1.13E-04 |
| | 5005 | 2.75 | | | 1.13E-04 |
| 50010 | 5008 | 1.875 | 3.724 | 6.597 | 4.61E-05 |
| | 5007 | 2.75 | | | 6.76E-05 |
| | 5006 | 2.75 | | | 6.76E-05 |
| | 5005 | 2.75 | | | 6.76E-05 |

Table A- 15 Distribution of pipe configuration mass over internal pipe supports.

A.8 Blast Load Calculations

Calculations of blast loads documented herein are based on the governing design blast-pulse as defined in Section 5.8 of the main report. The calculated blast loads are static and derived from the peak pressure of the design blast-pulse. They must therefore be scaled with an amplitude curve in Abaqus, with a shape according to the blast-pulse, in order to simulate a dynamic pulse excitation. This procedure is described in Section A.10.

Paragraphs below show calculations of all the blast loads that were implemented in the various FE analyses conducted within the FEA study. Calculations according to *Load Procedure 1, 2 and 3* are documented separately. Although not utilized explicitly herein, Equation (A.6) provided below show the governing formula for calculating uniformly distributed drag loads (UDL) on structural members according to the conventional method.

$$UDL = C_d \cdot p_1 \cdot W_m \cdot \eta \cdot DAF \quad (A.6)$$

where C_d is the drag coefficient associated with the member; p_1 is the design peak-pressure; W_m is the width/outer diameter of the member/pipe facing the direction of the blast wind; η is a shielding coefficient; and DAF is the dynamic amplification factor derived from the *Linear-elastic Biggs method*.

The same drag coefficients that were implemented in the original verification process according to the conventional method were used in all three load procedures for consistency. Values shown in Table A- 16 are specified by (DNV-RP-C205, 2010). The shape coefficient may be considered as zero however when the direction of the blast wave is parallel to the axial direction of the member, assuming that such members will not be subjected to loading.

| Member Type | C_d |
|-------------|-------|
| RHS/SHS | 1.6 |
| IPE | 2.0 |
| Pipe | 1.0 |

Table A- 16 Drag coefficients for blast load calculations.

Load Procedure 1

Blast loads calculated according to this procedure was implemented in analyses A.1 and B.1. Shielding effects are neglected and the governing equation for blast load calculations is therefore given by Equation (A.7), where the dynamic blast-pressure is converted into a drag load in accordance with conclusions from Chapter 2.

$$UDL = C_d \cdot p_1 \cdot W_m \quad (A.7)$$

Table A- 17 summarizes the uniformly distributed loads imposed on the rack members when calculated according to Equation (A.7) and associated input data presented in Section 5.3.2, Section 5.8 and Table A- 16.

| Section Profile | C_d | $W_{m,1}$ [m] | UDL_1 [MN/m] | $W_{m,2}$ [m] | UDL_2 [MN/m] |
|-----------------|-------|---------------|----------------|---------------|----------------|
| SHS150 | 1.6 | 0.15 | 0.0048 | N/A | N/A |
| IPE120 | 2.0 | 0.048 | 0.00192 | 0.12 | 0.0048 |

Table A- 17 UDL on rack members according to Load Procedure 1.

SHS sections are symmetric and will expose the same member width in all applicable load directions ($W_{m,1}$). Hence, calculation of one UDL is sufficient given by UDL_1 in Table A- 17. IPE sections however expose either the width of the flange ($W_{m,1}$) or the height of the section ($W_{m,2}$). Since the pipe rack design only contains one IPE member oriented in the global coordinate system as specified in Section 5.3.2, the load UDL_1 is strictly associated with loading in vertical direction and UDL_2 with loading in longitudinal direction.

Table A- 18 show the uniformly distributed loads imposed on the pipe lines from calculations according to Equation (A.7) and input data specified in Section 5.3.1, Section 5.8 and Table A- 16.

| Pipe Line | C_d | $W_m (=OD)$ [m] | UDL [MN/m] |
|-------------------|-------|-----------------|------------|
| 43057 | 1.0 | 0.457 | 0.00914 |
| 43127 | 1.0 | 0.2731 | 0.00546 |
| 20009 | 1.0 | 0.3239 | 0.00648 |
| 41009P/ 41001P | 1.0 | 0.2191 | 0.00438 |
| 43119 | 1.0 | 0.1683 | 0.00337 |
| 50023 | 1.0 | 0.2191 | 0.00438 |
| 50010 | 1.0 | 0.1683 | 0.00337 |

Table A- 18 UDL on pipe lines according to Load Procedure 1.

Explicit application of the UDLs above on the pipe line configuration was only relevant for analysis A.1 as it was the only one containing modeled pipe geometry. Figure A- 11 illustrates application of blast load in global +X-direction for this analysis.

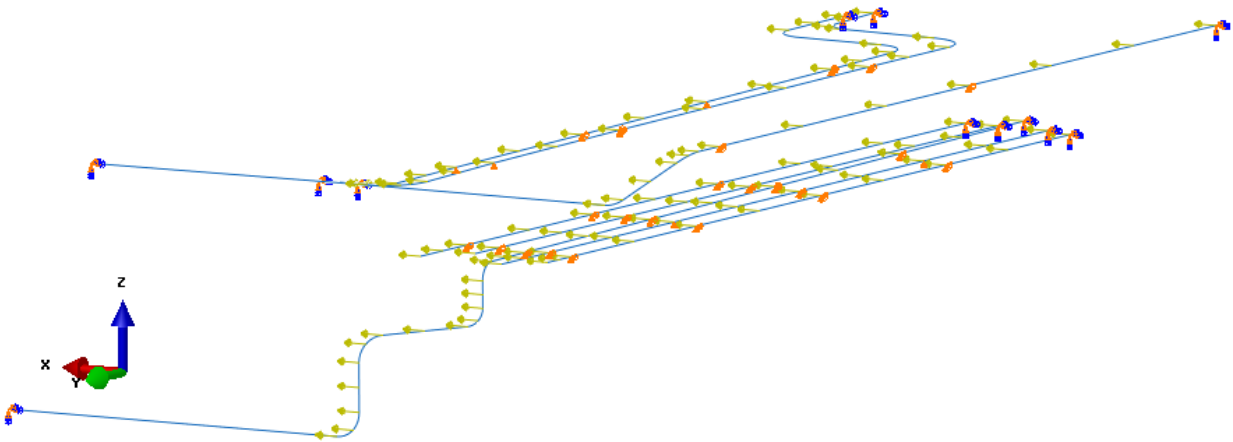


Figure A- 11 UDL applied on piping configuration for blast in global +X-direction according to Load Procedure 1.

For the analyses where the piping configuration was not modelled, the uniformly distributed load that would act on each pipe line were converted into support reactions in form of point loads. This was achieved by multiplying the distributed loads documented in Table A- 18 with the tributary length L_t associated with each support according to Equation (A.8).

$$PL = C_d \cdot p_1 \cdot W_m \cdot L_t \quad (A.8)$$

Tributary length calculations as outlined in Section A.6 will ensure an accurate distribution of piping blast-loads via the exact location of the pipe supports that constrain translational motion in the direction of loading. Table A- 19 summarizes the loads calculated according to Equation (A.8), Table A- 14 and data referenced in association with Equation (A.7).

| Pipe Line | Pipe Support | Direction of Loading | | | | | |
|-------------------|--------------|----------------------|---------|--------------------|---------|--------------------|---------|
| | | Transverse | | Longitudinal | | Vertical | |
| | | L _t [m] | PL [MN] | L _t [m] | PL [MN] | L _t [m] | PL [MN] |
| 43057 | 5016 | 0 | 0 | 0 | 0 | 4.314 | 0.0394 |
| | 5015 | 5.027 | 0.0459 | 1.947 | 0.0178 | 4.125 | 0.0377 |
| | 5013 | 4.433 | 0.0405 | 0 | 0 | 5.316 | 0.0486 |
| 43127 | 5016 | 0 | 0 | 0 | 0 | 2.446 | 0.0134 |
| | 5015 | 4.763 | 0.0260 | 0 | 0 | 2.750 | 0.0150 |
| | 5014 | 0 | 0 | 0 | 0 | 2.750 | 0.0150 |
| | 5013 | 4.433 | 0.0242 | 0.422 | 0.0023 | 3.891 | 0.0213 |
| 20009 | 5015 | 3.491 | 0.0226 | 0 | 0 | 5.214 | 0.0338 |
| | 5013 | 5.5 | 0.0356 | 0 | 0 | 5.5 | 0.0356 |
| 41009P/ 41001P | 5008 | 2.375 | 0.0104 | 0 | 0 | 2.375 | 0.0104 |
| | 5007 | 2.75 | 0.0121 | 0 | 0 | 2.75 | 0.0121 |
| | 5006 | 4.125 | 0.0181 | 0 | 0 | 4.125 | 0.0181 |
| 43119 | 5008 | 3.539 | 0.0119 | 0 | 0 | 4.923 | 0.0166 |
| | 5007 | 2.75 | 0.0093 | 0 | 0 | 2.75 | 0.0093 |
| | 5006 | 2.75 | 0.0093 | 2.683 | 0.0090 | 2.75 | 0.0093 |
| | 5005 | 2.75 | 0.0093 | 0 | 0 | 2.75 | 0.0093 |
| 50023 | 5008 | 3.774 | 0.0165 | 0 | 0 | 2.399 | 0.0105 |
| | 5007 | 0 | 0 | 0 | 0 | 2.75 | 0.0121 |
| | 5006 | 5.5 | 0.0241 | 0 | 0 | 2.75 | 0.0121 |
| | 5005 | 0 | 0 | 0 | 0 | 2.75 | 0.0121 |
| 50010 | 5008 | 1.875 | 0.0063 | 0 | 0 | 1.875 | 0.0063 |
| | 5007 | 2.75 | 0.0093 | 0 | 0 | 2.75 | 0.0093 |
| | 5006 | 2.75 | 0.0093 | 0 | 0 | 2.75 | 0.0093 |
| | 5005 | 2.75 | 0.0093 | 0 | 0 | 2.75 | 0.0093 |

Table A-19 Point loads at internal pipe supports transferred via UDLs acting on pipe lines according to Load Procedure 1.

Load Procedure 2

Blast loads calculated according to *Load Procedure 2* were implemented in FE analyses B.2, B.4, B.5 and B.6. Only transverse blast loading is considered in calculations documented below. Shielding effects were accounted for and calculations of the governing shielding coefficient as well as the procedures outlining how to apply it are fully described in Appendix B.

The loads documented below were calculated according to Equation (A.9) and Equation (A.10) with application of the shielding coefficient as described by the procedure outlined in Appendix B.

$$UDL = C_d \cdot p_1 \cdot W_m \cdot \eta \quad (A.9)$$

$$PL = C_d \cdot p_1 \cdot W_m \cdot L_t \cdot \eta \quad (A.10)$$

Note that only the shielding coefficient η differentiates *Load Procedure 2* from the governing equations in *Load Procedure 1*. Hence, the load data provided in Table A- 17 and Table A- 19 is scaled with a factor of $\eta = 0.5$ when applicable, which is the value that was used consistently to account for mitigating effects for shielded members.

Table A- 20 summarizes the uniformly distributed loads imposed on shielded ($\eta = 0.5$) and fully exposed ($\eta = 1$) rack members when calculated according to *Load Procedure 2*. Note that the single IPE beam used in design of *Piperack01_P30_M50* is not subjected to blast load in transverse direction.

| Section Profile | Direction of Loading | |
|-----------------|----------------------|------------|
| | Global $\pm X$ | |
| | η | UDL [MN/m] |
| SHS150 | N/A (=1) | 0.0048 |
| | 0.5 | 0.0024 |

Table A- 20 UDL on rack members according to *Load Procedure 2*.

Table A- 21 summarizes the point loads calculated at each support according to *Load Procedure 2*. Shielded pipe lines in each blast direction are identified by associated shielding factor of $\eta = 0.5$.

| Pipe Line | Pipe Support | Direction of Loading | | | |
|-----------|--------------|----------------------|---------|-----------|---------|
| | | Global +X | | Global -X | |
| | | η | PL [MN] | η | PL [MN] |
| 43057 | 5016 | 0.5 | 0 | 0.5 | 0 |
| | 5015 | | 0.02295 | | 0.02295 |
| | 5013 | | 0.02025 | | 0.02025 |
| 43127 | 5016 | 0.5 | 0 | N/A (=1) | 0 |
| | 5015 | | 0.0130 | | 0.0260 |
| | 5014 | | 0 | | 0 |
| | 5013 | | 0.0121 | | 0.0242 |
| 20009 | 5015 | N/A (=1) | 0.0226 | 0.5 | 0.0113 |
| | 5013 | | 0.0356 | | 0.0178 |
| 41009P | 5008 | 0.5 | 0.0052 | N/A (=1) | 0.0104 |
| | 5007 | | 0.00605 | | 0.0121 |
| | 5006 | | 0.00905 | | 0.0181 |
| 41001P | 5008 | 0.5 | 0.0052 | 0.5 | 0.0052 |
| | 5007 | | 0.00605 | | 0.00605 |
| | 5006 | | 0.00905 | | 0.00905 |
| 43119 | 5008 | 0.5 | 0.00595 | 0.5 | 0.00595 |
| | 5007 | | 0.00465 | | 0.00465 |
| | 5006 | | 0.00465 | | 0.00465 |
| | 5005 | | 0.00465 | | 0.00465 |
| 50023 | 5008 | 0.5 | 0.00825 | 0.5 | 0.00825 |
| | 5007 | | 0 | | 0 |

| | | | | | |
|-------|------|----------|---------|-----|---------|
| | 5006 | | 0.01205 | | 0.01205 |
| | 5005 | | 0 | | 0 |
| 50010 | 5008 | N/A (=1) | 0.0063 | 0.5 | 0.00315 |
| | 5007 | | 0.0093 | | 0.00465 |
| | 5006 | | 0.0093 | | 0.00465 |
| | 5005 | | 0.0093 | | 0.00465 |

Table A- 21 Point loads at internal pipe supports transferred via UDLs acting on pipe lines according to Load Procedure 2.

Load Procedure 3

Blast loads on rack members were calculated and assigned according to *Load Procedure 2* and reference is made to Table A- 20.

Blast loads transferred to the rack structure via pipe supports were calculated according to the simplified approach outlined below. Note that this procedure does not account for shielding effects or the true tributary length of individual pipe supports as defined in Section A.6.

For each applicable frame section n , axially distributed loads q_{nL} and q_{nU} were calculated for application to horizontal rack members supporting the piping configuration. Figure A- 13 show the four frame sections ($n = 1, 2, 3, 4$) of *Piperack01_P30_M50* and associated horizontal members (X-Y plane) at the upper and lower rack level that were assigned loading.

Figure A- 12 illustrates an arbitrary configuration of a planar rack section. The variables shown are defined as follows:

- $H1$ is the outer diameter (OD) of the largest pipe section that is attached to the lower rack level and constrained in the direction of the loading. Constraints are governed by the support functions of associated pipe support as defined in previous sections of this appendix.
- $H2$ is the outer diameter (OD) of the largest pipe section that is attached to the upper rack level and constrained in the direction of the loading.
- W_{RS} is the width of the rack section.
- P_{nL} and P_{nU} are the total forces transferred to the lower respectively upper horizontal member of the rack section.

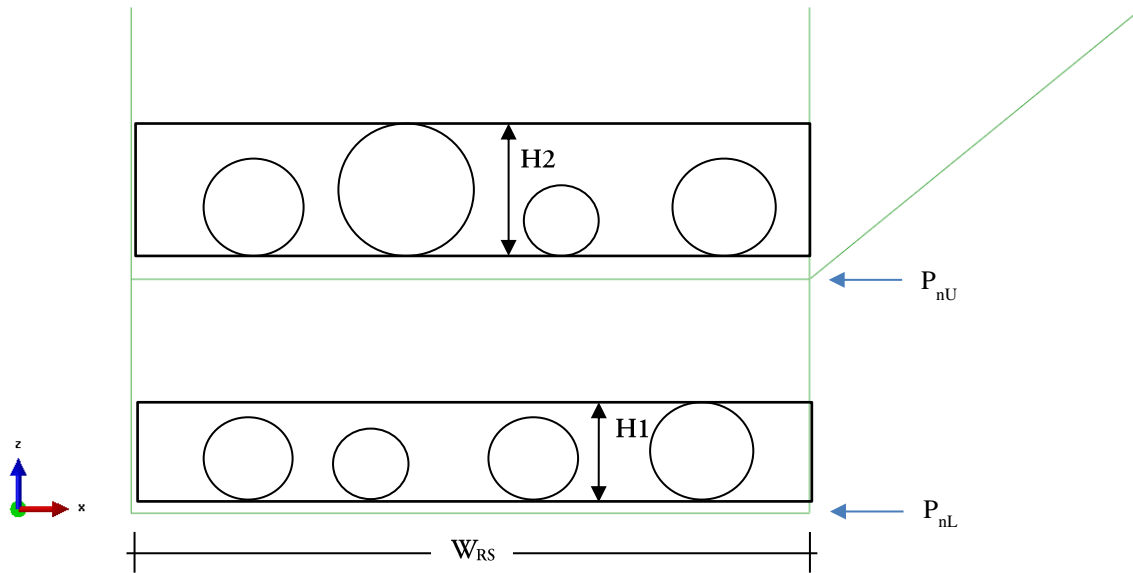


Figure A- 12 Arbitrary frame section illustrating blast load calculation according to Load Procedure 3.

The forces P_{nL} and P_{nU} are calculated according to Equation (A.11).

$$\begin{aligned}
 P_{nL} &= H1 \cdot L_{eff} \cdot C_d \cdot p_1 \\
 P_{nU} &= H2 \cdot L_{eff} \cdot C_d \cdot p_1
 \end{aligned}
 \tag{A.11}$$

where L_{eff} is the effective length associated with the n^{th} frame section.

The load is assumed to be distributed equally between two rack sections which define how to obtain the effective length L_{eff} . Figure A- 13 and Table A- 22 show how the effective lengths and forces associated with each frame section in *Piperack01_P30_M50* were calculated. Table A- 22 also show the governing pipe diameters $H1$ and $H2$, the rack section width W_{RS} , and the uniformly distributed loads q_{nL} and q_{nU} calculated according to Equation (A.12).

$$\begin{aligned}
 q_{nL} &= P_{nL}/W_{RS} \\
 q_{nU} &= P_{nU}/W_{RS}
 \end{aligned}
 \tag{A.12}$$

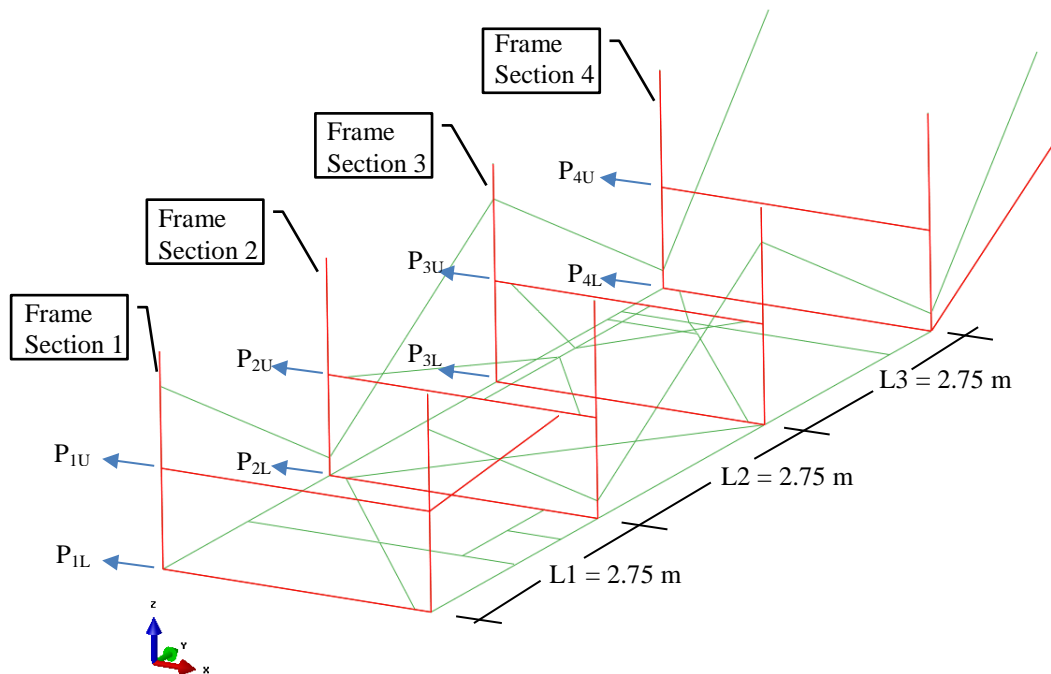


Figure A- 13 Frame section layout of Piperack01_P30_M50 governing blast load calculation according to Load Procedure 3.

| Frame Section | L_{eff} [m] | W_{RS} [m] | Blast Loads in Global $\pm X$ Direction | | | | | |
|---------------|--------------------|--------------|---|---------------|-----------------|-----------------------|---------------|-----------------|
| | | | Lower Rack Level | | | Upper Rack Level | | |
| | | | H1 [m] / Pipe Line | P_{nL} [MN] | q_{nL} [MN/m] | H2 [m] / Pipe Line | P_{nU} [MN] | q_{nU} [MN/m] |
| 1 | $L1/2 = 1.375$ | 2.5 | 0.2191 / 50023 | 0.0060 | 0.0024 | 0 | 0 | 0 |
| 2 | $(L1+L2)/2 = 2.75$ | 2.5 | 0.2191 / 41001P | 0.0121 | 0.0048 | 0.457 / 43057 | 0.0251 | 0.0101 |
| 3 | $(L2+L3)/2 = 2.75$ | 2.5 | 0.2191 / 50023 | 0.0121 | 0.0048 | 0 | 0 | 0 |
| 4 | $L3/2 = 1.375$ | 2.5 | 0.1683 / 50010 | 0.0046 | 0.0019 | 0.457 / 43057 | 0.0126 | 0.0050 |

Table A- 22 UDLs at horizontal rack members transferred via blast acting on pipe lines according to Load Procedure 3.

A.9 Exposed Blast-Area Calculations

The procedure of deriving a limiting blast-pressure according to the proposed method requires that the total member area in the system exposed to the blast wave, A_{Blast} , is calculated. Calculations of exposed blast-area in transverse direction are presented below. Note that the exposed area is identical for global $\pm X$ directions.

The total piping area exposed to blast is calculated from data provided in Table A- 14 and Section 5.3.1. To calculate the exposed area for each pipe line, the tributary lengths in transverse direction of all attached pipe supports are summed and multiplied by the outer diameter of the pipe section. The

total pipe area exposed to blast, A_P , is calculated by adding the exposed areas of each individual pipe line together and the result is presented in Table A- 23.

The total rack-member area exposed to blast, A_{RM} , was calculated by adding the exposed lengths of all applicable members in FE model B , and multiplying the combined length by a member width of 0.15 meters. Note that all rack members exposed to transverse blast loading are of type SHS150. Figure A- 14 and Figure A- 15 illustrate the sets defined in Abaqus that governed which rack members were assigned uniformly distributed blast loads in transverse direction. The distinction between shielded and non-shielded members applicable to analyses utilizing *Load Procedure 2* or *Load Procedure 3* is also illustrated.

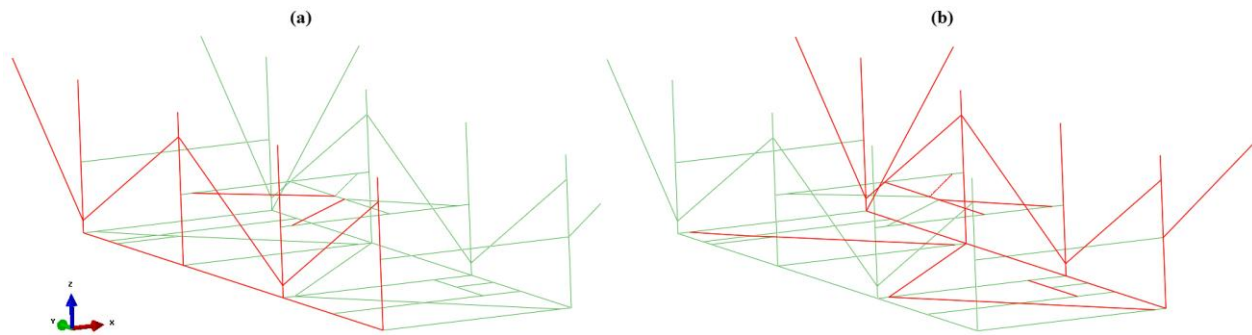


Figure A- 14 Shielded (b) and non-shielded (a) rack members exposed to blast in global +X direction.

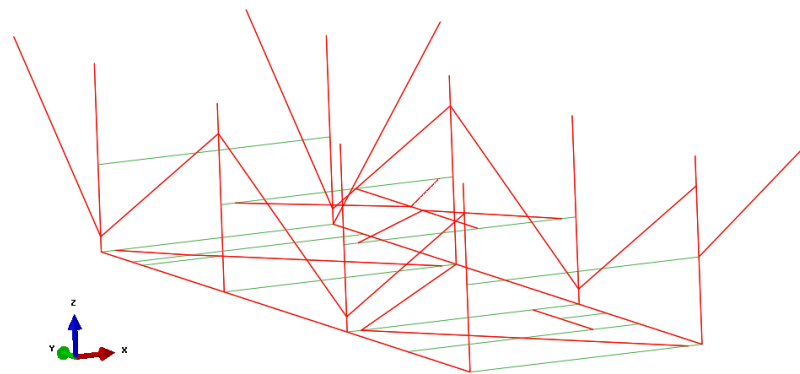


Figure A- 15 All rack members exposed to blast in transverse direction.

| Total Blast-exposed Pipe Area A_P [m ²] | Total Blast-exposed Rack Area A_{RM} [m ²] | Total Blast-exposed Area A_{Blast} [m ²] |
|--|---|---|
| 19.52 | 12.02 | 31.54 |

Table A- 23 Blast-exposed area in transverse direction of loading.

A.10 Abaqus FE Simulations | Methods & Modeling

This section describes all features and modeling techniques used for pre-processing and FE simulation in Abaqus. Reference is made to (Abaqus, 2015a) and (Abaqus, 2015b) for information on the Abaqus toolbox. The complete numerical implementation procedure associated with each analysis is also summarized herein, where utilized input data and modeling techniques are referenced.

General Procedures

All FE analyses in this study were simulated in Abaqus/Standard. Hence, system equilibrium was enforced at every time increment via an implicit numerical FE formulation.

Field variables documented in Chapter 6 correspond to the following requested Abaqus/Standard output variables:

Reaction forces in direction n – RFn

Stress - $MISES$

Plastic strain - $PEEQ$

Displacements in direction n – Un

For modelling of boundary conditions, reference is made to Section A.2 for representation of pipe supports in FE model A and Section A.3 for representation of connections to deck structure in FE model B.

The rack configuration in FE model B was modeled by use of *3D deformable parts*. Beam profiles with cross-sectional dimensions defined in Section 5.3.2 were assigned to the individual members accordingly.

Identical mesh properties were assigned to FE model B in all analyses within the study utilizing this model. A global mesh size of 0.2 meters was used, generating a mesh containing a total of 2217 elements and 3067 nodes. All rack members were modelled as 3D beam elements of type *B31* with linear interpolation.

The material properties assigned to rack members in FE model B are fully defined in Section 5.6. The data specifying the plastic mechanical properties of the material was only implemented in Analyses B.4, B.5 and B.6.

The *reference point* feature in Abaqus was used to define the exact location of all internal pipe supports in FE model B. Locations are specified in Section A.2.

The *coupling constraint* feature in Abaqus was employed to transfer point loads associated with the piping configuration to the meshed elements in FE model B via the exact location of the pipe supports. This approach was enforced in analyses utilizing *Load Procedure 1* or *Load Procedure 2* as described in Section A.8. *Coupling constraints* of type *Kinematic* were created for all internal pipe supports. The above mentioned *reference point* was chosen as the *control point* of the constraint and the two FE nodes of the mesh closest to the reference point were chosen as the *coupling nodes*. For all the kinematic coupling constraints created, all translational and rotational DOFs of the *coupling nodes* were constrained relative the *reference point*.

The *point mass/inertia* feature was used to account for the pipe configuration's contribution in mass in all analyses utilizing FE model B. The masses documented in Table A- 15 were assigned as *isotropic* masses via the *point mass/inertia* feature to the FE node closest to the *reference point* defining the location of the specific support.

Analysis A.1

The step sequence implemented in Analysis A.1 comprise of one single analysis step of type *Static, General*. Geometric nonlinearity effects were not accounted for.

The piping configuration in FE model A was modeled by use of *3D deformable parts*. *Thin walled* pipe profiles with cross-sectional dimensions defined in Section 5.3.1 were assigned to the individual pipe lines accordingly.

The piping configuration was meshed with a global mesh size of 0.2 m. The global mesh contains a total of 599 elements and 607 nodes. All pipe lines were modelled as 3D beam elements of type *B31* with linear interpolation.

Material properties of each pipe line defined by the associated material code referenced in Section 5.3.1 were assigned pipe members in FE model A according to data provided in Table A- 11 and Table A- 12, the latter governing the material density data implemented in Abaqus as it accounts for mass contribution from the piping content through calculations of a fluid content factor (FCF) as specified in Section A.4.

Structural self-weight of the piping configuration was accounted for by creating a load of type *gravity*. Loads of type *line load* were created to simulate blast loading in different directions. Line loads implemented in Analysis A.1 were calculated according to *Load Procedure 1* as specified in Table A- 18 and assigned to the modeled geometry in accordance with procedures documented in Section A.8.

Analysis B.1

The step sequence implemented in Analysis B.1 comprise of one single analysis step of type *Static, General*. Geometric nonlinearity effects were not accounted for.

Structural self-weight of the rack configuration was accounted for by creating a load of type *gravity*. Loads of type *line load* and *concentrated force* were created to simulate blast loading in all directions defined in Section A.5. Line loads and concentrated forces implemented in Analysis B.1 were calculated according to *Load Procedure 1* as specified in Table A- 17 and Table A- 19. Line loads were assigned to the modeled geometry in accordance with procedures documented in Section A.8 and concentrated forces were applied to their associated *reference point* attached to a *kinematic coupling constraint*.

Analysis B.2

The step sequence implemented in Analysis B.2 comprise of one single analysis step of type *Static, General* with a time period equal to 1 second. Geometric nonlinearity effects were not accounted for.

Structural self-weight of the rack configuration was accounted for by creating a load of type *gravity*. Loads of type *line load* and *concentrated force* were created to simulate blast loading in global $\pm X$ directions. Two different load procedures were utilized as explain in Section 6.3. Line loads implemented in Analysis B.2 are specified in Table A- 20 for both *Load Procedure 2* and *Load Procedure 3*. Line loads were assigned to the modeled geometry in accordance with procedures documented in Section A.8. Blast loads associated with the piping configuration were implemented as concentrated forces considering *Load Procedure 2*. Loads documented in Table A- 21 were applied to their associated *reference point* attached to a *kinematic coupling constraint*. For *Load Procedure 3*, line loads documented in Table A- 22 were assigned horizontal rack members to account for contribution from the piping in accordance with procedures documented in Section A.8.

All of the static blast loads implemented as either *line loads* or *concentrated forces* were gradually amplified during the FE simulations via implementation of an *amplitude curve* defined from *tabular* data. The amplitude curve implemented in all simulations within the scope of Analysis B.2 was set up to increase linearly from 0 to 5 for a fixed increment size of 0.05 seconds over the time period assigned to the *Static, General* analysis step. Properties of the implemented *amplitude curve* are shown in Figure A- 16. Abaqus interpolates linearly between prescribed values in order to find the amplitude used to scale the external loading at each time increment.

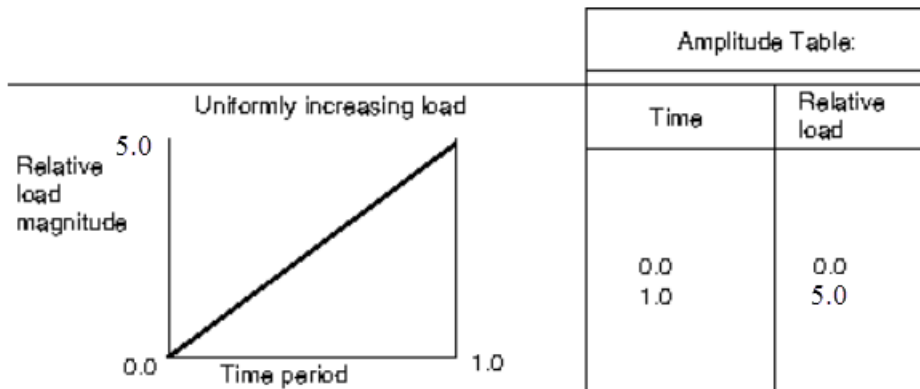


Figure A- 16 Amplitude curve implemented in Analysis B.2.

Analysis B.3

The step sequence implemented in Analysis B.3 comprise of two analysis steps. The first step is of type *Static, General*, associated with gravity loading only. The second step is of type *Linear Perturbation, Frequency*, solving the Eigenvalue problem. The first 30 eigenvalues were requested as output for this step. By implementation of this two-step simulation, the deformed configuration from the initial gravity step of type *Static General* will provide governing initial conditions for the eigenvalue analysis performed in the proceeding step of type *Linear Perturbation, Frequency*.

Structural self-weight of the rack configuration was accounted for by creating a load of type *gravity* in the initial analysis step of type *Static, General*.

Analysis B.4

The step sequence implemented in Analysis B.4 comprise of two analysis steps. The first step is of type *Static, General*, associated with gravity loading only and assigned a time period of 1 second. The second step is of type *Dynamic, Implicit*, associated with the blast-loading and dynamic response. Numerous simulations considering different governing values of pulse durations were conducted within the scope of Analysis B.4 as shown in Chapter 6. To capture both the forced and free vibration phase in all simulations, the time period of the *Dynamic, Implicit* step was consistently assigned as $3t_d$, i.e. three times the length of the pulse duration evaluated in the specific simulation. Geometric nonlinearity effects were accounted for in the *Dynamic, Implicit* step only.

Structural self-weight of the rack configuration was accounted for by creating a load of type *gravity* in the *Static, General* analysis step. Gravity loads then propagate to the following *Dynamic, Implicit* step during the simulation. Loads of type *line load* and *concentrated force* were created in the *Dynamic, Implicit* step to simulate blast loading in global +X direction. Line loads and concentrated forces implemented in Analysis B.4 were calculated according to *Load Procedure 2* as specified in Table A-20 and Table A-21. Line loads were assigned to the modeled geometry in accordance with procedures documented in Section A.8 and concentrated forces were applied to their associated *reference point* attached to a *kinematic coupling constraint*.

All of the static blast loads implemented as either *line loads* or *concentrated forces* were scaled with an *amplitude curve*, defined from *tabular* data to represent the properties of the governing triangular blast-pulse. The amplitude curves implemented in the different simulations within the scope of Analysis B.4 were set up to represent the design blast-pulse as documented in Section 5.8. Since the implemented loads defined in Table A-20 and Table A-21 were calculated based on the peak pressure of 20 kPa associated with the design-pulse, the implemented amplitude curves were all characterized by an amplitude of 1 at time $t_d/2$. Properties of the implemented *amplitude curves* are shown in Figure A-17. Abaqus interpolates linearly between prescribed values in order to find the amplitude used to scale the external loading at each time increment.

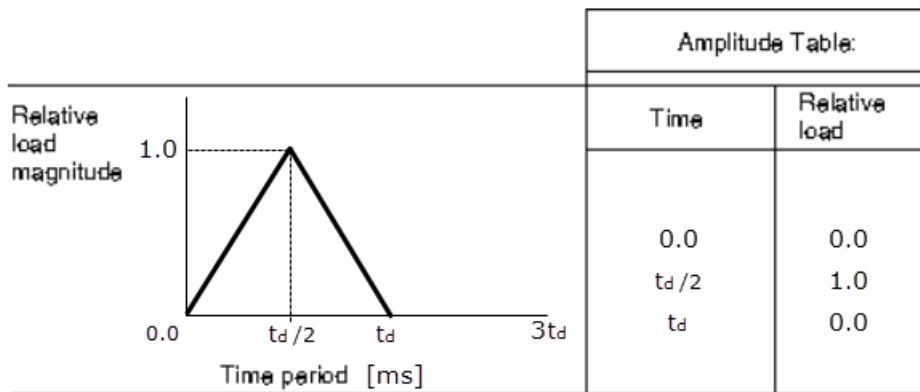


Figure A-17 Amplitude curves implemented in Analysis B.4.

Analysis B.5

The step sequence and loading implemented in Analysis B.5 is identical to implementation described above for Analysis B.4 with one exception.

The peak blast-pressure of 69.4 kPa characterizing the blast-pulse implemented in Analysis B.5 was determined by the highest value of limiting peak-pressure calculated according to the proposed method. Since the implemented loads defined in Table A- 20 and Table A- 21 were calculated based on the peak pressure of 20 kPa associated with the design-pulse, the implemented amplitude curves in Analysis B.5 were all characterized by an amplitude of $69.4/20 = 3.47$ at time $t_d/2$. Properties of the implemented *amplitude curves* are shown in Figure A- 18.

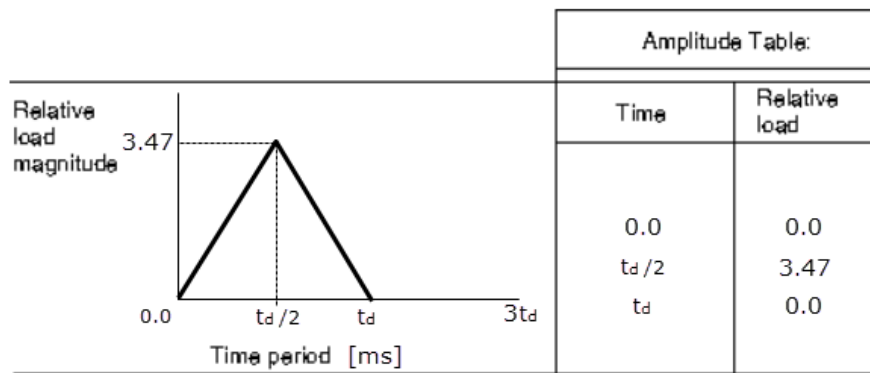


Figure A- 18 *Amplitude curves implemented in Analysis B.5.*

Analysis B.6

The step sequence and loading implemented in Analysis B.6 is identical to implementation described above for Analysis B.4 with one exception.

The peak blast-pressure of 96 kPa characterizing the blast-pulse implemented in Analysis B.6 was found to generate system failure as defined in Section 5.5. Since the implemented loads defined in Table A- 20 and Table A- 21 were calculated based on the peak pressure of 20 kPa associated with the design-pulse, the implemented amplitude curves in Analysis B.6 were all characterized by an amplitude of $96/20 = 4.8$ at time $t_d/2$. Properties of the implemented *amplitude curves* are shown in Figure A- 19.

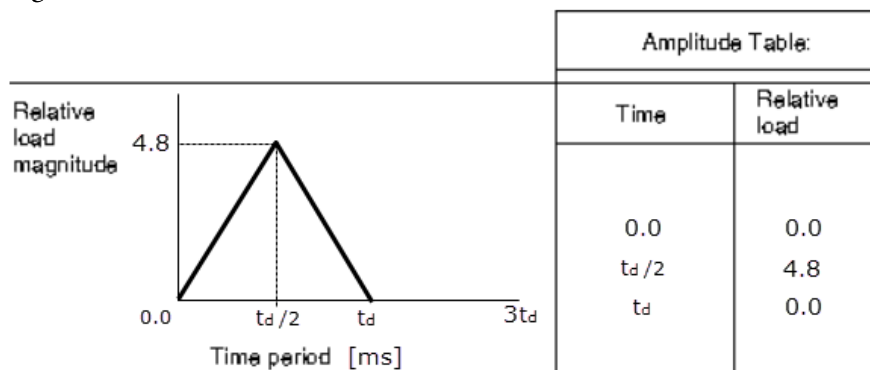


Figure A- 19 *Amplitude curves implemented in Analysis B.6.*

Appendix B Shielding Coefficient

The simplified approach of accounting for mitigating shielding effects for members that are not directly exposed to blast wind in the load direction is covered herein. The calculations shown below are taken from an internal AKSO project document. They relate to a typical pipe rack configuration loaded in longitudinal and transverse direction, and follow the recommended practice of (DNV-RP-C205, 2010).

Shielding factor:

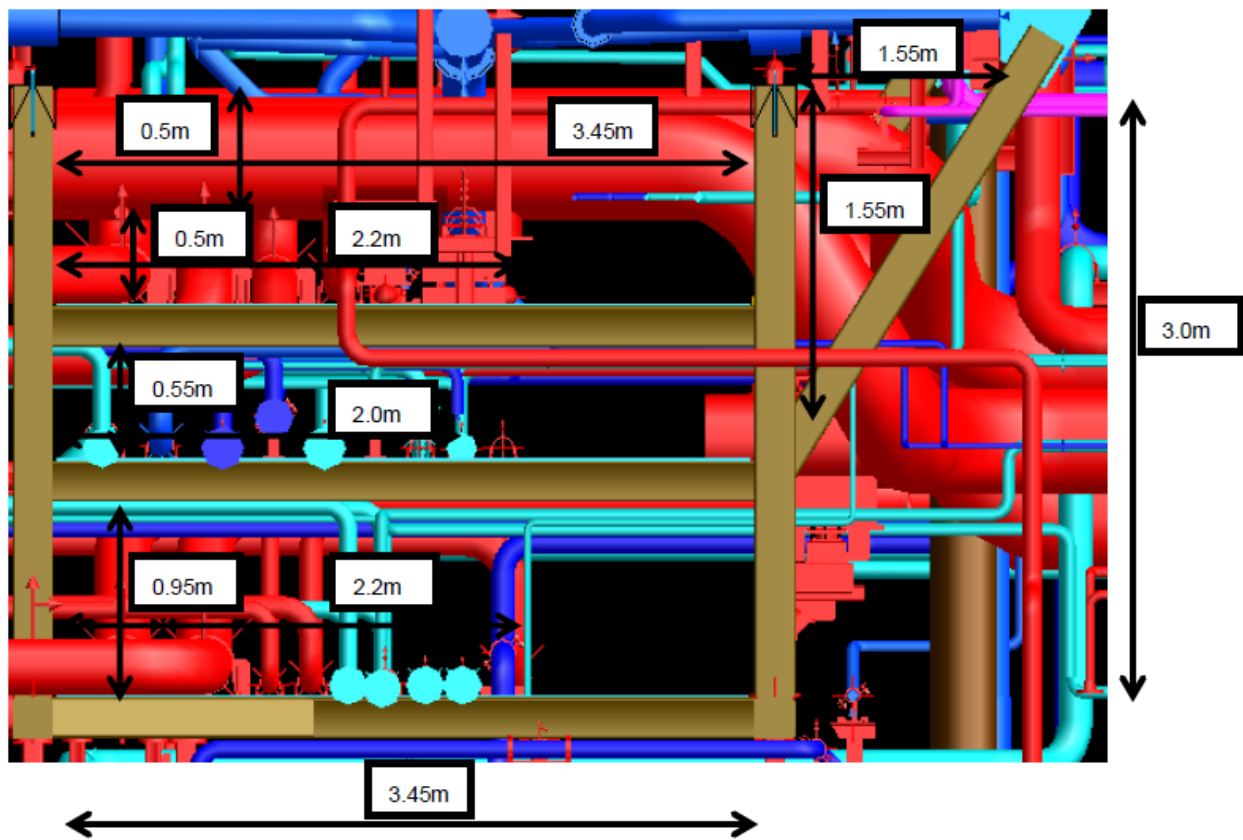


Figure 1.0: Piperack longitudinal cross section

Projected solid area of frame normal to wind direction

$$\begin{aligned}
 &= A = 0.5 \times 3.45 + 0.5 \times 2.2 + 0.55 \times 2 + \\
 &0.95 \times 2.2 + 3.2 \times 0.15 \times 2 + 3.45 \times 0.15 \times 3 \\
 &+ 0.5 \times 1.55 \times 1.55 \\
 &= 9.65 \text{ m}^2
 \end{aligned}$$

| | |
|---|--|
| Area enclosed by boundary of frame normal to wind direction | = $A_c = 3 \times 3.45 = 10.35\text{m}^2$ |
| Solidity ratio | = $\Phi = 9.65 / 10.35 = 0.93$ |
| a (Factor for flat sided members as per DNV-RP-C205) | = 1.6 |
| $\beta = \Phi \times a$ | = $0.93 \times 1.6 = 1.5$ |
| α (Frame spacing ratio) | = C/C dist. of frames / least overall dimension of frame perpendicular direction of wind |
| | = $1.6 / 3$ |
| | = 0.53 |
| So from Table 5.1 of DNV-RP-C205, shielding factor η | = 0.4 |

Similarly shielding factor in other directions shall be calculated.

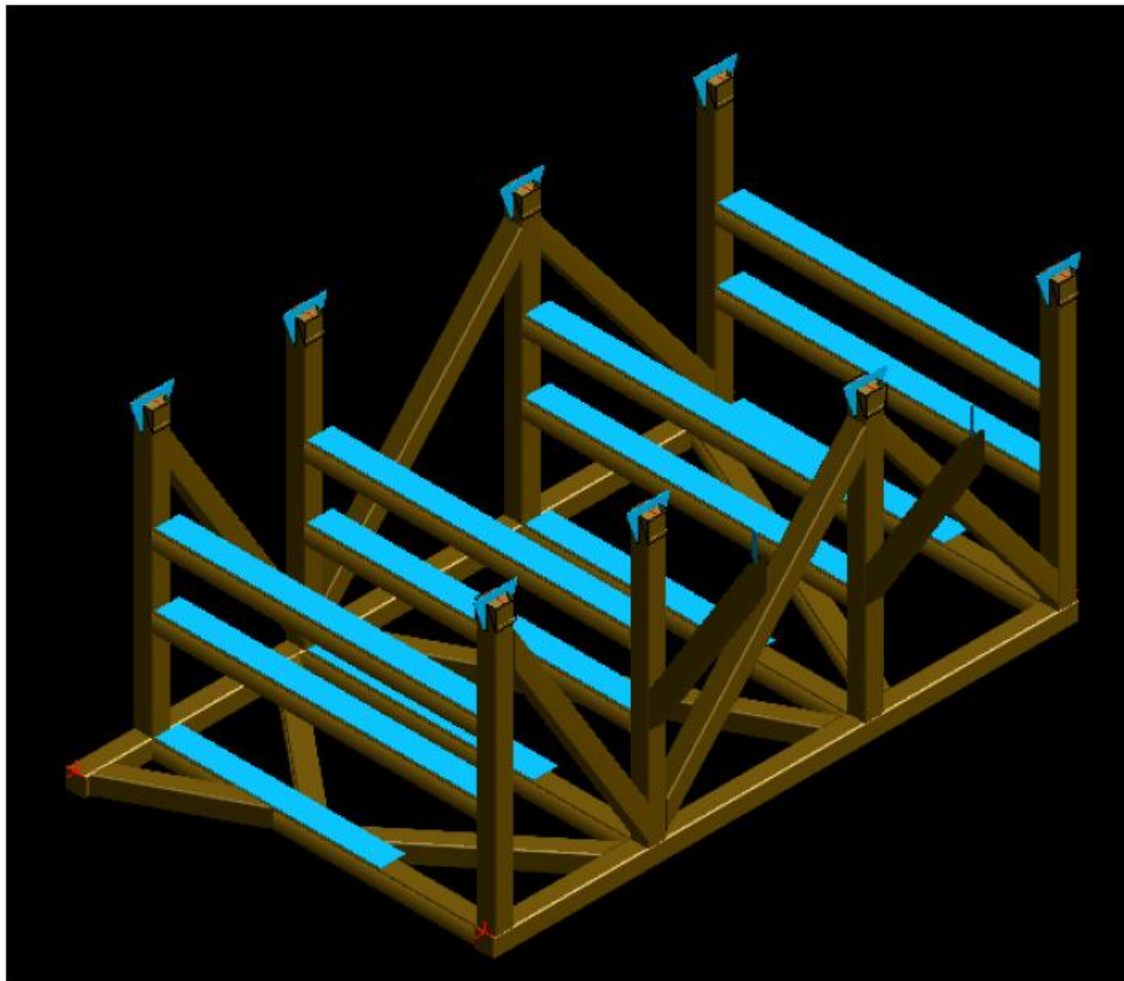


Figure 1.1: Piperack showing structural member arrangement

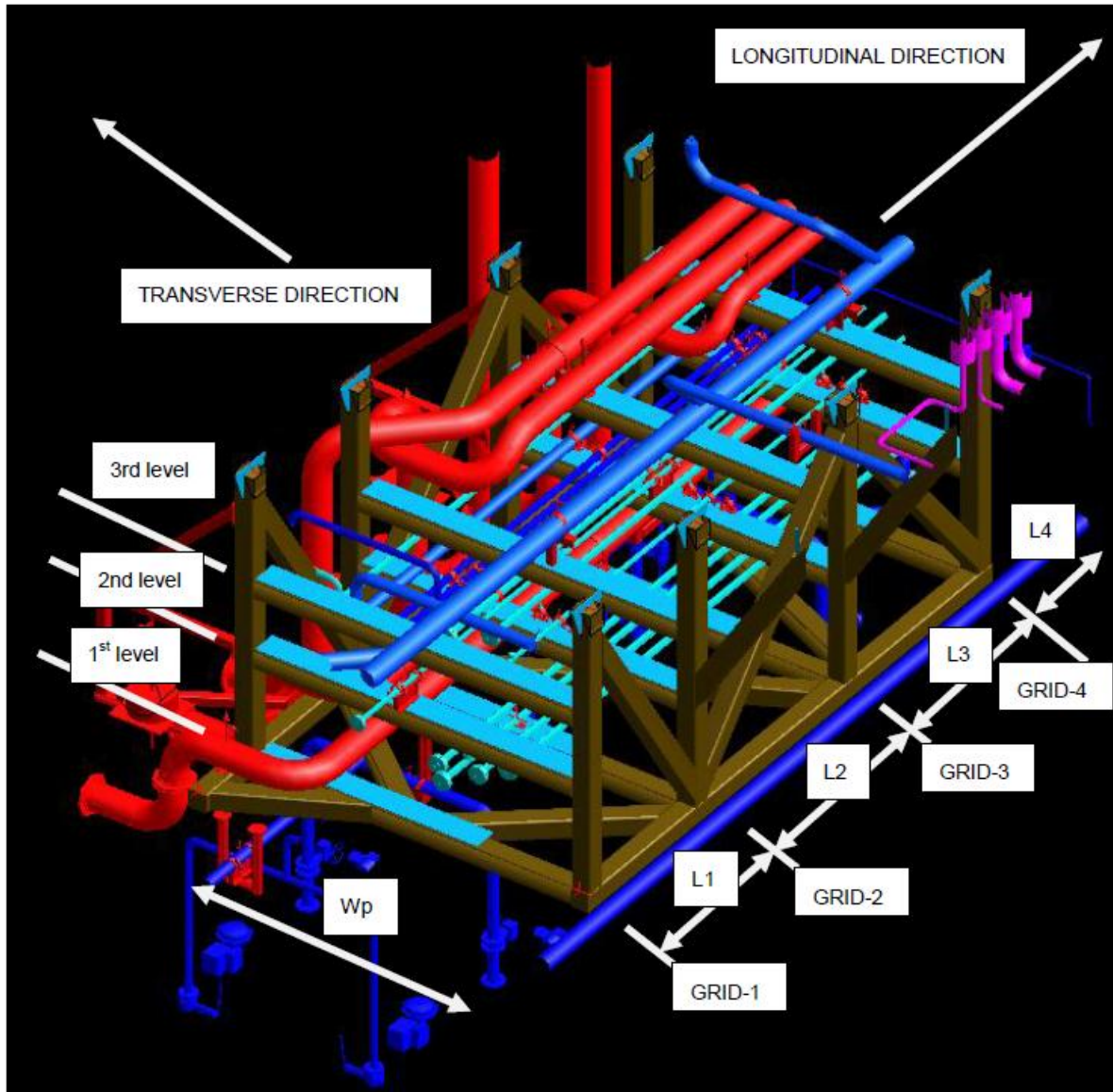


Figure 1.2: Piperack showing structural members and piping arrangement

Calculations of the shielding coefficient for the same pipe rack configuration referenced above, but considering loading in transverse direction, yielded a less conservative value of $\eta = 0.5$. It is assumed that the typical pipe rack configuration from where this value was derived is similar to *Piperack01_P30_M50*. Hence, a value of $\eta = 0.5$ was consistently used within this study.

Paragraphs below define the members that were considered shielded from loading in transverse direction and thus assigned a shielding coefficient of $\eta = 0.5$ in the load calculations. Considering the rack configuration and Figure B- 1 shown below, non-shielded members are seen to be directly exposed to the blast while shielded sections are located within a plane in which coverage is offered by members closer to the origin of the blast.

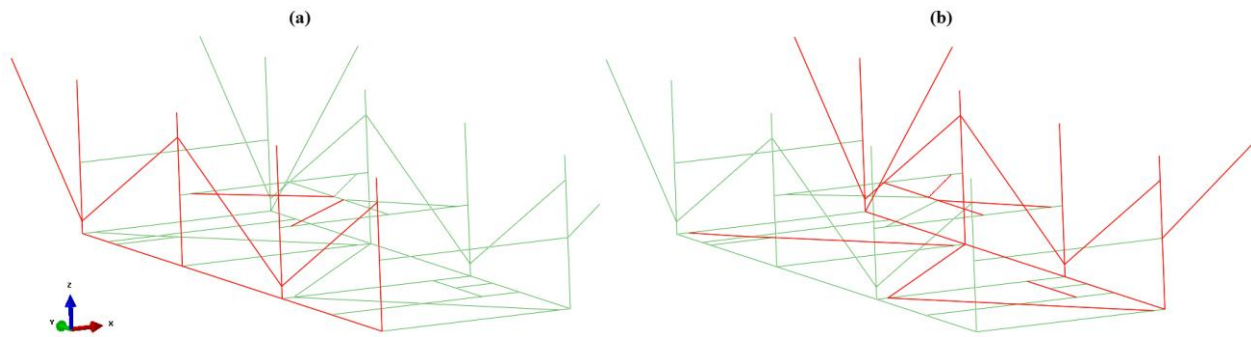


Figure B-1 Shielded (b) and non-shielded (a) rack members exposed to blast in global +X direction.

Figure B- 2 shown below defines shielded pipe sections, denoted far pipe sections, and non-shielded pipe lines, denoted near pipe sections.

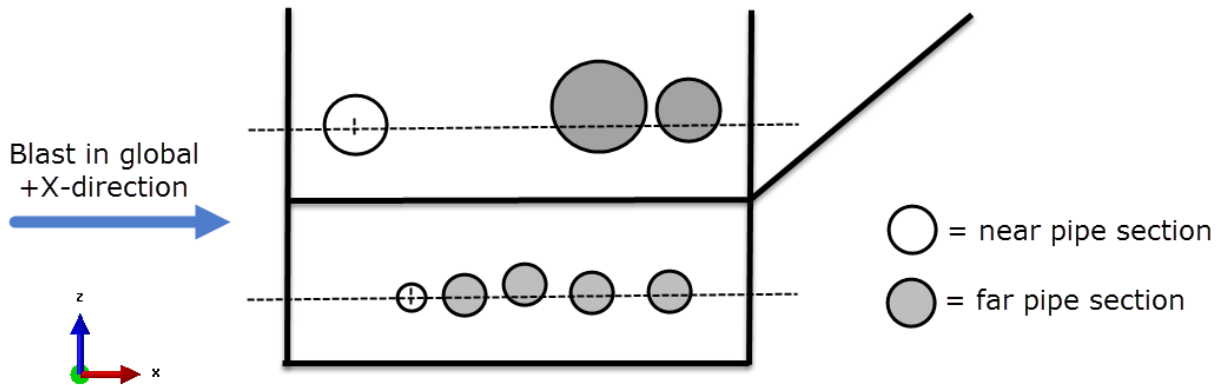


Figure B- 2 Definition of far and near pipe sections governing procedures accounting for shielding.

For application of shielding factors to blast loads associated with pipe lines, all pipe lines which cross-section intersect with the centreline of a *near pipe section* will be treated as a *far pipe section* as shown by Figure B- 2.

Appendix C Plastic Strain Criterion Study

The internal AKSO-study referenced in Section 5.5 has been included below.

Effect of numerical modelling on strains and stresses of a girder subjected to blast condition.

A 420 steel of IG 800x400x20x30 with length of 10.6 meters is subjected to different blast pressure magnitude. The duration of the blast pressure is 200 mili-seconds. The blast pressure has triangular impulse shape. The girder is fixed at both ends. The shell and beam element models are created to observe the effect of different models on structural stress and strain. The element size is 50 mm. The following table shows that the beam elements will experience less strain compared to shell elements. To be conservative, 3% critical plastic strain on beam elements could be plastic strain related to a fracture on shell element.

Table 6.9-1 Maximum equivalent plastic strains on different models of IG800x400x20x30 subjected to blast pressure

| Blast pressure (bar) | Maximum plastic strain in beam element | Maximum plastic strain in shell element |
|----------------------|--|---|
| 2.5 bar | 5.98% | 16.65% |
| 2.2 bar | 3.13% | 7.82% |
| 2 bar | 2% | 4% |

Appendix D Matlab Script

The Matlab script attached to this appendix calculates the normalized dynamic response or DAF of a linear-elastic, undamped SDOF-system subjected to a symmetrical triangular pulse. The full time-history response is graphically displayed along with the magnitude of the DAF. The numerical implementation is based on the closed-form solution of this response given by Equation (D.1).

$$\frac{u(t)}{(u_{st})_0} = \begin{cases} 2 \left(\frac{t}{t_d} - \frac{T_n}{2\pi t_d} \sin \left(2\pi \frac{t}{T_n} \right) \right) & \text{if } 0 \leq t \leq \frac{t_d}{2} \quad (\text{D.1a}) \\ 2 \left\{ 1 - \frac{t}{t_d} + \frac{T_n}{2\pi t_d} \left[2 \sin \left(\frac{2\pi}{T_n} \left(t - \frac{1}{2} t_d \right) \right) - \sin \left(\frac{2\pi t}{T_n} \right) \right] \right\} & \text{if } \frac{t_d}{2} \leq t \leq t_d \quad (\text{D.1b}) \\ 2 \left\{ \frac{T_n}{2\pi t_d} \left[2 \sin \left(\frac{2\pi}{T_n} \left(t - \frac{1}{2} t_d \right) \right) - \sin \left(\frac{2\pi}{T_n} (t - t_d) \right) - \sin \left(\frac{2\pi t}{T_n} \right) \right] \right\} & \text{if } t \geq t_d \quad (\text{D.1c}) \end{cases}$$

where t is the time after load application at which the displacement is calculated; t_d is the phase duration of the symmetrical triangular pulse; and T_n is the natural period of the SDOF-system.

The amplitude of the static equilibrium is defined by Equation (D.2).

$$(u_{st})_0 = \frac{p_0}{k} = \frac{P_{so}A}{k} \quad (\text{D.2})$$

where $(u_{st})_0$ define the displacement generated from static application of the peak pulse-force p_0 ; P_{so} is the peak pulse-pressure converted to unit force through multiplication with the applicable area A of the idealized SDOF-system facing the blast-wave; and k is the stiffness of the SDOF-system.

MATLAB SCRIPT

```
function [DAF,Plot]=s doftriangular(T_n,t_d)

%%%%%%%%%%%%%%%%%%%%%%%%%%%%%%%%%%%%%%%%%%%%%%%%%%%%%%%%%%%%%%%%%%%%%%%%
% SDOF-response (DAF) to symmetric triangular pulse-excitation.
% Reference: Chopra (2011, Eq. 4.9.1)
% Written by: Adam Stålmarck,      Oslo 2015-05-16
%
% INSTRUCTIONS:
%
% Call the function '[DAF,Plot]=s doftriangular(T_n,t_d)' from the Matlab
% Command Window, specifying the following input:
%
% a. Pulse duration in milliseconds, t_d=[ms] **
% b. Natural period in milliseconds, T_n=[ms]
%
% ** NOTE: Script will only run if specified pulse duration t_d is
% an even number. It is required that t_d/2 is an integer.
%%%%%%%%%%%%%%%%%%%%%%%%%%%%%%%%%%%%%%%%%%%%%%%%%%%%%%%%%%%%%%%%%%%%%%%%

check=round(t_d/2);

if check ~= t_d/2
    msg='Pulse duration t_d must be specified as an even number. It is required
that t_d/2 is an integer. ';
    error(msg)
else

time_vec_stat1=linspace(0,t_d/2,t_d/2+1);
time_vec_stat2=linspace(t_d/2,t_d,t_d/2+1);
stat_vec1=(2/t_d).*time_vec_stat1;
stat_vec2=(-2/t_d).*time_vec_stat2+2;

time_vec=linspace(0,t_d*4,(t_d*4)+1);

DAF1=zeros(1,t_d/2);
DAF2=zeros(1,t_d/2);
DAF3=zeros(1,t_d*3);

for i=1:t_d/2+1

    DAF1i=2*((time_vec(i)/t_d)-((T_n/(2*pi*t_d))*sin((2*pi*time_vec(i))/T_n)));

    DAF1(i)=DAF1i;
end

DAF1;

for j=t_d/2+2:t_d+1

    DAF2i=2*(1-(time_vec(j)/t_d)+((T_n/(2*pi*t_d))*((2*sin(((2*pi)/(T_n*10^-
3)))*(time_vec(j)*10^-3)-(0.5*(t_d*10^-3)))))-sin((2*pi*time_vec(j))/T_n));
```

```

    DAF2(j-(t_d/2)-1)=DAF2i;
end

DAF2;

for k=t_d+2:t_d*4+1

    DAF3i=2*((T_n/(2*pi*t_d))*((2*sin((2*pi)/(T_n*10^-3))*((time_vec(k)*10^-
3)-(0.5*(t_d*10^-3)))))-(sin((2*pi)/(T_n*10^-3))*((time_vec(k)*10^-3)-
(t_d*10^-3))))-sin((2*pi*time_vec(k)/T_n));

    DAF3(k-t_d-1)=DAF3i;
end

DAF3;

DAF_vec=[DAF1,DAF2,DAF3];

Plot=plot(time_vec,DAF_vec,'-b')
title('Linear-Elastic, Undamped SDOF-response to Symmetric Triangular Pulse-
Excitation')
xlabel('Time [ms]')
ylabel('Normalized Dynamic Response')

indexmax=find(max(DAF_vec) == DAF_vec);
xmax=time_vec(indexmax);
ymax=DAF_vec(indexmax);
strmax=['DAF = ',num2str(ymax)];
text(xmax,ymax,strmax,'HorizontalAlignment','right');

hold on
plot(time_vec_stat1,stat_vec1,'--k')

hold on
plot(time_vec_stat2,stat_vec2,'--k')
legend('Normalized Dynamic Response','Normalized Static
Solution','Location','southeast')

DAF=max(DAF_vec)

end

```

Appendix E Static Pushover Analysis

Attached to this appendix is an example illustrating how the inelastic capacity of a simple structural system may be determined through a static pushover analysis. The analytical method and its application to the two-dimensional beam with fixed ends shown in Figure E- 1(a) is explained below according to Kanvinde (2014).

In a static pushover analysis, the external forces acting on the system are gradually increased until any one member reaches its plastic moment-resisting capacity. The fully utilized cross-section of this member is treated as a *perfect plastic hinge* as the incremental loading is increased further. The process of incremental load increase and hinge formation is continued until the structure becomes unstable, i.e. a *mechanism*, or until other predefined failure criteria are reached. The definition of a perfect plastic hinge is that it continues to carry the plastic moment capacity M_p as incremental loading is added to the system, without accounting for additional forces from incremental rotations of the hinge.

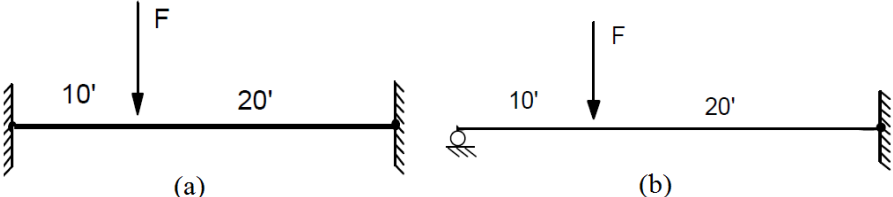


Figure E- 1 Idealized beam models for (a) initial configuration and (b) configuration after development of first plastic hinge.

The beam in Figure E- 1(a) is subjected to a point load of magnitude F , eccentrically located 10 meters from its left end and 20 meters from its right end. The associated bending moment diagram illustrated in Figure E- 2 (a) may be obtained from conventional bending moment formulas for two-dimensional beams subjected to uniaxial bending.

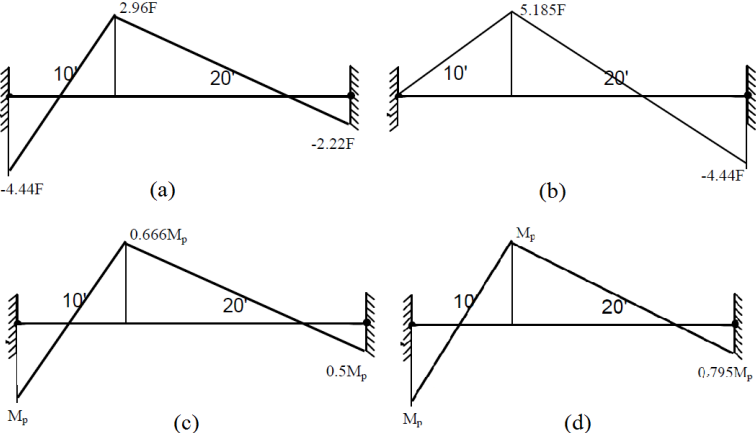


Figure E- 2 Bending moment diagrams up until development of second hinge.

Figure E- 2 (a) show that a maximum moment equal to $4.44F$ is reached at the left end, implying that the first plastic hinge will form at this location. This will occur at a load level F_1 calculated from the relation $M_p = 4.44F_1 \rightarrow F_1 = 0.225M_p$.

At this stage a hinge has formed at the left end and the system may be idealized according to Figure E- 1 (b) as the incremental loading is increased further. The corresponding incremental moment diagram for the idealized system with one plastic hinge is shown in Figure E- 2 (b), defining the redistribution of forces within the system after formation of the first hinge. The incremental distribution is added to the initial distribution prior to the first hinge formation to obtain the total distribution since the hinge continues to carry M_p . The total moment distribution at this stage is shown in Figure E- 2 (c), calculated by substituting $F = F_1 = 0.225M_p$ in Figure E- 2 (a) and (b) and adding the two distributions together by superposition.

It is evident from Figure E- 2 (c) that the second hinge will form at the point of load application. This will occur at a load level of $F_2 = F_1 + \Delta F$, where the incremental load is determined from the relation $M_p = 0.666M_p + 5.185\Delta F \rightarrow \Delta F = 0.0644M_p$. When the second hinge has reached full plastic moment-capacity, the moment distribution in the system is given by Figure E- 2 (d) and the idealized system and associated incremental moment diagram is given by Figure E- 3.

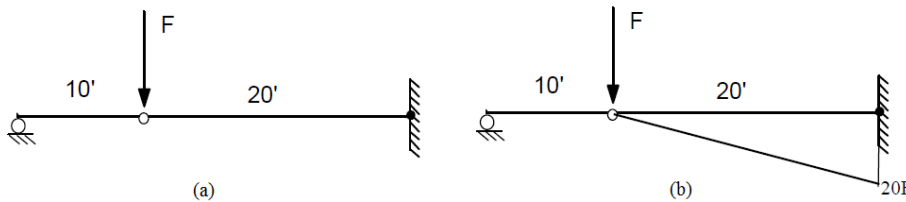


Figure E- 3 Idealized beam model (a) and incremental moment distribution (b) after second hinge formation.

After development of the third hinge which will form at the right end, the system becomes a mechanism as it has no stiffness left to resist further loading. The mechanism model of the beam is shown in Figure E- 4 along with the associated moment distribution. According to procedures defined above, the mechanism load which causes the formation of the third hinge can be calculated to $F_3 = F_{mechanism} = 0.3M_p$.

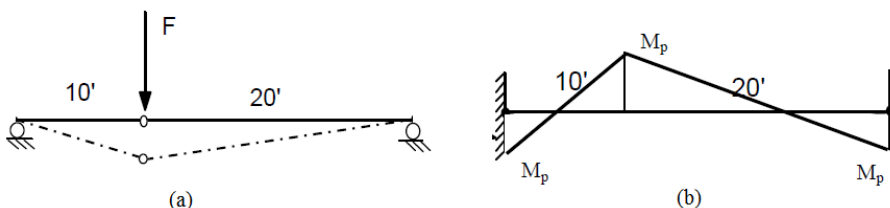


Figure E- 4 Final mechanism model (a) and moment distribution (b) at development of third hinge.

The inelastic behavior of the analyzed system can be summarized by the associated *pushover curve* which is shown in the main body of the report in Section 3.3.